UNIVERSITÀ DELLA CALABRIA

UNIVERSITA' DELLA CALABRIA
Dipartimento di Fisica

Dottorato di Ricerca in
SCIENZE E TECNOLOGIE FISICHE, CHIMICHE E DEI MATERIALI

CICLO
XXIX

EFFECTS OF THE SOLAR ACTIVITY ON SPACE WEATHER AND EARTH'S CLIMATE

Settore Scientifico Disciplinare FIS/06

Coordinatore: Ch.mo Prof. Vincenzo CARBONE
Vincenzo Carbone

Supervisore/Tutor: Ch.mo Dott. Fabio LEPRETI
Fabio Lepreti

Dottorando: Dott. Tommaso ALBERTI
Tommaso Alberti

To *Alessandra,*
Mamma, Papà,
Milena e Nonna

Available energy is the main object at stake in the struggle for existence and the evolution of the world.

Ludwig Eduard Boltzmann

Acknowledgements

Firstly, I would like to express my sincere gratitude to my supervisor Dr. Fabio Lepreti for the continuous support of my PhD study and related research. His guidance helped me in all the time of research and writing of this thesis.

Besides my supervisor, my sincere thanks also goes to Prof. Vincenzo Carbone for his motivation and immense knowledge, I was honored to work with him.

My deepest heartfelt appreciation goes to Dr. Antonio Vecchio for his insightful suggestions, constructive comments and warm encouragement.

I would like to show my greatest appreciation to Dr. Giuseppe Consolini and Dr. Monica Laurenza for their support to my research, their invaluable encouragement and suggestions. Without they precious support it would not be possible to conduct some part of my research.

Acknowledgements need to be due to Dr. Mirko Piersanti and Prof. Umberto Villante for their kindness and courtesy, in addition to their support in my research.

A remarkable thanks also goes to Dr. Paola De Michelis for her courtesy and knowledge, very useful in several parts of my research.

Finally, I want to thank my extra-european co-author, Dr. E.W. Cliver, for his patience and kindness as well as his knowledge, always useful during my research activity.

A special thanks to my family. Words cannot express how grateful I am to my mother, my father, my sister and my grandmother for all of the sacrifices that you've made on my behalf.

I would also like to thank Dr. Christian Leonardo Vasconez Vega for his sincere and honest friendship, I wish him all the best for his life.

At the end I would like express appreciation to my beloved girlfriend Alessandra who was always my support in the moments when there was no one to answer my queries, whose enthusiasm, interest and support have given me the motivation to realize this achievement.

Sommario

Lo studio delle relazioni Sole–Terra riguarda l'analisi e comprensione dei fenomeni di origine solare che provocano effetti sull'ambiente circumterrestre. Il Sole è la sorgente primaria di energia sulla Terra ed è proprio l'energia che continuamente riceviamo dal Sole che consente, all'interno di un sistema complesso noto come sistema climatico, di poter raggiungere temperature medie superficiali che consentono lo sviluppo della vita sul nostro pianeta, anche se con differenze da luogo a luogo e da stagione a stagione. Inoltre, l'estrema complessità e variabilià delle condisioni fisiche del Sole determina cambiamenti sia globali che locali all'interno dell'eliosfera. In particolare, questi cambiamenti sono legati a fenomeni di attività magnetica che avvengono sia all'interno del Sole che nella sua atmosfera, che si manifestano attraverso variazioni dell'irradianza solare (dall'ultravioletto fino ai raggi X), emissioni di massa coronale e brillamenti solari (flares), che sono caratterizzati dal rilascio di grandi quantità di energia e particelle ad alta velocità. Quest'ultime, con una velocità media di circa 450 km/s ed una temperatura che raggiunge il milione di gradi, formano il "vento solare", che interagisce con la nostra magnetosfera esercitando su di essa una pressione tale da determinarne così la forma, ma anche i suoi cambiamenti. Entro circa otto minuti dalla comparsa del fenomeno sul Sole, l'ambiente circumterrestre viene raggiunto dall'ondata di radiazione ultravioletta ed X che viaggia alla velocità della luce nel vuoto, producendo una fortissima ionizzazione dell'alta atmosfera, con fortissimi disturbi nelle radiocomunicazioni. Circa un'ora dopo, giungono i protoni più veloci, appena deviati dal campo magnetico terrestre. Nelle successive 20–40 ore, la maggior parte delle particelle, che per effetto della deflessione generata dal campo magnetico terrestre si concentrano nelle regioni polari, penetra all'interno della magnetosfera, generando perturbazioni alle correnti presenti e producendo una intensa ionizzazione della ionosfera. Viene così generata quella che è nota come tempesta geomagnetica che innesca diversi effetti: dal malfunzionamento delle radio– e tele–comunicazioni allo sfasamento delle bussole, fino a disturbi nella comunicazione GPS e a danni all'elettronica dei satelliti, così come possibili serie conseguenze sulla salute degli astronauti in orbita. Nel cielo notturno delle regioni polari si sviluppa una forte luminescenza caratteristica, nota come aurora polare, attraverso cui il cielo ap-

pare drappeggiato da coltri luminescenti che ondeggiano, intensificandosi ed attenuandosi per diverse ore. Al di là di queste evidenti manifestazioni, non vi è alcun dubbio sul fatto che il ciclo di attività solare, un fenomeno quasi–periodico in cui si alternano, su un periodo di circa 11 anni, fasi di massima e minima attività solare, produca effetti sulla Terra, sulle sue vicende meteorologiche, sulle stagioni, forse sulla fisiologia stessa delle piante e degli animali, uomo compreso.

Lo scopo di questo lavoro di tesi riguarda lo studio, l'analisi e la modellizzazione dei fenomeni che avvengono nell'ambiente circumterrestre, dalla magnetosfera fino alla superficie terrestre, passando per la ionosfera, nonchè l'evoluzione e la dinamica del clima terrestre, in relazione alle variazioni dell'attività solare.

In particolare, viene affrontato lo studio delle interazioni tra il vento solare e la magnetosfera terrestre nel corso di due tempeste geomagnetiche, avvenute nello stesso giorno, il 17 marzo, ma in due anni differenti, 2013 e 2015, e note come tempeste di San Patrizio. In tale studio, si identificano le scale caratteristiche di oscillazione presenti sia in dati relativi al vento solare (campo magnetico e tasso di trasferimento di energia) che alla dinamica delle correnti aurorali ed equatoriali (auroral electrojets e ring current), mediante l'utilizzo di una tecnica avanzata di decomposizione di segnali nota come Empirical Mode Decomposition (EMD). Da un'analisi di correlazione sia lineare che non lineare, basata sulla teoria dell'informazione (Delayed Mutual Information, DMI), è possibile verificare quantitativamente l'esistenza di una separazione di scala tra processi legati alla dinamica interna della magnetosfera (e quindi non direttamente guidati dalle fluttuazioni del vento solare) e processi in cui il vento solare induce variazioni alla stabilità della configurazione magnetosferica. Questi processi vengono identificati come "loading–unloading mechanism" e "directly driven process". Il primo è legato alla dinamica interna della magnetosfera ed in particolare agli effetti convettivi delle correnti di coda sulle altre correnti magnetosferiche, mentre il secondo alle variazioni della struttura della magnetosfera direttamente connesse con i cambiamenti osservati nelle condizioni del vento solare.

Grazie allo studio combinato di misure del campo geomagnetico, ottenute mediante l'utilizzo di magnetometri terrestri, e di misure del campo magnetosferico, ottenute grazie all'ausilio dei satelliti geostazionari della missione GOES, è stato possibile evidenziare il contributo della ionosfera alle variazioni del campo magnetico terrestre sia durante periodi di quiete del vento solare che in periodi in cui si osservavano tempeste geomagnetiche. Inoltre, è stato possibile identificare il contributo a grande scala del campo geomagnetico che potrebbe essere utilizzato ai fini della definizione di un nuovo indice locale di attività geomagnetica per monitorare le variazioni sia nei giorni di quiete che in un periodo di disturbo.

Nell'ambito dei fenomeni a scale temporali più brevi, è stata, poi, proposta una validazione di un modello di previsione di particelle energetiche su un periodo diverso rispetto a quello su cui era stato validato in precedenza. I parametri di valutazione, ovvero la probabilità che un evento sia previsto e si verifichi così come il tasso di falsi allarmi, risultano in accordo con i valori precedentemente trovati, dimostrando la robustezza e l'accuratezza del modello di previsione. Inoltre, attraverso lo studio dei parametri utili alla validazione del modello stesso (localizzazione sulla superficie solare, emissione di raggi X e onde radio) è stato possibile evidenziare le differenze nell'attività solare degli ultimi due cicli solari (ciclo 23 e 24). In particolare, si è notata una sensibile riduzione nel numero di fenomeni di attività solare noti come brillamenti solari (flares) di circa il 40% con una conseguente diminuzione degli eventi connessi alla generazione di particelle energetiche nell'ambiente circumterrestre.

Per quel che riguarda invece la dinamica a grande scala delle relazioni Sole–Terra sono state studiate prevalentemente le variazioni a grande scala osservate nel corso della storia paleoclimatica del clima terrestre e due modelli di bilancio energetico al fine di descrivere i cambiamenti climatici così come le condizioni per l'abitabilità della Terra.

In particolare, dall'analisi delle concentrazioni dell'isotopo 18 dell'ossigeno, nei carotaggi eseguiti al polo Nord ed al polo Sud e riferiti all'ultimo periodo glaciale, 20.000–120.000 anni fa, è stato possibile individuare due cicli di variabilità all'interno delle variazioni del clima terrestre: una dinamica su scale temporali dell'ordine di 1.500 anni, caratterizzata da rapidi e repentini incrementi di temperatura noti come eventi di Dansgaard–Oeschger, e l'evoluzione, su scale tipiche di decine di migliaia di anni, associata all'alternarsi di periodi globalmente più caldi o più freddi. Mentre gli eventi di Dansgaard–Oeschger sono associati a fluttuazioni di temperatura all'interno di uno stesso stato climatico, la dinamica a grande scala temporale è legata a fluttuazioni che avvengono tra due diversi stati climatici, caratterizzati da diverse temperature globali, ed identificabili come fasi stadiali e interstadiali nel corso di un periodo glaciale. Inoltre, è stato osservato come i cambiamenti climatici che avvengono al polo Nord siano guidati da precedenti variazioni nella storia climatica terrestre registrati nell'emisfero opposto, con un ritardo temporale dell'ordine di 3.000 anni che potrebbe essere legato a fenomeni connessi con la circolazione termoalina oceanica.

Infine, all'interno del contesto dei modelli climatici basati sull'equilibrio termico tra la radiazione solare incidente e quella emessa dalla superficie terrestre, è stato sviluppato un modello che consente di descrivere l'evoluzione della temperatura sulla superficie terrestre al variare della latitudine, dell'irradianza solare e dell'effetto serra. In particolare, i risultati delle simulazioni numeriche mostrano come l'effetto serra sia di fondamentale importanza all'interno dei meccanismi di stabilizzazione e regolazione del clima terrestre così come i cambiamenti ciclici e non, osservati nell'irradianza solare, possono influenzare l'evoluzione della temperatura terrestre. In particolare, in riferimento alle attuali condizioni di irradianza solare è stato osservato un comportamento oscillante legato alle fluttuazioni di temperatura, con variazioni dell'ordine di ~ 3 °C ed un periodo dell'ordine di circa 800 anni, che potrebbe essere utile per descrivere il comportamento quasi–periodico evidenziato dall'analisi di serie temporali legate alle variazioni climatiche.

Abstract

The large variability of the physical conditions of the Sun, over a wide range of spatial and temporal scales, represents the primary source which determines global and local changes inside the heliosphere and, what is perhaps more interesting, in the near Earth space. However, due to the extreme complexity of the system, nonlinear interactions among different parts of the Sun–Earth system play a key role, enormously increasing the range of physical processes involved. Indeed, fluctuations in the magnetic field within the solar atmosphere act as a complex modulation of plasma conditions in the interplanetary space, producing sudden enhancements of the solar energetic particles (SEP) fluxes and cosmic rays, as well as sudden coronal mass ejections (CMEs), or solar irradiance changes in several spectral ranges (from UV to visible). These events are associated with the origin of geomagnetic storms, which have important effects on our technological society, and possibly on global changes in the climate conditions through complex interactions with the Earth's atmosphere. The investigation of the physical processes which mainly affect solar and interplanetary space conditions, and the observation and understanding of the interactions of the solar wind with the Earth's magnetosphere are crucial to be able to predict and mitigate those phenomena that affect space and ground infrastructures or impair the human health.

This thesis addresses, through both data analysis and theoretical models, some of the main issues concerning the nature of the variability of solar activity which affect Space Weather and Earth's climate.

The solar wind–magnetosphere coupling during geomagnetic storms is investigated considering the two events occurred on March 17, 2013 and the same day of 2015, well–known as St. Patrick's Day storms. To this purpose, we analyze interplanetary magnetic field and energy transfer function (i.e., known as Perreault–Akasofu coupling function) time series to study the solar wind variability, as well as geomagnetic indices, related to the ring current and auroral electrojets activity, to investigate their response to solar wind variations. Through the Empirical Mode Decomposition (EMD) we identify the intrinsic oscillation timescales in both solar and magnetospheric time series. A clear timescale separation between directly driven processes, through which solar wind affects magnetospheric current systems,

and loading–unloading processes, which, although triggered by solar wind variations, are related to the internal dynamics of the magnetosphere, is found. These results are obtained by the combined analysis between EMD and information theory (i.e., Delayed Mutual Information analysis) allowing us to investigate linear and non–linear coupling mechanisms, without any assumptions on the linearity or stationarity of the processes.

By using both geostationary and ground–based observations of the Earth's magnetic field, we investigate, then, the role of the ionosphere into the variations of the geomagnetic field, during both quiet and disturbed periods. We also provide a separation of both magnetospheric and ionospheric signatures in the geomagnetic field as well as the large–timescale contribution which could be useful to define a new local index to monitor geomagnetic activity, since it is free from any magnetospheric or ionospheric contribution.

In the framework of the short–term effects of solar activity on Earth's environment, we investigate the occurrence of SEP events in both solar cycles 23 and 24 and we validate a short–term prediction model (termed ESPERTA) on a new database, different from that on which it was previously evaluated. We found a reduction of SEP events occurrence of $\sim$40%, suggesting that several differences can be found between the latter two solar cycles. Although these differences, the performance of the ESPERTA model are quite similar in both periods, confirming the robustness and efficiency of the model.

Concering solar–terrestrial relations on larger timescales we propose two different climate models to investigate the role of solar irradiance changes on the stability of the Earth climate as well as the effects of greenhouse variations on the planetary surface temperature. We find that the greenhouse effect plays a key role into the stabilization and self–regulation properties of the Earth climate and that solar irradiance changes could affect the evolution of Earth's climate. Interestingly, for the present conditions of solar irradiance an oscillatory behavior is found with temperature fluctuations $\Delta T \sim 3$ K and oscillations on 800–yr timescale that needs to be investigated with more accuracy because it can reproduce several quasi–periodic behaviors observed in climatic time series.

Moreover, by analyzing the time–behavior of oxygen isotope δ^{18}O during the last glacial period (i.e., 20–120 kyr before present) we find that the climate variability is governed by physical mechanisms operating at two different timescales: on 1.500–yr timescale, climate dynamics is related to the occurrence of fast warming events, known as Dansgaard–Oeschger (DO) events, while on multi–millennial timescales, climate variations are related to the switch between warming/cooling periods. While DO events can be seen as fluctuations within the same climate state, warming/cooling phases are associated to fluctuations between two climate states, characterized by global increase/decrease of temperature. Finally, the results of cross–correlation analysis show that Antarctic climate changes lead those observed in Northern Hemisphere with a time delay of ∼3 kyr, which could be related to the oceanic thermohaline circulation.

Contents

Chapter 1

Introduction

The Solar-Terrestrial interactions involve physical processes related to the coupling between the Sun's variability and the Earth's environment, including both dynamical and energetic processes. These phenomena take place in the *Heliosphere*, a large bubble formed by the hot plasma blowing out from the Sun (i.e., the solar wind), in which the Sun and planets reside. The solar wind creates and maintains this bubble against the outside pressure of the interstellar medium, formed by hydrogen and helium gases permeating the Milky Way Galaxy. The solar wind flows outward from the Sun until encountering the termination shock, where motion slows abruptly, passing through the shock and entering the heliosheath, a transitional region which is in turn bounded by the outermost edge of the heliosphere, called the heliopause. The investigation of these phenomena is made in the framework of *Heliophysics*, the science of the Sun–solar-system connections, exploration, discovery and understanding of our space environment. It focuses on the Sun and its effects on Earth, the other planets of the solar system, and the changing conditions in space. Heliophysics studies the magnetosphere, ionosphere, thermosphere, mesosphere and upper atmosphere of the Earth and other planets, combined with the science of the Sun, corona, heliosphere and geospace environment. It encompasses particle acceleration mechanisms, space weather and radiation hazards, solar activity and cycles, planetary climate, space plasmas and changes in magnetic field topology (NASA, 2006).

Nowadays, the increase in knowledge of the Sun's magnetic activity changes allows the investigation of several phenomena occurring in the Earth's environment, covering a wide range of temporal and spatial scales, among which the interaction between the solar wind and the Earth's magnetic field (geodynamo field) and the effects on the atmospheric and climate systems. The solar wind alters the magnetospheric configuration, modifying the magnetospheric current systems through the injection of charged particles, and affects the ionospheric layers (i.e., F and E layers). Conversely, changes

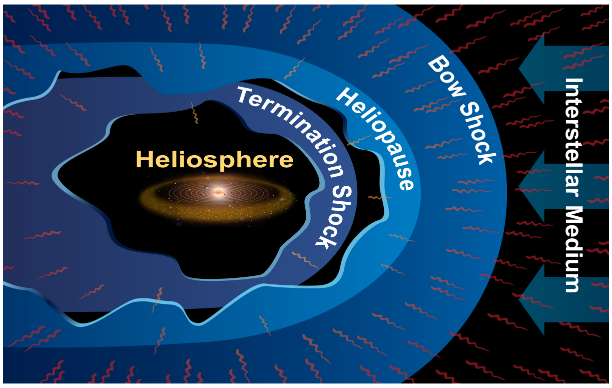

Figure 1.1: The structure of the Heliosphere.

in solar irradiance can affect the atmospheric circulation and composition (i.e., greenhouse effect), and the ocean-atmosphere coupling, producing local micro-climates and modifying the thermal equilibrium between incoming and outcoming energy fluxes.

One of the main aims in heliospheric studies corcerns the effects of magnetic fields on ionized matter. Indeed, this field-plasma coupling characterizes many different phenomena, ranging from the Earth's ionosphere to the Sun's surface, such as the acceleration of ions and electrons to higher energies (with respect to the plasma bulk kinetic energy) through wave-particle interaction. This characterizes large solar flares and their associated coronal mass ejections, producing changes of the magnetic field topology, and consequent effects on the Earth's environment when they interact with the Earth's magnetic field (i.e., generation of geomagnetic storms and substorms, aurora manifestation, Van Allen radiation belts enhancements). The coupling with neutral components within the plasma also produces several effects in terms of electrical conductivity changes, shifting the ionization balance by collisions and modifying the ionospheric and upper atmospheric electrodynamics (i.e., affecting the Pedersen and Hall conductivities, radiative trasfer and stratospheric ozone dynamics). Moreover, solar photons are Earth's primary energy source: Earth is habitable only because the Sun shines, radiating energy throughout the heliosphere, and the greenhouse effect controls the thermal energy balance, giving rise to a mean global surface temperature $T \sim 10 - 15°$C (without greenhouse effect it would be $\sim -20°$C). The Sun shines because its surface, warmed by energy produced in its nuclear burning core, is hotter ($\sim$ 5770 K) than the surrouding cosmos ($\sim$ 4 K). Electromagnetic energy traveling radially outward from the Sun reaches the Earth's upper atmosphere, it is continously absorbed and re-emitted within the atmosphere until it reaches the Earth's surface. The average total solar irradiance, at a distance of 1 astronomical unit (AU), is 1361 ± 4 W m^{-2}, with higher energy confined in the visible part of the spectrum (due to solar surface temperature value); conversely, Earth emits in the infrared part of the spectrum (following the Wien's displacement law). The thermal energy balance between solar incoming radiation and that outgoing from Earth's surface determines the conditions for life (habitability), the climate evolution and affects the cryosphere-atmosphere-biosphere interactions.

The Sun is a magnetically variable star which produces profound consequences and impacts on planets with intrinsic magnetic field, with atmospheres or with both properties (like Earth). Its magnetic activity and the associated changes evolve on timescales that range from minutes up to billions of years, involving nonstationary and nonequilibrium active processes, broadly regarded as *solar activity*. Whereas this concept is quite common nowadays, it is neither straightforwardly interpreted nor unambiguously defined (Usoskin, 2013). For instance, magnetic variability on the solar surface, eruption phenomena, coronal activity, interplanetary transient phenomena (i.e., corotating interaction regions, interplanetary coronal mass ejections), solar energetic particles as well as geomagnetic storms and substorms, tail current disruption, wave-particle interactions can be related to the concept of solar activity (Parker, 1965; Gonzalez et al., 1994; Cane and Lario, 2006; Love, 2011). Several indices, quantifying solar activity, have been proposed to represent different observables and caused effects, for both solar and geospace monitoring. Most of these indices are well-correlated to each other, due to the dominant 11-year Schwabe solar cycle (Schwabe, 1843), but they differ in short-term and/or long-term dynamics. The most common used indices of solar activity are reported in Table 1.1.

Indices	Type	Associated physical meaning
Wolf Sunspot Number (WSN)	Solar	Magnetic spots
Group Sunspot Number (GSN)	Solar	Active regions
Flare index	Solar	Solar flares activity
F10.7 index	Solar	Radio-flux at $\lambda = 10.7$ cm
MgII / Ca II-K	Solar	Spectral emission properties
Sym-H / Dst	Geomagnetic	Magnetospheric ring current activity
AE, AU, AL, AO indices	Geomagnetic	Auroral electrojets activity

Table 1.1: Solar and geomagnetic indices used to monitor solar activity.

The short-term (from minutes to months) variability of the solar activity is generally associated with eruptive phenomena (i.e., faculae, flares, coronal mass ejections) which extend from the solar surface to the inner heliosphere, carried out from the Sun by the solar wind (Emery et al., 2011). The dominant short-term quasi-periodicity in the solar activity (found in several solar wind parameters like speed and interplanetary magnetic field) is the rotation of the Sun, that is the apparent (synodic) rotation, known as Carrington rotation, with a period of ∼27 days (as seen at the Earth) at ∼25° heliolatitude near the solar disk part in which several active regions develop. The sidereal rotation rate of the Sun is ∼24 days at the solar equator increasing to ∼30 days at the poles (Chandra et al., 2009). Studies of the periodicities in the near-Earth solar wind and geomagnetic indices have found a 27-day signature, ranging between 25- and 29-day periods (Svalgaard and Wilcox, 1975; Emery et al., 2011). Mursula and Zieger (1996) found a second harmonic structure of the solar rotation periodicity (i.e., a ∼13.5-day period) in solar, heliospheric, and Earth-based parameters. Indeed, the analysis of the power spectra of the sunspot number, the Ca K-line index, the Mg II core to wing (c/w) ratio and Geostationary Operational Environmental Satellites (GOES) background X-ray intensity showed peaks at the fundamental 27-day periodicity and at its second harmonic. The 13.5-day amplitudes in these solar variables indicated the presence of two active solar longitudes approximately 180° apart. The position of the active solar longitudes could abruptly change by even 90° between two successive 13.5-day activations. Higher (and lower) harmonics were also found (Emery et al., 2009, 2011), particularly evident during solar minimum conditions (of the Schwabe cycle), which can be related to high-speed streams (HSSs) solar structures. These are the 7-day and 9-day periodicities which can be associated to a sub-harmonic structure of the synodic solar rotation (~ 27 days), due to the four-sector structure topology of the solar magnetic field. This structures can also lead to the formation of corotating interaction regions (CIRs) (Thayer et al., 2008; Emery et al., 2009). On the other hand, lower harmonics ($\sim 40, 54, 81$ days) correspond to multiple or combinatory timescales of the 27-day periodicity (Willson and Mordvinov, 1999).

The observed quasi-periodicities act in different ways on the Earth's environment, producing short-term transient phenomena (like geomagnetic storms and substorms), occurring when CMEs hit the Earth's magnetosphere, and generating global and local disturbances of the geomagnetic field, also able to modify the ionospheric electrodynamics via the auroral electrojets dynamics. Moreover, daily solar radiation changes also affect ionospheric current systems (i.e., Solar quiet mid-latitude current pattern) and atmospheric composition via ionization processes of the atmospheric gases (i.e., oxygen, ozone, carbon dioxide). Solar rotational structures are also responsible for ultra-low frequency (ULF) waves generation in the magnetosphere and enhancements of the Van Allen electrons (via wave-particle interaction which produces relativistic electrons energization) (Mann et al., 2004).

A clear evidence of short-term Sun-Earth connection is the well-known solar storm of 1859, famous as Carrington event (Carrington, 1860; Hodgson, 1860), classified as the first recognized space weather event (Cliver and Svalgaard, 2004). At 11:18 AM of the cloudless morning of Thursday, September 1, 1859, Richard Carrington, widely accepted as one of the England's foremost solar astronomers, was observing the central disk portion of the Sun, sketching a group of sunspots (see Figure 1.2).

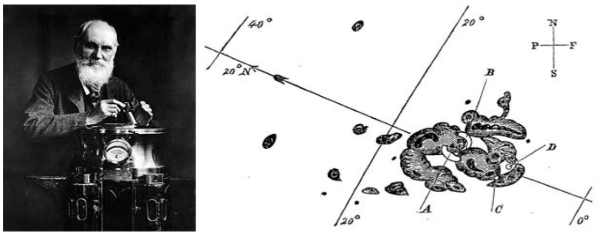

Figure 1.2: Richard Carrington (on the left) and the sunspots sketched on Sep 1, 1859 (on the right).

Suddenly, before his eyes, two brilliant enhancements of white light appeared over the sunspots, intensified rapidly, and became kidney-shaped. Realizing that he was witnessing something unprecedented and *"being somewhat flurried by the surprise,"* Carrington later wrote, *"I hastily ran to call someone to witness the exhibition with me. On returning within 60 seconds, I was mortified to find that it was already much changed and enfeebled"*. Just before dawn the next day, skies all over the Earth erupted in red, green, and purple auroras so brilliant that newspapers could be read as easily as in daylight. Indeed, stunning auroras pulsated even at near tropical latitudes over Cuba, the Bahamas, Jamaica, El Salvador, and Hawaii. Even more disconcerting, telegraph systems worldwide went haywire, spark discharges shocked telegraph operators and set the telegraph paper on fire. Even when telegraphers disconnected the batteries powering the lines, aurora-induced electric currents in the wires still allowed messages to be transmitted. What Carrington saw was a white-light solar flare, a magnetic explosion on the Sun, the first one observed from the Earth, while the next day people observed its effect on the Earth's environment, i.e., large auroral activity (quite far from the Poles) and the first evidence of a geomagnetic storm, causing "technological" disruptions. Now we know that solar flares happen frequently, especially during solar cycle maximum phases, emitting X-rays (recorded by X-ray telescopes in space) and radio noise (recorded by instruments in space and on Earth).

In Carrington's days, however, there were no X-ray satellites or radio telescopes, no one knew the existence of flares, until that September morning when one super-flare produced enough light to reveal the brightness of the Sun itself. Newspapers such as the New York Times were active in running extensive stories about the 1859 solar storm, and collecting reports from other countries. The great geomagnetic storm of 1859 is really composed of two closely spaced massive worldwide auroral events. The first event began on August 28th and the second began on September 2nd. It is the storm on September 2nd that resulted from the Carrington white light flare that occurred on the Sun the previous day. What if a similar biggest solar storm happened today? The explosive heat of a solar flare cannot make it all

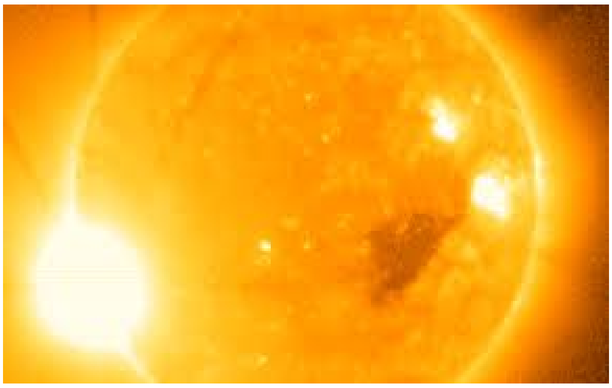

Figure 1.3: A modern solar flare recorded on Dec 5, 2006, by the X-ray Imager on board of NOAA's GOES-13 satellite. The flare was so intense that damaged the instrument that took the picture, although researchers believe Carrington's flare was much more energetic than this one.

the way to our globe, but electromagnetic radiation and energetic particles certainly can. Solar flares can temporarily alter the upper atmosphere, creating, for example, disruptions in signal transmission from a GPS satellite to Earth, causing it to be off. Minutes to hours after a solar flare lights up the sky, a stream of charged particles (electrons and protons) arrive at the Earth, bombarding the magnetosphere. These solar explosions produce bursts of particles and electromagnetic fluctuations into the Earth's atmosphere, inducing electric fluctuations at ground level that could blow out transformers in power grids. Occasionally, a large pulse of charged particles can hit orbiting satellites and damage their electronics, while particle radiation is also a big health risk for humans in space. In an increasingly technological world, where almost everyone relies on smartphones, GPS controls not only in-car map system, but also airplane navigation and the extremely accurate clocks that govern financial transactions. These phenomena need to be treated with convergency of several scientific branches, from physics to engineering, to develop a monitoring (and also forecasting) system. The study of these phenomena and their effects on the Earth's environment and technological impacts is made in the framework of the *Space weather*. This is a branch of space physics and aeronomy concerned with the time varying conditions on the Sun and in the solar wind, magnetosphere, ionosphere and thermosphere that can influence the performance and reliability of space-borne and ground-based technological systems and can endanger human life or health. It is influenced by the solar wind and the interplanetary magnetic field (IMF) carried by the solar wind plasma, inducing a variety of physical phenomena, including geomagnetic storms and substorms, energization of the Van Allen radiation belts, ionospheric disturbances, scintillation of satellite-to-ground radio signals, long-range radar signals, aurora and geomagnetically induced currents at Earth's surface (Cade and Christina, 2015).

However, the main feature of solar activity is its pronounced quasi-periodicity with a period of about 11 years, known as the Schwabe cycle (Schwabe, 1843). It varies in both amplitude and duration (Usoskin and Mursula, 2003; Vecchio et al., 2017) and it is recognized as a fundamental feature of solar activity originating from the solar-dynamo process. This 11-year cyclicity is prominent in many other parameters, including solar and geomagnetic indices, but also in climate proxies and observables, as for example Sea Surface Temperature (SST). The background for the Schwabe cycle is the 22-year Hale magnetic polarity cycle (Hale et al., 1919), an observed quasi-periodicity of the sunspot magnetic field polarity reversal due to the inner solar dynamo reversal (Hathaway, 2010). Sometimes, the regular time evolution of solar activity is broken up by periods of greatly depressed activity called grand minima, one of the most recent of which was the famous Maunder minimum from 1645-1715 (Eddy, 1976, 1983). Other grand minima in the past, derived from the analysis of cosmogenic isotope data (Usoskin et al., 2007, 2016), include the Spörer minimum around 1450-1550 and the Wolf minimum around the 14th century (Vecchio et al., 2017, Table 3). Although sunspot activity was not completely suppressed and still showed Schwabe cyclicity, sometimes the Dalton minimum (ca. 1790-1820) is also considered to be a grand minimum.

The long-term change in the Schwabe cycle amplitude is known as the secular Gleissberg cycle (Gleissberg, 1939, 1948, 1952) with a mean period of about 90 years. However, the Gleissberg cycle is not a cycle in the strict periodic sense but rather a modulation of the cycle envelope with a varying timescale of 60-120 years (e.g., Gleissberg, 1971; Ogurtsov et al., 2002; Vecchio et al., 2017). Longer (super-secular) cycles cannot be studied using direct solar observations, but only indicatively by means of indirect proxies such as cosmogenic isotopes and paleo-reconstructions of the solar irradiance and sunspot number (Solanki et al., 2004). These indirect proxies allow to show the existence of several longer cycles, as for example, a cycle with a period of 205-210 years, known as the de Vries or Suess cycle, a prominent feature observed in various cosmogenic data (e.g., Suess, 1980; Usoskin et al., 2004; Vecchio et al., 2017). Sometimes, variations with a characteristic time of 600-700 years or 1000-1200 years are discussed (e.g., Vitinsky et al., 1986; Steinhilber et al., 2012) but they are intermittent and can hardly be regarded as a typical feature of solar activity. A 2000–2400-year cycle is also noticeable in radiocarbon and cosmogenic time series (e.g., Vitinsky et al., 1986; Usoskin et al., 2016; Vecchio et al., 2017). However, the non-solar origin of these super-secular cycles (e.g., geomagnetic or climatic variability) cannot be excluded (Usoskin et al., 2016; Vecchio et al., 2017).

How these larger timescale periodicities can affect Earth's environment? The Sun-Earth connections on large-timescales (above months) are typically related to energy-balance processes, radiative and thermal equilibrium variations, atmospheric and climatic effects, principally affecting Earth's surface temperature evolution. One of the most famous example of Sun-Earth connection on large-timescales is the period between 1645 and 1715, known as Maunder minimum (Eddy, 1976, 1983; Usoskin et al., 2007; Vecchio et al., 2017). It is also known as the "prolonged sunspot minimum", since sunspots became exceedingly rare, as noted by solar observers of the time and reported in several works (Spörer, 1887, 1889; Maunder, 1890, 1894). The Maunder minimum is representative of grand minima in solar activity, during which sunspots almost completely vanished on the Sun's surface and solar wind kept blowing (Cliver et al., 1998; Usoskin, 2013). It was amazingly well recovered by direct sunspot observations, although they appeared rarely and seemingly sporadically (∼ 2% of the days), without any indication of the Schwabe solar cycle (Usoskin and Mursula, 2003). Therefore, some uncertainty about its duration is also present: the "formal" duration is 1645-1715 (Eddy, 1976), although its deep phase, characterized by apparent absence of solar cycle activity, is often considered as 1645-1700, with a recovery solar cycle variation during 1700-1712 (Usoskin, 2013). Usoskin et al. (2001) and Mursula et al. (2001) have shown that sunspot occurence during the Maunder minimum was characterized by two larger sunspot clusters (1652-1662 and 1672-1689), implying a dominant 22-year periodicity in sunspot activity.

Interestingly, the Maunder Minimum roughly coincided with the middle part of the Little Ice Age, a period of climatic cooling occurred from ∼ 1300 to ∼ 1800, reaching its chilliest point in the 17th century. During the Maunder Minimum, temperature across the Northern Hemisphere declined (if compared to the 20th century averages this decline was about 1 °C), contributing to a global crisis that destabilized social life. Indeed, as growing seasons shortened, food shortages spread, economies unraveled, rebellions and revolutions took place. The observed cooling was not the primary cause of these disasters but it often played an important role. Whether there is a causal relationship, however, is still controversial, as no convincing mechanism for the solar activity to produce cold temperatures has been proposed. What seems certain is that many of the coldest decades of the Little Ice Age coincided with periods of reduced solar activity: the Spörer Minimum (1450-1530), the Maunder Minimum (1645-1715), and the Dalton Minimum (1790-1820). However, one of the chilliest periods of all, known as Grindelwald Fluctuation (1560-1630), actually unfolded during a modest rise in solar activity. The current hypothesis for the cause of the Little Ice Age is that it was the result of volcanic action (Miller et al., 2012), which played an important role in bringing about cooler decades, as did the natural internal variability of the climate system. Indeed, both the absence of eruptions and a solar grand maximum likely set the stage for the Medieval Climate Anomaly, a warmer period in the Earth's geological hystory. However, an increase in volcanic eruptions and the associated grand minima states of solar activity can induce lower surface temperature. This occurred in the days of the Maunder minimum when the water in the river Thames and the Danube River froze, the Moscow River was covered by ice every six months, snow lay on some plains all year round and Greenland was covered by glaciers (see Figure 1.4).

Figure 1.4: In this 1677 painting by Abraham Hondius, "The Frozen Thames, looking Eastwards towards Old London Bridge", people are shown enjoying themselves on the ice.

What would happen during a new Maunder Minimum? It is well known that the influence of the Sun on our climate since pre-industrial times, in terms of radiative forcing, is very small compared to the effect of greenhouse gases (IPCC, 2014). The estimated increase in radiative forcing due to the Sun since 1750 (just after Maunder Minimum) is only 0.05 W m^{-2} compared to a total increase that is mainly caused by greenhouse gases of 2.29 W m^{-2}. Bond et al. (2001) showed that a possible larger solar effect on climate could be related to some amplification mechanisms such as energy stored in oceans and their interaction with atmosphere. Another mechanism is associated to the cosmic rays variations (related to the solar activity) in cloud formation and corresponding changes in atmospheric composition as well as the effect of solar UV changes into the stratospheric ozone dynamics.

If a new grand minimum state occurred this could lead to similar cooling of the Earth atmosphere ($\sim$ -0.5 °C) as during the Maunder minimum (Lockwood et al., 2010), although the current anthropogenic warming would lead to a temperature increase of $\sim$ 4 °C, deleting solar activity effects. However, variability in ultraviolet solar irradiance is linked to modulation of the Arctic and North Atlantic Oscillations, suggesting the potential for larger regional surface climate effects. This would induce a wintertime response, producing a cooling over northern Eurasia and eastern United States, similar to the observed temperature reductions during the Little Ice Age (Ineson et al., 2015).

The main purpose of this thesis is the investigation of solar-terrestrial physical processes at different timescales, considering both short- and long-term processes, in order to understand the effects of the changing Sun over the Earth's environment. This thesis includes two main parts: (i) the study of short-term processes characterizing solar activity, and (ii) the investigation of the role of solar irradiance changes on the climate system. Chapter 2 presents the main data analysis technique used to investigate nonlinear and nonstationary time series at different timescales, Chapter 3 illustrates some aspects of the solar wind and Earth's magnetosphere, while Chapters 4 and 5 focus on solar wind-magnetosphere and magnetosphere-ionosphere couplings, respectively. Then, Chapters 6 presents an empirical model to provide short-term warming of solar energetic particle (SEP) events. Chapter 7 describes the main characteristics of the Earth's climate, Chapter 8 focuses on larger timescales variations of the climate system, while Chapters 9 and 10 present two numerical energy-balance models to investigate climate changes and the role of the greenhouse effect. Finally, a conclusion chapter summarises the current research in the field and highlights possible further areas of research.

Chapter 2

The Hilbert-Huang Transform (HHT)

Theoretically, data analysis techniques should require no assumptions to be made about the nature of the investigated time series, i.e., neither linearity, nor stationarity should be assumed. This is because the behavior of physical processes that have generated the data is usually not known beforehand. Morever, adaptivity to the analyzed time series would also be a sought after feature, letting the data itself drive the decomposition. The latter criterion ensures both that the extracted components carry physical meaning, and that the influence of mathematical artefacts and assumptions is kept to a minimum (Wu and Huang, 2011). Since such a decomposition is only determined by the local characteristic timescales of a time series, its suitability to nonlinear and nonstationary time series analysis is important (Huang et al., 1998).

In this chapter, the Hilbert-Huang Transform (HHT), an adaptive data analysis technique built with the previous considerations in mind, is presented. It involves two distinct steps, the empirical mode decomposition (EMD) followed by Hilbert spectral analysis.

2.1 The Empirical Mode Decomposition (EMD)

The first step of the HHT is the empirical mode decomposition (EMD), an algorithmic procedure, by which oscillations that present a common local timescale are iteratively extracted from the data. The empirical mode decomposition has been developed to process non-stationary data (Huang et al., 1998) and successfully applied in many different contexts (Cummings et al., 2004; McDonald et al., 2007; Terradas et al., 2004; Vecchio et al., 2010; Wu and Huang, 2009), including geophysical systems (Alberti et al., 2014, 2016; Balasis and Egbert, 2006; De Michelis et al., 2012). It is an adaptive and a posteriori decomposition method in which the basis functions are derived from the data. This technique decomposes a set of observed data $X(t)$ into a finite number m of intrinsic oscillatory functions $C_j(t)$, named Intrinsic Mode Functions (*IMFs*), so that

$$X(t) = \sum_{j=1}^{m} C_j(t) + r(t), \tag{2.1}$$

where $r(t)$ is the final residue of the decomposition from which no more *IMFs* can be extracted. Each mode $C_j(t)$ can be derived by the so-called *sifting* process which represents the core of the decomposition procedure. This procedure can be summarized by the following steps:

1. identification of the local extrema of the time series $X(t)$
2. interpolation of local minima (maxima) by using a spline function to obtain the local envelope $e_{min}(t)$ $(e_{max}(t))$
3. computation of the mean envelope $m_1(t) = mean([e_{min}(t), e_{max}(t)])$
4. evaluation of the first "candidate" *IMF* $h_1(t) = X(t) - m_1(t)$

The previous steps are iterated k times until the obtained detail $h_{1k} = h_{1(k-1)} - m_{1k}$ can be identified as an *IMF* such that the two following properties are satisfied:

1. the number of extrema and the number of zero-crossings must either be equal or differ at most by one
2. at any point (locally), the mean value of the envelope defined by the local maxima and by the local minima is zero.

In addition, the number of sifting steps to produce an *IMF* is defined by the stopping criterion proposed by Huang et al. (1998), similar to the Cauchy convergence test, which defines a sum of the difference (standard deviation), σ_k, between two sifting steps as

$$\sigma_k = \sum_{t=0}^{T} \frac{|h_{k-1}(t) - h_k(t)|^2}{h_{k-1}^2(t)} \tag{2.2}$$

The sifting process stops when σ_k is smaller than a given value, typically into the range 0.2-0.3 (Huang et al., 1998). This is not the only stopping criterion proposed, since there are several works in which different methods have been proposed. One of these is the threshold method proposed by Flandrin et al. (2004) which sets two threshold values to guarantee globally small fluctuations and, in the mean while, takes into account locally large excursions. Another one is called the "S Number Criterion", based on the so-called S-number, which is defined as the number of consecutive siftings for which the number of zero-crossings and extrema are equal or at most differing by one. Specifically, an S-number is pre-selected. The sifting process will stop only if, for S consecutive siftings, the numbers of zero-crossings and extrema stay the same and are equal or at most differ by one.

2.2 Hilbert Spectral Analysis

Once the empirical mode decomposition is completed, the second and last step of the HHT consists in the Hilbert spectral analysis of the previously obtained *IMFs*. Each *IMF* and its Hilbert transform are used to construct a complex analytic signal, described by an amplitude modulation - frequency modulation (AM-FM) model. This decomposition into two time-varying parts corresponding respectively to instantaneous amplitude and instantaneous frequency enables the identification, in a time-varying sense, of how much power (i.e., the square of amplitude) occurs at which time-scale (i.e., the inverse of frequency).

An *IMF* is an oscillating function modulated in both amplitude and frequency, as $C_j(t) = A_j(t)\cos[\Phi_j(t)]$, where $\Phi_j(t)$ is the instantaneous phase of the j-th mode, related to the instantaneous frequency $\omega_j(t) = d\Phi_j(t)/dt$ (Huang et al., 1998). Since other decomposition techniques do not consider a time-dependent frequency (e.g. Fourier analysis), this concept of instantaneous frequency is the major point of the EMD technique, allowing a decomposition of non-stationary time series without any assumption on the basis of the decomposition. It can be derived by using the so-called Hilbert-Huang transform (Huang et al., 1998), through which for each $C_j(t)$ we can derive the corresponding Hilbert transform $\tilde{C}_j(t)$ as

$$\tilde{C}_j(t) = \frac{1}{\pi}\mathbf{P}\int_{-\infty}^{+\infty}\frac{C_j(t')}{t-t'}dt' \tag{2.3}$$

where $\mathbf{P}$ denotes the Cauchy's principal value. The function defined by Eq. (2.3) exists for all $\mathbf{L}^p$ space functions, allowing us to define an analytical signal $Z(t)$ from the conjugate pair $(C_j(t), \tilde{C}_j(t))$, such that

$$Z_j(t) = C_j(t) + i\tilde{C}_j(t) = A_j(t)e^{i\Phi_j(t)} \tag{2.4}$$

in which $A_j(t)$ and $\Phi_j(t)$ are the instantaneous amplitude and phase of the j-th mode, respectively, derived as

$$A_j(t) = \sqrt{C_j(t)^2 + \tilde{C}_j(t)^2} \tag{2.5}$$

$$\Phi_j(t) = \arctan\frac{\tilde{C}_j(t)}{C_j(t)} \tag{2.6}$$

In this way, the instantaneous frequency can be derived by the instantaneous phase as $\omega_j(t) = d\Phi_j(t)/dt$ (Huang et al., 1998). Consequently, a typical average period T_j can be estimated for all the *IMFs* as $T_j = 2\pi / < \omega_j(t) >_t$ ($<>_t$ representing the time average). The decomposition is clearly local and complete, which means that the *IMFs* can reconstruct the original signal (see Eq. (2.1)), while the orthogonality property is not theoretically ensured. However, it can be verified by evaluating the orthogonal index (OI) as proposed in Huang et al. (1998) by checking the inner product of each *IMF* with respect to the others. In this case, the EMD can be used as a filter through partial sums of a subset of modes (Alberti et al., 2014). Finally, based on numerical experiments on white noise using the empirical mode decomposition (EMD) method, Wu and Huang (2004) empirically found that the EMD is effectively a dyadic filter, the intrinsic mode functions are all normally distributed, and the Fourier spectra of the IMF components are all identical and cover the same area on a semi–logarithmic period scale. They also deduced that the product of the energy density of *IMF* and its corresponding averaged period is a constant, and that the energy–density function is chi–squared distributed. Furthermore, they derived an energy–density spread function of the *IMFs*, establishing a method of assigning statistical significance of information content for *IMFs* from any noisy data. In this way, the statistical significance of each *IMF* with respect to white noise can be verified by a comparison of the mean square amplitude of the *IMFs* with the theoretical spread function of white noise computed for different confidence levels.

In addition, EMD is capable of overcoming some limitations of other decomposition analysis techniques. EMD does not require any “a priori” assumption on the functional form of the basis of the decomposition (as for Fourier or Wavelet analysis). In this way, several misleading results can be avoided and this allows us to extract from the time series local nonstationary and nonlinear features which are usually difficult to be highlighted by decomposition methods based on fixed eigenfunctions. However, as for other analysis techniques, we need to outline outstanding open problems with EMD, including end effects of the EMD or stopping criteria selection. More specifically, boundary effects occur because there is no point before the first data point and after the last data point. In most cases, these boundary points are not the extreme value of the signal, therefore they can cause significant errors around the extreme envelopes. These errors can produce misleading MF waveforms at its endpoints, which can propagate into the decomposition through the sifting process. To avoid problems due to boundary effects, various methods have been proposed, including mirror or data extending methods (Huang and Wu, 2008; Yang et al., 2014). A comparison between HHT and other decomposition techniques is presented in Table 2.1.

Transform	**Fourier**	**Wavelet**	**Hilbert**
Basis	a priori	a priori	adaptive
Theoretical base	theory complete	theory complete	empirical
Nonlinear	no	no	yes
Non-stationary	no	yes	yes
Frequency	convolution: global	convolution: global	differentiation: local
Spectrum	energy-frequency	energy-time-frequency	energy-time-frequency
Feature extraction	no	discrete: no, continuous: yes	yes

Table 2.1: Comparison between time series analysis methods based on transforms.

Part I

Short-term solar-terrestrial processes

Chapter 3

The solar wind and the Earth's magnetosphere: background theory

3.1 The solar wind

One of the most fundamental problems in solar physics research is still unsolved: how can the Sun with a surface temperature of only 5800 K heat up its atmosphere to more than 10^6 K? In fact, the solar outer atmosphere is so hot that not even the Sun's gravity can contain it such that a part of it is continuously evaporating in the interplanetary space. This forms the solar wind, a flow of a tenuous ionized solar plasma and a remnant of the solar magnetic field, consisting of electrons, protons and alpha particles with temperature $\sim 10^5 - 10^6$ K. The existence of the solar wind was firstly suggested by Richard C. Carrington when, in 1859, observed for the first time a solar flare and, on the following day, a geomagnetic storm. He suspected that a connection between these two events occurred and that the interplanetary medium is permeated by a stream of charged particles. In the next century, Parker (1958) showed that even though the Sun's upper atmosphere is strongly attracted by solar gravity, it is such a good heat conductor that it is still very hot at large distances. Since gravity weakens as distance from the Sun increases, the outer solar atmosphere escapes supersonically into the interplanetary medium. Our knowledge of the solar wind properties is based on *in situ* spacecraft observations covering a wide range of distances (from 0.3 AU on) and a wide interval of heliospheric latitude range (Bruno and Carbone, 2016). Generally, the solar wind is divided into two components, respectively termed the slow solar wind and the fast solar wind. The slow solar wind has a velocity of about 400 km/s, a temperature of $1.4 - 1.6 \times 10^6$ K and a composition that is a close match to the corona (i.e., to the upper solar atmosphere). By contrast, the fast solar wind has a typical velocity of 750 km/s, a temperature of $\sim 8 \times 10^5$ K and it nearly matches the composition of the Sun's photosphere (i.e., the deepest region of the Sun's surface from which light is radiated). The slow solar wind is twice as dense and more variable in intensity that the fast solar wind, having also a more complex structure, with turbulent regions and large-scale structures. Embedded in the solar wind plasma there is a weak magnetic field that a 1 AU is oriented in a direction parallel to the ecliptic plane with a 45° angle to the Sun radial direction.

Proton density	6.6 cm^{-3}
Electron density	7.1 cm^{-3}
Alpha particles	0.25 cm^{-3}
Mean flow speed	450 km/s
Magnetic field	10 nT

Table 3.1: Solar wind features at 1 AU.

This magnetic field is usually named as interplanetary magnetic field (IMF), which is the solar magnetic field carried by the solar wind among the planets of the solar system. Indeed, since the solar wind is highly electrically conductive, the magnetic field lines from the Sun are carried along with the solar wind. The dynamic pressure of the solar wind is usually higher than the magnetic pressure, so that the magnetic field is pulled into a spiral pattern (the Parker spiral) by the combination of the outward motion and the Sun's rotation. Depending on the hemisphere and phase of the solar cycle, the magnetic field spirals inward or outward, following the same shape in the northern and southern parts of the heliosphere, but with opposite field direction. These two magnetic domains are separated by a current sheet (i.e., the heliospheric current sheet) which has a shape similar to a twirled ballerina skirt, and changes in shape through the solar cycle as the Sun's magnetic field reverses.

Both fast and slow solar wind can be interrupted by large, fast-moving bursts of plasma called interplanetary coronal mass ejections, or ICMEs. ICMEs are the interplanetary manifestation of solar coronal mass ejections (CMEs), which are caused by release of magnetic energy at the Sun's surface. CMEs are often called "solar storms" or "space storms" and are sometimes, but not always, associated with solar flares, another manifestation of magnetic energy release at the Sun. ICMEs cause shock waves in the thin plasma of the heliosphere, launching electromagnetic waves and accelerating particles (mostly protons and electrons) to form showers of ionizing radiation that precede the CME.

When a CME impacts the Earth's magnetosphere, it temporarily deforms the Earth's magnetic field, producing a global phenomenon knwon as geomagnetic storm which induces large electrical ground currents in the

Earth itself. CME impacts can induce magnetic reconnection in Earth's magnetotail (the midnight side of the magnetosphere), producing proton and electron enhancements toward Earth's atmosphere, where they form auroras.

Sometimes, high-energy particles, termed Solar Energetic Particles (SEPs), consisting of protons, electrons and heavy ions, with energy ranging from few tens of keV up to GeV, are associated with CMEs. They represent an important hazard to interplanetary space and Earth's environment and can originate from a solar flare or by shock waves associated with coronal mass ejections. SEP events are conventionally classified into two defined categories: impulsive and gradual. Impulsive SEP events have durations from hours up to a day and are related to short-duration soft X-ray emission. These SEP events, often associated with flare acceleration processes, are characterized by small interplanetary ion intensities, a high electron to proton intensity ration and enhanced abundances of heavy ions. Conversely, gradual SEP events have durations of days and are related to long-duration ($>$10 min) soft X-ray flares and to interplanetary shocks driven by fast CMEs (generally, $\gtrsim$ 750 km s^{-1}). They are characterized by large interplanetary ion intensities, small electron to proton ratios and ionic charge states in consistency with solar coronal abundances. Moreover, they have a longidute distribution of the associated flare that is much wider than for impulsive events, spreading over the whole solar disk.

3.2 The Earth's magnetosphere

The Earth's magnetic field is composed of two parts: an internal dipolar magnetic field, originating in the liquid external core, and the more dynamic external magnetic field created by the combined effects of the solar wind and various magnetospheric currents. The magnetosphere of the Earth is defined as the region of influence of the Earth's magnetic field. The magnetosphere is formed when the solar wind pushes against the Earth's magnetic field and creates a cavity in the solar wind. The various regions of the magnetosphere are shown in Figure 3.1.

The Earth's magnetosphere is bounded by a thin current layer called the magnetopause, preceded upstream by a hyperboloidal bow shock through which the solar wind makes a transition from super-magnetosonic to sub-magnetosonic flow velocity. A distance of 2-3 R_E (Earth radii, 1 $R_E = 6371.2$ km) separates the bow shock from the magnetopause along the Earth-Sun line. The interaction with the solar wind deforms the Earth's basically dipolar magnetic field, compressing the field lines on the dayside and stretching them out to form a long comet-like tail (the magnetotail) on the nightside. On the dayside, the magnetosphere extends out to a distance of approximately 10 Earth radii (under quiet conditions), while the magnetotail ex-

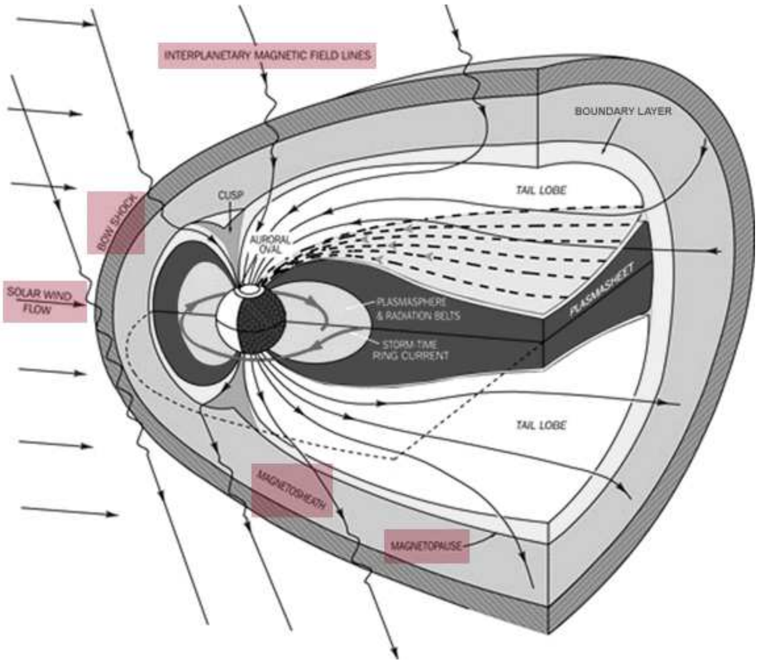

Figure 3.1: A schematic view of the different regions of the Earth's magnetosphere.

tends several hundred Earth radii in the anti-sunward direction. In the next sections, the different magnetospheric currents and some of their physical processes are briefly discussed. In addition, space weather indices which are used frequently in this work are explained.

3.2.1 Magnetospheric Currents

The distortion of the Earth's internal dipole field into the typical shape of a magnetosphere produced by the interaction with the solar wind is accompanied by electrical currents in the magnetosphere. The major currents in the magnetosphere are: (i) the magnetopause current, shielding the Earth's dipole, (ii) the symmetric ring current, (iii) the cross-tail current along with the closure currents on the magnetopause, and (iv) the partial ring current, which develops under storm or substorm activity. Figure 3.2 shows the various currents and their locations inside the magnetosphere.

We note that each of the systems is closed and are not only topologically different but have different origins. The current on the magnetopause is carried by the solar wind protons, with the energy of about 1 keV, shielding Earth's dipole and it is controlled by the solar wind dynamic pressure. The ring current is formed by the steadily trapped particles, mostly protons with the energy of 10-100 keV, although oxygen ions of ionospheric origin

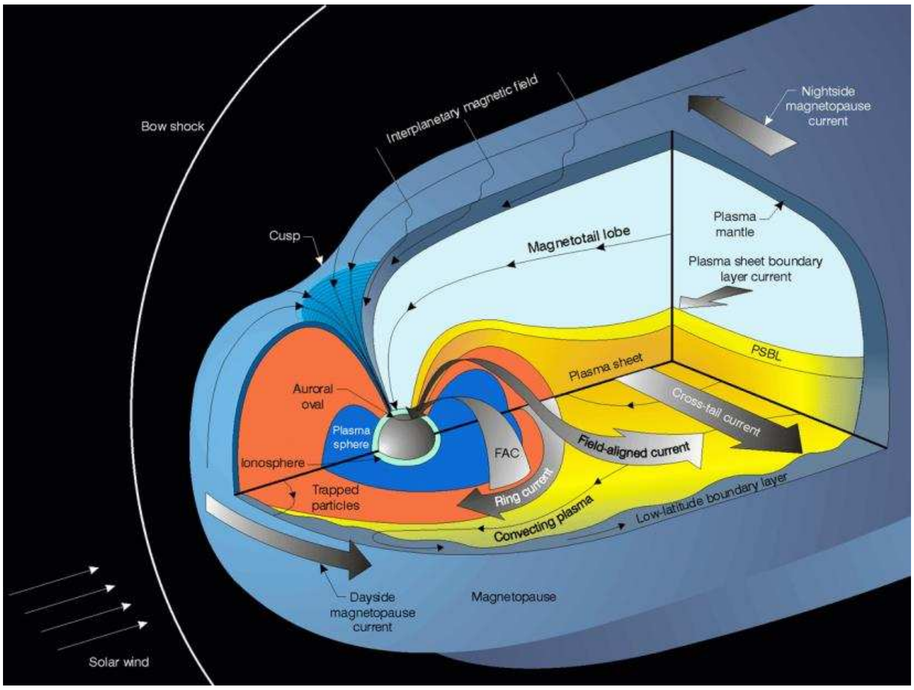

Figure 3.2: A schematic view of the magnetospheric current systems.

being added during strong storm events. The cross-tail current is formed by temporarily trapped particles in the magnetospheric plasma sheet (protons with the energy of 10 keV), while the origin of the partial ring current is typically related to the charge separation in the course of the particle drift from the magnetospheric tail to the Sun through the non-uniform magnetic field.

Magnetopause current

Approaching Earth and its magnetosphere from interplanetary space, the first signature of its existence is the bow shock, a shock wave standing in the supersonic solar wind flow in front of the magnetosphere. Closer to the Earth, a surface current layer where the magnetic field strength jumps from its low interplanetary value to the high magnetospheric field strength is found: the magnetopause. It separates the shocked solar wind, known as the magnetosheath plasma, from the magnetospheric region, dominated by the geomagnetic field. The compression of the internal magnetic field on the dayside is associated with current flow across the magnetopause surface, the magnetopause current, also named the Chapman-Ferraro current, a current system flowing around the magnetopause. This current system generates a magnetic field that "prevents" the terrestrial dipole field from penetrating into the solar wind.

The effect of the magnetopause current is also felt at the Earth's surface. Indeed, when a sudden increase in solar wind dynamic pressure, for example due to the passage of an interplanetary shock, reaches the Earth, the magnetosphere is compressed, causing the magnetopause approach to the Earth. The position of the dayside magnetopause is essentially determined as the surface of equilibrium between the magnetic pressure of the terrestrial magnetic field and the dynamic pressure of the solar wind. Whenever the speed of the solar wind increases, the terrestrial field is compressed and the magnetopause recedes to a new equilibrium position. At the same time, the magnetopause current intensifies due to charged particle density increase caused by the solar wind. On the Earth's surface a sudden increase in the geomagnetic field intensity of a few tens of nanotesla, known as sudden impulse (SI) or sudden storm commencement (SSC) if a geomagnetic storm follows, is observed. This excursion is the magnetic signature of the solar wind impinging faster than usual onto the magnetopause.

Ring current

The Earth's ring current is a westward flowing toroidal electric current around the Earth, centered at the equatorial plane and at altitudes ranging from 2 R_E to 7 R_E. This current produces a magnetic field in opposition to the geomagnetic field such that an Earth observer would observe a decrease in the magnetic field. It is mainly formed by the ions, most of which are protons, with a small contribution of alpha particles (of solar wind origin) and oxygen ions (O^+), similar to those observed in the ionosphere of the Earth but more energetic. This suggests that ring current particles probably come from more than one source. Enhancements in this current are responsible for global decreases in the Earth's surface magnetic field, which have been used to define geomagnetic storms.

During geomagnetic storms, ring current particle fluxes increase, with enhancements peak occurring in the inner ring current (at <4 R_E). While the quiet-time ring current consists predominantly of H^+, the storm-time ring current contains a significant component of ionospheric O^+, whose contribution to ring current energy density may even exceed that of H^+ for brief periods near the maximum of particularly intense storms. The formation of the storm-time ring current has been attributed to two different processes: (i) the injection of plasma into the inner magnetosphere during the expansion phase of magnetospheric substorms and (ii) the increase of the convective transport of charged particles from the nightside plasma sheet deep into the inner magnetosphere as a result of an intensification of the Earth's dawn-dusk convection electric field during extended periods of strong southward IMF.

The storm-time growth of the ring current lasts from 3 to 12 hours and constitutes the "main phase" of a geomagnetic storm. Following this main phase, the ring current begins to decay, returning to its pre-storm state (recovery phase). During the storm recovery phase, particle transport into the ring current slows, allowing various loss processes to reduce ring current particle fluxes to their quiet-time level. One of these loss processes is related to the precipitative loss of ring current particles into the ionosphere, through particle precipitation along the magnetic field lines, and into the atmosphere as a result of wave-particle interactions.

A measure of the ring current activity can be obtained by the Dst (disturbance storm time) index which will be described below.

Field Aligned Currents

While previous magnetospheric currents flow in closed loops (i.e., they are divergence-free), other magnetospheric current systems may accumulate charges in specific regions. This can generate electric potential drops between different regions or connect to permanent sources of electric potential difference, like the solar wind when the planetary field is reconnected with interplanetary field lines. These generate electric current flows along conducting paths connecting regions of different potential: the so-called field aligned currents (FACs, also called Birkeland currents). They are most important at high latitudes, where near-vertical ionospheric field lines provide a direct electrical connection between the auroral ionosphere and distant magnetospheric regions as shown in Figure 3.3. However, field aligned currents do not contribute to the electromagnetic stress because:

$$\vec{J} \times \vec{B} = \vec{0} \tag{3.1}$$

such that these currents are associated with a "force-free" magnetic configuration. They are responsible of the magnetosphere-ionosphere coupling, producing particle precipitation, and they are also a source of visual auroras. Indeed, in magnetospheric regions where the density is low, the reservoir of free current-carrying electrons is limited, and the mirror force along converging field lines limits the access of electrons to the ionosphere. The current-carrying electrons are thus accelerated along their guiding field line and precipitated into the ionosphere, where they produce an aurora.

Ionospheric currents

Ionospheric currents flow in a narrow horizontal layer at an altitude between 100 and 150 Km concentric with Earth's surface. Ionospheric currents are observed during both quiet and disturbed solar wind conditions. The quiet ionospheric currents, designated as Sq (e.g., Solar quiet) currents, are produced by the motion of the ionized ionospheric particles across the planetary magnetic field. This motion, driven by the daily heating of the ionosphere

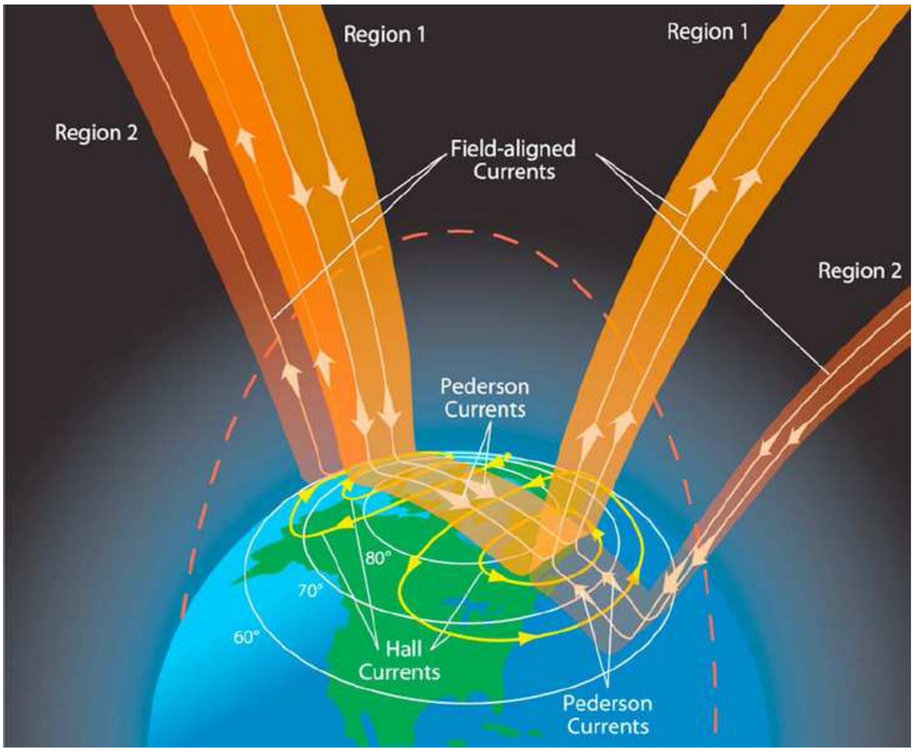

Figure 3.3: A schematic view of the Field Aligned Currents.

by the Sun and the lunar and solar tidal forces, induces an electromotive force that produces an equivalent current pattern that is fixed with respect to the Sun.

The disturbed ionospheric currents, designated as S_D, are observed in conjunction with the auroral activity at northern magnetic latitudes. During an aurora, an excess of 10^{19} ergs of particle energy is deposited into the auroral ionosphere, producing enhancements in the ionospheric conductivity and ionospheric currents flow in both eastward and westward directions. These currents are referred to as the eastward and westward auroral electrojets, producing a magnetic field of several hundred nanoteslas, generally associated with the occurrence of substorms.

Moreover, at certain ionospheric altitudes, the ions and, to a lesser degree, also the electrons are coupled by collisions to the neutral components of the upper atmosphere and follow their dynamics. When the atmosphere is magnetized, atmospheric winds and tidal oscillations of the atmosphere can produce an electromotive force which drives the ion component across the magnetic field lines, while the electrons move much more slowly. This relative movement constitutes an additional electric current driven by the neutral wind, and such a region bears the name dynamo layer, the generator of which is the atmospheric wind motion as shown in Figure 3.4.

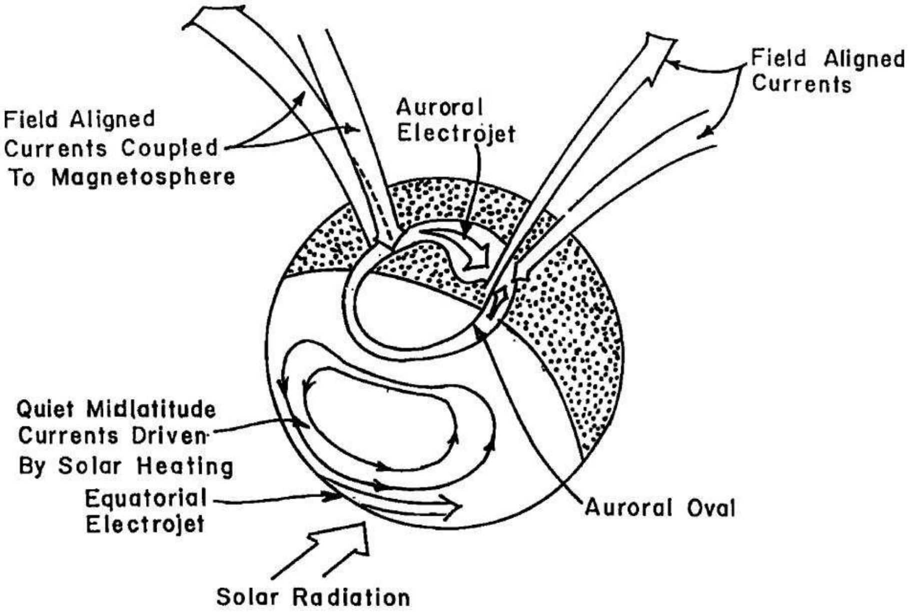

Figure 3.4: A schematic view of the ionospheric current systems.

The presence of mobile charges makes the ionosphere a highly conducting collisional medium, penetrated by a strong magnetic field. The ionospheric current system can be described with the help of the generalized Ohm's law:

$$\vec{J} = \sigma_{\|}\vec{E_{\|}} + \sigma_P\vec{E_{\perp}} - \sigma_H(\vec{E_{\perp}} \times \vec{B})/B \tag{3.2}$$

The Hall conductivity, σ_H, determines the Hall current in the direction perpendicular to both the electric and magnetic field. It maximizes at a height where the ions collide so frequently with the neutrals that they are essentially at rest, while the electrons already undergo a somewhat impeded $\vec{E} \times \vec{B}$ drift.

The Pedersen conductivity, σ_P, governs the Pedersen current in the direction of that part of the electric field, $\vec{E_{\perp}}$, which is transverse to the magnetic field. The Pedersen conductivity maximizes typically at a somewhat higher altitude than the Hall conductivity, namely where the ions are scattered in the direction of the electric field before they can start to gyrate about the magnetic field.

The quantity $\sigma_{\|}$ is called the parallel conductivity since it governs the magnetic field-aligned current driven by the parallel electric field component, $\vec{E_{\|}}$.

3.2.2 Geomagnetic storms and substorms

Geomagnetic storms and substorms are indicators of geomagnetic activity, with the first driven directly by solar drivers like coronal mass ejections, solar flares, fast streams etc., while the latter are the disturbances occurring within the magnetosphere that are ultimately caused by the solar wind. Solar wind energy input in the magnetosphere is $\sim 10^{11}$ W during substorms, reaching up to $\sim 10^{13}$ W during moderate magnetic storm. The basic process of energy transfer is the magnetic reconnection, but it occurs on different time and spatial scales. Magnetospheric substorms usually last for a period of few hours, during which there is an explosive release of stored magnetotail energy in the form of energetic particles ($\sim$5-50 keV) and strong plasma flows ($\sim$100-1000 km/s or so) and dissipated in the near-Earth nightside auroral region. This results in the excitation of discrete auroras which become widespread and intense (as also explained in previous sections), due to intensified field-aligned currents and auroral electrojets. Geomagnetic storms are characterized by a main phase during which the horizontal component of the Earth's low-latitude magnetic fields are significantly depressed over a time span of one to a few hours followed by its recovery which may extend over several days (Rostoker, 1997). They occur when fast moving solar structures, like coronal mass ejections (CMEs), accompanied by long intervals of southward interplanetary magnetic field (IMF) which produce enhancements in the efficiency of magnetic reconnection, hit the magnetopause surface (Dungey, 1961; Tsurutani et al., 1990; Gonzalez et al., 1994). This leads plasma injection from the magnetotail towards the inner magnetosphere, causing energetic protons drift to the west and electrons to the east, affecting the ring current which produce a diamagnetic decrease in the Earth's magnetic field measured at near-equatorial magnetic stations. This decrease in the equatorial magnetic field strength is directly related to the total kinetic energy of the ring current particles (Dessler and Parker, 1959; Sckopke, 1966). Generally, magnetic storms are caused by frequent occurrence of intense substorms (Akasofu and Chapman, 1961), although there were several evidences of substorm activity without any manifestation of storms (Tsurutani et al., 2015). From the analysis of geomagnetic perturbations, two prominent current patterns are found: a two-cell current pattern, associated with the magnetospheric convection which is well-correlated with solar wind parameters, and an impulsive one-cell system, associated with the substorm and highly correlated with storm occurrence and poorly with the solar wind (Kamide and Kokubun, 1996; Consolini et al., 1996, and references therein), suggesting a magnetic storm-substorm relationship. Indeed, it is noticed that interplanetary electric fields Ey (dawn-dusk component corresponding to southwards IMF) play important roles in both magnetic storm and substorm activity. It is believed that fluctuating Ey gives rise to substorms and quasi-steady Ey can drive magnetic storms (Kamide and

Kokubun, 1996). Neverthless, the magnetic storm-substorm relationship is an active topic of debate (Rostoker et al., 1987; Tsurutani et al., 1990; Kamide, 1992; Sharma, 1995; Kamide, 2001; Consolini and De Michelis, 2005; De Michelis et al., 2011; Tsurutani et al., 2015).

3.2.3 Geomagnetic indices

Geomagnetic indices provide a measure of the geomagnetic activity as a signature of the response of the Earth's magnetosphere and ionosphere to solar activity, and play a significant role in describing the magnetic configuration of different current systems. Several indices have been proposed which represent some region or phenomenon in the magnetosphere-ionosphere system.

Dst/Sym-H index

The disturbance storm time (Dst) index has been widely used as an indicator of geomagnetic activity. It is derived from measurements made at four ground magnetic observatories: Hermanus, Kakioka, Honolulu, and San Juan. These observatories were chosen on the basis of the quality of observation and of their locations, sufficiently far from the auroral and equatorial electrojets, with a longitudinal distribution as evenly as possible (within -35° to +35° latitude). A map of the network is given in Figure 3.5. Magnetic disturbances are determined by removing the Earth's main magnetic field contribution and daily variations from the measurements of the north-south component of the geomagnetic field (namely the H component).

The Dst index represents the axially symmetric disturbance magnetic field at the dipole equator on the Earth's surface. The observed disturbance in Dst is negative, corresponding to a decreases in the geomagnetic field, mainly produced by the equatorial ring current system in the magnetosphere. Conversely, positive variations in Dst are mostly caused by the compression of the magnetosphere from solar wind pressure increases.

The main problem with magnetometer-derived Dst information is that magnetometers cannot distinguish between the different current systems (ring current, tail current, field aligned currents, magnetopause current, and ground-induced currents) and their variations on different timescales, since the Dst index has a low (hourly) resolution. For these reason, higher resolution indices have been proposed, together with different methods to remove the quiet time variations of the ring current. The Sym-H (a 1 minute version of the well-known Dst index) and Asy-H indices, being derived from a network of near-equatorial geomagnetic observatories, allow us to get an estimate of the ring current dynamics and of the asymmetric low-latitude disturbance (partial ring current), respectively, in the course of a storm (Sugiura and Poros, 1971; Kawasaki and Akasofu, 1971; Crooker and Siscoe, 1971; Crooker, 1972; Clauer and McPherron, 1980; Clauer et al., 1983).

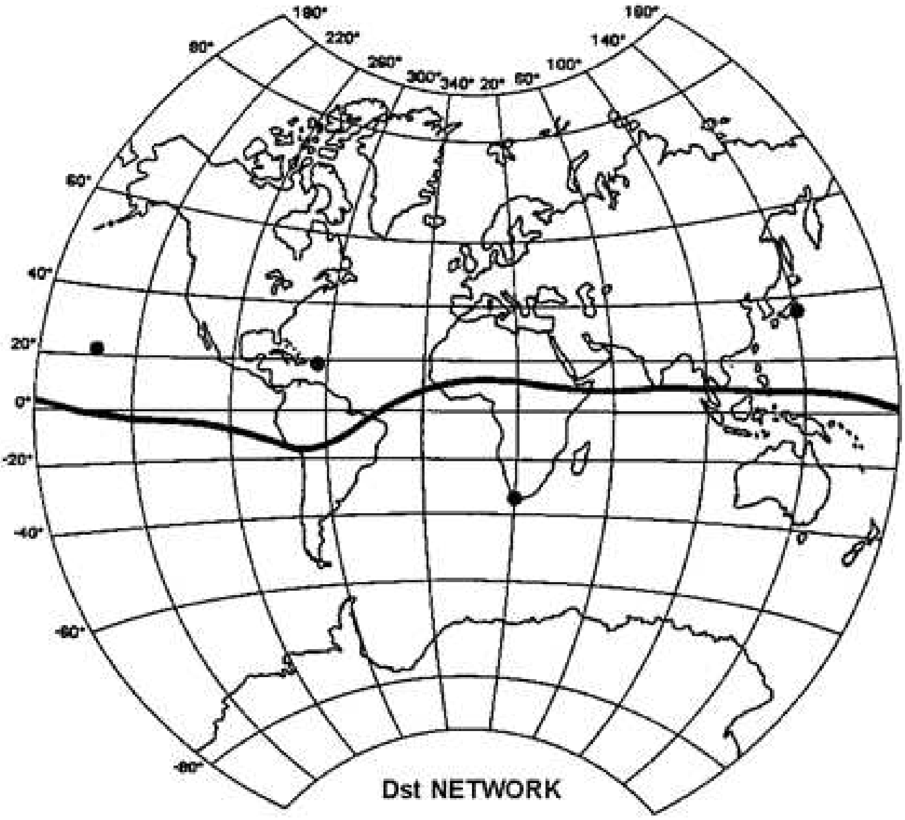

Figure 3.5: Geographic locations of the four magnetometer stations used in calculating Dst index.

They are both calculated by using six ground magnetic observatories, chosen in a list formed by the same stations used for Dst calculation and higher latitudes ones (i.e., Urumqi, Fredericksburg, Boulder, Tucson, Memambetsu, Martin de Vivies and Chambon-la-Foret), as shown in Figure 3.6.

The derivation procedure of Sym-H/Asy-H indices essentially consists of the following steps:

1. subtraction of the geomagnetic main field and Sq field to calculate the disturbed field component;

2. coordinate transformation to a dipole coordinate system;

3. calculation of the longitudinally symmetric and asymmetric components.

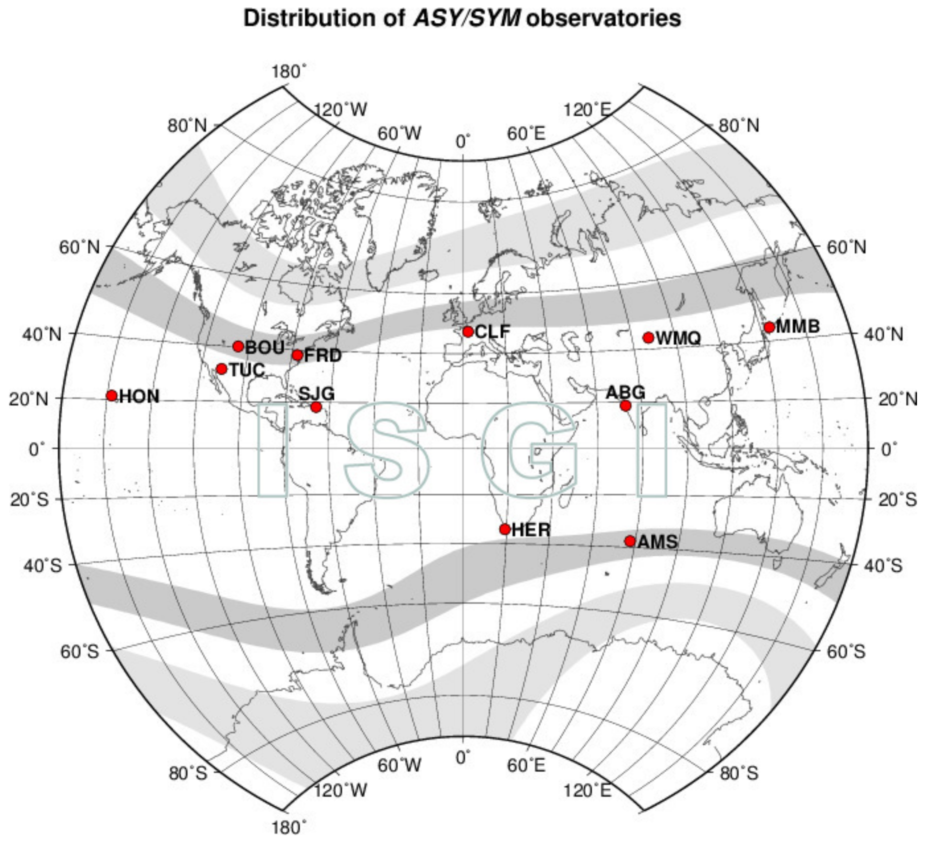

Figure 3.6: Geographic locations of the magnetometer stations used in calculating Sym-H/Asy-H indices.

Auroral indices: AE, AL, AU and AO

The auroral electrojets indices were originally introduced by Davis and Sugiura (1966) as a measure of the electrojets activity in the auroral zone. They are derived from geomagnetic variations in the horizontal component (H) observed at 10-13 selected observatories along the auroral zone in the northern hemisphere (see Figure 3.7).

Monthly mean values are subtracted from each station's measurements to give a baseline value of zero. Then, the traces are plotted with respect to a common baseline, and upper and lower envelopes are calculated. The AU (auroral upper) index is defined as the maximum positive disturbance recorded by any station in the chain. Similarly, AL is defined as the minimum disturbance defined by the lower envelope. If the disturbances were caused by an infinite sheet of current, the AU and AL would be proportional to the maximum overhead current density in the two electrojets. A single measure that approximated the total effect of both electrojets is defined as AE = AU - AL. For completeness, AO is the defined as the average

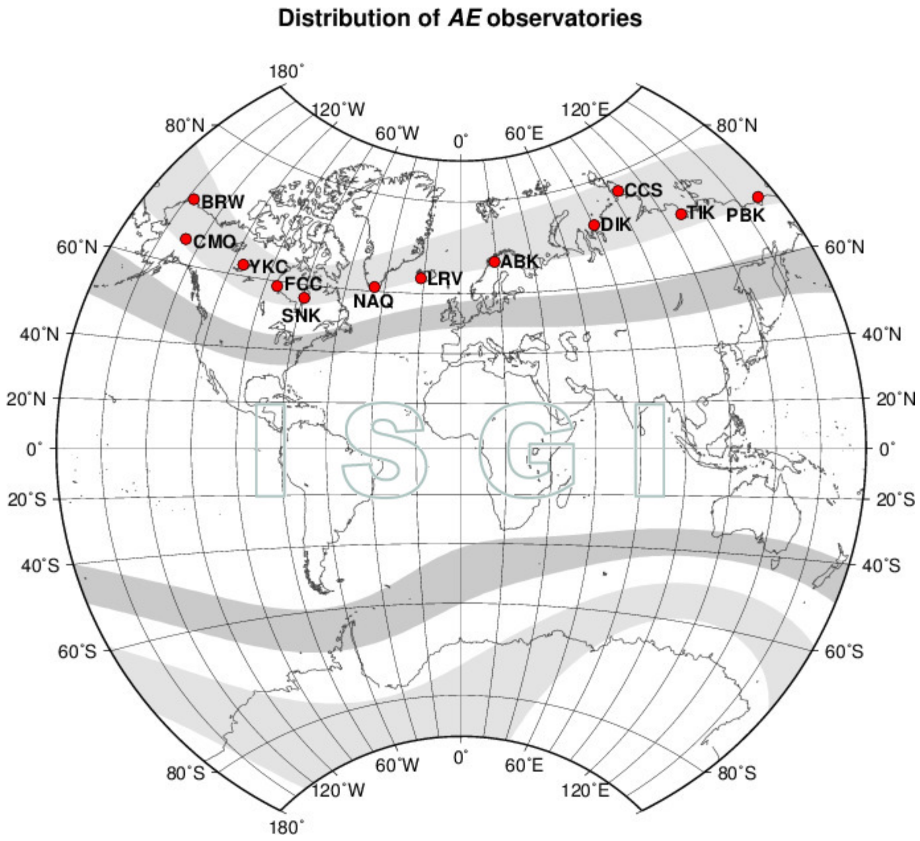

Figure 3.7: Geographic locations of the magnetometer stations used in calculating auroral indices.

of AU and AL: AO = (AU + AL)/2. AU is a measure of the eastward auroral electrojet (EEJ), flowing in the dayside auroral oval and coupled to magnetopause currents. It measures the directly driven response of the magnetosphere to changes of the interplanetary medium (solar-wind) conditions. AL is a measure of the westward auroral electroject (WEJ) that intensifies during substorms. Thus AL provides a good tool to follow the evolution and the different phases of a substorm. AE index reflects the integrated effect of different current systems and not necessarily quantify specific physical processes occurring in the magnetosphere-ionosphere coupling system, while AO provides a measure of the equivalent zonal current.

K index

K index summarises geomagnetic activity at an observatory by assigning a code, an integer in the range from 0 to 9, to each 3-hour Universal Time (UT) interval, therefore each day is characterized by 8 K indices. It quantifies disturbances in the horizontal (H) and eastward (D) components of the

Earth's magnetic field with an integer in the range 0-9 with 1 being quiet and 5 or more indicating a geomagnetic storm. It is derived from the maximum fluctuations of H or D component observed on a magnetometer during a three-hour interval.

Chapter 4

Solar wind-magnetosphere interactions during Geomagnetic Storms[1]

This study presents a new view of the relevant timescales responsible for the effects of the changing solar wind and Interplanetary Magnetic Field (IMF) conditions on the magnetospheric dynamics during Geomagnetic Storms. The studied events are the St. Patrick's Day Geomagnetic Storms in 2013 and 2015. To this purpose, the behavior of the Interplanetary Magnetic Field (IMF) component Bz, the Perreault-Akasofu coupling function and the auroral and low-latitude geomagnetic indices is investigated at different timescales by means of the Empirical Mode Decomposition (EMD) method and the Delayed Mutual Information (DMI). First of all, the EMD allows to extract the intrinsic oscillations (modes) present into the different datasets, while the DMI provides a measure of the total amount of the linear and nonlinear shared information (correlation degree) in the solar wind-magnetosphere coupling. We clearly show that a timescale separation occurs in the solar wind-magnetosphere coupling. Fluctuations at long-timescales ($\tau > 200$ min) show a large degree of correlation between solar wind parameters and magnetospheric dynamics proxies; conversely, at short-timescales ($\tau < 200$ min) this direct link is missing. This suggests that magnetospheric fluctuations at timescales lower than 200 min, although triggered by changes of the interplanetary conditions, are mainly dominated by internal processes, while the magnetospheric dynamics at timescales longer than 200 min resembles the changes observed in the solar wind/IMF features.

---

[1] The work presented in this chapter is included in the paper Alberti, Consolini, Lepreti, Laurenza, Vecchio and Carbone (2017*a*).

4.1 Introduction

As presented in Chapter 3, the Earth's magnetospheric dynamics is the result of both externally driven and internal processes which can be investigated by using a set of geomagnetic indices. These indices measure the activity changes of the most important current systems such as the high-latitude ionospheric auroral electrojets, monitored by the Auroral Electroject indices (AE, AU, AL and AO), and the equatorial ring current, provided by the Dst, Sym-H and Asy-H. The observed changes of these current systems set the magnetospheric configuration and dynamics, which is mainly the result of energy transfer from the solar wind to different regions of the magnetosphere through electromagnetic processes (Perreault and Akasofu, 1978), involving a considerable amount of energy and manifesting itself in several fast phenomena occurring in the magnetosphere such as auroral displays, magnetic substorms and storms (Tsurutani et al., 2015).

As a consequence, these indices display both regular and irregular variations on a wide interval of timescales (De Michelis et al., 2015), ranging from minutes up to hours, due to a complex and nonlinear dynamics of the Earth's magnetosphere (Tsurutani et al., 1990; Sharma, 1995; Vassiliadis, 2006). Indeed, the multi-scale character of the fluctuations/variations of geomagnetic indices can be associated with fractal/multifractal scaling features of the corresponding time series (Consolini et al., 1996; Consolini, 1998; Uritsky and Pudovkin, 1998; Kovacs et al., 2001; Wanliss, 2005; Consolini and De Michelis, 2011) and power law distributions of the associated energy dissipation events (Consolini, 1998, 2002; Wanliss and Uritsky, 2010). These features suggest a far-from-equilibrium nonlinear dynamics near a critical state of the magnetosphere configuration (see e.g., Klimas et al. (1996); Sitnov et al. (2001); Consolini (2002); Uritsky et al. (2002)), evidencing the absence of a one-to-one correspondence between the SW/IMF condition changes and those of the magnetospheric configuration (Sitnov et al., 2001; Consolini, 2002). An important consequence is that the local and overall magnetospheric dynamics, although triggered by interplanetary condition variations, is strongly affected by the internal conditions. This is exactly what has been understood since the early works on the nonlinear and pseudo-chaotic dynamics of the Earth's magnetosphere (see e.g. Tsurutani et al. (1990); Klimas et al. (1996)).

A main point in the study of the solar wind-magnetosphere coupling is related to the different timescales involved in the internal and externally driven processes. Indeed, geomagnetic substorms can be seen as the result of two different phenomena: the increase of plasma convection and fast energy relaxations occurring in the near-Earth tail central plasma sheet (CPS) (Rostoker et al., 1987; Kamide and Kokubun, 1996; Consolini and De Michelis, 2005). These two phenomena, connected to the direct-driven and loading-unloading processes, are characterized by different timescales.

Particularly, loading-unloading processes generally occur on short timescales ($\tau < 100$ min), with coherent intermittent activity bursts manifestation, while externally direct-driven ones take place on longer timescales (Kamide and Kokubun, 1996; Consolini and De Michelis, 2005).

Another relevant point in Space Weather studies is the identification of the timescales directly connected to the external solar-wind variability and to the internal magnetospheric dynamics. Indeed, this affects the forecast of the magnetospheric dynamics starting from the measurement of the solar wind conditions. Attempts to forecast high latitude geomagnetic disturbances as monitored by auroral electrojet indices (such as, for instance, AE-index) via artificial neural networks have clearly shown how AE variations on timescales shorter than 1 hour, cannot be correctly forecasted from IMF and solar wind plasma parameters only (see e.g., Pallocchia et al. (2007)). These studies suggest that fluctuations on timescale shorter than 1 hour are essentially not coupled to solar wind variations but result from internal magnetospheric processes only.

For these reasons, we present a detailed study of the timescale coupling between SW/IMF condition changes and the magnetospheric response in the course of the two St. Patrick's Day geomagnetic storms occurred in 2013 and 2015. To investigate the range of the coupled timescales we use the Empirical Mode Decomposition (EMD), particularly useful to analyze nonlinear and nonstationary time series (Huang et al., 1998), and the Delayed Mutual Information (DMI), to provide a measure of the total linear and nonlinear correlation in terms of shared information.

4.2 Methodology

4.2.1 Geospace Conditions

For our analysis, we consider two periods of 21 days, from 10 to 30 of March 2013 and March 2015, since these time intervals comprise both periods of low geomagnetic activity and the well-known St. Patrick's Day Geomagnetic Storms. The main property of the geospace during both periods are summarized in Table 4.1.

4.2.2 Data sets

Solar wind time series are obtained from Advanced Composition Explorer (ACE) spacecraft (http://cdaweb.gsfc.nasa.gov), located at the Lagrangian point L1[2]. We use data related to the three components (Bx, By, Bz) of

---

[2] The L1 point corresponds to the distance at which an object will move around the Sun with the same orbital velocity of the Earth.

	St. Patrick's Day 2013	St. Patrick's Day 2015
Solar storm	Halo CME	Asymmetric partial halo CME
Solar source	M1 flare	C9.1 flare
Solar disk location	N11E12	S22W25
Active region	NOAA 1692	NOAA 2297
CME linear speed	1063 km/s	719 km/s
Bz orientation	Southward	Southward
Storm Sudden Commencement (SSC)	06:00 UT on March 17	04:45 UT on March 17
NOAA Class	G2 Moderate (Kp=6)	G4 Severe (Kp=8)

Table 4.1: Geospace conditions during the St. Patrick's Day storms in 2013 and 2015.

the Interplanetary Magnetic Field (IMF) in GSM coordinates[3] and the solar wind plasma bulk speed, such that we are able to evaluate the Perrault-Akasofu coupling function ϵ defined as (Perreault and Akasofu, 1978)

$$\epsilon = \frac{4\pi}{\mu_0} l_0^2 v B^2 sin^4(\theta_c/2) \quad [GW] \tag{4.1}$$

where $\mu_0 = 4\pi \times 10^{-7} N/A^2$ is the permeability of free space, $l_0 = 7R_E$ is the stand-off distance of the nose of the magnetosphere, v is the solar wind speed (in km/s), B is the magnitude of the solar wind magnetic field (in nT) and θ_c is the clock angle defined as

$$\theta_c = \begin{cases} \tan^{-1}(|\frac{By}{Bz}|), & \text{if}\, Bz > 0 \\ \pi - \tan^{-1}(|\frac{By}{Bz}|), & \text{if}\, Bz < 0. \end{cases}$$

Moreover, geomagnetic time series of the low-latitude Sym-H and Asy-H indices and the Auroral Electrojet indices, AE, AU and AL, are retrieved at OMNI website (http://omniweb.gsfc.nasa.gov), with a 1 min time resolution. The Sym-H (a 1 minute version of the well-known Dst index) and Asy-H indices, being derived from a network of near-equatorial geomagnetic observatories, allow us to get an estimate of the ring current dynamics and of the asymmetric low-latitude disturbance (partial ring current), respectively, in the course of a storm (Sugiura and Poros, 1971; Kawasaki and Akasofu, 1971; Crooker and Siscoe, 1971; Crooker, 1972; Clauer and McPherron, 1980; Clauer et al., 1983). On the other hand, the Auroral Electroject (AE, AU and AL) indices provide an estimation of the intensity of the electrojet currents in the auroral ionosphere and of the energy deposition in those regions (Davis and Sugiura, 1966; Ahn et al., 1983). As explained in Chapter 3, AE index represents the overall activity of the auroral electrojets, while the AU and AL indices quantify the current intensity variations of the eastward and

---

[3] Geocentric Solar Magnetospheric: this system has its X axis towards the Sun and its Z axis is the projection of the Earth's magnetic dipole axis (positive North) on to the plane perpendicular to the X axis. The Y GSM supplements the right three, toward to the dusk.

westward auroral electrojets, which are mainly related to the tail activity during magnetic storms and substorms.

Figure 4.1 shows the time series of the considered quantities (Sym-H, IMF-Bz, ϵ, Asy-H, AE, AU and AL) for the two selected periods relative to the 2013 and 2015 St. Patrick's Day storms.

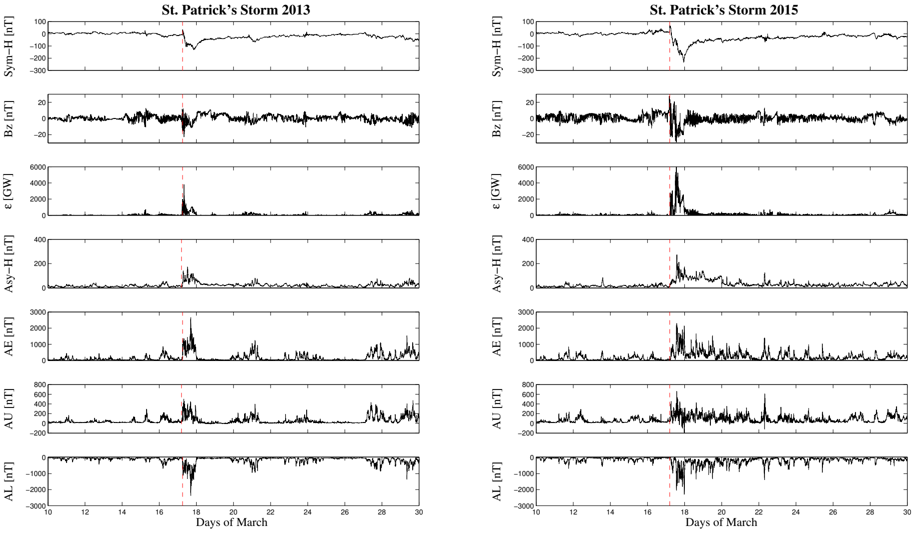

Figure 4.1: Time behavior of the solar wind parameters and the geomagnetic indices for both Storm time periods. The red dashed line identifies the SSC time.

4.2.3 The Empirical Mode Decomposition (EMD) Method

The standard approach to identify the relevant timescales in a time series is based on Fourier analysis. Although this method is powerful in the case of stationary signals, it can produce misleading results when it is applied to nonstationary time series. An alternative method to process nonstationary signals is the Empirical Mode Decomposition (EMD) technique, introduced by Huang et al. (1998) [see also Wu and Huang (2004)], as a preconditioning method for the application of the Hilbert transform, as discussed in detail in Chapter 2. An example of the results of EMD analysis is shown in Figures 4.2 and 4.3 for the *IMFs* obtained using the Sym-H and AE indices for both periods.

A set of $n = 15$ (14) and $n = 16$ (15) modes are extracted for the March 2013 (2015) time periods from Sym-H and AE indices, respectively, with characteristic timescales ranging from $\tau = 4$ min to $\tau \sim 10^4$ min. Similar numbers $(14-17)$ of *IMFs* are found for the other parameters (Bz, ϵ, Asy-H,

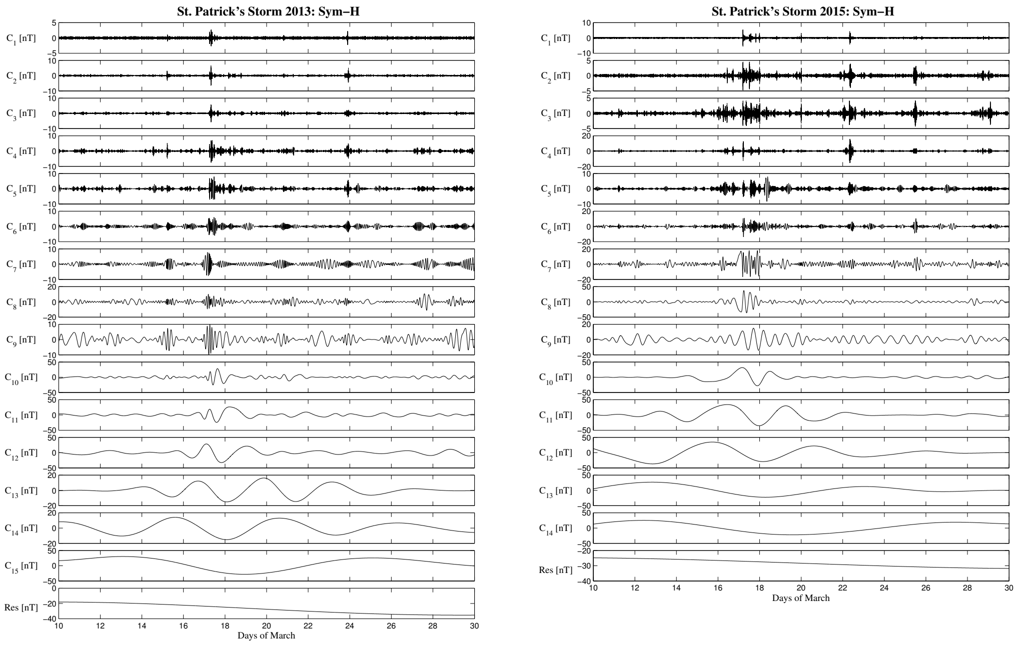

Figure 4.2: EMD results obtained by analyzing Sym-H index for both Storm time periods.

AU, AL) in both selected time intervals.

To characterize the typical timescale associated with every *IMFs*, different methods can be used, from spectral method, based on the Fourier analysis of each *IMFs*, to auto-correlation based methods and Max-Max/min-min distance once. Here, we use the spectral method. In particular, the characteristic mean frequency f_n of all the *IMFs* is estimated by means of the associated Fourier power spectral density $S_n(f)$ as

$$f_n = \frac{\int_0^\infty f S_n(f) df}{\int_0^\infty S_n(f) df}. \tag{4.2}$$

This allows us to obtain the characteristic oscillation timescale of each mode as $\tau_n = f_n^{-1}$. Moreover, since the decomposition is local, complete and orthogonal, the EMD can be used as a filter by reconstructing partial sums of Eq. (2.1) in a chosen frequency range (Alberti et al., 2014; De Michelis and Consolini, 2015).

Figure 4.4 shows the characteristic frequencies f_n as a function of the mode number n corresponding to the *IMFs* shown in Figures 4.2 and 4.3 relative to Sym-H and AE indices for both periods.

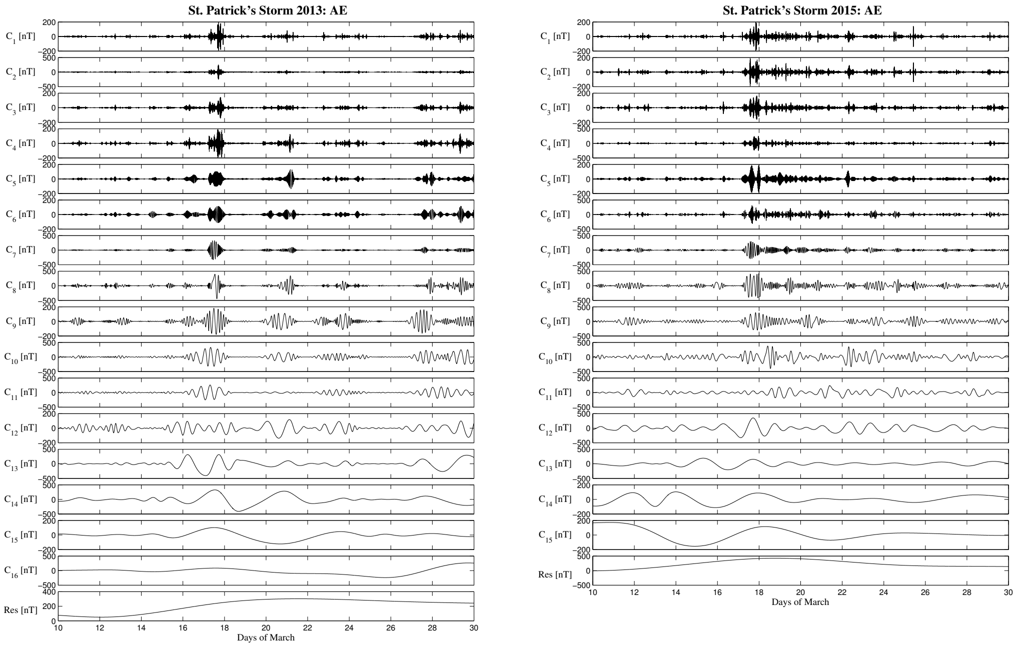

Figure 4.3: EMD results obtained by analyzing AE index for both Storm time periods.

4.2.4 The Delayed Mutual Information (DMI) Approach

The behavior of a system X or the interference between two systems X and Y can be characterized by estimating some quantities defined in the framework of information theory. For instance, useful quantities to characterize the behavior of a system X and the degree of statistical independence between two systems (X and Y), on the basis of the set of states the systems visit as they evolve in time, are the *Shannon information entropy* $H(X)$ and the *mutual information* $MI(X, Y)$ (Shannon, 1948).

If we define $p(x)$ and $p(x, y)$ the probability of finding a system in state x and the joint probability for the systems X and Y, respectively, then the *Shannon information entropy* $H(X)$ and the *mutual information* $MI(X, Y)$ are:

$$H(X) = \sum_{x \in X} p(x) \log \frac{1}{p(x)}, \tag{4.3}$$

$$MI(X, Y) = \sum_{x \in X} \sum_{y \in Y} p(x, y) \log \frac{p(x, y)}{p(x)p(y)}. \tag{4.4}$$

Now, although the mutual information $MI(X, Y)$ is able to quantify the statistical independence between two signals/systems, no information is

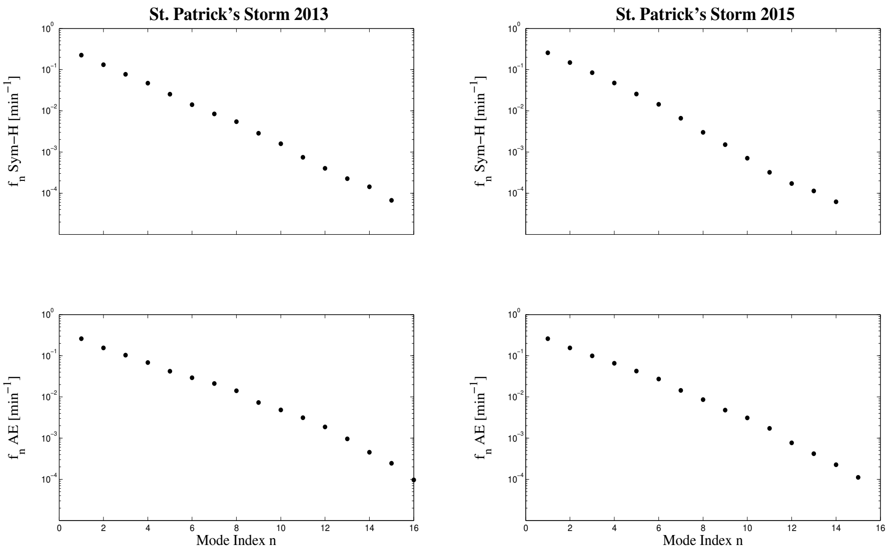

Figure 4.4: The characteristic frequencies, f_n, versus the mode index n for the *IMFs* relative to Sym-H and AE reported in Figures 4.2 and 4.3, respectively.

provided for a delay of the interference between the two systems X and Y. A better quantity to address this point is the Delayed Mutual Information $MI(X,Y \mid \Delta)$ (DMI), which is capable of quantifying a time dependent statistical independence between the two systems. This quantity is defined as follows

$$MI(X,Y \mid \Delta) = \sum_{i,j=1}^{N} p_{ij}(X(t),Y(t+\Delta)) \log \frac{p_{ij}(X(t),Y(t+\Delta))}{p_i(X)p_j(Y)} \tag{4.5}$$

where $p_{ij}(X(t),Y(t+\Delta))$ is the joint probability of observing the couple of values (X,Y), while $p_i(X)$ and $p_j(Y)$ are the probabilities of observing X and Y as independent variables. It can be considered the analog of a cross-correlation function, although it provides an estimation of the total (linear and nonlinear) dependence between two systems/signals (De Michelis et al., 2011) by quantifying the amount of information shared. We underline that the use of DMI to quantify the amount of shared information in the case of SW/IMF parameters (input) and geomagnetic indices (output) is particularly appropriated because of the nonlinear features of the magnetospheric dynamics in response to SW/IMF changes.

The relevance of the dependence/independence degree between two signals using the Delayed Mutual Information $MI(X,Y \mid \Delta)$ can be investigated by setting a significance threshold. This can be done by means of the following procedure. Given two time series $\{X_i\}$ and $\{Y_i\}$, an ensemble of $Nr = 10000$ couples of time series is generated by randomly sorting the two original ones in order to disrupt any time correlation in each sequence and any possible correspondence between the two time series, without altering the statistics of the values of the time series. Then, for each couple of the randomized time series, we compute the corresponding value of the mutual information $MI(X, Y \mid \Delta = 0)$, and the statistics of $MI(X, Y \mid \Delta = 0)$ values is evaluated by computing the cumulative distribution $C(MI)$. The threshold is chosen at the value MI_{thr} for which $C(MI_{thr}) = 0.95$. This value corresponds to the 5% confidence limit which assures that, if the observed value of $MI(X, Y \mid \Delta)$ is larger than the threshold MI_{thr}, we can say that the observed dependence is significative with an error of 5% at the most.

4.3 Results and Discussion

The first step of our analysis of the timescale coupling between solar wind parameters and geomagnetic indices is the investigation of the scale-to-scale DMI between the *IMFs* of solar wind parameters and that of geomagnetic indices with similar characteristic frequency.

Figure 4.5 shows the scale-to-scale DMI in the case of the *IMFs* relative to the interplanetary magnetic field Bz component and the AE-index for the 2013 St. Patrick's Day storm. This analysis clearly suggests that for timescales $\tau < 200$ min the coupling is not-significative, while at timescales $\tau \gtrsim 200$ min the coupling becomes significative for time delays Δ in the range $\Delta \in [0, \sim 600 - 800)$ min. Moreover, at these large timescales, a maximum of the DMI for a delay $\Delta \sim 100$ min is observed, consistent with the propagation time of the perturbation from the ACE L1 position to the internal magnetosphere. To avoid any confusion in what follows we stress that this delay time is not strictly representative of the response time of the Earth's magnetosphere to SW/IMF changes because it also includes the propagation time.

Similar results are found for the scale-to-scale DMI of other quantities (ϵ, Sym-H, AsyH, AU, AL) in both the two geomagnetic storms (2013 and 2015 St. Patrick's storms), suggesting that there is a timescale separation in the solar wind-magnetosphere coupling. We also observe that this timescale separation occurs at a timescale $\tau \simeq 200$ min, in agreement with the typical timescale discerning direct driven and loading-unloading magnetospheric processes (Kamide and Kokubun, 1996; Consolini and De Michelis, 2005), where the term "direct driven" here is intended according to the linear response theory, i.e., a correspondence between input and output fluctuations at the different timescales unless of a linear filtering.

Taking into account this observation of a clear timescale separation for

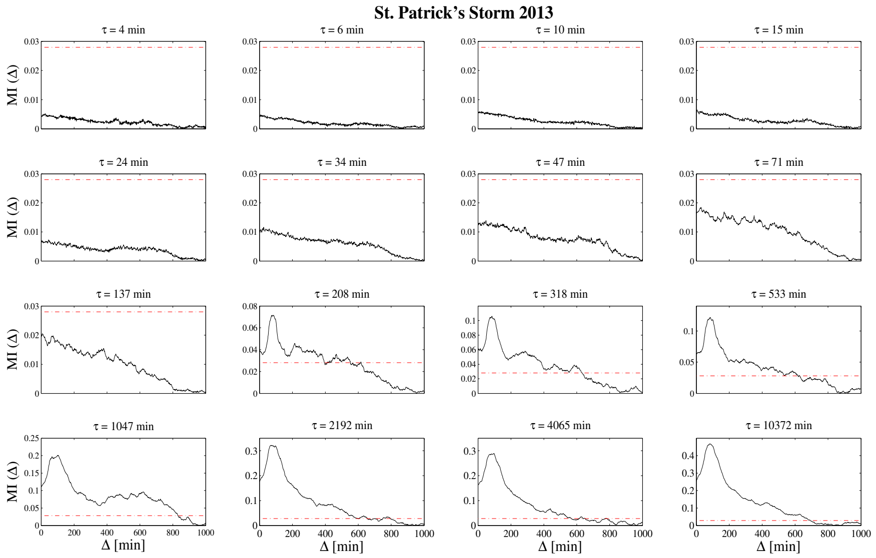

Figure 4.5: The scale-to-scale DMI between *IMFs* of the Interplanetary Magnetic Field Bz component and Auroral Electroject AE index for the St. Patrick's storm 2013 time period. Red dashed line indicates the significance (5% null hypothesis) DMI threshold, $MI_{thr} = 0.028$.

the coupling, we use the EMD decomposition to reconstruct two different signals. In detail, we divide each set of modes into two subsets: (i) a short-timescale set, with characteristic timescales $\tau \lesssim 200$ min, and (ii) a long-timescale one, with $\tau \gtrsim 200$ min.

Figures 4.6 and 4.7 show an example of the reconstructed short- and long-timescale signals in comparison with the complete one for the AE-index relative to the 2013 St. Patrick's Day storm, and the corresponding Fourier spectra (PSD), respectively.

We note that the PSD clearly shows the relative contribution of the two reconstructed signals to the total PSD of the complete time series, with a frequency cut-off occurring at $f_c \sim 5 \times 10^{-3}$ min^{-1} ($\tau \sim 200$ min). We also need to underline that, different from standard Fourier-based filters, the EMD does not alter the phases of the different spectral contributions, when separating the short- and long-timescale fluctuations.

We then perform the DMI analysis on the reconstructed short- and long-timescale signals relative to the interplanetary magnetic field Bz component and the AE-index for the 2013 St. Patrick's Day storm.

As shown in Figure 4.8, a clear and significant amount of shared information (correlation) is found in the case of the long-timescale signals with a maximum of the DMI for a time delay $\Delta \sim 100$ min. Conversely, in the

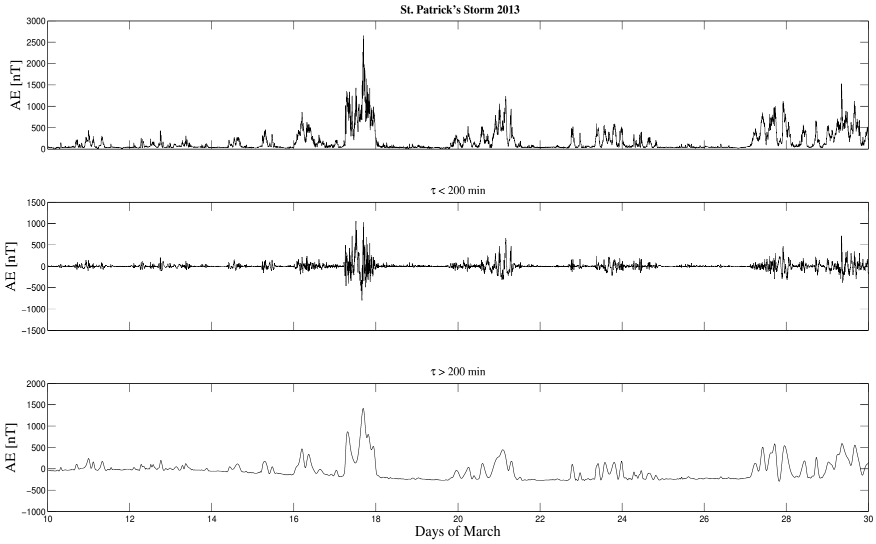

Figure 4.6: The complete (upper panel), the short-timescale ($\tau < 200$ min, middle panel) and the long-timescale ($\tau > 200$ min, lower panel) signals of AE index for the St. Patrick's storm 2013 time period.

case of short-timescale signals the observed correlation is not significant, indicating that it is reasonable to assume that the processes responsible for the dynamics of Earth's magnetosphere at these timescales are not directly driven by the solar wind parameters.

To better investigate this point we extend the above analysis to all the other parameters considered in this work and also to the St. Patrick's Day storm occurred in 2015.

Figure 4.9 shows the results of the DMI analysis for the complete and reconstructed time series in the case of Sym-H, Asy-H, AU and AL versus IMF Bz component, and Sym-H, Asy-H, AE, AU and AL versus the Perrault-Akasofu coupling function ϵ. All the cases confirm the previous results.

This suggests that timescales longer than 200 min are directly coupled to (driven by) solar wind, while for timescales shorter than 200 min there is no direct coupling to solar wind parameter fluctuations. The same results are found in the case of 2015 St. Patrick's Day storm as shown in Figure 4.10.

Interestingly, we also note that at long timescales the response of the magnetospheric ring-current, monitored by Sym-H, is delayed with respect to the high-latitude electrojet current systems. Indeed, for high-latitude geomagnetic indices (AE, AU and AL) the maximum of the $MI(\Delta)$ is

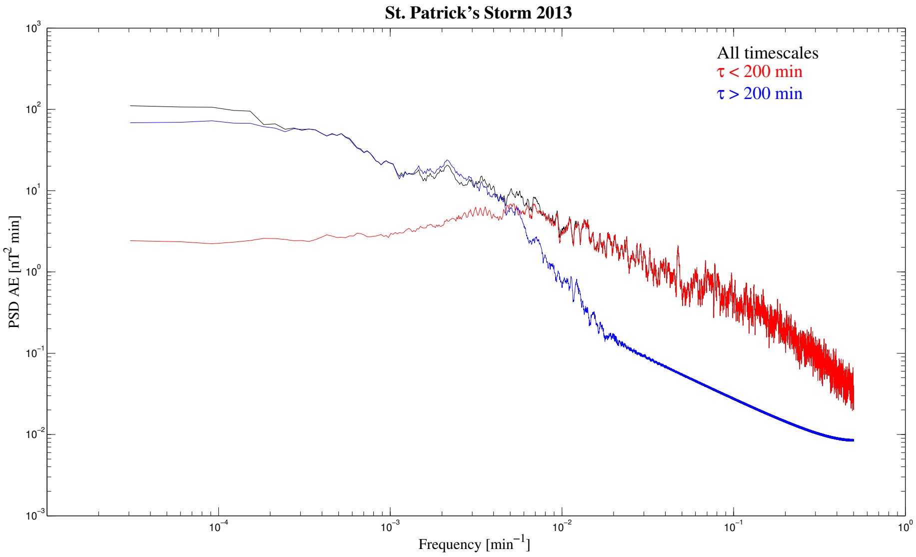

Figure 4.7: The PSD of the complete and reconstructed signals of AE index for the St. Patrick's storm 2013 time period. Black, red and blue lines refer to complete, short-timescale ($\tau < 200$ min) and long-timescale ($\tau > 200$ min) signals, respectively.

found in correspondence of $\Delta \sim 100$ min, while Sym-H responds later being $\Delta \sim 150 - 200$ min. A more different behavior is shown by Asy-H, which indeed shows a maximum of the $MI(\Delta)$ for a time delay of $\Delta \sim 100$ min, i.e., a time delay similar to the high-latitude geomagnetic indices. This result confirms the previous findings by Crooker (1972) and Clauer and McPherron (1980) that show that the asymmetric part of the variation of the horizontal component H of geomagnetic field at low-latitude well correlates with the general trend of the Auroral Electrojet index AE. Moreover, the time delay corresponding to the maximum DMI observed in the case of AE-indices and Asy-H seems to be in good agreement with the time necessary to the interplanetary disturbance (CME) to propagate from L1 (ACE) to the magnetopause plus the typical $\sim 64 - 72$ min of the median growth-phase period of southward IMF preceding a classical substorm (see e.g., Lyons et al. (1997)). The explanation of this point has to be found in the link between the development of the partial ring-current and the increase of the dawn-dusk interplanetary electric field. Conversely, the possible explanation of this different response time delay observed in the case of Sym-H suggests that the ring current enhancement requires a longer time being this related to the time for plasma to be convected/advected to the Earth's distances in the inner regions of the magnetosphere where the ring current is located.

Finally, the absolute and maximum values of the shared information

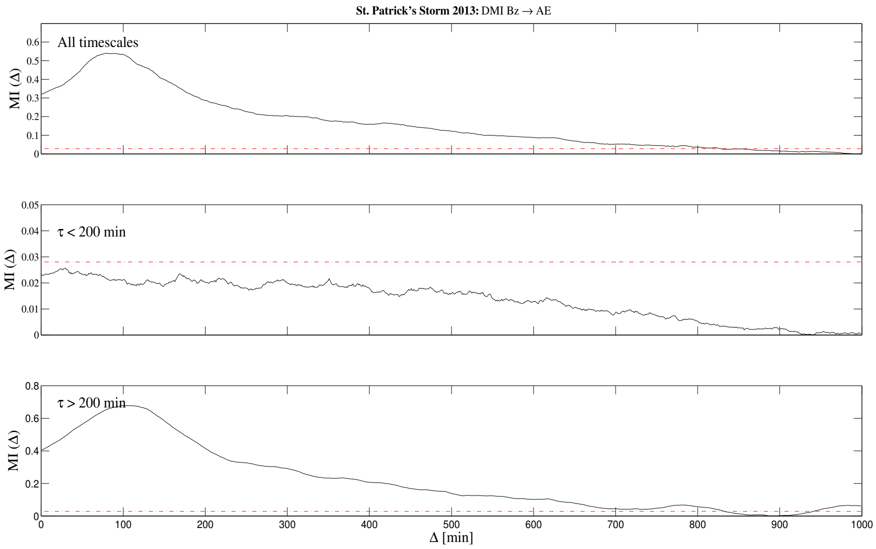

Figure 4.8: The DMI analysis between *IMFs* of the Interplanetary Magnetic Field Bz component and Auroral Electroject AE index for the complete (upper panel), the short-timescale ($\tau < 200$ min, middle panel) and the long-timescale ($\tau > 200$ min, lower panel) signals for the 2013 St. Patrick's storm time period. The dashed red line is the significance (5% null hypothesis) DMI threshold, $MI_{thr} = 0.028$.

MI at long timescales are generally higher for geomagnetic high-latitude indices (AE, AU and AL) than for Sym-H and Asy-H. This suggests that there could be inner physical processes that tend to reduce the correlation between Sym-H and Asy-H and external drivers.

4.4 Effect of propagation from L1 position to bow shock nose

The solar wind data are obtained by using measurements made by the ACE spacecraft which is located approximately at about 1.5 million kilometers from Earth (or $\sim$ 235 R_E). As shown in Chapter 3 the magnetopause is located at about 10-12 R_E, while the bow shock surface, generated by the solar wind itself, is at $\sim$ 14 R_E. As a consequence solar wind properties could change during the travel from L1 point to the bow shock nose, with different effects on the Earth's magnetospheric response with respect to that showed in the previous section. Indeed, the observed absence of a significant correlation at timescales shorter than 200 minutes could be due to a *random phase* effect as a consequence of the fact that ACE data have not been

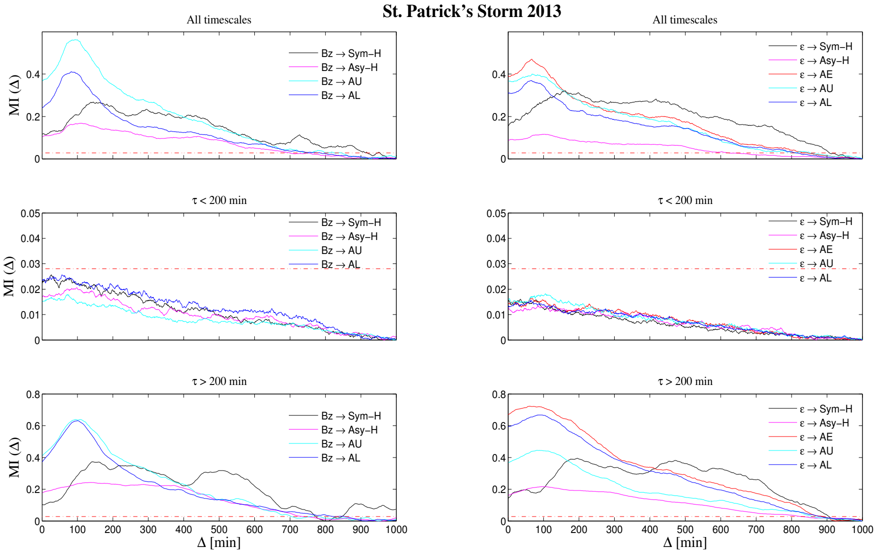

Figure 4.9: The DMI results on different timescales between solar wind IMF Bz-component, the Perrault-Akasofu coupling function, ϵ, and magnetospheric response proxies, Sym-H, Asy-H, AE, AU and AL, for the 2013 St. Patrick's storm time period. The dashed red line represents the significance (5% null hypothesis) DMI threshold, $MI_{thr} = 0.028$.

adjusted to account for the propagation time between L1 point and the bow shock nose. This random phase effect (acting as a *jitter*) could, indeed, smear out some significant correlation. To check if this hypothesis/interpretation is reasonable, we have attempted two different approaches to correct the results at timescales below 200 min: i) a OMNI-based propagation method and ii) a fluid-like based propagation method.

4.4.1 OMNI-based propagation method

To best support solar wind-magnetosphere coupling studies, it is desired to time shift solar wind data from their location of observation, which may be an hour upstream of the magnetosphere and several tens of R_E from the magnetosphere, to a point close to the magnetosphere, the bow shock nose. One way to study solar wind properties at the bow shock nose position is to use the OMNI database, built up by shifting single spacecraft measurements made by ACE and WIND, assuming that solar wind variations are organized in series of phase fronts, convecting with the solar wind bulk speed. In this way, the time shift equation is

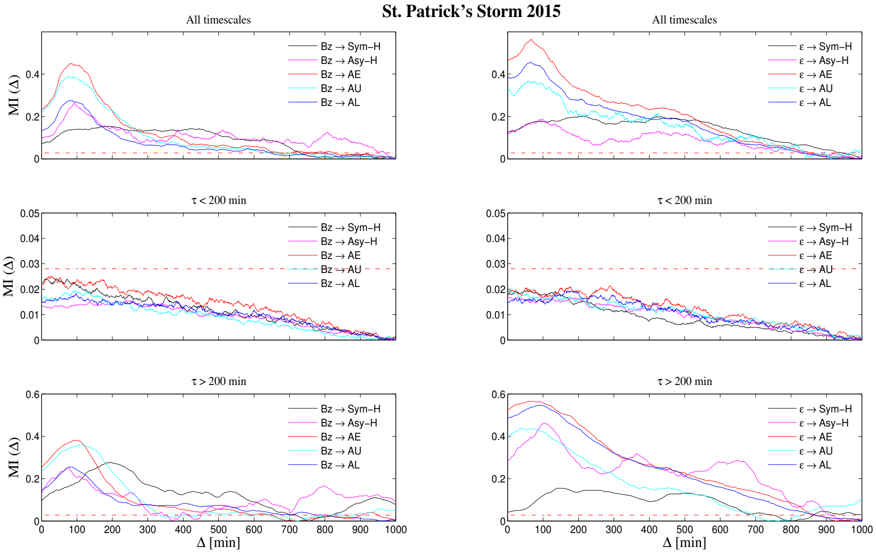

Figure 4.10: As in Figure 4.9 for the 2015 St. Patrick's storm time period.

$$\delta t = \frac{\vec{n} \cdot (\vec{R_d} - \vec{R_o})}{\vec{n} \cdot \vec{V}}, \tag{4.6}$$

where $\vec{n}$ is the variation phase front normal (PFN), $\vec{R_d}$ is the bow shock position, $\vec{R_o}$ is the spacecraft position (L1) and $\vec{V}$ is the solar wind velocity. To determine normals to discontinuity planes in the solar wind magnetic field a modified version of the Minimum Variance Analysis (MVA) technique is used. The MVA is only applied on magnetic field data, although the location of the bow shock nose $\vec{R_d}$ requires the knowledge of others solar wind parameters such as velocity, proton and alpha particle densities, proton temperature and ram pressure. Indeed, it is assumed that the geocentric direction to the bow shock nose is parallel to the solar wind flow direction (a correction is needed to take into account mean orbital speed of the Earth around the Sun) such that:

$$|\vec{R_d}| = R_{mp} \left[1.0 + 1.1 \frac{\frac{2}{3}M^2 + 2}{\frac{8}{3}(M^2 - 1)} \right] \tag{4.7}$$

with

$$\begin{aligned}
M &= \frac{V_{sw}}{V_{ms}} && (4.8)\\
V_{ms} &= \sqrt{0.5\left\{V_A^2+V_s^2+\sqrt{[(V_A^2+V_S^2)^2+4(V_A^2V_S^2\cos^2(\theta)]}\right\}} && (4.9)\\
V_A &= \frac{B}{\sqrt{4\pi(4N_a+N_p)M_p}} && (4.10)\\
V_s &= 0.12\sqrt{T_p+1.28\times 10^5} && (4.11)\\
R_{mp} &= (11.4+KBz)P^{-1/6.6} && (4.12)\\
P &= (2\times 10^{-6})N_pV_p^2 && (4.13)
\end{aligned}$$

where R_{mp} is the geocentric magnetopause nose distance, M is the magnetosonic Mach number, V_{ms} is the magnetosonic speed, V_A is the Alfven speed, V_S is the sound speed, θ is the angle between $\vec{B}$ and $\vec{v}$, N_a and N_p are the alpha particle and proton densities, M_p is the proton mass, T_p is the proton temperature, V_p is the proton velocity and P is the pressure.

Nevertheless, the time shift procedure is built up by making a "rigid" time shift between the L1 and the nose of the bow shock positions that does not consider the "real" solar wind structure propagation. Indeed, solar wind streams can interact and generate new types of structures which cannot be simply monitored by "rigidly" shifting solar wind parameters values. As also pointed out by OMNI documentation their time shift technique "is a very simplified approach, neglecting finite response times of the magnetosphere to solar wind variations, that may introduce some errors". Additional details can be found at `http://omniweb.gsfc.nasa.gov/html/HROdocum.html`.

4.4.2 Fluid-like based propagation method

We also try to propagate, in a "fluid" sense, different from the "wave-like" propagation made by OMNI (by using shock front direction), ACE spacecraft data. We built up a procedure characterized by the following steps: (i) we identified the direction of the relative positions of ACE spacecraft and bow shock nose ($\vec{r}$), (ii) we projected the solar wind vector measured by ACE ($\vec{v}$) on that direction and (iii) we evaluate the corresponding time shift as

$$\tau_s = \frac{|\vec{r}|}{\vec{v}\cdot\vec{r}} \tag{4.14}$$

where $\vec{r} = \vec{R_d} - \vec{R_o}$ in which the bow shock nose position $\vec{R_d}$ is calculated as in Eq. (4.7). As for the OMNI procedure, our approach is based on "rigid" time shift, without any consideration of the "in situ" solar wind structure generation. Indeed, the solar wind is a complex system in which several processes can develop and the bow shock surface is not "static" but it is continously modified by the solar wind itself. This problem could be solved by making the necessary time shift, which implies a complete knowledge of the solar wind properties at L1 position and, simultaneously, the bow shock properties, including magnetic field topology and geometry (this cannot be correctly done since only two satellites are present at L1 and a "topological and geometrical view" of solar wind structures is not possible). Moreover, we should also know the properties of the heliospheric medium between L1 and the bow shock nose positions, since, as stated above, several structures can be generated "in situ" due to solar wind streams interaction and a correct estimation of their formation is not possible by using only spacecraft data from L1 position. A solution of this problem could be found if we had a numerical model for the bow shock position and also for each solar wind structure in order to investigate its evolution in the heliospheric medium between L1 and bow shock nose positions (in particular, the "real" bow shock position when the solar wind structure hits it).

4.4.3 Effect on DMI analysis

Using the two methods described above, we have computed the time shifts for the two geomagnetic storms under consideration. The obtained time shifts for both St. Patrick's Day storms in 2013 and 2015, which are shown in Figure 4.11, allow us to reconstruct propagated (time-shifted) signals (see Figure 4.12) to which we can apply all the same analysis described previously to compute the DMI.

In Figures 4.13 and 4.14 we report the results of the DMI analysis between B_Z and AE or Sym-H for the 2013 and 2015 St. Patricks's storms, respectively.

The results clearly show:

i) a reduction of the time delay Δ from $\sim 100-150$ min to $\sim 70-80$ min. The observed time delay for propagated data is well in agreement with what generally reported in the literature (see, e.g. Lyons et al., 1997);

ii) the absence of a significative correlation at time scales shorter than 200 min, which confirms the previous results on the meaningfulness of DMI at these time-scales;

iii) an increase of the value of the DMI maximum value for OMNI-based shifted data when all the timescales are considered. This is generally true also at timescales larger than 200 min.

The same results have been found also for the other interplanetary quantities considered in this study (i.e., ϵ, AU, AL, Asy-H).

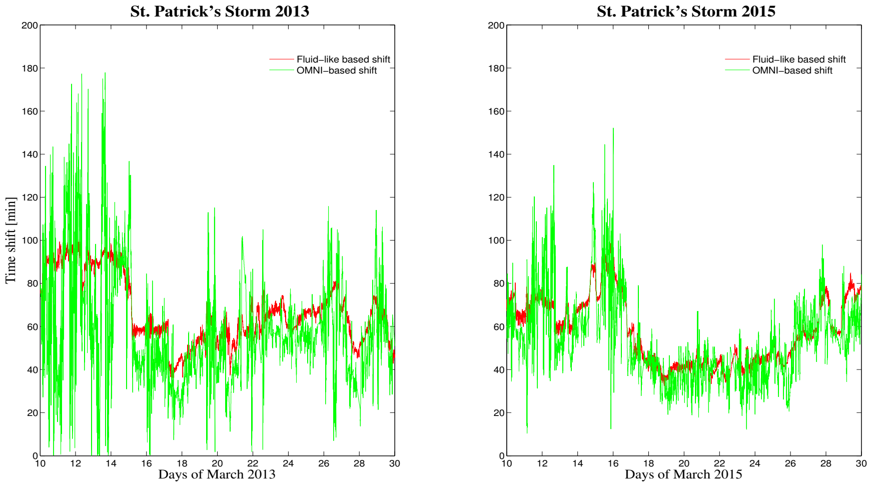

Figure 4.11: Time shifts obtained with the two different methods described in Section 4.4 for both St. Patrick's Day storms in 2013 and 2015. Green line refers to the OMNI-based shift procedure (sub-section 4.4.1), while red line shows the time shift obtained via the procedure (sub-section 4.4.2).

4.5 Summary and Conclusions

The Earth's magnetosphere response to solar wind disturbances during two major geomagnetic storms (the 2013 and 2015 St. Patrick's Day storms) was investigated through novel analysis approaches based on the EMD and the DMI, allowing an efficient separation between fluctuations at different timescales and an analysis of linear/nonlinear interference/coupling between two signals. We found the following results.

1. The magnetospheric short-timescale fluctuations seem to be not directly related to the same timescale fluctations in the SW/IMF, because the MI is under the null hypothesis threshold. This is a relevant result suggesting that internal magnetospheric processes strongly affect the magnetospheric response at timescales lower than 200 min in the magnetospheric dynamics. With the term "internal origin" we mean that there is not a one-to-one coupling, although the transient activities at these timescales (see e.g., the bursty enhancement of high latitude electrojet currents, the occurrence of fast relaxation processes in the tail regions, such as bursty bulk-flows, etc.), that are responsible for the fast variations observed in the geomagnetic indices at short timescales, are certainly triggered by IMF and solar wind changes but do not seem directly driven in terms of fluctuations.

2. On the contrary, the SW/IMF fluctuations at long timescales play a

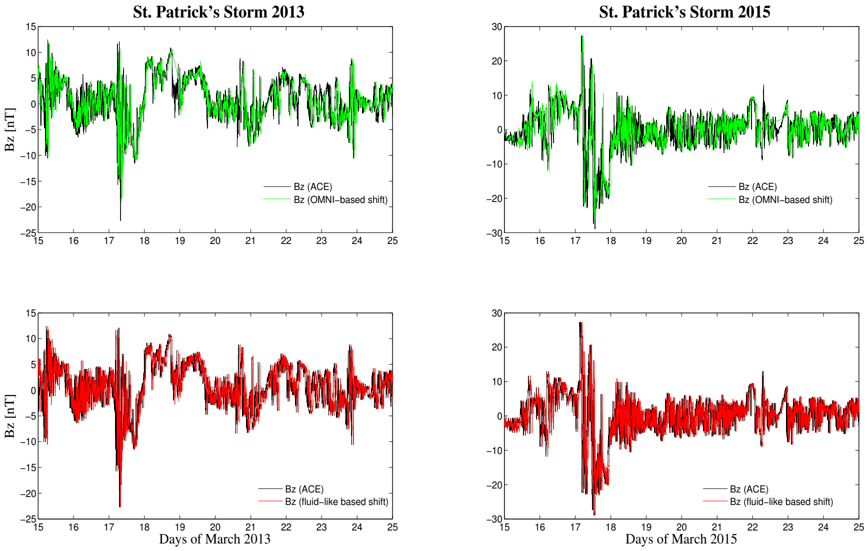

Figure 4.12: Time behavior of the Interplanetary Magnetic Field Bz component as obtained from raw data by ACE and by using both time-shift propagation methods. Black lines refer to the observed values (i.e., ACE data), green lines to OMNI-based time-shifted data and red line to fluid-like based time-shifted data. We zoom over the time interval 15-25 March in both cases for a more convenient visual inspection.

primary role into the coupling of timescales greater than 200 min in the magnetosphere. This indicates that the magnetospheric response to the SW/IMF driver at these timescales is well correlated, suggesting that direct driven processes are responsible for the geomagnetic indices fluctuations at these timescales.

3. A time delay of $\sim 100 - 150$ min is found between solar wind/IMF parameters (observed at L1 position) and magnetospheric overall dynamics (measured by indices), which is quite well in agreement to the travel time necessary to the SW/IMF perturbation to propagate from the ACE spacecraft position to the Earth's magnetopause plus the response time of the Earth's magnetosphere for the occurrence of storms/substorms.

4. A great information transfer can be observed between IMF-Bz component and AE, AU and AL indices, while a lower transfer is found when IMF-Bz component and Sym-H/Asy-H are considered.

Moreover, the same analyses have been performed to other solar wind parameters: the solar wind dynamic pressure p_{SW}, the velocity flow v, vB_{South}

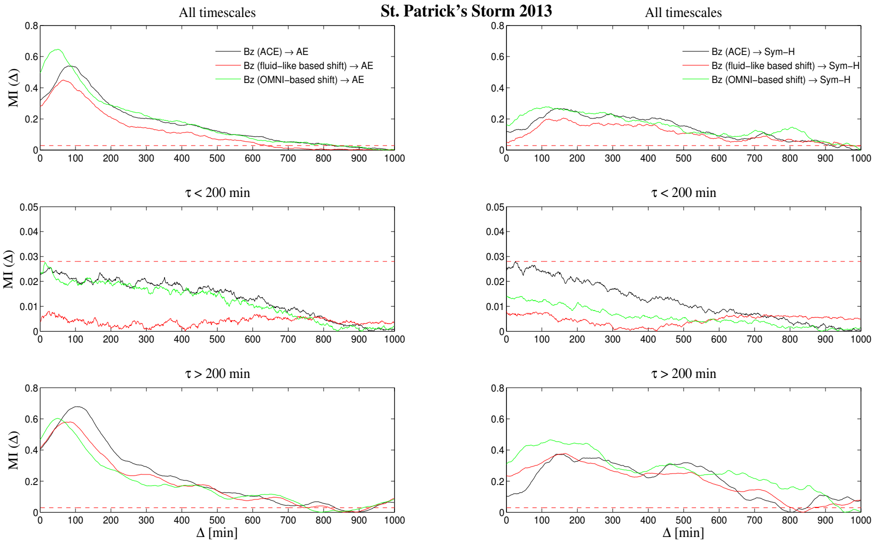

Figure 4.13: The DMI analysis between IMFs of the Interplanetary Magnetic Field Bz component and Auroral Electroject AE index for the actual (upper panel), the short-timescale ($\tau < 200$ min, middle panel) and the long-timescale ($\tau > 200$ min, lower panel) signals for the 2013 St. Patrick's storm time period. Black lines is related to the DMI applied by using observed value of Bz by ACE, while green and red lines refer to the different time-shift method used. The dashed red line is the significance (5% null hypothesis) DMI threshold, $MI_{thr} = 0.028$.

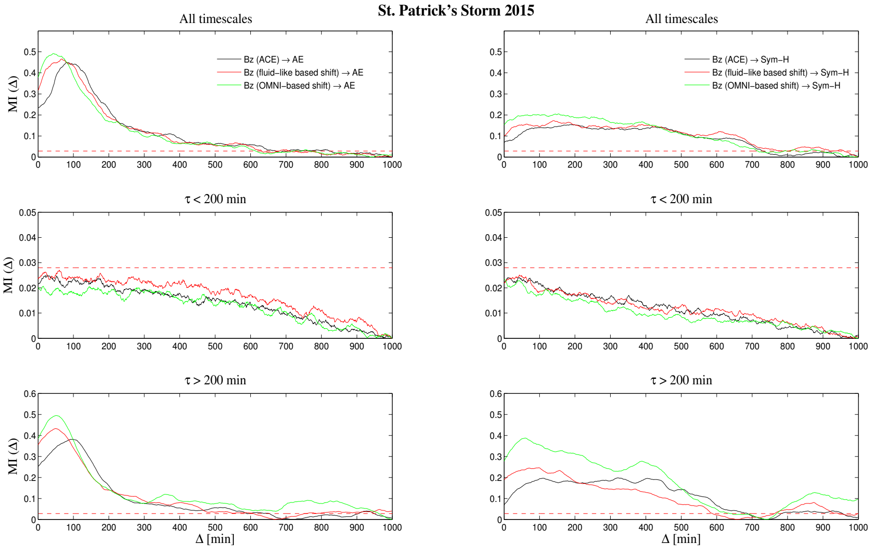

Figure 4.14: As in Figure 4.13 for the 2015 St. Patrick's storm time period.

and the Newell coupling function $d\Phi_{MP}/dt$ (Newell et al., 2007) (not shown here). The obtained results do not show any substantial difference from those reported in this work.

Our findings support the common idea that the Earth's magnetosphere response consists of both direct driven and internal processes, where the internal processes can be considered more reasonably as only triggered by external solar wind changes. Furthermore, there is a clear separation of timescales between the internal processes and the direct driven ones, being the characteristic separation timescale of the order of 100-200 min. This timescale separation is well in agreement with previous findings on loading-unloading typical timescales (Kamide and Kokubun, 1996; Consolini and De Michelis, 2005) and also with typical timescales involved in the nonlinear response of the Earth's magnetosphere (Tsurutani et al., 1990). Furthermore, the smaller MI maximum value for Sym-H could be due to the effect that internal processes (like loading-unloading ones taking place in the central plasma sheet of the magnetotail region) play on the enhancement of the Earth's ring current. We remind as part of the Earth's ring current enhancement during geomagnetic storms is due to high latitude ionospheric ion species (typically oxygen O^+) outflowing as a consequence of FAC activation (Daglis et al., 1994).

The observed absence of coupling (direct inference) between Earth's magnetospheric short timescales and the corresponding solar wind ones supports the inherent difficulties in forecasting high latitude geomagnetic disturbances, as monitored by auroral electrojet index AE, using artificial neural networks based on IMF and solar wind parameters at timescales shorter than 1 hour (Pallocchia et al., 2007). The fluctuations at these timescales, although triggered by the transfer of external energy, mass and momentum, are not directly coupled to the solar wind parameter fluctuations but result from a complex interplay of external and internal processes. Consequently, a better forecasting of processes occurring on fast timescales requires to find a valid proxy of the internal magnetosphere dynamical state, with a special attention to the state of the Earth's magnetotail plasma sheet.

In conclusion, our analysis of relevant coupling timescales during geomagnetic storms and substorms can be useful for Space Weather prediction models.

Chapter 5

Magnetosphere-Ionosphere signatures on ground measurements[1]

In this study, we investigate the time variation of the magnetospheric and Earth's magnetic field during both quiet and disturbed periods. We identify the timescale variations associated with different magnetospheric current systems, solar-wind–magnetosphere high-frequency interactions, ionospheric processes, and internal dynamics of the magnetosphere.

5.1 Introduction

Geomagnetic storms (GSs) are global magnetic disturbances resulting from the interaction between solar wind magnetic field and magnetic fields in the near-Earth space environment. Generally, they produce strong perturbations of the geomagnetic field which can induce disturbances of the terrestrial environments, affecting technological and social life (i.e. high-frequency communications, GPS navigation and so on) (Schwenn, 2006; Pulkkinen, 2007).

As also pointed out in previous chapters, the strength of geomagnetic storms can be assessed by the Disturbance Storm Time (Dst) index that reveals the decrease of the horizontal geomagnetic field component and gives a global measure of equatorial magnetic disturbances. According to the well-known Dessler-Parker-Sckopke relationship (Dessler and Parker, 1959; Sckopke, 1966), the Dst values are proportional to the total kinetic energy of the particles entering from the solar wind and forming the ring current (McPherron et al., 1986). It has been recently suggested that local geomagnetic indices could represent very useful tools, complementary to global

---

[1] The work presented in this chapter is included in the paper Alberti et al. (2016).

indices, in defining deviations from the usual geomagnetic activity. Indeed, local geomagnetic disturbances play a key role in assessing potential risk factor of extreme events in specific regions (Cid et al., 2013). So, it can be useful to discriminate between the large timescale geomagnetic activity and short timescale one.

Theoretically, a separation between a time dependent background magnetic field (baseline) and its fluctuations can be explored if a clear timescale separation between them exists. This is an open question in many fields of space research, from solar wind to magnetosphere, due to the nonlinear and complex character of space physics phenomena. Indeed, when a timescale separation is not present, it is difficult to identify an average magnetic field.

To investigate the existence of a timescale separation in magnetosphere-ionosphere-ground system we use the Empirical Mode Decomposition (EMD) and a statistical test which allows to suggest a method to separate the average magnetic field by its variations, identifying the physical meaning of each contribution.

5.2 Data sets and methodology

In this study, we use 1 minute data from the horizontal (H) and the eastward (D) components of the geomagnetic field measured at L'Aquila (AQU: $\lambda_g = 42.38°$ N and $\phi_g = 13.32°$ E; λ_g and ϕ_g are the geographic latitude and longitude, respectively) permanent geomagnetic observatory to study the time variations of the geomagnetic field.

We also use 1 minute geosynchronous satellite observations at 6.6 R_E (GOES10: LT=UT-9; GOES12: LT=UT-5; both in the Geocentric Solar Ecliptic - GSE - coordinate system)[2] for the magnetospheric field (http://cdaweb.gsfc.nasa.gov/). More specifically, we use the $B_{Z,GSE}$ magnetospheric component and the H ground component. At high and middle latitudes, their behaviour should be comparable because of the 90° rotation of the polarization axes through the ionosphere (Sciffer et al., 2005; Piersanti et al., 2012; Waters et al., 2013).

For our analysis we select two time intervals corresponding to a Super Solar Quiet (SSQ) period and to a Storm Time (ST) event. In order to distinguish between SSQ and ST, we use the K-index. According to its definition (see Chapter 3), we define a SSQ period when K<1, while a ST event is identified when K>5. We consider, as ST event, the Halloween Super Storm, occurred between 28 October and 1 November 2003.

---

[2] GOES: Geostationary Operational Environmental Satellites

5.2.1 Empirical Mode Decomposition (EMD) and Standardized Mean Test (SMT)

The nonlinear and nonstationary oscillations of each time series are extracted by using the Empirical Mode Decomposition (EMD) method. We remark that this data analysis tool is particularly suitable when the behavior of the observed time series is nonlinear and nonstationary as for geomagnetic observations, reflecting the internal dynamics of the magnesphere-ionosphere system and its interaction with the solar wind. In this study, to investigate the physical meaning of the EMD modes and connect them to the timescales involved in the variations of magnetospheric and geomagnetic field, we use the method proposed by Flandrin et al. (2004). They suggest that, if a clear time scale separation exists in a data set, this can be divided into two different contributions:

$$X(t) = \delta X(t) + X_0(t), \tag{5.1}$$

where $X_0(t)$ is the so called baseline field and $\delta X(t)$ are variations around $X_0(t)$.
The basic idea is that $\delta X(t)$:

- has a close to zero standardized mean (SM) (defined as the mean divided by the standard deviation);
- represents the fluctuating/oscillatory high-frequency contribution to the time series.

Using the orthogonality and completeness properties of EMD, we define $\delta X(t)$ as the reconstruction of a subset S_1 of $k < m$ empirical modes (where m is the number of *IMFs* obtained by Eq. (2.1)) which satisfies the previous two properties:

$$\delta X(t) = \sum_{j=1}^{k} C_j(t). \tag{5.2}$$

The k value represents the last mode index for which the reconstruction given by Eq. (5.2) has a close to zero SM. To investigate if the k value could be dependent on the length of the considered time series, we applied the following procedure. First of all, for each j we evaluated the SM on the whole time range considered. Then, we consider a set of $N_s = 1000$ time windows, with different length, moving within the whole time range, we evaluate the standardized mean for each partial reconstruction, obtaining a set of N_s values, and, consequently, we calculate the corresponding standard deviations at each j. In this way, we associate an error to each standardized mean evaluated over the whole time range, corresponding to three times the standard deviation for the considered partial reconstruction.

For all the considered cases, the k value remains unchanged within the error band, indicating that the SMT is not significantly dependent on the choice of the time window length. This implies that the first k modes are able to reproduce the fluctuating contribution to the time series, while the remaining $m - k$ modes represent the larger timescale variations. This could be very useful for research into the framework of turbulent-like processes where a high-frequency component needs to be properly identified. Moreover, as shown in the next sections, the $k-$th mode characteristic timescale is also not dependent on the geomagnetic activity of the considered period, indicating that this separation between high- and low-frequency processes exists in both quiet and disturbed periods.

5.3 Magnetospheric and ground observations: EMD approach

5.3.1 Super Solar Quiet (SSQ) period: 10-12 October 2003

Figure 5.1 shows the observations of the geomagnetic field at AQU for the horizontal component of the vector along local magnetic meridian (H, left panel) and the eastward component (D, right panel) during the Super Solar Quiet period 10-12 October 2003.

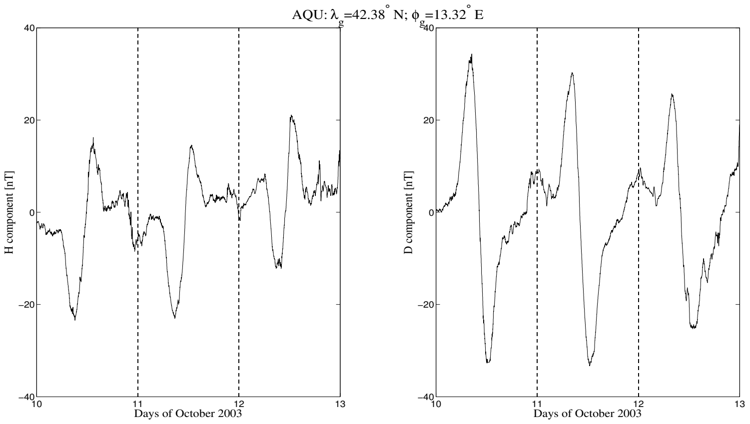

Figure 5.1: SSQ, 10-12 October, 2003: mid-latitude ground observations (AQU: $\lambda_g = 42.38°$ N and $\phi_g = 13.32°$ E) for the H (left panel) and D (right panel) components. The time resolution is 1 min.

During this period the K-index ranges between 0 and 1 (for more details, see http://roma2.rm.ingv.it/en/). Both H and D components show the typical mid-latitude solar quiet (Sq) daily variation (Chapman, 1929; Matsushita and Maeda, 1965; De Michelis et al., 2010). This current pattern is due to two different sources: the current systems flowing in the so-called ionospheric dynamo region and the induced telluric currents in the Earth's upper mantle. These currents generate additional magnetic field variations that are almost in phase with the main geomagnetic field variations. The dynamo currents flowing in the E region of the Earth's ionosphere, depending on the local properties of the tensor of conductivity, are driven by the global thermotidal wind systems, producing a pattern characterized by two couples of vortices. Two great vortices in the sunlit hemisphere, most intense because the ionospheric conductivity is larger, and the others two in the dark one. The sunlit pattern consists of counterclockwise current in the Northern Hemisphere and clockwise current in the Southern Hemisphere, when viewed from the Sun (Richmond et al., 1976; Hawary et al., 2012; Shinbori et al., 2014). In this case, by applying the EMD procedure we found a set of 13 modes and 11 modes for the H and D component, respectively (see Figure 5.2), while characteristic timescales are reported in Table 5.1. We note the existence of short-timescale modes which are characterized by a low mean amplitude ($j = 1 - 8$ for H, $j = 1 - 7$ for D), while modes with timescales greater than ~ 4 hours are characterized by higher mean amplitudes. In particular, $j = 12$ for H and $j = 10$ for D show the characteristic diurnal contribution in the geomagnetic components.

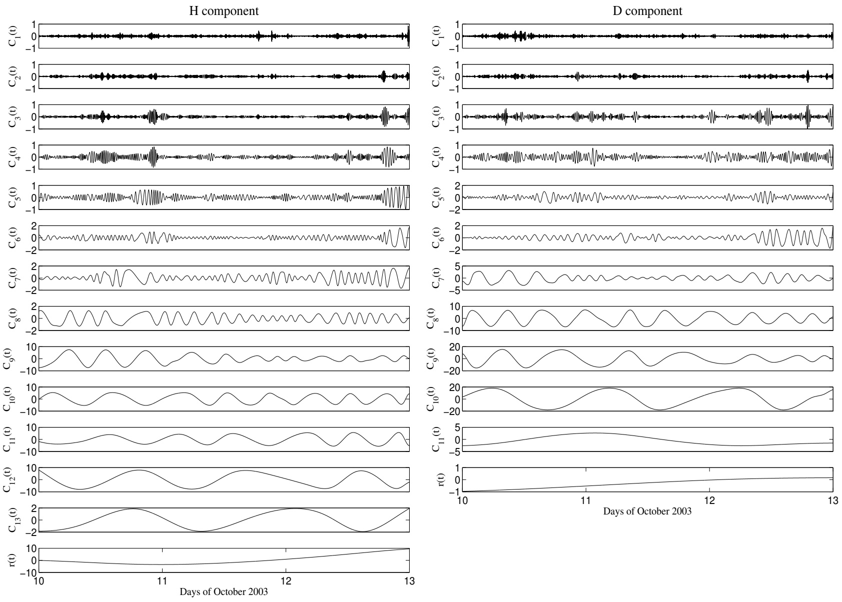

Figure 5.2: SSQ, 10-12 October, 2003: empirical modes extracted via EMD from AQU H component (left panels) and AQU D component (right panels). The modes and the residue are expressed in nT, and the time resolution is 1 min.

Then, we applied the SMT to the EMD decomposition of the H (left

	Super Solar Quiet Periods [hours]			
	T_H	T_D	T_{G10}	T_{G12}
$\delta H(D)/\delta Bz$	0.05 ± 0.01	0.05 ± 0.01	0.05 ± 0.02	0.05 ± 0.01
	0.10 ± 0.02	0.10 ± 0.02	0.16 ± 0.03	0.17 ± 0.02
	0.16 ± 0.02	0.19 ± 0.02	0.28 ± 0.05	0.29 ± 0.04
	0.28 ± 0.04	0.40 ± 0.03	0.46 ± 0.05	0.51 ± 0.06
	0.51 ± 0.04	0.73 ± 0.06	2.20 ± 0.4	1.90 ± 0.4
	0.92 ± 0.08	1.4 ± 0.2	3.80 ± 0.5	3.0 ± 0.5
	1.7 ± 0.2	3.3 ± 0.3		3.7 ± 0.6
	3.0 ± 0.4			
$H^*(D^*)$	6.1 ± 0.6	8.2 ± 0.6		
	8.7 ± 0.7	12 ± 1		
	12 ± 1	24 ± 1		
	24 ± 1			
$H_0(D_0)/Bz_0$	34 ± 2	31 ± 2	24 ± 1	24 ± 1
	-	-	30 ± 2	32 ± 3
			34 ± 3	-

Table 5.1: Mean periods of intrinsic modes during the Super Solar Quiet period (the "-" corresponds to the period of the residue $r(t)$ which cannot be evaluated).

panel) and D (right panel) components (Figure 5.3).

From Figure 5.3 we note that the empirical modes can be divided into 3 different sets: modes $j = 1 - 8$ for H and $j = 1 - 7$ for D are identified as *short-timescale* reconstructions whose time scale is $\leq$4 hours and for which the SM of the reconstructions is close to zero; modes $j = 9 - 12$ for H and $j = 8 - 10$ for D are identified as *intermediate-timescale* reconstructions with a timescale in the range $6 - 24$ hours. Mode $j = 13$ and the residue for H and mode $j = 10$ and residue for D are identified as *large-timescale* reconstructions for which the SM of the reconstructions departs significantly from zero. This grouping can be made by observing that, for the intermediate timescales, a significant non-null value is found when $j = 9$ for H ($j = 8$ for D), while when $j = 12$ ($j = 10$ for D) a SM$\sim$0 is again obtained. According to the SMT results (Figure 5.3), AQU data split into 3 different contributions:

$$\begin{aligned} H(t) &= \delta H(t) + H^*(t) + H_0(t), \\ D(t) &= \delta D(t) + D^*(t) + D_0(t). \end{aligned}$$

Figure 5.4 shows the EMD reconstructions for the H (left panels) and D (right panels) components.

$\delta H(t)$ and $\delta D(t)$ (Figure 5.4 upper panels) represent short-timescale reconstructions, $H^*(t)$ and $D^*(t)$ (Figure 5.4 middle panels) are intermediate-

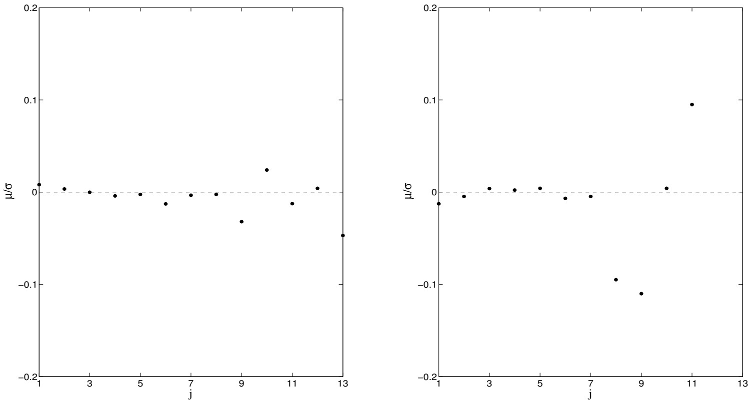

Figure 5.3: SSQ, 10-12 October, 2003: SMT applied to the EMD reconstruction of the ground observations for the H (left panel) and D (right panel) components. The x-axis values correspond to the last mode involved into the partial sums (see Eq. (5.2)).

timescale reconstructions, $H_0(t)$ and $D_0(t)$ (Figure 5.4 lower panels) represent the large-timescale reconstructions.

In order to detect if the same timescale separation is found in magnetosphere, we analyzed magnetospheric observations at geosynchronous orbit by applying the same techniques. Figure 5.5 shows the time series obtained from GOES10 (left panel) and GOES12 (right panel) observations with corresponding color scale related to the Magnetic Local Time (MLT) of the spacecraft. Both GOES spacecraft show the characteristic orbital variation (see color scale related to the MLT).

The EMD procedure produce a set of 9 modes for both GOES spacecraft, as shown in Figure 5.6. We note that the modes $j = 7$ for GOES10 and $j = 8$ for GOES12 reproduce the diurnal orbital variation observed by the spacecraft.

Moreover, the SMT results (see Figure 5.7) reveal the existence of two timescales of variability, characterized by different mean amplitudes.

For these reasons, both GOES10 (left panels) and GOES12 (right panels), are split into only two different sets of modes: the short-timescale reconstructions, characterized by a nearly zero mean contributions to the signal, and the large-timescale reconstructions, characterized by a non-zero mean contribution to the signal.

So, according to the SMT results, GOES10 and GOES12 EMD results are split into 2 different contributions (see Figure 5.8):

$$Bz(t) = \delta Bz(t) + Bz_0(t), \tag{5.3}$$

where $\delta Bz(t)$ represents short-timescale reconstructions (GOES10: $j = 1 - 6$

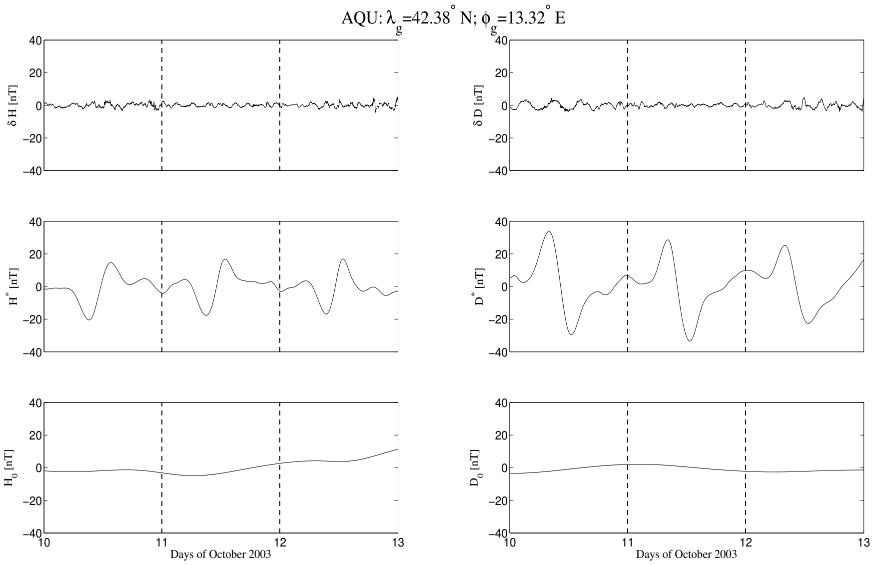

Figure 5.4: SSQ, 10-12 October, 2003: EMD reconstruction for the H (left panels) and D (right panels) components at mid-latitude ground station (AQU: $\lambda_g = 42.38°$ N and $\phi_g = 13.32°$ E). The time resolution is 1 min.

modes; GOES12: $j = 1-7$ modes) and $Bz_0(t)$ represents the large-timescale reconstructions (GOES10: $j = 7-9$ modes and $r(t)$; GOES12: $j = 8-9$ modes and $r(t)$).

5.3.2 Storm Time (ST) event: 28 October-01 November 2003

The same approach is applied to the Halloween Super Storm (28 October-01 November 2003).

In Figure 5.9 we show the observations at AQU geomagnetic observatory for the North-South (H, left panel) and the East-West (D, right panel) components during this time interval.

At the end of October 2003 two consecutive Coronal Mass Ejections (CMEs) impacted the Earth's magnetosphere (Balasis et al., 2012; Mannucci et al., 2014; Balasis et al., 2015). These produced the famous Halloween super storm, 29-31 October 2003, which has received considerable interest and analysis from both ground and space instrumentation, since it offers a great opportunity of understanding the response of the magnetosphere-ionosphere system to strong and continuous forcing. From Figure 5.9 we note that the H component shows a first storm peak (~ -500 nT at 06:58 UT of the 29 October) with an associated short recovery phase, a second storm peak (~ -250 nT at 20:13 UT of the 29 October) with an irregular recovery phase and a third peak (~ -280 nT at 22:53 UT of 30 October)

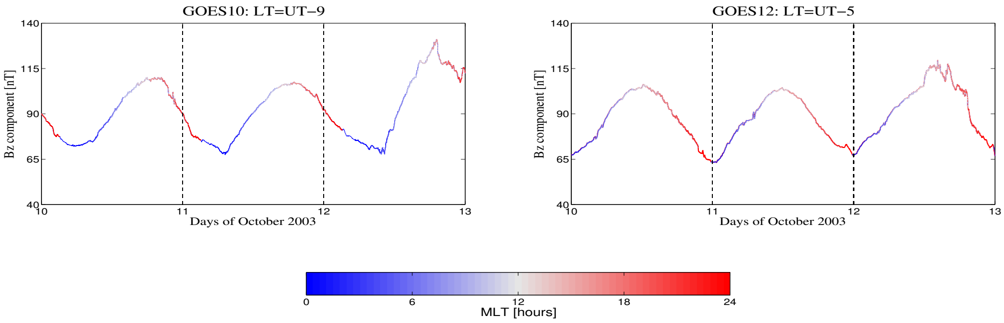

Figure 5.5: SSQ 10-12 October, 2003: magnetospheric observations at geosynchronous orbit for GOES10 (LT=UT-9; left panel) and GOES12 (LT=UT-5; right panel) spacecrafts. The time resolution is 1 min.

associated to a longer recovery phase.

From the EMD procedure we found a set of 15 modes and 14 modes for the H and D components, respectively (see Figure 5.10). We note an enhancement of the amplitude of short-timescale modes due to the arrival of the CMEs, together with the characteristic diurnal contribution due to the Sq ($j = 14$ for H, $j = 12$ for D).

We also applied the SMT to empirical modes as shown in Figure 5.11 for H (left panel) and D (right panel) components.

Also in this case, 3 different sets of modes are recovered which we reconstructed as shown in Figure 5.12 (H (left panels) and D (right panels) components).

These reconstructions are related to timescales $\leq$ 4 hours ($\delta H(t)$ and $\delta D(t)$, Figure 5.12 upper panels), timescales in the range $6-24$ hours ($H^*(t)$ and $D^*(t)$, Figure 5.12 middle panels) and to timescales greater than 24 hours ($H_0(t)$ and $D_0(t)$, Figure 5.12 lower panels).

As for the SSQ case, we also analyzed magnetospheric observations during the ST period which are shown in Figure 5.13 by using a color scale for the MLT. In this case, a superposition of current systems can be seen at noon, related to the magnetopause current, and at midnight, due to tail current contribution.

In this case, we also note the enhancements of amplitudes due to the impact of the CMEs on short timescales and their effects on the orbital variation (see Figure 5.14, $j = 12-13$ for GOES10, $j = 11-12$ for GOES12).

At geosynchronous orbit (Figure 5.15), the SMT analysis shows for both GOES10 (left panels) and GOES12 (right panels) only two different sets of modes.

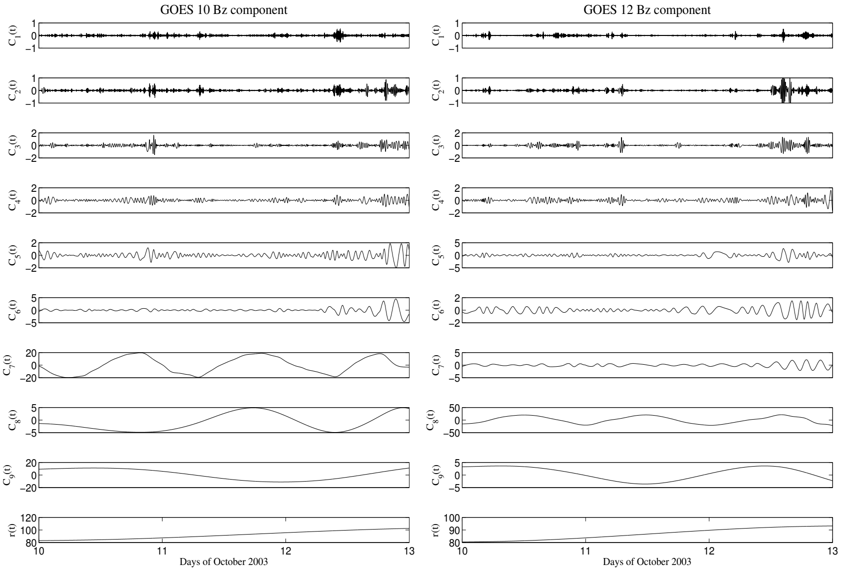

Figure 5.6: SSQ, 10-12 October, 2003: empirical modes extracted via EMD from GOES10 (left panels) and GOES12 (right panels) Bz components. The modes and the residues are expressed in nT, with a time resolution of 1 min.

As a consequence, GOES10 and GOES12 are split into 2 different contributions: $\delta Bz(t)$ (GOES10: $j = 1-10$ modes; GOES12: $j = 1-9$ modes) and $Bz_0(t)$ (GOES10: $j = 11 - 15$ modes and $r(t)$; GOES12: $j = 10 - 14$ modes and $r(t)$). Figure 5.16 shows the results of the EMD reconstructions for GOES10 (left panels) and GOES12 (right panels).

As expected, $\delta Bz(t)$ at both GOES spacecraft orbits (Figure 5.16 upper panels) increases during the main phase of the geomagnetic storm as a consequence of the magnetospheric response to the CME arrival and comes back close to its initial values at the end of the storm time. Concerning the GOES baseline $Bz_0(t)$ (Figure 5.16 lower panels), it is evident that before/after the storm is characterized by the typical diurnal variation, while during the storm is characterized by a huge decrease due to the increase of the intensities of the magnetospheric currents (the main phase of the geomagnetic storm). Moreover, its behaviour is influenced by the ring and magnetopause currents activity at noon, while at midnight the superimposed effect of the ring and tail currents can be seen, with a greater contribution related to the tail current activity.

A summary of the percentage of each contribution to the total signal for both SSQ and ST periods is reported in Table 5.3.

During the SSQ period the ground signals (H and D components) variations are principally due to $H^*(t)$ and $D^*(t)$ ($\sim 95\%$), while for geostation-

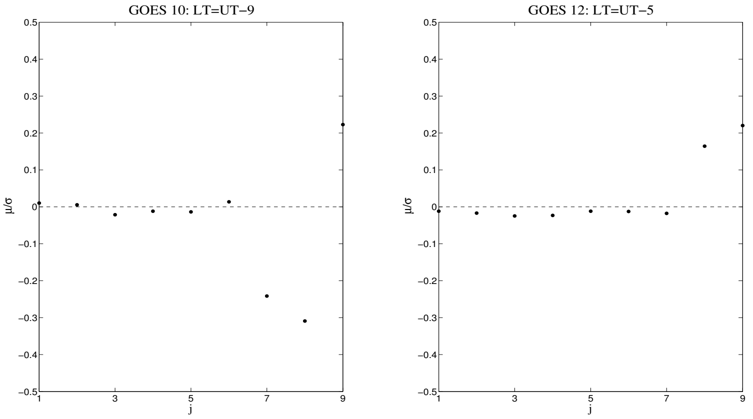

Figure 5.7: SSQ, 10-12 October, 2003: SMT applied to the EMD reconstruction of the magnetospheric observations for GOES10 (left panel) and GOES12 (right panel) Bz components. The x-axis values correspond to the last mode involved into the partial sums (see Eq. (5.2)).

ary observations they are mostly reproduced by using the baseline $Bz_0(t)$ ($\sim$ 99%). Conversely, during the ST period, the short-timescale reconstructions, $\delta H(t)$ and $\delta D(t)$ for ground measurements and $\delta Bz(t)$ for magnetospheric observations, contribute more significantly to the signals ($\sim$ 30%).

5.4 Results and Discussion

The EMD and SMT methods applied to satellite and ground-based observations of the Earth's magnetic field during both quiet and disturbed period allow to detect a timescale separation between the baseline and the time variations of the magnetospheric and ground magnetic field. Why in ground-based observations we detect three different contributions, while only two are obtained from the analysis of geostationary measurements? The answer to this question can be obtained by observing that the main difference between ground-based and geostationary observations is the ionosphere. Indeed, the effects of the ionospheric currents produce local magnetic fields which induce variations in the geomagnetic field, without any effects on geostationary measurements due to the different location. Indeed, the ionosphere is a layer of the atmosphere extending from 60 to 1000 km, while geostationary orbit is located at $\sim$ 35000 km.

5.4.1 SSQ contributions

Three different contributions are found in groud-based observations, related to the short-timescale contribution, associated with the internal dynamics

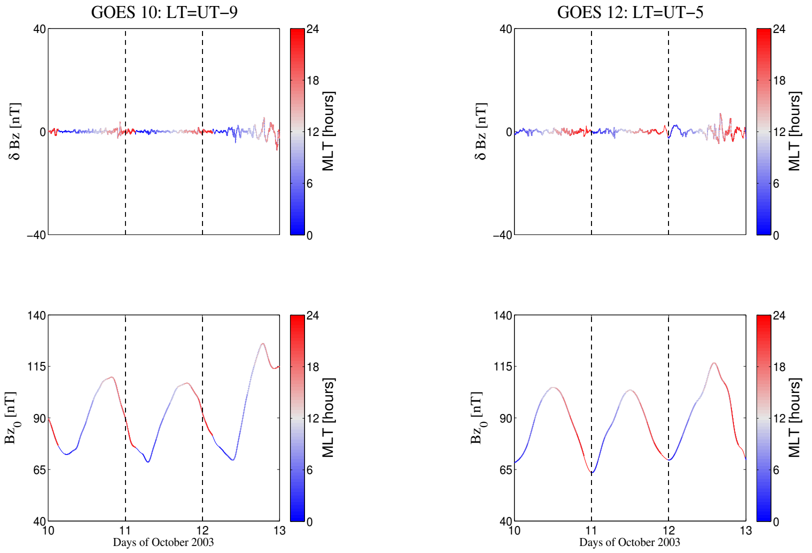

Figure 5.8: SSQ, 10-12 October, 2003: EMD reconstruction for GOES10 (left panels) and GOES12 (right panels) geosynchronous observations. The time resolution is 1 min.

of the magnetosphere, the intermediate-timescale contribution, related to ionospheric processes, and the large-timescale contribution, related to the local time-dependent geomagnetic field. The association of intermediate-timescale ($H^*(t)$ and $D^*(t)$) contributions with ionospheric physical processes has been made by looking at their characteristic timescales (Table 5.1) (Fytterer et al., 2013, and references therein) and taking into account that the time behaviour of $H^*(t)$ and $D^*(t)$ is in agreement with the solar quiet daily variation observed in October at L'Aquila, as determined by De Michelis et al. (2010). So, our finding seems to suggest that the $H^*(t)$ and the $D^*(t)$ fields are of ionospheric origin.

This hypothesis is also confirmed by analyzing the magnetospheric observations from which only two contributions are detected. It can be easily seen (Figure 5.8 lower panels) that $Bz_0(t)$ reproduces the diurnal orbital magnetospheric field variation due to the geosynchronous orbit (Rufenach et al., 1992), while $\delta Bz(t)$ (Figure 5.8 upper panels) is related to its fluctuations (one order of magnitude lower than $Bz_0(t)$). Interestingly, since $Bz_0(t)$ by definition represents the baseline field observed by GOES and it is completely free of any magnetospheric field fluctuations, it can be used for the calibration of the IGRF/DGRF field. In fact, by a direct comparison between IGRF model, such as the Geomag 7.0C (Thebault et al., 2015), and $Bz_0(t)$, the IGRF degree coefficients can be tuned and better evaluated.

We did not found any evidence of timescales into the range $6-24$ hours,

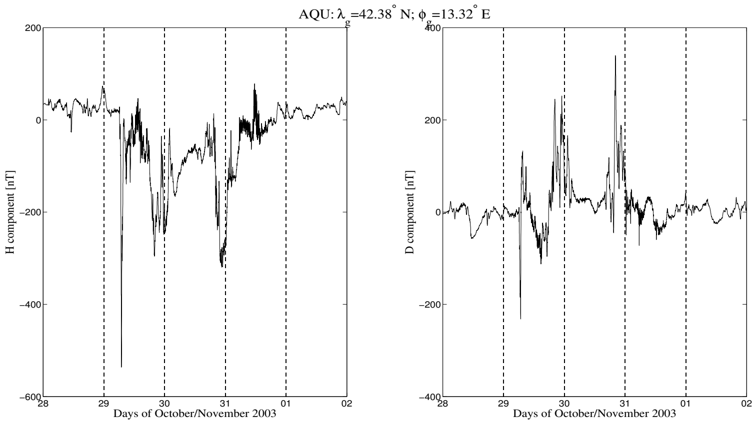

Figure 5.9: Halloween super storm, 28 October-01 November, 2003: mid latitude ground observations (AQU: $\lambda_g = 42.38°$ N and $\phi_g = 13.32°$ E) for the H (left panel) and D (right panel) components. The time resolution is 1 min.

suggesting that this lack is due to ionospheric processes operating on these timescales. Since the only difference between ground and magnetospheric data during a SSQ period is the ionospheric contribution, we can reasonably assert that $H^*(t)$ and $D^*(t)$ are of ionospheric origin. Moreover, the characteristic periods of the modes involved in the $\delta H(t)$ and $\delta D(t)$ reconstructions are consistent with the relative characteristic periods involved in the $\delta Bz(t)$ reconstruction at both GOES spacecraft (Table 5.1). This indicates that they might be of magnetospheric origin.

5.4.2 ST contributions

Similar results are found when the EMD and SMT methods are applied on both H and D components for the ST case. Both $\delta H(t)$ and $\delta D(t)$ (Figure 5.12 upper panels) show two increases of the fluctuation amplitudes, as a consequence of the magnetospheric response to the two consecutive CME impacts on the Earth's magnetosphere (Balasis et al., 2012; Mannucci et al., 2014). $H_0(t)$ (Figure 5.12 lower left panel) can be used as a representation of the large-timescale geomagnetic disturbance associated with the Halloween super storm (Balasis et al., 2012), characterized by three storm peaks and the relative recovery phases, while $D_0(t)$ (Figure 5.12 lower right panel) shows only a slight modulation around zero. Furthermore, $H^*(t)$ and $D^*(t)$ (Figure 5.12 middle panels), due to their ionospheric origin, show variations in the range $6 - 24$ hours, increasing in amplitude during the storm time, characterized by amplitude peaks of ~ -250 nT and ~ -200 nT, respectively, during the first main phase. Moreover, $D^*(t)$ shows two huge

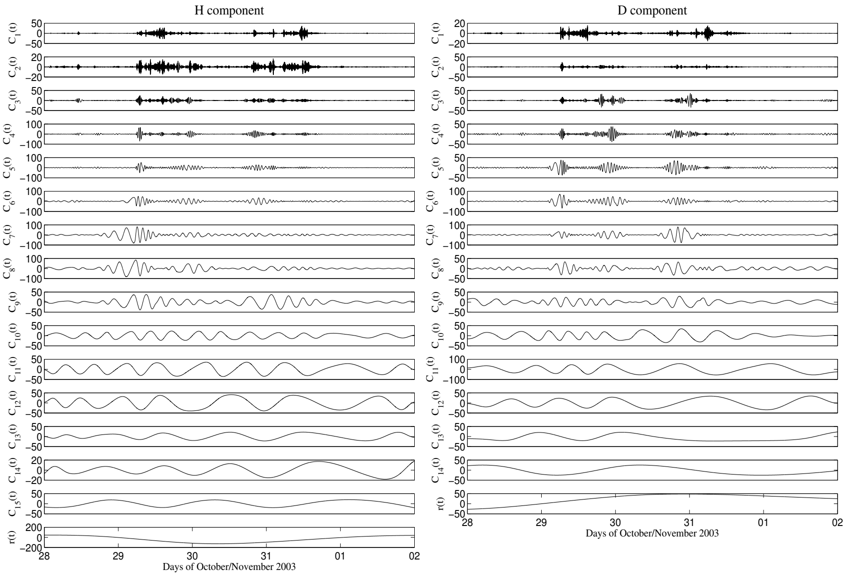

Figure 5.10: Halloween super storm, 28 October-01 November, 2003: empirical modes extracted via EMD from H (left panels) and D (right panels) components recorded at AQU observatory. The modes and the residue are expressed in nT, and the time resolution is 1 min.

increases ($\sim$ 220 nT and $\sim$ 270 nT) during the second and the third main phase of the storm. Since it can be used as a measure of the Sq ionospheric current system we suggest that the observed enhancements are related to the magnetic field variations induced on ground by this current system.

5.5 Summary

The main results of this study can be summarized as reported below.

5.5.1 Magnetosphere

Both in the quiet (Figure 5.5) and storm time periods (Figure 5.13), the SMT applied to the EMD decomposition shows 2 different contributions:

1. short-timescale ($\delta\mathbf{Bz(t)}$): it gives a representation of the magnetospheric field variations reflecting the dynamic of the ring current system. Indeed, in both periods GOES spacecraft orbit into the ring current (De Michelis et al., 1999).

2. baseline ($\mathbf{Bz_0(t)}$): it describes the magnetospheric field observed by the spacecraft during its diurnal orbit (Figure 5.8 lower panels). Its

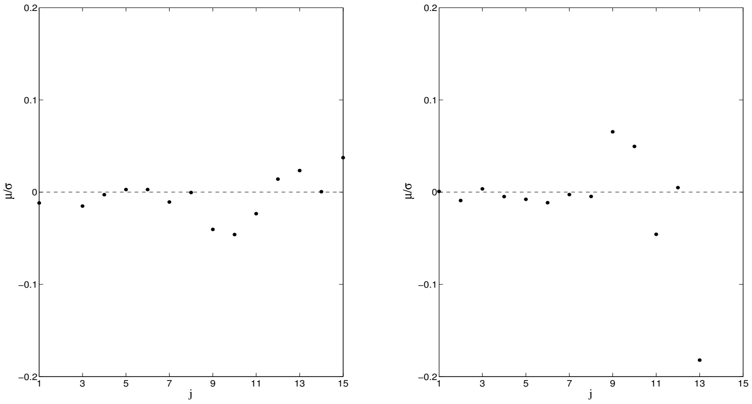

Figure 5.11: Halloween super storm, 28 October-01 November, 2003: SMT applied to the EMD reconstruction of the ground observations for the H (left panel) and D (right panel) components. The x-axis values correspond to the last mode involved into the partial sums (see Eq. (5.2)).

mean periodicity is about 24 hours and its average value is $\sim$ 70 nT at 6.6 R_E (http://www.ngdc.noaa.gov/IAGA/vmod/igrfhw.html), during both SSQ and pre-storm period. This suggest that, during SSQ conditions, it could be useful to calibration of the IGRF model in the magnetosphere, while its time evolution can be used as a measure of the local magnetospheric current activity, especially during storm time periods when fluctuations increase and the evaluation of an average magnetic field is not straightforward (Figure 5.16 lower panels).

5.5.2 Ground

Both in the SSQ (Figure 5.1) and in the storm period (Figure 5.9), the SMT applied to the EMD decomposition shows 3 different contributions:

1. short-timescale ($\delta\mathbf{H}(\mathbf{t})$ and $\delta\mathbf{D}(\mathbf{t})$): they represent the geomagnetic field variations due to the magnetospheric field fluctuations. This hypothesis is confirmed by similar temporal scales between $\delta H(t)$ and $\delta Bz(t)$ (Table 5.1 and Table 5.2).

2. intermediate-timescale ($\mathbf{H}^*(\mathbf{t})$ and $\mathbf{D}^*(\mathbf{t})$): they represent the geomagnetic field variations of ionospheric origin, as confirmed by their lack in the magnetospheric EMD reconstructions and by their characteristic timescales (Table 5.1 and Table 5.2), in the range $6-24$ hours.

3. baseline ($\mathbf{H_0}(\mathbf{t})$ and $\mathbf{D_0}(\mathbf{t})$): they represent the local average deviation of the geomagnetic field. During the SSQ (Figure 5.4 lower panels),

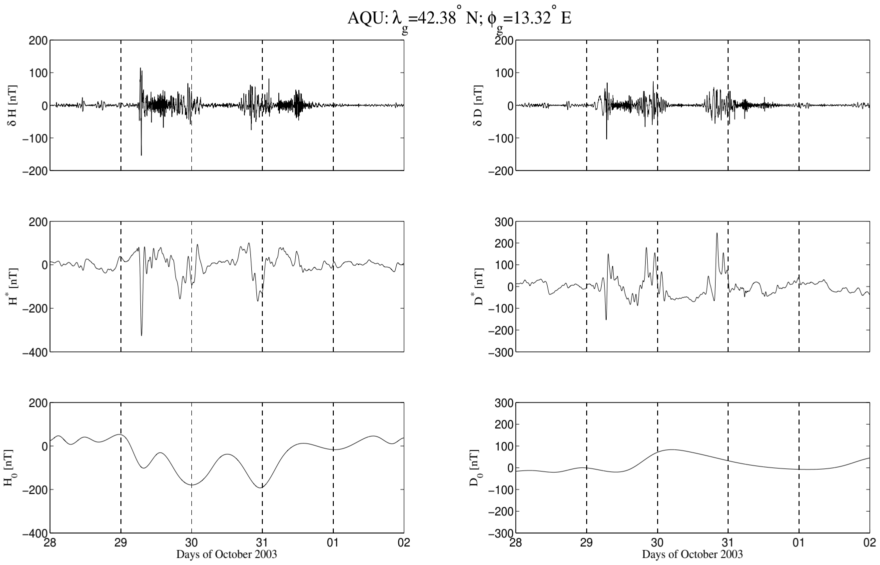

Figure 5.12: Halloween super storm, 28 October-01 November, 2003: EMD reconstruction for the H (left panels) and D (right panels) components at mid-latitude ground station (AQU: $\lambda_g = 42.38°$ N and $\phi_g = 13.32°$ E). The time resolution is 1 min.

their mean value is set around zero, as a consequence of the lack of the baseline value from AQU ground measurements (we used the relative measurements of the geomagnetic field variations recorded by a triaxial fluxgate magnetometer). On the other hand, during the storm time period (Figure 5.12 lower panels), $H_0(t)$ shows the typical behaviour of a geomagnetic storm, characterized by huge decreases (main phases) followed by a smooth increase of the magnetic field (recovery phases), similar to the characteristic behavior of the Sym-H index during the different phases of the storm.

5.6 Conclusions

In this study, we provide a method to easily discriminate between a time-dependent large-timescale magnetic field and its time variations in both magnetospheric and ground observations.

In magnetosphere, we associated the large-timescale variation (baseline) to the magnetic field observed by the spacecraft during its diurnal orbit (Rufenach et al., 1992). During a SSQ period, this baseline could be very useful to efficiently calibrate the IGRF model. On the other hand, the short-timescale variations could be related to the magnetospheric field fluctuations

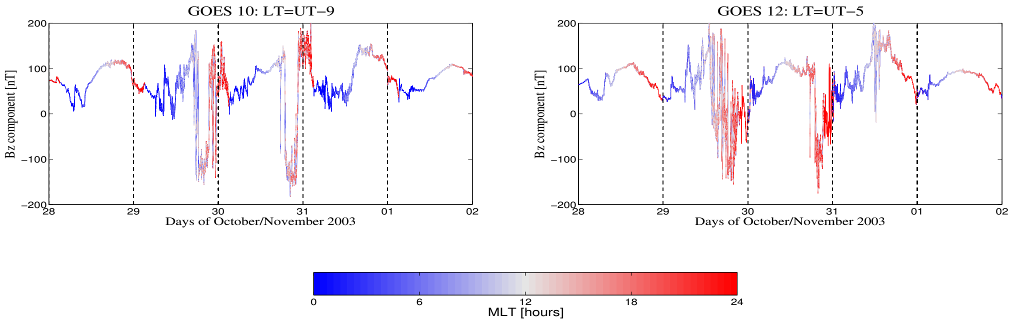

Figure 5.13: Halloween super storm, 28 October-01 November, 2003: magnetospheric observations of the Bz component at geosynchronous orbit for GOES10 (LT=UT-9; left panel) and GOES12 (LT=UT-5; right panel) spacecrafts. The time resolution is 1 min.

that could be associated to the symmetric and partial ring current dynamics (De Michelis et al., 1999).

At ground, the short-timescale reconstructions can be related to the variations of the geomagnetic field driven by the different magnetospheric current system dynamics, as confirmed by the similar timescales between $\delta H(t)$ and $\delta Bz(t)$ (Table 5.1 and Table 5.2). Conversely, the intermediate-timescale variations are associated to the ionospheric origin contribution, as confirmed by their lack in the magnetospheric reconstructions and looking at their characteristic time periods in the range $6-24$ hours. Finally, the large-timescale variations are related to the local average of the geomagnetic field, showing a mean value set around zero, during SSQ period, while during active magnetic conditions, the baseline ($H_0(t)$) presents the typical feature observed in the Sym-H time-behavior, characterized by sudden impulse, main phase and recovery one. The main difference between $H_0(t)$ and Sym-H is related to the different large-timescale effects that they measure. Indeed, while Sym-H (or Dst) are related to the global effect of the ring current variations, $H_0(t)$ evaluate the local intensity of a geomagnetic storm on the ground, without any calculation and subtraction of average value for its evaluation (including the Sq field), as it is free from any magnetospheric fluctuations and ionospheric origin contributions. Since it is easily evaluated at any ground and magnetospheric observatory, it can be used as a local geomagnetic disturbance index.

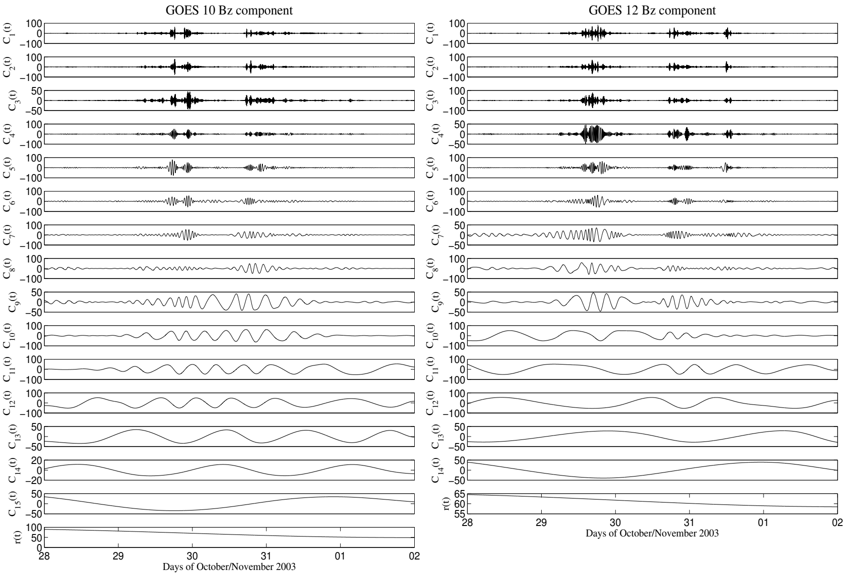

Figure 5.14: Halloween super storm, 28 October-01 November, 2003: empirical modes extracted via EMD from GOES10 (left panels) and GOES12 (right panels) Bz components. The modes and the residues are expressed in nT, and the time resolution is 1 min.

Data availability

The GOES magnetic field data were provided by H. Singer (National Oceanic and Atmospheric Administration Space Environment Center, Asheville, N.C.) through the NASA's cdaweb site (cdaweb.gsfc.nasa.gov). The results presented here rely on public data collected at AQU magnetic observatories and available by INTERMAGNET (www.intermagnet.org).

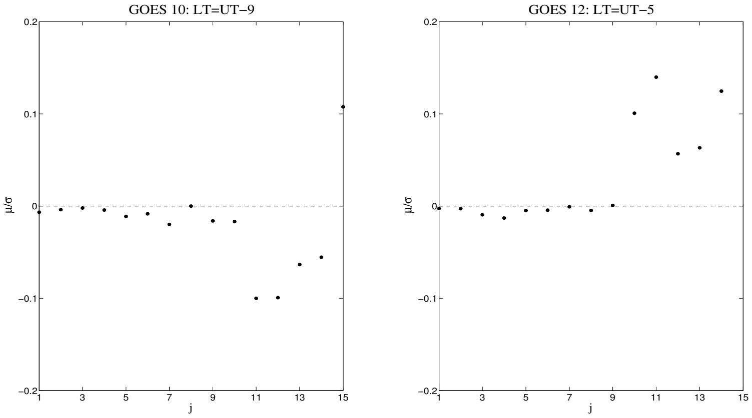

Figure 5.15: Halloween super storm, 28 October-01 November, 2003: SMT applied to the EMD reconstruction of the magnetospheric observations for GOES10 (left panel) and GOES12 (right panel) Bz component. The x-axis values correspond to the last mode involved into the partial sums (see Eq. (5.2)).

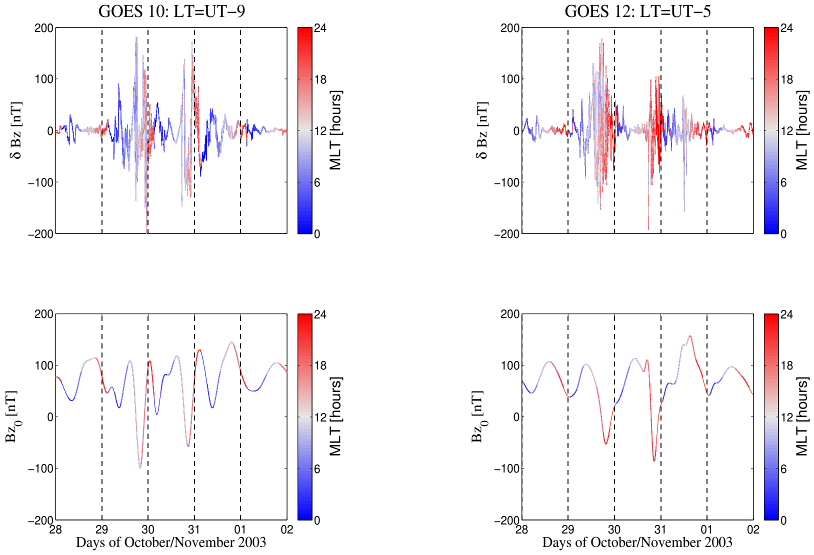

Figure 5.16: Halloween super storm, 28 October-01 November, 2003: EMD reconstruction for GOES10 (left panels) and GOES12 (right panels) geosynchronous observations. The time resolution is 1 min.

	Halloween super storm Periods [hours]			
	T_H	T_D	T_{G10}	T_{G12}
$\delta H(D)/\delta Bz$	0.06 ± 0.01	0.06 ± 0.01	0.06 ± 0.02	0.06 ± 0.01
	0.12 ± 0.03	0.12 ± 0.02	0.11 ± 0.03	0.11 ± 0.02
	0.23 ± 0.04	0.22 ± 0.02	0.19 ± 0.03	0.29 ± 0.03
	0.41 ± 0.07	0.45 ± 0.03	0.32 ± 0.05	0.49 ± 0.04
	0.75 ± 0.08	0.71 ± 0.06	0.57 ± 0.05	0.87 ± 0.05
	1.3 ± 0.2	1.1 ± 0.2	0.96 ± 0.08	1.3 ± 0.2
	2.4 ± 0.2	1.8 ± 0.3	1.4 ± 0.2	2.2 ± 0.3
	3.4 ± 0.5	2.8 ± 0.5	2.3 ± 0.3	2.9 ± 0.5
			3.0 ± 0.4	3.7 ± 0.6
			3.9 ± 0.4	
$H^*(D^*)$	5.6 ± 0.6	5.8 ± 0.6		
	8.6 ± 0.7	12 ± 1		
	12 ± 1	16 ± 1		
	24 ± 1	24 ± 1		
$H_0(D_0)/Bz_0$	30 ± 2	43 ± 4	18 ± 1	20 ± 1
	38 ± 3	-	24 ± 1	24 ± 1
	48 ± 6		34 ± 3	33 ± 2
	-		41 ± 3	38 ± 3
			48 ± 4	47 ± 5
			-	-

Table 5.2: Mean periods of intrinsic modes during the Halloween storm (the ”-” corresponds to the period of the residue $r(t)$ which cannot be evaluated).

Percentage of each contribution to the total signal (%)		
Contribution	SSQ	ST
δBz	1	28
Bz_0	99	72
δH	2	33
H^*	95	62
H_0	3	5
δD	1	28
D^*	97	63
D_0	2	9

Table 5.3: Percentage of each contribution to the total signal (%) during both SSQ and ST periods.

Chapter 6

Short-term forecast of solar energetic particle events[1]

6.1 Introduction

Solar energetic particle (SEP) events are defined as those that meet or exceed the Space Weather Prediction Center (SWPC) threshold of 10 particles $\mathrm{cm}^{-2}\ \mathrm{s}^{-1}\ \mathrm{sr}^{-1}$ at energies > 10 MeV and represent a hazard in the interplanetary space and near-Earth environment. They have similar effects on the Earth's environment as geomagnetic storms, disrupting space operations and radio communications, damaging satellite electronics, and posing a health hazard to astronauts, as well as airline passengers and crew on polar flights. In the last decades, several short-term forecasting techniques have been studied intensively to mitigate SEP event impacts. It has been shown that SEP events occur in association with solar flares and coronal mass ejections (CMEs), believed to be responsible for particle acceleration in both impulsive and gradual events (e.g., Reames, 1999).

Several SEP forecasting models have been proposed (e.g., Storini et al., 2008; Laurenza et al., 2009, and references therein), based on flare- and CME-related phenomena, such as soft X-ray (SXR) and low-frequency type III and type II radio bursts. Chronologically, one of the first SEP prediction model, the Proton Prediction System (PPS), developed by Smart and Shea (1989), predicts the occurrence of SEP events based only on the properties of solar flares, without any evaluation of the metric type II/IV radio burst occurrence. Kahler et al. (2007) validated the PPS by using 78 $\geq$ M5 X-ray flares observed during the period 1997-2001 which yields approximately equal numbers of correct predictions, false predictions, and missed SEP events.

In 1999, Balch (1999) proposed a new forecasting model, named Protons

---

[1] The work presented in this chapter is included in the paper Alberti, Laurenza, Cliver, Storini, Consolini and Lepreti (2017*b*).

and operated at NOAA[2] SWPC, relying on the time-integrated SXR flux, the SXR peak flux, the occurrence or non-occurrence of metric radio type II and type IV bursts, and the location of the associated flare. The evaluation of this model was based on proton events occurred between 1986 and 2004 (Balch, 2008), giving a fair probability of detection (POD = 57%), but a high false alarm rate (FAR = 55%). More recently, Kahler and Ling (2015) derived an algorithm for a dynamic SEP event forecast to improve the Protons model.

To increase the SEP event prediction accuracy and warning time, Laurenza et al. (2009) developed the ESPERTA model (acronym of Empirical model for Solar Proton Events Real Time Alert), based on a statistical approach, by using logistic regression analysis, of the flare location, 1-8 $\AA$ SXR and $\sim$ 1 MHz Type III fluences, to provide a warning within 10 minutes following the SXR peak for $\geq$ M2 flares (see also Storini et al., 2008; Signoretti et al., 2011). One of the main points of a good SEP forecasting tool is to consider parameters that are available close to flare maximum and that should guarantee a reasonable warning time. This timing requirement could exclude the use of CME-based parameters (e.g., speed) and CME-related phenomena (e.g., type II occurrence). Among the forecasting techniques satisfying this timing requirement, the method developed by Posner (2007) exploits the short transit time of relativistic electrons to forecast SEP events with a lead time of up to 1 hour. Similarly, ESPERTA provided a median warning time of $\sim$ 55 min, by using 19 successfully predicted events for which SEP event onset times were provided by Posner (2007), before the occurrence of a SEP event, along with resasonable verification measures (POD = 63%, FAR = 42%), for the 1995-2005 interval.

In 2011, the UMASEP system (Núñez, 2011) analyzed correlations between a sequence of first derivatives of flare SXR flux and of at least one differential proton flux in the energy range 9-500 MeV, to give a warning that the >10 MeV integral channel will reach the SWPC threshold following SXR bursts of class > C7. By considering events registered in solar cycles 22 and 23 and listed by the NOAA/SWPC SEP list, UMASEP verification measures are: POD=81% (134/166) for all well- and poorly-connected events and FAR = 34% (69/203).

Winter and Ledbetter (2015), by using logistic regression and principal component analysis on decametric-hectometric (1-14 MHz) type III radio bursts that accompanied DH type II bursts, obtained a prediction method with a FAR = 22% and a POD = 62% for the period 2010-2013.

Recently, Dierckxsens et al. (2015), by applying a statistical analysis on the relationship between SEP events and properties of $\geq$ M1 SXR flares and CMEs, determined the probability for the occurrence of a SEP event near Earth during Solar Cycle 23. However, this model will be used as input for

---

[2] National Oceanic and Atmospheric Administration

the COMESEP forecast technique and actually has not been validated in term of verification measures (POD, FAR).

In the framework of the PROTEAS project of the National Observatory of Athens (Kontogiannis et al., 2016), the FORSPEF forecasting tool has been developed (Papaioannou et al., 2015). This tool uses an homogeneous SEP database of the re-calibrated GOES proton data within the energy range 6-243 MeV, covering the period 1984-2003, as well as the SEP associated solar sources in terms of flare (magnitude, location) and CME (width, velocity) characteristics. It provides the probability of SEP occurrence based on information of solar flares with known features, with the maximum probability of SEP occurrence obtained by overlapping the probabilities of the occurrence of a solar flare occurrence (based on the magnetic field observed in its associated active region) with the probabilities derived from the FORSPEF database. In terms of POD and FAR, the FORSPEF scheme has not been validated.

Furthermore, as shown by Huang et al. (2012), a forecasting ensemble prediction model involving the complementary information of solar flares and CMEs can have better performance than each prediction model which considers them separately.

In this study, the performance of ESPERTA is evaluated on a newly compiled database covering the time period 2006-2014, encompassing the minimum between solar cycles 23 and 24 and the rise to the maximum of cycle 24. This time interval is characterized by unusually low solar and geomagnetic activity relative to the preceding 100 years (see Diego et al., 2010; Otkidychev and Skorbezh, 2014; Singh and Tonk, 2014; Prasanna Subramanian and Shanmugaraju, 2016, among others). For this interval, we calculated the basic parameters used by ESPERTA and compared them to those for the 1995-2005 period used to develop the original model. Then, the forecast verification measures for the 2006-2014 interval were computed to test the robustness of model.

6.2 Database

For our analysis, we use 5-min proton data retrieved from both Geostationary Operational Environmental Satellite (GOES) 13 and 15 spacecraft during their operational time, choosing the data from the spacecraft with the higher measured proton intensity. Moreover, we use the NOAA SEP event list as reference, although we tried to correct some of its limitations including: i) in many cases the SEP event originated from behind the solar limb and the associated flare emissions are partially occulted; ii) if the SEP intensity lies above 10 pfu[3], then any new SEP event increases are not included in the list; iii) some SEP events are included only because

---

[3] 1 pfu = 1 particle cm^{-2} s^{-1} sr^{-1}

of short SEP increases associated with the passages of shocks at 1 AU 1-3 days after the flare (there were no such events from 2006-2014); and iv) the flare associations are sometimes not obvious, and errors or questionable flare associations are included in the list.

Table 6.1 is a listing of all SEP events during the period 2006-2014 for which the $>$ 10 MeV proton flux was $\geq$ 10 pfu for three consecutive 5-min intervals.

As in Laurenza et al. (2009), each identified SEP event is associated with a visible disk flare or a behind-the-limb eruption. Proton enhancements due to different solar flares are separated and attributed to a single solar event if they increase above the $\geq$ 10 pfu threshold or by a factor of two above it. Generally, the largest SXR flare near the SEP event onset time is identified as the SEP source by considering time coincidence with fast CMEs and type II and IV bursts. In this way, we identified a total of 36 SEP events which we divided into 3 groups, according to the SXR importance of the associated flare:

1. 23 SEP events associated with $\geq$ M2 flares
2. 9 SEP events associated with $<$ M2 flares
3. 4 farside SEP events for which no flare data are available

We also made a comparison with lists proposed by Richardson (2014) and Gopalswamy et al. (2014) to verify the consistency of our database, finding that both the identified SEP events and flare associations are consistent with their lists.

Table 6.1, reporting the 2006-2014 SEP event list (36 events), is organized as follows: event number (column 1), flare date (column 2), peak time of the SXR burst (column 3), SXR burst class[4] (column 4), heliographic coordinates of the associated flare (column 5), time-integrated SXR intensity (column 6), SXR integration flag[5] (column 7), time-integrated $\sim$ 1 MHz Wind/Waves type III intensity[6] (column 8), exact radio frequency used (column 9), warning time for 10 pfu threshold crossing[7] (column 10), SEP Forecast Result (column 11), where “Hit”, ”Miss”, “MISS” and “blank” refer to SEP events correctly predicted, SEP events with associated frontside or backside $\geq$ M2 SXR flares that were not predicted, SEP events with associated frontside $<$ M2 SXR flares (no prediction made), farside SEP events with associated $<$ M2 SXR flares, respectively.

---

[4] in terms of the GOES 1-8 Å peak SXR intensity, defined as follows: classes C1-9, M1-9, and X1-9 correspond to flare peak intensities of 1-9 $\times$ 10^{-6}, 1-9 $\times$ 10^{-5}, and 1-9 $\times$ 10^{-4}, respectively.

[5] see section 6.2.1 for its definition.

[6] see section 6.2.2 for the method of integration.

[7] defined to be the difference between the time when the SXR reaches its maximum + 10 minutes and the end of three consecutive 5-minute period for which the $>$10 MeV SEP flux is $\geq$ 10 pfu.

Event Number	SXR Date	SXR Peak Time (hh:mm)	SXR Class	Hα Location	SXR Fluence (J/m^2)	SXR Flag	Radio Fluence (SFU x min)	Radio Frequency (kHz)	Warning Time >10 pfu (min)	SEP Forecast Result
1	2006 Dec 5	10:35	X9	S07E79	6.12e-1	5	1.90e+6	916	1760	Hit
2	2006 Dec 13	02:39	X3	S05W23	5.88e-1	5	1.82e+7	916	31	Hit
3	2010 Aug 14	10:05	C4	N17W52	1.19e-2		1.29e+5	916		MISS
4	2011 Mar 7	20:12	M3	N24W59	1.38e-1	2	1.12e+4	916		Miss
5	2011 Mar 21	(farside)								
6	2011 Jun 7	06:41	M2	S21W64	4.91e-2	5	1.80e+7	916	99	Hit
7	2011 Aug 4	03:57	M9	N15W49	6.07e-2	5	8.78e+6	916	158	Hit
8	2011 Aug 9	08:05	X6	N17W83	1.77e-1	7	5.71e+6	916	40	Hit
9	2011 Sep 22	11:01	X1	N11E74	4.78e-1	2	4.32e+6	916	2154	Hit
10	2011 Nov 26	07:10	C1	N08W49	1.47e-2		1.74e+5	916		MISS
11	2012 Jan 23	03:59	M8	N28W36	3.97e-2	5	5.26e+5	916		Miss
12	2012 Jan 27	18:37	X1	N27W71	2.33e-1	5	4.38e+6	916	28	Hit
13	2012 Mar 7	00:24	X5	N17E15	6.89e-1	5	2.19e+7	916	286	Hit
14	2012 Mar 13	17:41	M7	N18W62	2.65e-1	3	2.92e+6	916	29	Hit
15	2012 May 17	01:47	M5	N12W89	1.21e-1	5	9.08e+6	916	23	Hit
16	2012 May 27	(farside)								
17	2012 Jun 14	14:35	M1	S17E14	1.55e-1		9.52e+4	916		MISS
18	2012 Jul 6	23:08	X1	S18W50	5.33e-2	5	1.21e+7	916	292	Hit
19	2012 Jul 12	16:49	X1	S16W09	5.28e-1	3	7.54e+5	916	106	Hit
20	2012 Jul 17	17:15	M1	S17W75	1.86e-1		3.27e+5	916		MISS
21	2012 Jul 23	(farside)								
22	2012 Aug 31	20:43	C8	S06E20	6.57e-2		3.19e+6	916		MISS
23	2012 Sep 27	23:57	C3	N08W41	4.19e-3		6.18e+4	916		MISS
24	2013 Mar 15	06:58	M1	N11E12	6.64e-2		3.92e+4	916		MISS
25	2013 Apr 11	07:16	M6	N09E12	7.11e-2	5	3.38e+7	916	62	Hit
26	2013 May 15	01:48	X1	N11E51	1.19e-1	5	1.58e+4	916		Miss
27	2013 May 22	13:32	M5	N15W70	1.77e-1	3	5.74e+5	916	48	Hit
28	2013 Jun 21	03:14	M2	S16E66	8.11e-2	2	6.18e+4	916		Miss
29	2013 Sep 29	23:37	C1	N15W40	3.07e-3		6.94e+4	916		MISS
30	2013 Dec 28	18:02	C9	S18E07	4.80e-3		1.23e+4	916		MISS
31	2014 Jan 6	(farside)								
32	2014 Jan 7	18:32	X1	S15W11	2.95e-1	5	7.85e+6	916	0	Hit
33	2014 Feb 20	07:55	M3	S15W67	7.38e-2	3	1.75e+6	916	55	Hit
34	2014 Feb 25	00:49	X4	S12E82	4.64e-1	5	6.83e+6	916	786	Hit
35	2014 Apr 18	13:03	M7	S16W41	1.13e-1	5	7.98e+6	916	143	Hit
36	2014 Sep 10	17:45	X1	N16W06	3.88e-1	5	3.49e+7	916	415	Hit

Table 6.1: SEP Flare List (2006-2014).

We show in Figure 6.1 the time profile of all 23 SEP events that were associated with $\geq$ M2 SXR flares. In each plot, the dashed red line indicates the SXR peak time (+10 min), while the next two dashed green lines refer to 10 pfu and 100 pfu threshold crossings, respectively. A blue arrow identifies the maximum of each SEP event.

We also identified 276 X-ray flares of class $\geq$ M2 by using 1-minute average SXR data recorded by instruments on board the GOES satellite (http://spidr.ngdc.noaa.gov/spidr/index.jsp). If no $H\alpha$ flare was reported, we determined flare locations using the evolution of active regions on the solar disk reported in the *Preliminary Report and Forecast of Solar Geophysical Data*.

Finally, the Wind/WAVES (Bougeret et al., 1995) record of low-frequency ($\sim$ 1 MHz) type III radio bursts was used.

6.2.1 Time-Integrated SXR Intensity

As pointed out before, to maximize the warning time in a reliable SEP forecast scheme, the use of the X-ray intensity integrated over the whole flare

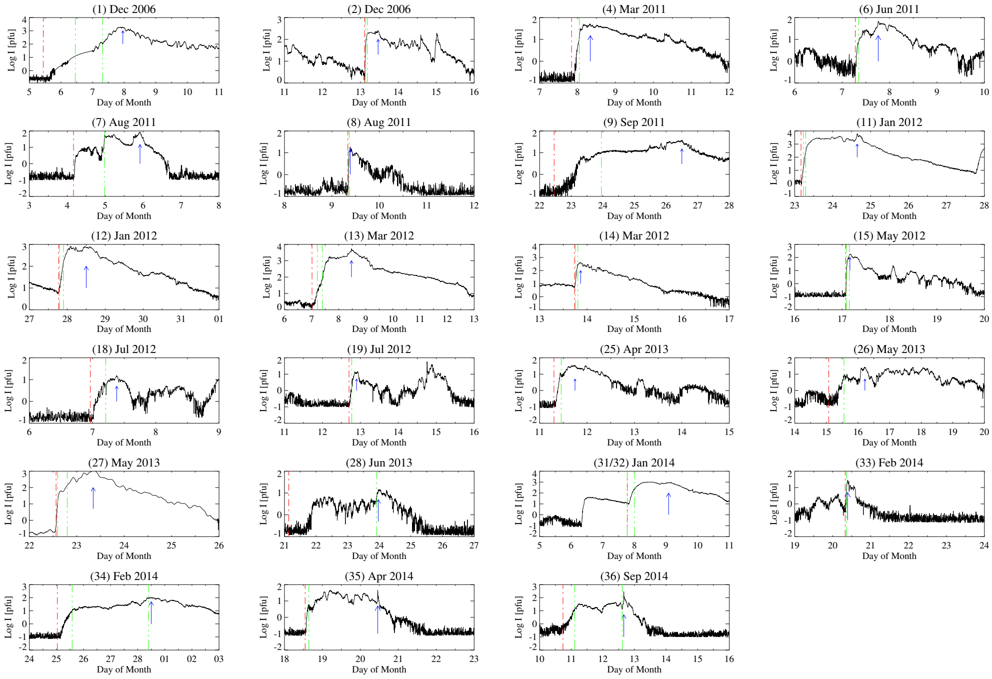

Figure 6.1: Proton flux as measured by GOES spacecraft for the ≥M2 flare events in Table 6.1. The red line evidences the time when the forecast is made, while the next two green lines refer to 10 pfu and 100 pfu threshold crossings. Finally, a blue arrow is used to show the maximum of each event.

duration seems to be limiting, since it can reach hours. As shown by Laurenza et al. (2009), a representative measure of the X-ray fluence can be obtained by integrating the X-ray intensity between the 1/3 power point before the X-ray peak and the 1/3 power point after it. Moreover, the intensity values from 6 to 10 minutes after the SXR peak can be reproduced by an esponential fit, performed to obtain an estimate of the SXR fluence (between the 1/3 power points) in real time for bursts that did not decay to 1/3 peak intensity within 10 minutes. The use of a curve fit to extrapolate the SXR time-profile is necessary in order to estimate the SXR fluence because, for about two-thirds of the ≥ M2 SXR bursts, the intensity did not drop below the 1/3 power point within 10 minutes following peak intensity.

Moreover, Laurenza et al. (2009) noted that when the ratio of the peak SXR intensity at 10 minutes following burst peak (I_{10}) to the burst peak intensity (I_P) was > 0.85 ($\sim 15\%$ of the sample), the calculated fluence was an over-estimate of the actual fluence. Thus they used an empirical prescription based on I_{10}/I_P to reduce the fluence for such events. The SXR integration flag in column 7 of Table 6.1, with values from 1-7, specifies any empirical adjustments that were made to the curve fits depending on the value of I_{10}/I_P. These adjustments are specified in Table 6.2, which also gives the number of SXR events in each group.

SXR Flag	I_{10}/I_P Range	Value Assigned to I_{10}/I_P	Decay Time to $I_{10}/I_P < 0.33$ (min)	Number of Cases
1	$I_{10}/I_P \geq 1.0$	$I_{10}/I_P = 0.75$	38	4
2	$0.85 < I_{10}/I_P \leq 0.90$	$I_{10}/I_P = 0.85$	68	13
3	$0.90 < I_{10}/I_P \leq 0.95$	$I_{10}/I_P = 0.90$	104	11
4	$0.95 < I_{10}/I_P < 1.0$	$I_{10}/I_P = 0.95$	214	5
5	$0.33 < I_{10}/I_P \leq 0.85$	No Adjustments		147
6	$I_{10}/I_P \leq 0.33$	No Adjustments		1
7	$I_{10}(d)/I_P(d) \leq 0.33$	No Extrapolation		95

Table 6.2: Soft X-ray Flare Integration Flag.

6.2.2 Time-Integrated 1 MHz Radio Intensity

We also use the Wind/Waves data provided in terms of ratio (R) of the radio flux to background, with the background (B) provided in units of $\mu V/Hz^{1/2}$. The radio flux, provided in solar flux units[8], can be written as $J(SFU) = 10^{10}\ (R*B)^2/(Z_0\ A)$, in which Z_0 is the characteristic impedance of the free space (Z_0=377 W), while A is the area of the RAD1 antenna (1225 m^2). For the 2006-2014 time interval considered, the closest frequency to 1 MHz at which measurements were usually provided was 916 kHz. Since the $\sim$ 1 MHz intensity-time curves are more irregular than the SXR time-intensity profiles, the radio integration extends from 10 minutes before the time of the SXR integration to 10 minutes after the X-ray peak (Laurenza et al., 2009).

In Figure 6.2 we show an example of the computation of key parameters for the 2006 December 13 SEP event. The various hatched areas refer to the different types of integration: the green area refers to SXR integration using actual data (from the 1/3 point before the SXR peak to 5 min after the SXR peak); violet area corresponds to the integration made using the exponential fit (from 6 min after the peak to the 1/3 point after the SXR peak); and magenta area refers to radio time-integration using 916 kHz channel (from 10 min before the 1/3 point on the rise of the SXR burst to 10 min after the SXR peak).

---

[8] 1 SFU = 1 solar flux unit = 10^{-22} W m^{-2} Hz^{-1}.

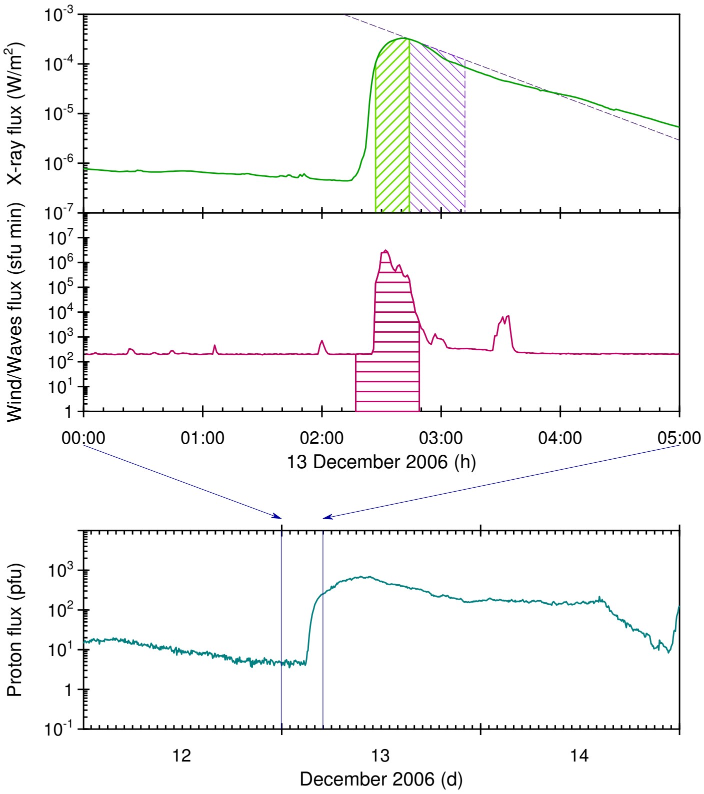

Figure 6.2: Key parameters for the 2006 December 13 SEP event. From top to bottom: X-ray flux, Radio Waves flux and Proton flux.

6.3 X-ray and Type III bursts statistics

6.3.1 Comparison of Numbers and Sizes of Events During the Rise Phases of Cycles 23 (Sep 1996 - Sep 2002) and 24 (Dec 2008 - Dec 2014)

In this section, we compare the SXR and radio fluences as computed in sections 6.2.1 and 6.2.2 for SEP source flares from Dec 2008 - Dec 2014 corresponding to the first six full years of solar cycle 24 (hereafter, period B) with those from the corresponding years, Sep 1996 - Sep 2002 (hereafter, period A (Harvey and White, 1999)), for cycle 23. Current solar cycle 24 followed one of the deeper and longer 11-yr minima since $\sim$ 1900 (Otkidychev and Skorbezh, 2014) and had one of the weakest activity maxima during this period (Richardson, 2013; Wang and Colaninno, 2014; Singh and Tonk, 2014). We note that 63 SEP events, out of the 94 that met the SWPC threshold during cycle 23, fell within interval A, while only 34 such SEP events occurred within the corresponding years (Interval B) of solar cycle

24, a 46% reduction. Reflecting the lower rate of SEP activity in interval B, we find that the number of $\geq$ M2 X-ray bursts during this period (257) is 40% lower than the number (430) of such events in interval A. Nonentheless, the percentage of $\geq$ M2 X-ray bursts associated with SEP events is about 8-10% in both periods (43/430 in the period A, 21/257 in the period B). The percentages of $\geq$ M2 X-ray bursts associated with SXR and radio fluences above two thresholds, viz., 0.1 J/m^2 for SXR and 6×10^5 SFU × min for radio, are 26% (112/430) and 29% (125/430), respectively for period A, versus 18% (46/257) and 21% (53/257), respectively for Period B, indicating a $\sim$ 30% decrease in these two parameters from period A to period B.

The above SXR and $\sim$1 MHz parameters (number of events, median fluence, standard deviation) are listed in Table 6.3 and Table 6.4 for inerval A and B, respectively. It can be seen that both the median fluences of $\geq$ M2 SXR and $\sim$ 1 MHz radio bursts, were higher during the rise phase of cycle 23 than for the corresponding interval of cycle 24.

		SXR [J/m^2]		RAD [$\times 10^6$ SFU $\times$ min]	
	N	<SXR>	SXR$_{SD}$	<RAD>	RAD$_{SD}$
All	430	0.11	0.02	1.7	0.3
SEP	43	0.34	0.07	3.2	0.6
Non SEP	387	0.08	0.01	1.2	0.2

Table 6.3: Characteristics of SXR and $\sim$ 1 MHz bursts that occurred during the first six years of solar cycle 23 (1996 Sep 15 - 2002 Sep 15): number of $\geq$ M2 SXR events (N), median SXR fluence (<SXR>) with standard deviation (SXR$_{SD}$), median $\sim$ 1 MHz radio fluence (<RAD>) with standard deviation (RAD$_{SD}$).

		SXR [J/m^2]		RAD [$\times 10^6$ SFU $\times$ min]	
	N	<SXR>	SXR$_{SD}$	<RAD>	RAD$_{SD}$
All	257	0.06	0.01	1.4	0.4
SEP	21	0.17	0.03	4.4	0.6
Non SEP	236	0.02	0.01	0.7	0.2

Table 6.4: Characteristics of SXR and $\sim$ 1 MHz bursts that occurred during the first six years of solar cycle 24 (2008 Dec 15 - 2014 Dec 15): number of $\geq$ M2 SXR events (N), median SXR fluence (<SXR>) with standard deviation (SXR$_{SD}$), median $\sim$ 1 MHz radio fluence (<RAD>) with standard deviation (RAD$_{SD}$).

6.3.2 Comparison of Numbers and Sizes of Events During 1995-2005 and 2006-2014

In this section, we compare the solar activity parameters for the 1995-2005 interval on which ESPERTA was developed (termed period C) to the corresponding data for the 2006-2014 interval (period D) on which this SEP forecast model is being evaluated. The flare data for these two intervals are given in Table 6.5 and Table 6.6, respectively.

		SXR [J/m^2]		RAD [$\times 10^6$ SFU $\times$ min]	
	N	<SXR>	SXR_{SD}	<RAD>	RAD_{SD}
All	704	0.10	0.03	1.9	0.4
SEP	63	0.31	0.08	4.1	0.5
Non SEP	641	0.07	0.02	1.5	0.3

Table 6.5: Characteristics of SXR and $\sim$ 1 MHz bursts that occurred during the period 1995-2005: number of $\geq$ M2 SXR events (N), median SXR fluence (<SXR>) with standard deviation (SXR_{SD}), median $\sim$ 1 MHz radio fluence (<RAD>) with standard deviation (RAD_{SD}).

		SXR [J/m^2]		RAD [$\times 10^6$ SFU $\times$ min]	
	N	<SXR>	SXR_{SD}	<RAD>	RAD_{SD}
All	276	0.06	0.01	1.4	0.5
SEP	23	0.18	0.02	5.7	0.9
Non SEP	253	0.02	0.01	0.8	0.3

Table 6.6: Characteristics of SXR and $\sim$ 1 MHz bursts that occurred during the period 2006-2014: number of $\geq$ M2 SXR events (N), median SXR fluence (<SXR>) with standard deviation (SXR_{SD}), median $\sim$ 1 MHz radio fluence (<RAD>) with standard deviation (RAD_{SD}).

We observe that the $\geq$ M2 X-ray bursts occurrence is reduced of 39% in period D (276 events) with respect to period C (704 events). In addition, the percentage of $\geq$M2 X-ray bursts associated with SEP events is $\sim$ 9% (63/704) and 8% (23/276) for period C and period D, respectively.

When all the $\geq$ M2 X-ray bursts are considered, 33% (234/704) in period C are found to have an SXR fluence > 0.1 J/m^2, versus 19% (53/276) in period D. A similar behavior is observed for the type III radio bursts: 36% (254/704) of all events in period C (60/276, 22% in period D) are found to have a $\sim$ 1 MHz fluence $> 6 \times 10^5$ SFU $\times$ min.

We also note that both SXR and radio fluences are higher for SEP associated events, in both the time periods: the ratio between the median SXR (radio) fluence of SEP associated events and that of the non SEP associated ones is 4.4 (2.7) and 9 (7.1) for period C and D, respectively. Note that all the ratios are higher in period D. Moreover, it is found that the median SXR fluence in period C exceeds that in period D of a factor 1.72 (3.5), when the SEP (non SEP) associated events are considered. On the contary, the median radio fluence in period C is slightly lower (by the ratio of 0.72) than that of period D for SEP events, while for the more numerous non SEP events the median fluence in period C is higher by a factor of 1.9.

6.3.3 Comparison of Probability Density Functions for 1995-2005 and 2006-2014

A SEP prediction model needs to be probabilistic, since the occurrence frequency of energetic particles has a probabilistic nature (Nymmik, 1999). This requires a statistical approach to study solar flares which can/cannot generate a SEP event. Nymmik (1999) noticed that the mean SEP occurrence frequency can be described by a power-law function of the solar activity, characterized via the sunspot number, as well as the SEP size distribution. Conversely, a log-normal distribution is found to describe the SEP event particle energy spectra. Recently, Papaioannou et al. (2015), to assess the performance of the FORSPEF model, explored the conditional-probability for flares for a given active region target, under fixed condition of the effective connected magnetic field strength (used in their model). They found that the maximum CME likelihood (peak value ~ 0.27) corresponds to the flare class M2.0, indicating that the likelihood that a given flare is associated with a CME is higher for flares of class $\geq$ M2. Here, the probability density functions (PDFs) associated with the SXR and the radio fluences are explored by distinguishing between SEP and non SEP associated events. The empirical PDFs are estimated through the kernel density estimator technique (see Appendix C for more details) (Silvermann, 1998; Alberti et al., 2014). It is a non-parametric way to estimate the probability density function of a time series based on the definition of a non-negative function that integrates to one and has zero mean, called the kernel function, and a smoothing parameter, termed the bandwidth. A range of kernel functions are commonly used (uniform, triangular, weighted, Epanechnikov, Gaussian) but we choose to use the Epanechnikov kernel because it is optimal in a mean square error sense such that the variance is minimized. This procedure is quite similar to histogram method but presents some advantages such as smoothness or continuity if a suitable kernel is chosen. Moreover, we normalized the PDFs with respect to the number of events considered (see Table 6.5 and 6.6) such that the integrated PDF over the entire range of values is equal to 1. Since the range of SXR and radio fluences values is quite different, we are not able to choose a unique binsize for both periods C and D. For instance, since the number of events is similar (between SXR and radio fluences for the same period), for the binning procedure we choose the same number of bins for both SXR and radio PDFs estimations.

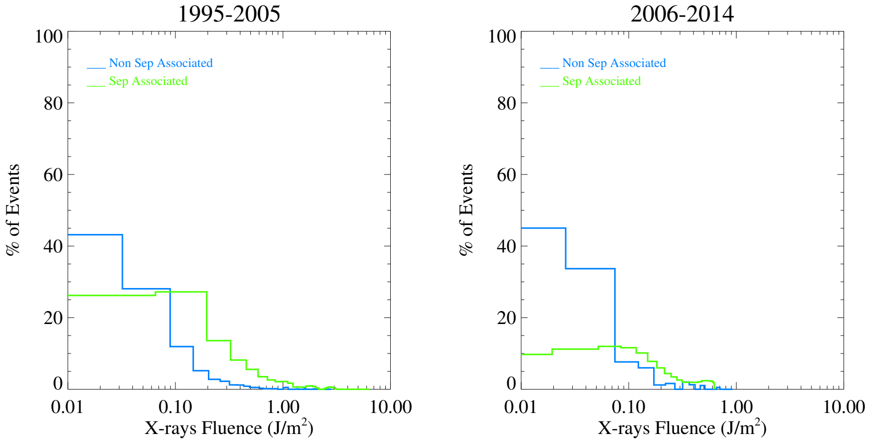

Figure 6.3: SXR fluence probability density functions: 1995-2005 database (left panel) and 2006-2014 database (right panel).

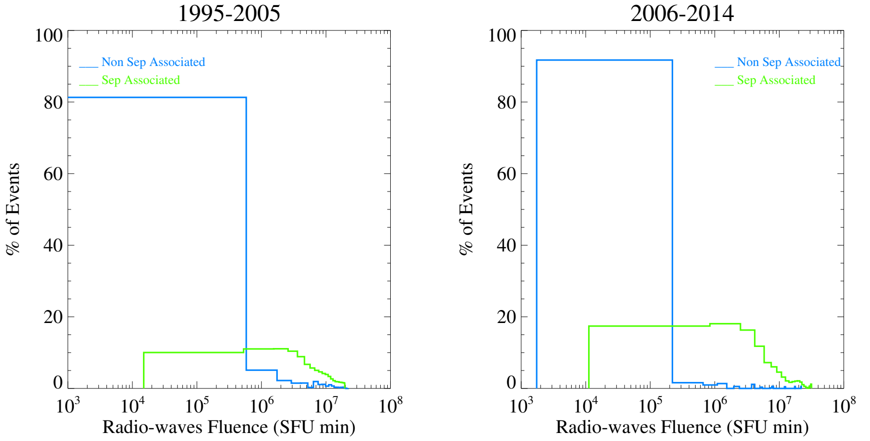

Figure 6.4: Radio fluence probability density functions: 1995-2005 database (left panel) and 2006-2014 database (right panel).

Figure 6.3 shows the comparison between the SXR fluence PDFs obtained for period C (left panel) and period D (right panel). Generally, high values of SXR fluence are found to be associated with SEP events. We first note that the PDF associated with SEP events is shifted toward higher values compared to the non SEP associated PDF. In particular, a critical value for the SXR fluence (0.1 J/m^2) can be identified above which the percentage of SEP associated (green line in Figure 6.3) $\geq$ M2 SXR bursts increases to

78% (49/63) and 65% (15/23) for period C and D, respectively). In comparison, the percentage of non SEP associated (blue line in Figure 6.3) $\geq$ M2 SXR bursts having SXR fluence greater than 0.1 J/m^2 is quite low: 29% (185/641) and 15% (38/253) for period C and D, respectively.

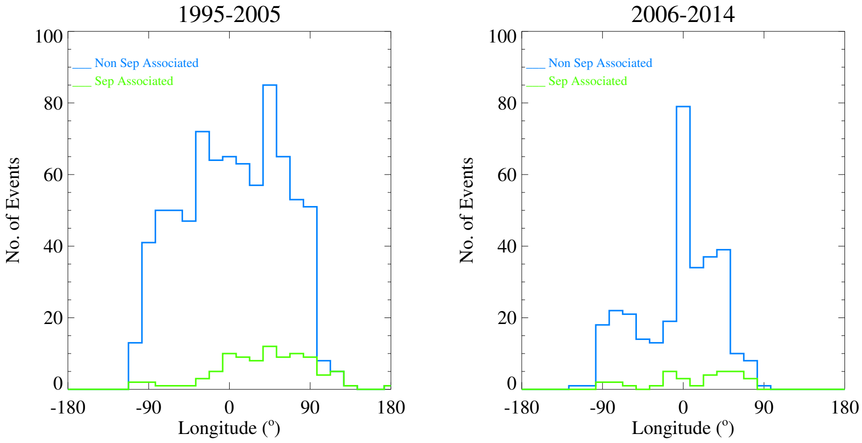

Figure 6.5: Longitudinal distributions of flare locations: 1995-2005 database (left panel) and 2006-2014 database (right panel).

Similar results are obtained analyzing PDFs related to 1 MHz radio fluence for both time periods. As shown in Figure 6.4, the percentage of SEP associated (green line) $\geq$ M2 X-ray bursts having radio fluence greater than 6×10^5 SFU×min is 90% (57/63) and 83% (19/23) for period C and D, respectively. On the other, the percentage of non SEP associated (blue line in Figure 6.4) $\geq$ M2 X-ray bursts having radio fluence greater than 6×10^5 SFU×min is very reduced in both periods, i. e., 31% (197/641) and 16% (41/253).

6.3.4 Solar Longitude Distribution of $\geq$ M2 SXR Flares With and Without Associated SEP Events for 1995-2005 and 2006-2014

Finally, we investigated the longitudinal distribution associated with the location of the $\geq$ M2 SXR flares. Figure 6.5 shows that:

- for the period C (1995-2005), the longitudinal distribution of non SEP associated flares is higher in the central disk region, while the longiditunal distribution of SEP associated events is higher for western events
- for the period D (2006-2014), a somewhat similar pattern is observed for a smaller sample of events: a clear peak for the nonSEP flares at around 0 degrees, whereas for SEP associated events, there is a comparable number of events in the longitude intervals W20-W90 and

E20-W19 (17 vs 9, respectively), although the statistics are small for the sub-groupings in longitude.

Our findings confirm the well known result that solar proton events preferentially originate in western and, to a lesser degree, central flares (e.g., Belov et al., 2005; Gopalswamy et al., 2008; Park et al., 2012). Moreover, given the noticeable presence of central solar flares associated with SEP events (especially in the 2006-2014 period), it is reasonable to invoke the contribution of fast CME-driven shock continuously feeding accelerated particles in the magnetic field lines connecting the shock to the observer with accelerated particles (Papaioannou et al., 2016).

6.4 Validation of ESPERTA

The model called ESPERTA, developed by Laurenza et al. (2009), is based on 1-8 $\mathring{A}$ SXR and $\sim$ 1 MHz radio fluence and flare location, to provide short-term warnings of solar energetic proton (SEP) events that meet or exceed the Space Weather Prediction Center threshold of J ($> 10MeV$) = 10 pr cm^{-2} s^{-1} sr^{-1}, within 10 minutes after the maximum of the associated soft X-ray flare. ESPERTA can be applied by using the above parameters, as computed in section 6.2 for period D, i.e. a new dataset, independent from the interval C (1995-2005) used to develop the model. Moreover, the analysis performed in section 6.3 has pointed out that the dataset for period D noticeably differs from the dataset in period C. Hence period D is well suited to test the accuracy and the performance of the ESPERTA model. It takes advantage of the logistic regression analysis (McCullagh and Nelder, 1983; Garcia, 1994), to provide a continuous probability function for the occurrence of SEP events depending on the SXR and radio fluences for the considered $\geq$ M2 SXR flares. This technique is suitable for investigations where each event is associated with a set of independent variables and characterized by binary response (yes/no). In logistic regression technique, the probability (P) that an event will occur can be expressed as:

$$\log\left[\frac{Prob(SEPevent)}{Prob(NoSEPevent)}\right] = \sum_{i=1}^{k} \beta_i x_i \tag{6.1}$$

In our case, the probability (P) is a function of the chosen parameters, i.e. SXR and radio fluence (X and R, respectively) as:

$$P(\log X, \log R) = \frac{e^{\eta}}{1+e^{\eta}} \tag{6.2}$$

where $\eta = \eta(\log X, \log R)$. In the ESPERTA model, the dependence of the probability by the heliographic longitude was taken into account by separating the $\geq$ M2 flares into three different longitude bands:

- E 120° - E 41°
- E 40° - W 19°
- W 20° - W 120°

In this way, three different values for η corresponding to the three longitudinal bands were obtained :

- $\eta_1 = -6.07 - 1.75\log(X) + 1.14\log(R) + 0.56\log(X)\log(R)$
- $\eta_2 = -7.44 - 2.99\log(X) + 1.21\log(R) + 0.69\log(X)\log(R)$
- $\eta_3 = -5.02 - 1.74\log(X) + 0.64\log(R) + 0.40\log(X)\log(R)$

Figure 6.6 shows scatter plots of $\sim$ 1 MHz vs. 1-8 $\mathring{A}$ SXR fluence for $\geq$ M2 flares that occurred during interval D for three longitude ranges on which contour plots of SEP event probability have been drawn. It can be seen that, for each longitude range, the probability functions match the SEP event occurrence, depending on the SXR and radio fluences, as a great number of SEP events are located in the high-probability region, although not exclusively. In principle, when locating a solar flare in such diagrams, based on the SXR and radio fluences values, the probability of a following SEP event can be evaluated. Moreover, one probability curve can be selected to provide a yes/no result for the occurrence of a SEP event as follows: given a $\geq$ M2 solar flare if the related data point is above the chosen probability contour level, a warning is given; if it is below, no alert is issued.

The probability curve level Pt used to evaluate the ESPERTA performance during 2006-2014 (dashed lines in the three scatter plots) is 28%, 28% and 23% for western, intermediate and eastern events respectively, which maximize the Probability of Detection (POD) as discussed later.

The accuracy of the model can be investigated by evaluating the POD and the False Alarm Rate (FAR), which can be expressed in terms of three values:

1. the number of hits (a SEP event was forecast and one occurred) which we named A
2. the number of false alarms (a SEP was forecast but none occurred), designated B
3. the number of missed events (no SEP event was predicted but one occurred), designated C

In this way, a relation between POD (FAR) and these parameters is obtained as:

$$POD = \frac{A}{A+C} \tag{6.3}$$

$$FAR = \frac{B}{A+B} \tag{6.4}$$

Moreover, we defined three other parameters: the number of correct nulls, D (no SEP event forecast and none occurred), the number of forecasts expected to be correct by chance, E, and the total number of forecasts (both positive and null), N. Using the above parameters, the following statistical quantities allow us to specify the quality of our forecast technique:

1. the percent correct, PC = (A + D)/N
2. the Heidke Skill Score, HSS = (A + D - E)/(N - E)

in which $E = [(A+B)(A+C)+(B+D)(C+D)]/N$ (Balch, 2008). The number of correct forecasts by chance can be derived as (A + C)(A + B)/N^2 (Laurenza et al., 2009).

In order to test the efficiency and the accuracy of ESPERTA, we evaluate these statistical parameters for the database referred to the period between 2006 and 2014. Laurenza et al. (2009) showed that for the original 1995-2005 data set, both the POD and the FAR are high ($\sim$ 80-90%) for low-probability levels (< 20%), decreasing with increasing threshold, and the HSS is optimized for probabilities ranging from 20% to 40%. Nevertheless, the optimal Pt can be identified by maximizing the POD and HSS and minimizing the FAR. For the western $\geq$ M2 flares Laurenza et al. (2009) found the optimal point to be $Pt = 28\%$, versus 28% for the "intermediate" flares and 30% for eastern events. Here, for the 2006-2014 database, we confirm that the thresholds previously used are still valid for the new dataset in case of the western (POD = 61 % (11/18), FAR =35 % (6/17) and intermediate events (POD = 56 % (5/9), FAR = 29% (2/7)). For the small sample of eastern events, the optimization of POD, FAR and HSS are obtained for $pt = 23\%$ (POD = 60 % (3/5), FAR = 0% (0/3)). These verification measures are calculated by taking into account that 9 SEP events had associated disk flares with class < M2; 5 of these 9 "MISSES", which cannot be predicted by our method, were located in the western longitude bin and 4 in the central one. Moreover, we evaluate the contingency matrix (which includes values of A, B, C, and D), by combining events from all the heliolongitude ranges. The combined results are the following: POD = 59% (19/32), FAR = 30% (8/27), HSS = 0.55 (44/80) and PC = 87% (240/276), with the probability for a chance hit = 1% (864/76176).

Table 6.7 lists the POD and FAR values for intervals C (1995-2005) and D (2006-2014) as well as for the combined 1995-2014 period.

The similarity of the results for the three data sets shows that performance of the method is relatively independent of the interval considered, a useful property given that, as shown in Section 6.3, the solar activity level for interval D was significantly lower than that during interval C.

	C 1995 - 2005	D 2006 - 2014	C+D 1995 - 2014
POD	63 % (47/75)	59 % (19/32)	62 % (66/107)
FAR	42 % (34/81)	30 % (8/27)	39 % (42/108)

Table 6.7: POD and FAR parameters

6.5 Evaluation of SEP event warning times

A crucial aspect of any prediction method is the maximization of the warning time, i.e., the time difference between the SEP event start and the time when a warning is given. Since the GOES >10 MeV SEP time profiles, during the SEP onset period, are contaminated by relativistic electrons and protons (Posner, 2007), Laurenza et al. (2009) did not determine onset times for "Hit" events (made by ESPERTA) by using the GOES >10 MeV SEP data but the 31-50 MeV onset times published by Posner (2007), for 19 of their "Hit" events. Note that these onset times refer to the rise of the event above the preevent background instead of the NOAA (or equivalent at 31-50 MeV) event threshold crossing. ESPERTA would have issued a lead warning time (ranging from 8 min to 897 min and a median of 54 min) for all the 19 events.

Here, following Núñez (2011), we calculate warning times directly from the GOES $>$ 10 MeV proton fluxes, based on the difference between the time a forecast is issued (which for ESPERTA is 10 minutes after the SXR burst peak) and the time that the 10 pfu SWPC event flux threshold is reached (at the end of three consecutive 5-min periods at or above the 10 pfu threshold). Using this definition we obtain a median warning time of $\sim$ 4.8 hours (range from 0.4 hours to 52.8 hours) for our 66 "Hit" events during the period 1995-2014. Specifically, for the 2006-2014 interval the median warning time computed on "Hit" events was estimated to be $\sim$ 2 h (ranging from 0.4 to 35.9 h), versus $\sim$ 6 h (ranging from 0.8 to 52.8 h) for the 1995-2005 data set.

For a comparison with the result of Núñez (2011), we compute the average warning time as well, that is $\sim$ 9 h for the period 1995-2014 ($\sim$ 9 h in the 1995-2005 interval and $\sim$ 7 h in the 2006-2014 interval), versus $\sim$ 5 hours obtained by Núñez (2011) for a study of 134 "Hit" events from 1987-2006.

6.6 Discussion and conclusions

A database of 276 SXR flares and 23 $>$ 10 MeV SEP events that met the SWPC $\geq$ 10 pfu flux threshold criterion was compiled, covering the period 2006-2014, i.e., the declining phase of the 23rd solar cycle and the beginning part of the 24th solar cycle, in order to test the performance of ESPERTA, a

SEP forecasting model developed by Laurenza et al. (2009). The ESPERTA basic parameters, i.e., 1-8 $\AA$ SXR and radio (at $\sim$ 1 MHz) fluences, were computed by doing the time integration in real time according to the procedure proposed by Laurenza et al. (2009). The values of both parameters were obtained for the period 2006-2014 (designated interval D in this paper), and compared with those obtained for the period 1995-2005 (interval C) for which ESPERTA was developed. First, we compared the number of $\geq$ M2 1-8 $\AA$ SXR bursts for corresponding years, i.e., the first six years of solar cycles 23 (15 Sep 1996 - 15 Sep 2002, period A) and 24 (15 Dec 2008 - 15 Dec 2014, period B), within in periods C (1995-2005) and D (2006-2014), respectively, and found that 40% [1-(257/430)] fewer such bursts occurred during the rise phase of cycle 23 (Table 6.3 and Table 6.4). Moreover, Gopalswamy, Mäkelä, Yashiro, Xie, Akiyama and Thakur (2015) found a reduction in high-energy SEP events that could be attributed to several factors, such as the weak interplanetary magnetic field decreasing the efficiency of particle acceleration mechanisms. Indeed, Gopalswamy, Mäkelä, Akiyama, Yashiro and Thakur (2015) showed that a similar reduction is not observed in the overall CME rate. By a comparison of the first 73 months in solar cycles 23 and 24 (i.e., May 1996 - May 2002 versus Dec 2008 - Dec 2014), they found a reduction in the sunspot number (dropped by $\sim$ 40%), while the CME rate (normalized to the sunspot number SSN) was almost the same (i.e., 0.03/SSN versus 0.05/SSN). Similarly, Gopalswamy, Mäkelä, Yashiro, Xie, Akiyama and Thakur (2015) showed that the distributions of CMEs speeds are similar in both periods (see, e.g., Gopalswamy, Mäkelä, Yashiro, Xie, Akiyama and Thakur, 2015, Figure 1); conversely, the width distributions are quite different. They found that a great fraction of CMEs occurred in the solar cycle 24 was halos ($\sim$ 97%), while a lower fraction (i.e., $\sim$ 75%) was observed in solar cycle 23. This can be explained in terms of a reduction in the total heliospheric pressure, producing an anomalous expansion of CMEs, allowing them to become halos. Therefore, the observed 40% reduction in SEP activity between intervals A and B cannot be due to the paucity of halo CMEs, whereas it could be accounted for by the lower large-scale magnetic activity (i.e., active regions and sunspot areas), or to the paucity of CMEs producing the seed particles. Nevertheless, the lack of CME data in our study prevents us to test these hypotheses. The percentage of $\geq$ M2 SXR bursts associated with SEP events is observed to be about 8-10% for the first six years of both cycles 23 (43/430) and 24 (21/257), consistent with past findings both for large and weak SEP events (Gopalswamy, 2012; Chandra et al., 2013; Bazilevskaya et al., 2015). However, the SXR and $\sim$1 MHz radio fluences are only two parameters which characterize SEP occurrence. Indeed, Gopalswamy, Mäkelä, Akiyama, Yashiro and Thakur (2015) showed that a similar reduction is not observed in the overall CME rate. By a comparison of the first 73 months in solar cycles 23 and 24 (i.e., May 1996 - May 2002 versus Dec 2008 - Dec 2014), they found a reduction in the sunspot number (dropped by $\sim 40\%$), while the CME rate (normalized to the sunspot number SSN) was almost the same (i.e., 0.03/SSN versus 0.05/SSN). Similarly, Gopalswamy, Mäkelä, Yashiro, Xie, Akiyama and Thakur (2015) showed that the distributions of CMEs speeds are similar in both periods (see, e.g., Gopalswamy, Mäkelä, Yashiro, Xie, Akiyama and Thakur, 2015, Figure 1); conversely, the width distributions are quite different. Moreover, they also found that a great fraction of CMEs occurred in the solar cycle 24 was halos ($\sim 97\%$), while a lower fraction (i.e., $\sim 75\%$) was observed in solar cycle 23. These similarities/differences can be explained in terms of a reduction in the total heliospheric pressure, producing an anomalous expansion of CMEs, allowing them to become halos. Moreover, also a reduction in high-energy SEP events is found, due to the weak interplanetary magnetic field which reduces the efficiency of particle acceleration mechanisms. Therefore, the observed 40% reduction in SEP activity between intervals A and B cannot be related to the halo CMEs occurrence, while it could be accounted for by the lower large-scale magnetic activity (i.e., active regions and sunspot areas), as well as to the seed particles produced by CMEs.

From a comparison of the probability distribution functions of the 1-8 $\mathring{A}$ and ~ 1 MHz fluences of all $\geq$ M2 SXR bursts during the larger intervals C (1995-2005) and D (2006-2014), we found that the percentage of all the events exceeding the SXR fluence threshold of 0.1 J/m^2 is higher in period C than in period D (33% and 19%, respectively), as well as the percentage of all the events exceeding the radio fluence threshold of 6×10^5 SFU $\times$ min (36% and 21%, respectively). As expected, mainly high values of both the ESPERTA basic parameters are found to be associated with SEP associated flares, in both periods C and D. The ratio between the median SXR (radio) fluence of SEP associated events and that of the non SEP associated ones is 4.4 (2.7) and 9 (7.1) for period C and D, respectively, although both ratios are higher in period D. In addition, the percentage of SEP associated $\geq$ M2 X-ray bursts above the critical value 0.1 J/m^2 for the SXR fluence increases to 78% (70%) in period C (D), whereas the percentage of non SEP associated ones is quite low (29% and 15% for period C and D, respectively). This finding is more apparent when the radio fluence is considered: the percentage of SEP associated $\geq$ M2 SXR bursts having radio fluence greater than 6×10^5 SFU $\times$ min is 90% (83%) for period C (D), whereas the percentage of non SEP associated $\geq$ M2 flares having radio fluence greater than 6×10^5 SFU $\times$ min is 31% (16%). Our results show that the radio fluence is a more efficient parameter in distinguishing between the SEP associated events from the non associated ones; this is more marked for events of period D. As a matter of fact, most of the solar sources of SEP events exhibit Type III radio emission (e.g., Duffin et al., 2015; Winter and Ledbetter, 2015).

In order to test the reliability of the ESPERTA model (Laurenza et al., 2009), we evaluated the probability of detection (POD) and the False Alarm

Rate (FAR) of this method on a new (2006-2014) data base. We found that the POD and FAR levels (59% and 30%, respectively) were comparable to those (63%, 42%) obtained for the original 1995-2005 dataset, an indication of model robustness.

The ESPERTA median (average) warning time (delta between the time the forecast is issued and the time event threshold is crossed) for the 66 SEP events with peak fluxes $\geq$ 10 pfu that were correctly called ("Hits") from 1995-2014, was 4.8 h ($\sim$ 9 h), in the range 0.4-52.8 h, exceeding those obtained by other methods (e.g., Núñez (2011) average warning time of $\sim$ 5 hours). This median (average) warning time varies from $\sim$ 2 h ($\sim$ 7 h), ranging from 0.4 to 35.9 h, for the 2006-2014 interval, versus $\sim$ 6 h ($\sim$ 9 h), ranging from 0.8 to 52.8 h for the 1995-2005 data set. We remark that it is critical to provide an SEP warning immediately after the parent solar event, given that high energy particles may cause hazards before the integral $>$ 10 MeV flux reaches the SWPC $\geq$ 10 pfu threshold (Posner, 2007).

Data availability

All data used in this analysis are publicly accessible from NASA (Wind/WAVES) and NOAA (GOES) through `ftp://solar-radio.gsfc.nasa.gov/` (Wind/WAVES), `http://www.ngdc.noaa.gov/stp/satellite/goes/dataaccess.html` (GOES), `http://umbra.nascom.nasa.gov/SEP/` (SWPC SEP event list).

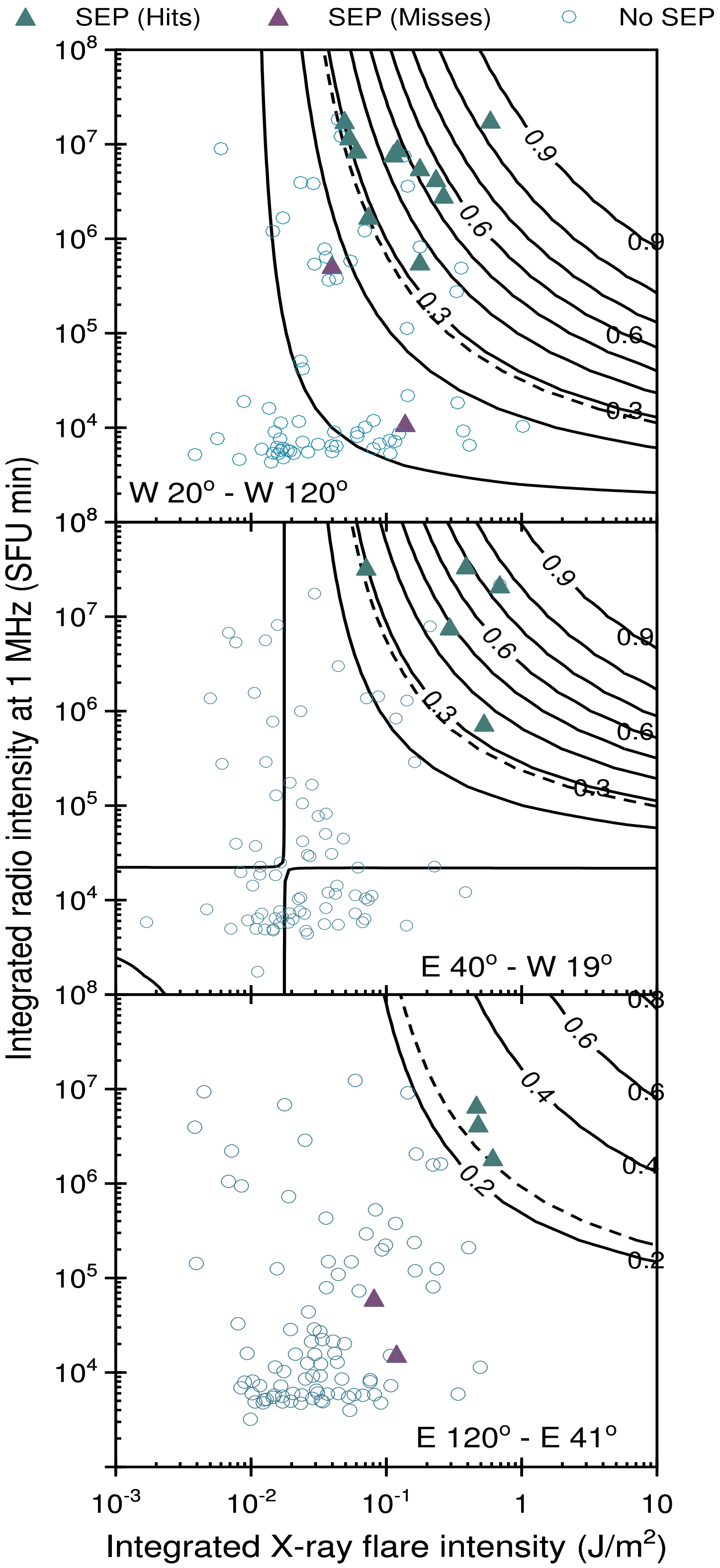

Figure 6.6: Probability contours for SEP forecasting for three different longitudinal bands: SEPs “Hit” (green triangles), SEPs “Miss” (violet triangles) and No SEPs associated (circles).

Part II

Long-term solar-terrestrial processes

Chapter 7

Solar irradiance changes and the Earth's climate system

The primary source of energy for the Earth is radiant energy coming from the Sun. This energy is measured and reported as the solar irradiance, the power per unit surface received from the Sun in the form of electromagnetic radiation in a wavelength range. When it is measured over the whole range of wavelengths is called Total Solar Irradiance (TSI), while when measured as a function of wavelength is named as Spectral Solar Irradiance (SSI). The Earth's atmosphere is reached by different wavelengths: visible and infrared radiation can reach the surface, warming it to livable conditions, while ultraviolet (UV) radiation is absorbed by greenhouse gases (typically, ozone) at high latitude ($\gtrsim$ 60 km). Each part of the solar irradiance spectrum changes over the 11-year solar cycle, becoming brighter than average at solar maximum and dimmer at solar minimum. Moreover, each wavelength also changes as the Sun rotates and during high-activity phenomena such as solar flares, implying different photon absorption/emission mechanisms through the Heliosphere. Indeed, solar irradiance can be also defined as "the photon energy incident on the Earth at its average distance from the Sun of 1 AU, and prior to absorption in the Earth's atmosphere" (Fröhlich and Lean, 2004). When the energy of the photons is integrated over all wavelengths across the electromagnetic spectrum, the average TSI is 1361 ± 4 W m^{-2}. Solar photons at visible wavelengths have the largest flux because the emission spectrum of a blackbody near 5770 K peaks around this region. Wavelength-dependent variations in photon fluxes are driven by the solar dynamo, generating different levels of magnetic flux in the Sun's atmosphere. Indeed, near-UV, visible and near-infrared (near-IR) radiations emanate from the Sun's surface and lower atmosphere (photosphere). Emissions at shorter wavelengths, in the far and extreme UV spectrum below $\sim$ 160 nm, and at longer radio wavelengths emerge from increasingly hotter and more tenuous upper layers of the Sun's atmosphere (cromosphere and corona). These emissions are produced *in situ* by radiation from plasma in the outer solar atmosphere. The radiation is a mixture of lines and continua, becoming increasingly line-dominated at shorter wavelengths. These suggest that the Sun is a variable star, without a constant radiative output such that the term "solar constant", referring to the total irradiance, is nowdays not properly correct, since several features, such as sunspots, have been observed to emerge and disappear from the Sun's disk. Indeed, solar irradiance at all wavelengths changes continuously in response to magnetic activity which alters the temperature and density in local regions of the solar surface and atmosphere, from which photons emerge, evolving with the 11-yr solar cycle. When viewed in the visible light, the solar disk displays two prominent types of active features, called sunspots and faculae, which are respectively darker and brighter than the surrouding surface. In ultraviolet light, magnetically active regions are composed of large bright points, while some coronal features, called coronal holes, can be seen as darker than the surrouding atmosphere. When solar photons arrive at Earth, some are absorbed by gases in Earth's atmosphere (primarily O_2, N_2, O and O_3), at different altitudes depending on their wavelengths, while the visible spectrum reaches the surface and lower atmosphere (troposphere), since Earth's atmosphere is largely transparent to these wavelengths.

7.0.1 Solar irradiance variations at different timescales

Solar irradiance variations can be related to different sources, acting on different timescales (Seleznyov et al., 2011). Short-timescale (from minutes to hours) are attributed to solar oscillations, the p-modes, to the evolution of granules and to the passage of sunspots and faculae over the solar disk. On daily and monthly timescale, the evolution of sunspots (on few days, typically) and active regions as well as the solar rotation itself can produce solar irradiance variations. From the solar rotation period ($\sim$ 27 days) to the 11-year solar cycle period, the growth, evolution, and decay of active regions, as well as the distribution of their remnant magnetic field over the solar surface provide the main contribution to the variability. This is strongly modulated by the activity cycle itself, which is a very strong contributor to irradiance variations. Beyond the solar cycle period, the possible evolution of the background field and other mechanisms may lead to secular changes, which might be visible in the form of different TSI levels at the different minima.

Indeed, one of the most striking feature in solar cycle activity is that each cycle lasts between 8 and 14 years, with an average length of approximately 11.2 years. Cycle amplitudes vary even more strongly, with the weakest known cycle (starting around 1700) being less than 10% in strength of the strongest cycle, cycle 19, although in the minima between the cycles the sunspot number reaches nearly zero (Hathaway, 2010). Almost as striking as the presence of the cycles is their absence, along with the near absence of sunspots themselves, between roughly 1640 and 1700 (Eddy, 1976). This is the so-called Maunder minimum, the primary example of a grand minimum of solar activity, which in this case overlapped with a particularly cold part of the Little Ice Age (LIA). Grand minima and maxima are almost randomly distributed, although grand minima tend to come in clusters separated by roughly 2.000 years. Unlike the grand maxima, whose duration follows an exponential distribution, the grand minima come in two varieties, a short (30-90 year) type, with the Maunder minimum being a classic example, and a long (>110 year) type, such as the Spörer minimum (1390-1550) (Solanki et al., 2004; Usoskin, 2013; Usoskin et al., 2016; Vecchio et al., 2017).

7.1 The Earth's climate system

It is well-established that the solar irradiance changes can affect global planetary surface temperature evolution, since oceans are able to store a considerable amount of solar incoming energy which is then released into the atmosphere (White et al., 1997; Solanki et al., 2013, and references therein). Indeed, any variation in the solar radiative energy can potentially affect our climate and, hence, the habitability of Earth. An important question is how this influence is strong if compared with other mechanisms, including the anthropogenic effects on greenhouse gases? This has been debated for a long time, with increasing urgency due to the "anomalous" global temperature rise affecting Earth's surface in the last 40 years. The recent global warming is usually attributed to the release of greenhouse gases, foremost among them carbon dioxide, into Earth's atmosphere, mainly produced by fossil fuel burning as well as tropical deforestation, with concentrations that have increased up to about 313 parts per million (ppm) in the last 3-4 decades (Solomon et al., 2007; IPCC, 2014). Indeed, the latest Assessment Report from the Intergovernmental Panel on Climate Change states that "atmospheric concentrations of carbon dioxide, methane and nitrous oxide are unprecedented in at least the last 800,000 years. Their effects, together with those of other anthropogenic drivers, have been detected throughout the climate system and are extremely likely to have been the dominant cause of the observed warming since the mid-20th century" (IPCC, 2014). More specifically, over the past 800.000 years, carbon dioxide has varied from low-values (180 ppm) to moderate-values during the pre-industrial era (270 ppm), until high-values nowdays. These variations can be a fundamental factor influencing climate variations over a centennial timescale (Hansen, 2005).

However, determining the exact level of warming due to "anthropogenic" greenhouse gases requires a good understanding of the natural causes of climate change. Indeed, these natural causes can lead temperature variations, on both positive and negative values, of the order of $\sim 5-10$ °C. They are partly related to both internal processes, including oceans, land surfaces, biosphere-cryosphere-atmosphere interactions, partly arising from Earth's interior dynamics (i.e., release of aerosols and dust through volcanic eruptions), and external ones, generally referred as astronomical effects.

A variety of astronomical effects can influence Earth's climate, as for example energetic radiation from a nearby supernova that could affect our atmosphere (Svensmark, 2012) or, also, modulation of cosmic rays as the Sun passes into and out of spiral arms during its orbit around the Galaxy (Shaviv, 2002). These processes have been proposed to explain slow variations in climate taking place over hundreds of millions of years. However, the most obvious astronomical influence is due, directly or indirectly, to the Sun, which can influence Earth's climate by variations in insolation through changes in the Sun's radiative output itself (direct influence) or modulations of the radiation reaching different hemispheres of Earth through changes in Earth's orbital parameters (indirect influence). The first of these is generally considered to be the main cause of the solar contribution to global climate change, affecting Earth's energy balance, with changes in TSI, or variations in SSI, particularly in UV irradiance, which can produce variations in the chemistry of Earth's middle atmosphere. The second one is now accepted as the primary cause of the pattern related to the formation of ice ages and the interglacial warm periods, dominating the longer term evolution of the climate over the past few million years. These variations, on larger timescales (typically thousands of years), are named as Milankovitch forcings (or effects) (Crucifix et al., 2006; Paillard, 2001). They include the collective effects of changes in the Earth's motion upon its climate such as variations in orbital shape (eccentricity), axial tilt (obliquity) and precession. Eccentricity variations induce seasonal changes with variations in the perihelion and aphelion positions. This produces an increase of summer and spring durations in northern hemisphere, with insolation changes reflecting on temperature, with a cyclicity of $\sim$ 100.000 years. Axial tilt is related to fluctuations of the angle of the Earth's rotation axis with respect to the plane of the Earth's orbit, which varies approximately in a roughly periodic way on 41.000 years. When the obliquity increases, the amplitude of the seasonal cycle in insolation increases, with summers in both hemispheres receiving more radiative energy, producing a global temperature increase. Precession, which is the trend in the direction of the Earth's axis of rotation relative to the fixed stars, with a period of $\sim$ 26.000 years, produces a tilt around the Sun of the poles, inducing both positive and negative temperature fluctuations. Other natural variations are related to internal fluctuations related to the ocean temperature and energy changes, and to volcanic eruptions. Indeed, oceans are a great reservoir of heat which can be redistributed across the Earth's surface, modifying the energy budget and increasing temperature, through their interactions with the atmosphere. Ocean circulation seems to be related to the occurrence of multi-millennial climate patterns, known as Dansgaard-Oeschger events, characterized by fast warmings of the surface temperature. Conversely, volcanic eruptions release several gases and dusty materials which change the atmospheric composition, producing both increase and decrease of temperature.

7.1.1 Solar influence on climate

Daily and seasonal fluctuations in Earth's surface temperature as well as atmospheric energy content variations can be partially related to the solar forcing. As also explained in Chapter 1, the Maunder minimum coincided with the Little Ice Age (LIA) during which most of the temperature records show cooler values. This interpretation does not imply a direct connection between solar variations and surface temperature because other factors may also have contributed. Indeed, in the same epoch, higher levels of volcanism were reported which can also have introduced a cooling tendency due to a veil of particles injected into the stratosphere reflecting the Sun's radiation back to space, as well as a negative phase of a natural variation in climate referred to as the North Atlantic Oscillation (NAO).

Across the Holocene (i.e., the time interval started around 10.000 years before present), isotope records provide evidence that solar grand maxima/minima affect climate, although these studies all rely on the reliability of the dating, which is complex and not always precise (Lockwood et al., 2010). During the last century, the temperature has increased by about 1 °C, while the solar forcing may have introduced an overall global warming of approximately 0.07 °C (Solanki et al., 2013), a small fractional contribution to global warming ($\sim$ 7%). This also suggests that it is not possible to reproduce the global warming of recent decades by only considering solar forcing variations.

Although it seems that a direct solar contribution is not present on Earth's surface temperature variations, a significant solar effect is found in atmospheric observations. Indeed, it is well-established that stratospheric ozone responds to solar activity, with variations in the vertically integrated ozone column of 1-3% in phase with the 11-year solar cycle, particularly evident in the subtropical regions, with solar cycle variations appearing peaked in the middle and lower stratosphere. These correlations imply temperature differences in those regions of up to 1 °C between minimum and maximum of the 11-year solar cycle.

To explain the observed solar signal in climate, a wide range of physical and chemical processes are proposed, that are summarized in Figure 7.1.

About one half of the TSI entering the top of the atmosphere is transmitted to and warms the Earth's surface so that variations in TSI have the potential to influence climate through what have become known as bottom-up mechanisms. Solar UV radiation, however, is largely absorbed by the

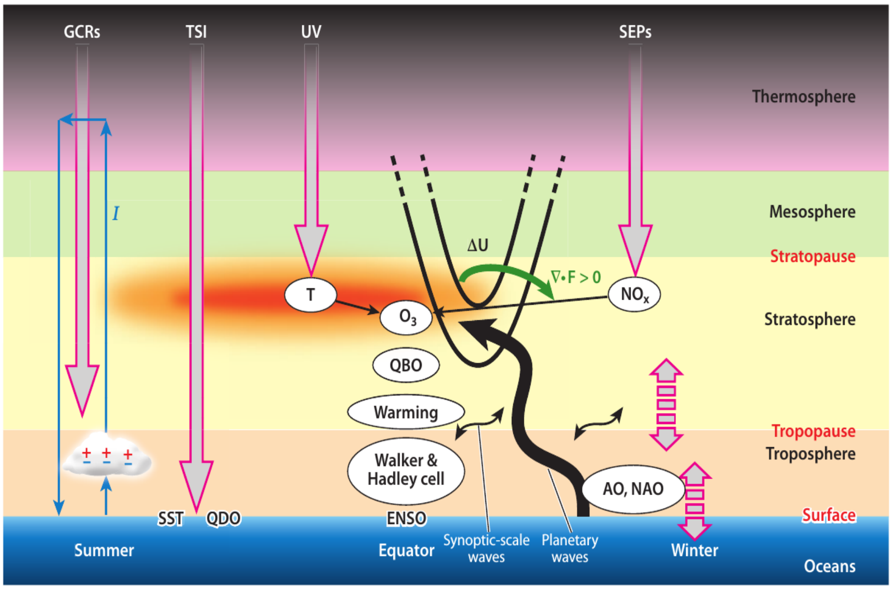

Figure 7.1: A view of mechanisms proposed to explain solar influence on climate.

middle atmosphere meaning that variations in UV have the potential to produce a top-down effect. In either cases, the response of the atmosphere and oceans involves complex feedbacks through changes in winds and circulations so that the directive radiative effects provide only the initiating step. The most famous mechanisms to investigate solar influence on climate is related to the study of the solar radiative forcing of climate. This concept is widely used to analyze and predict the response of surface temperature to climate change factors, including increasing concentrations of greenhouse gases, changes in planetary albedo as well as changes in solar input (Budyko, 1969; Sellers, 1969; Watson and Lovelock, 1983; Solomon et al., 2007; Alberti et al., 2015, and references therein). It is useful because, with the help of both general circulation models and observations, it has been shown that changes in globally averaged surface temperature are linearly related to the mean radiative forcing value, allowing the definition of a constant of proportionality, called the climate sensitivity parameter λ, estimated to be in the range of 0.4-1.2 K W^{-1} m^2 (Le Treut, 2012). This indicates that the response of the global mean surface temperature to a solar perturbation of 1 W m^{-2} would be 0.6 K. In this way, we can use λ to indicate the role of the Sun in global climate change.

7.1.2 The greenhouse effect

However, it is well-known that most of the climate variations can be attributed to the greenhouse effect. The greenhouse effect is a natural phenomenon which allows to regulate the thermal equilibrium of a planet with a surrouding atmosphere. Indeed, it is related to the absorption and reflection properties of peculiar gases, named as greenhouse gases, which are able to reflect the UV solar incoming radiation outside the planet and absorb a portion of the planetary infrared radiation in the atmosphere. It can be also seen as the process by which radiation stored in Earth's atmosphere warms the planetary surface to a temperature above what it would be without its atmosphere. How does greenhouse effect work on Earth? Earth receives energy from the Sun in the form of ultraviolet, visible and near-infrared radiation. Of the total amount of solar energy available at the top of the atmosphere, about 30% of the radiation striking Earth's atmosphere is immediately reflected back out to space by cloud, ice, snow and other reflective surfaces. The remaining 70% of incoming solar radiation is absorbed by the oceans, the land and the atmosphere. As they heat up, the oceans, the land and the atmosphere release heat in the form of IR thermal radiation, which passes out of the atmosphere and into space. It is this equilibrium of incoming and outgoing radiation that makes the Earth habitable, with an average temperature of about 15 °C. Without this atmospheric equilibrium, Earth would be as cold and lifeless as its moon, or as blazing hot as Venus.

7.1.3 Climate changes and modeling

Previous processes and phenomena are all involved into the so-called climate changes. Climate change is defined as the variation in global or regional climates over time, reflecting changes in the variability of the atmosphere over timescales ranging from decades to millions of years. These changes can be caused by internal processes, external forcings (e.g., variations in insolation) or, more recently, human activities.

In recent usage, the term "climate change" often refers only to changes in modern climate, including the rise in average surface temperature known as global warming. This is not properly true since Earth has undergone periodic climate shifts in the past, including four major ice ages. These consist of glacial periods where conditions are colder than normal, separated by interglacial periods, where temperature increases. The accumulation of snow and ice during a glacial period increases the surface albedo, reflecting more of the Sun's energy into space and maintaining a lower atmospheric temperature. Increases in greenhouse gases, such as by volcanic activity, can increase the global temperature and produce an interglacial period. Suggested causes of ice age periods include the positions of the continents, variations in the Earth's orbit, changes in the solar output, and volcanism. These processes suggest that, in the Earth's climate history, we can find both periods characterized by increases in temperature and time intervals in which the global mean temperature decreases. However, the observed rising in temperature cannot be only attributed to an intrinsic natural variability of the climate system. For these reasons, we need to investigate the dynamics of climate changes by using climate models, which can be helpful to study conditions for life on Earth as well as both internal and external variability. Climate models are used to simulate the interactions of the atmosphere, oceans, land surface and ice, for a variety of purposes: from the study of the dynamics of the weather and climate system to projections of future climate. The most complete models are based on General Circulation Models (GCMs) which have been built up to numerically solve nonlinear partial differential equations to take into account air-mass motion (i.e., by using fluid equations), ocean-atmosphere interactions and greenhouse gases variations. Simpler climate models, known as energy-balance models, are based on the balance between the incoming energy as short wave (including visible) electromagnetic radiation to the Earth and outgoing energy as long wave (infrared) electromagnetic radiation from the Earth. Both model types are used to infer the consequences of increasing greenhouse gases in the atmosphere, primarily carbon dioxide, and to predict an upward trend in the global mean surface temperature, showing that the most rapid increase in temperature is observed for the higher latitudes of the Northern Hemisphere. Chapter 8 will explore the climate dynamics during the last glacial period, i.e., the time interval between 20.000 and 120.000 years before present (BP), while in Chapters 9 and 10 two different energy-balance models and their stability properties as well as their numerical solutions will be discussed.

Chapter 8

Northern Hemisphere-Southern Hemisphere connection of fast temperature changes during the last glacial period[1]

This chapter concerns the investigation of both the time evolution of the so-called Dansgaard-Oeschger events and the dynamics at longer timescales during the last glacial period. It is shown that the time behavior at the typical timescales of Dansgaard-Oeschger events can be described as an excitation of the climate system within the same state, while the longer timescale behavior appears to be due to transitions between different climate states. Moreover, we evidence that the Antarctic climate changes lead those of Greenland by a lag of ∼3.05 kyr.

8.1 Introduction

The climate of the Holocene period, the time interval from 10.000 yr BP to the modern epoch, is much more variable than believed, reflecting a millennial-scale pattern (Denton and Karlèn, 1973; O'Brien et al., 1995; Bond et al., 1997). To investigate multi-scale patterns in paleoclimate research one of the most used proxy is the oxygen isotope δ^{18}O, which reveals that the sub-Milankovitch climate variability presents abrupt temperature

---

[1] The work presented in this chapter is included in the paper Alberti et al. (2014).

fluctuations, dominated the climate in Greenland between 11 and 74 thousand years before present (kyr BP) (NGRIP, 2004). These fluctuations, known as Dansgaard-Oeschger (DO) events, lasts few decades and produces fast warming, with temperature increasing up to 15 °C compared to glacial values. Generally, the counterpart of a DO event is knwon as Heinrich event (Heinrich, 1988), characterized by plateau phases and slow coolings of several centuries (e.g., Bond et al., 1992; Rahmstorf, 2002). These cooling events are recorded in North Atlantic Ocean sediments and are characterized by variable spacings of several thousand years, usually with massive iceberg releases from the Laurentide ice sheet into the North Atlantic (Bond et al., 1992; Broecker, 1994).

DO events are usually attributed to the coupling between the Atlantic Ocean thermohaline circulation (THC), changes in atmospheric circulation and sea-ice cover (e.g., Rahmstorf, 2002). In this context, several ideas have been developed to explain DO events as THC bistability (Broecker, 1994) and its internal oscillations (Broecker et al., 1990) as well as latitude shifts of oceanic convection (Rahmstorf, 1994).

In Antarctic records several events, known as Antarctic Isotope Maxima (AIM), less pronounced than DO, have been recognized. These are characterized by much more gradual warming and cooling with respect to DO (EPICA, 2004). Neverthless, previous works support the idea that an inter-hemispheric coupling could develop between DO and AIM events, with both synchronous evolution between north and south (e.g., Bender et al., 1994) and the existence of systematic lags between Antarctica and Greenland warming trends, with the first leading the second by 1-2.5 kyr (Blunier et al., 1998). The simplest model supporting these findings is based on the so-called classical bipolar seesaw (Broecker, 1998; Stocker, 1998), according to which an antiphase relation should exist between north and south. More recently, an advanced model has been proposed, the thermal bipolar seesaw model, to include the effect of a thermal reservoir, which is able to reproduce much of the variability observed in ice core records (Stocker and Johnsen, 2003; Barker et al., 2011).

Although, a criterion for the identification of DO events cannot be firmly established such that their claimed roughly periodic and non-sinusoidal character, with a basic period of about T $\simeq$ 1450-1500 yr, has been questioned on the basis of the fact that a null random hypothesis for these events cannot be fully rejected (Ditlevsen et al., 2007; Schulz, 2002; Peavoy and Franzke, 2010). Usually, DO events were firstly determined visually (Dansgaard et al., 1993), but when different definitions are used, some events are excluded from the list or additional events are included, thus changing the basic periodicity (Ditlevsen et al., 2007; Schulz, 2002; Rahmstorf, 2003; Alley et al., 2001; Ditlevsen et al., 1973; Bond et al., 1999). As an example, Schulz (2002) showed that the basic cycle is determined solely by DO events 5, 6, and 7, even if a fundamental period of about 1470 years seems to control the timing of the onset of the events. On the other hand, different periodicities in the range 1-2 kyr have been found from deep-sea sediment cores in the sub-polar North Atlantic (Bond et al., 1999). It is well recognized that one of the main problems comes from the non-stationarity of the oxygen isotope data sets (Ditlevsen et al., 2007; Schulz, 2002), and advanced signal processing tools turned out to be useful to characterize the observed climatic variability (e.g., Solé et al., 2007*a*).

In this study, we present a study of climate variability in Antarctica and Greenland, based on the EMD analysis which allows us to recognize the dominant variability patterns and characterize the climate transitions which can be associated with DO events and longer timescale changes. Moreover, though the cross-correlation analysis we identify the existence of correlation lags at different timescales between the two signals.

8.2 Data sets

The EPICA data set provides a record of the oxygen isotope δ^{18}O from the EPICA Dronning Maud Land (EDML) Ice Core (75.00° S, 0.07° E; 2892 m a.s.l.) covering the period 0-150 kyr BP (EPICA, 2006). Conversely, the NGRIP project (75.10° N, 42.32° W; 2917 m elevation) released a δ^{18}O record that extends back to 123 kyr BP (NGRIP, 2004). For our analysis, we consider the interval 20-120 kyr BP for both the data sets, since this is the interval in which significant temperature changes, which are the focus of the present work, are observed (see Figure 8.1). This is a part of the last glacial period, before the actual inter-glacial period known as Holocene. For both the data sets the AICC2012 age scale is used (Veres et al., 2013; Bazin et al., 2013).

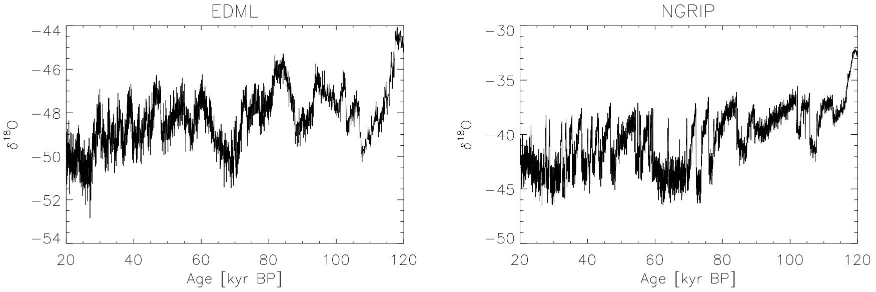

Figure 8.1: δ^{18}O data for the EDML (upper panel) and NGRIP (lower panel) data sets in the period 20–120 kyr BP.

8.3 EMD results

The main periodicities and their amplitudes are identified by means of the empirical mode decomposition (EMD), also used in the context of paleo-climatic studies (Solé et al., 2007*b*) to investigate the oscillation patterns in GRIP, Vostok and EPICA time series of temperature proxies. From the EMD procedure we obtain a set of m = 15 *IMFs* for EDML (see Figure 8.2), which we denote as $C_j^{(S)}(t)$, and m = 17 *IMFs*, named $C_j^{(N)}(t)$, for NGRIP (see Figure 8.3).

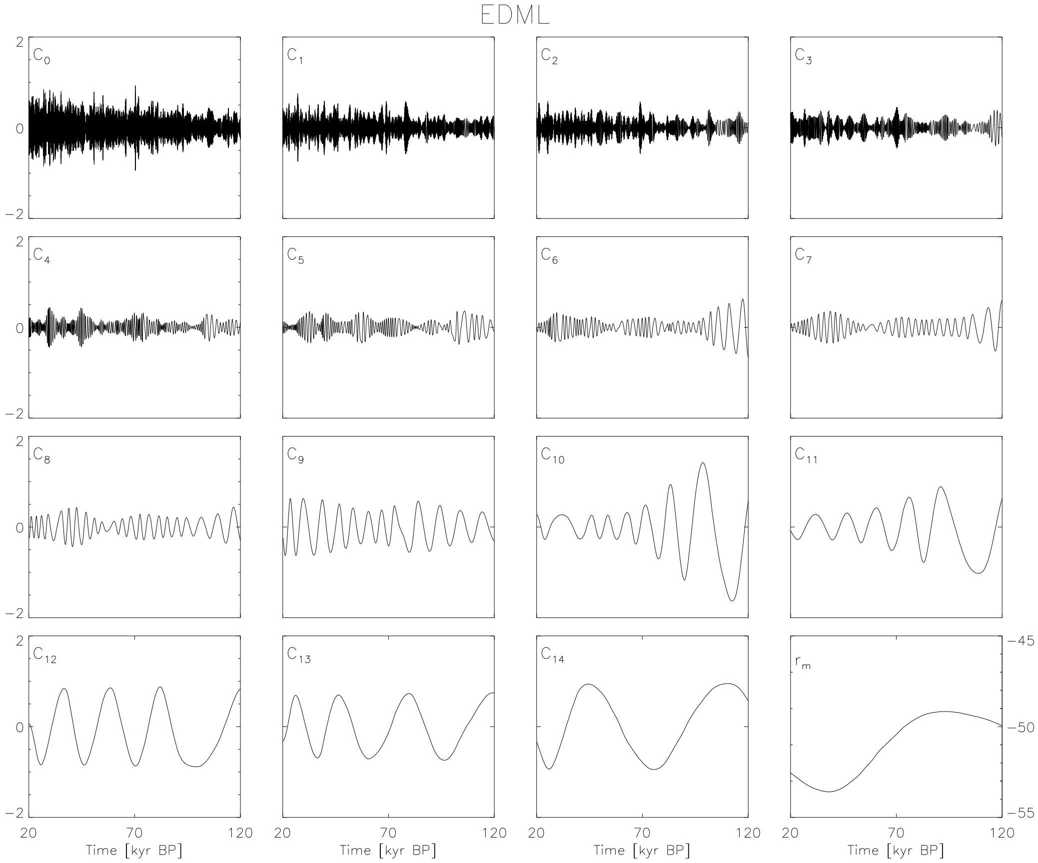

Figure 8.2: *IMFs* $C_j^{(S)}(t)$ and residue $r_m^{(S)}(t)$ for the EDML data set.

As shown in Figures 8.2 and 8.3, the well-known "mode mixing" problem seems to be evident for some *IMFs* for both data sets, e.g., $C_5^{(S)}(t)$, $C_6^{(S)}(t)$, $C_{10}^{(S)}(t)$, $C_8^{(N)}(t)$, $C_9^{(N)}(t)$, $C_{10}^{(N)}(t)$, $C_{11}^{(N)}(t)$, consisting of empirical modes containing different frequencies or similar timescale variations residing in different *IMFs* (Huang et al., 1998). However, this effect is not crucial in our analysis since in the following we will discuss signals obtained through

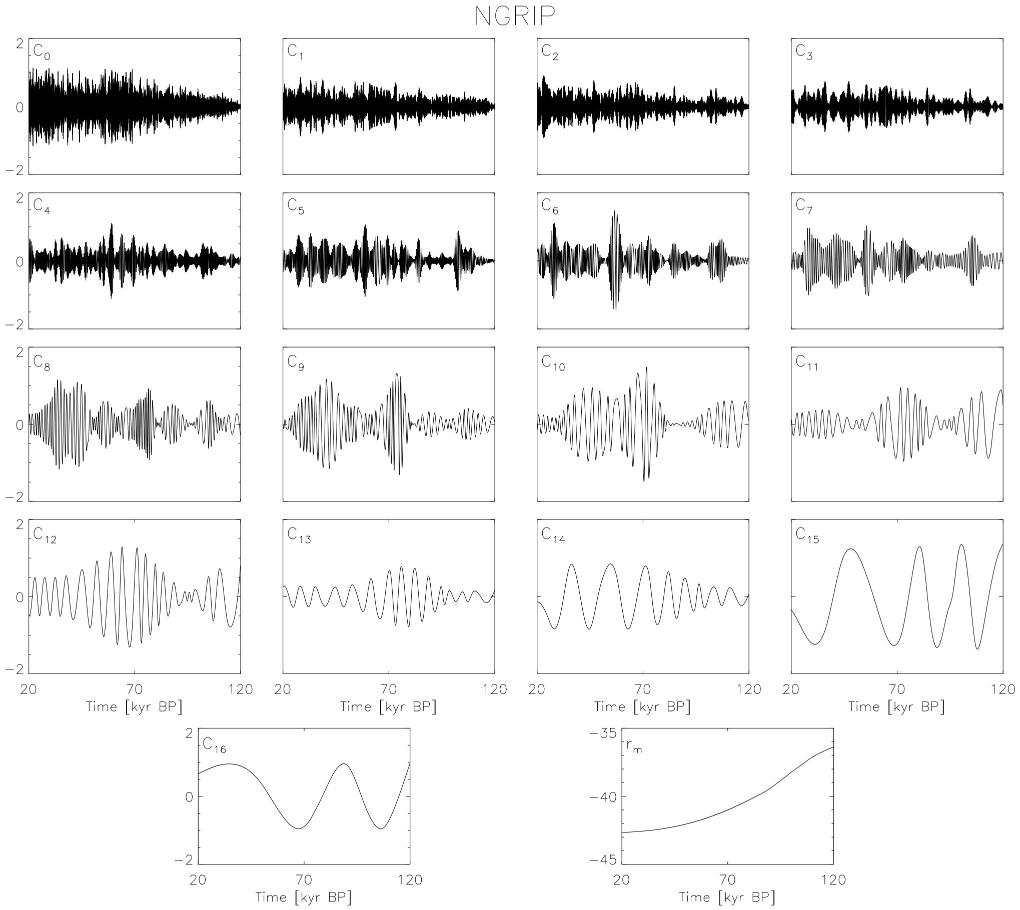

Figure 8.3: *IMFs* $C_j^{(N)}(t)$ and residue $r_m^{(N)}(t)$ for the NGRIP data set.

partial sums by adding *IMFs* ranging in a wide range of timescales.

Moreover, we also perform the significance test (Wu and Huang, 2004) as shown in Figure 8.4, by using a significance level of 99%. The empirical modes which are above the spread line in Figure 8.4 can be considered significant at 99th percentile. For EMDL data set, the significant modes are $j = 5 - 14$, while modes $j = 4 - 16$ are significant for NGRIP data. For both time series, the characteristic periods T_j are reported in Table 8.1.

We investigate the dynamics of the DO events by reconstructing the sum of the $j = 6 - 10$ NGRIP *IMFs* (which have characteristic periods between 0.7 kyr and 3.3 kyr) and, by choosing the same characteristic period range for EMDL, the modes $j = 5{-}8$ are selected. Therefore the two “short” timescale reconstructions $N_H(t)$ and S_H (t), for NGRIP and EDML respectively, are defined as

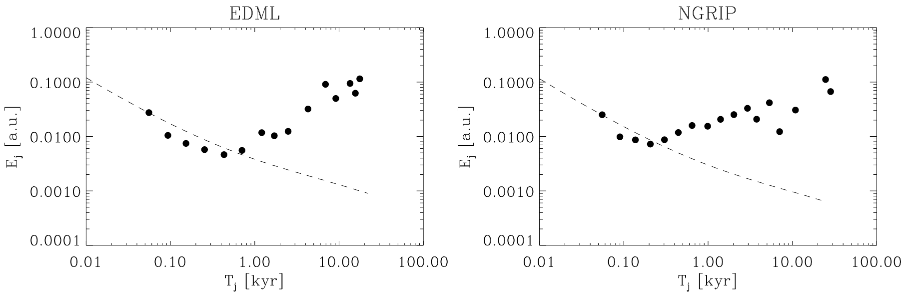

Figure 8.4: Normalized *IMF* square amplitude E$_j$ vs. the period T$_j$ for the EMD significance test applied to the EDML (upper panel) and NGRIP (lower panel) *IMFs*. The dashed lines represent the 99th percentile (Wu and Huang, 2004).

$$N_H(t) = \sum_{j=6}^{10} C_j^{(N)}(t), \tag{8.1}$$

$$S_H(t) = \sum_{j=5}^{8} C_j^{(S)}(t) \tag{8.2}$$

Moreover, the variability at longer timescales with respect to those involved in DO events can be investigated by using the modes $j = 11 - 16$ and $j = 9 - 14$ for NGRIP and EDML respectively. The corresponding two “long” timescale reconstructions N$_L$(t) and S$_L$(t) are thus given by

$$N_L(t) = \sum_{j=11}^{16} C_j^{(N)}(t), \tag{8.3}$$

$$S_L(t) = \sum_{j=9}^{14} C_j^{(S)}(t) \tag{8.4}$$

In Figure 8.5 the δ^{18}O original data (black lines), the short timescale (red lines) and the long timescale (blue lines) reconstructions are shown for the EDML (upper panel) and NGRIP (lower panel) data sets.

The results of the EMD decomposition suggest that the evolution of cooling-warming cycles over the investigated period can be described in terms of two dynamical processes occurring on different timescales. In the next section, we present a simple model to describe this phenomenology.

j	EDML $T_j \pm \Delta T_j$ [kyr]	NGRIP $T_j \pm \Delta T_j$ [kyr]
4		0.33 ± 0.10
5	0.77 ± 0.29	0.49 ± 0.15
6	1.30 ± 0.46	0.72 ± 0.26
7	1.84 ± 0.51	1.10 ± 0.41
8	2.70 ± 0.63	1.57 ± 0.64
9	4.7 ± 1.5	2.4 ± 1.1
10	7.4 ± 2.6	3.3 ± 1.4
11	10.3 ± 2.5	4.2 ± 1.7
12	15.0 ± 3.3	6.0 ± 2.3
13	16.4 ± 4.0	7.9 ± 1.9
14	30.7 ± 7.8	13.6 ± 7.9
15		29.0 ± 11.0

Table 8.1: Characteristic periods of the significant *IMFs* obtained for the EDML and NGRIP data sets through the EMD. Errors are estimated as standard deviations of the instantaneous periods. The period T_{16} calculated for the $j = 16$ NGRIP mode is not reported as it is not sufficiently shorter than the time series length, although the mode is significant.

8.4 Potential analysis

As shown by Paillard (2001), glacial-interglacial cycles can be modeled as transitions between different climate states. Similarly, the dynamics of DO events is commonly modeled as a two-state, cold/stadial and warm/interstadial, system. Following the approach proposed by Livina et al. (2010) we are able to identify the number of climate states present in both NGRIP and EDML records. To this purpose, we describe the climate system as a nonlinear system with many dynamical states, assuming that transitions among states are triggered by a stochastic forcing. A very simple model for this is the one-dimensional Langevin equation

$$dz = -U(z)dt + \sigma dW \tag{8.5}$$

where z represents, in our case, the oxygen isotope δ^{18}O, $U(z)$ is the potential, σ is the noise level and W is a stochastic Wiener process. Equation (8.5) admits a stationary solution when $U(z) = 0$, with $U(z)$ generally defined as a polynomial of even order and positive leading coefficient. In this way, the order of the polynomial fixes the number of available states: for example, a fourth-order polynomial, corresponding to a double-well potential, identifies a system with two states. The number of states can be

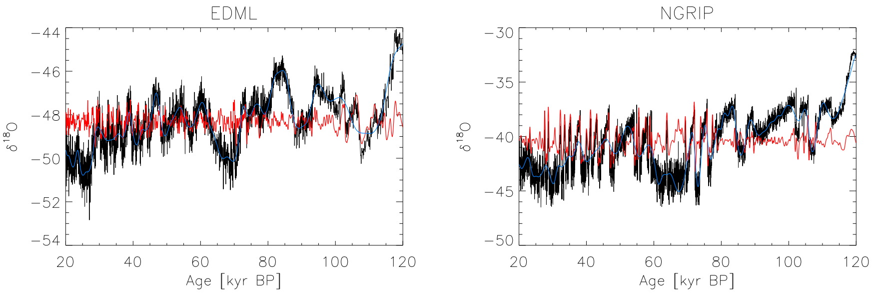

Figure 8.5: δ^{18}O data (black lines), short timescale reconstructions N$_H$(t) and S$_H$(t) (red lines), and long timescale reconstructions N$_L$(t) and S$_L$(t) (blue lines) for the EDML (upper panel) and NGRIP (lower panel) data sets. An offset corresponding to the temporal mean of the δ^{18}O original data was applied to the EMD reconstructions in order to allow visualization in the same plot.

evaluated from the data by performing a polynomial fit of the probability density function (pdf) calculated as

$$p(z) \sim exp[-2U(Z)/\sigma^2] \tag{8.6}$$

representing a stationary solution of the Fokker-Planck equation

$$\frac{\partial p(z,t)}{\partial t} = \frac{\partial [U(z)p(z,t)]}{\partial z} + \frac{1}{2}\sigma^2 \frac{\partial^2 p(z,t)}{\partial z^2} \tag{8.7}$$

Equation (8.6) establishes a one-to-one correspondence between the potential and the pdf of the system so that

$$U(z) = -\frac{\sigma^2}{2} \log p_{emp}(z) \tag{8.8}$$

where $p_{emp}(z)$ is the empirical pdf extracted from data. To estimate $p_{emp}(z)$ we used the well-knwon kernel density estimator method (Silvermann, 1998; Hall, 1992), described in Appendix C. This procedure allows the calculation of $U(z)$ and the corresponding uncertainty from Eq. (8.8). In order to investigate the short- and long-timescale dynamics, potentials have been calculated for N$_H$(t), S$_H$(t), N$_L$(t) and S$_L$(t), and are reported in Figure 8.6.

The potentials associated with N$_H$(t), S$_H$(t) and the corresponding best fits are shown in panels a and b, respectively. They are well-fitted by second-order polynomials, thus corresponding to a single-well potential. This suggest that the occurrence of a DO event is not due to a transition of the

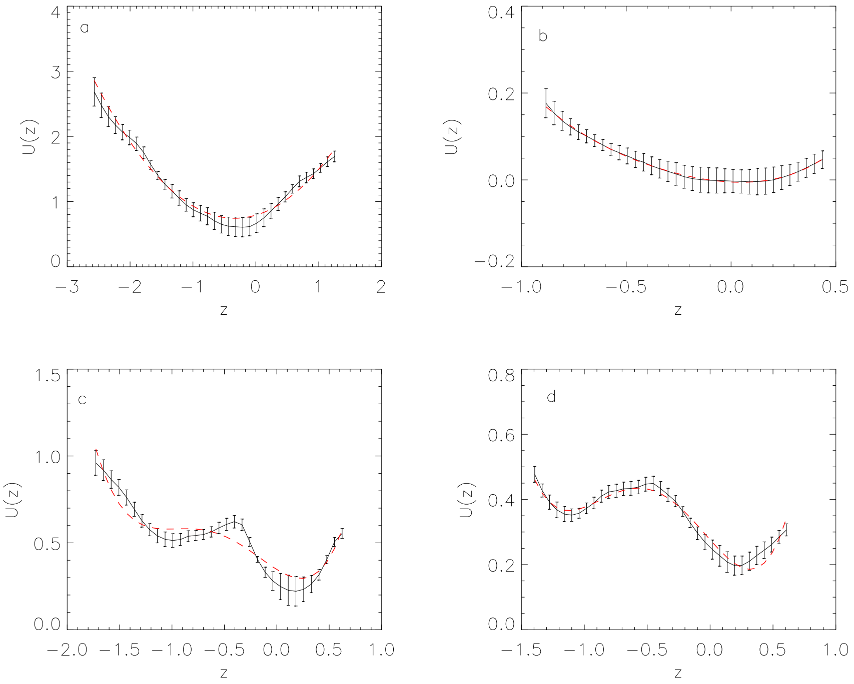

Figure 8.6: Potentials $U(z)$ calculated from the data (black curves and error bars) using Eq. (8.8) and polynomial best fits (red dashed curves) for NGRIP reconstructions $\mathrm{N}_H(\mathrm{t})$ (a), $\mathrm{N}_L(\mathrm{t})$ (c), and EDML reconstructions $\mathrm{S}_H(\mathrm{t})$ (b), $\mathrm{S}_L(\mathrm{t})$ (d).

system between different dynamical states but to an excitation of the system within the same state. On the other hand, the $U(z)$ calculated for $\mathrm{N}_L(\mathrm{t})$ and $\mathrm{S}_L(\mathrm{t})$ show a double-well potential function, fitted by forth-order polynomials, thus suggesting that longer timescale dynamics is characterized by two different dynamical states: high activity, when the DO events are observed, and low activity periods.

This approach presents some differences with respect to Livina et al. (2010) since we perform the potential analysis on the EMD reconstructions of the EDML and NGRIP data sets, using the time range 20-120 kyr BP. Differently, Livina et al. (2010) used only Greenland data sets (GRIP and NGRIP δ^{18}O time series) and a shorter time interval (0-60 kyr BP). Moreover we calculate the potential shape from the full time range of the EMD reconstructions, while they used sliding windows of varying length through each data set to detect the number of climate states as a function of time.

8.5 The north-south asynchrony

One of the main aspects in polar climate dynamics is the understanding of how Earth's hemispheres have beed coupled during past climate changes. Several mechanisms have been proposed by invoking partial deglaciation and changes in ocean circulation which transfer warmings in Northern Hemisphere climate to Antarctica (Bender et al., 1994), although different analyses showed that southern changes cannot be related to abrupt changes in North Atlantic thermohaline circulation (Morgan et al., 2002). Indeed, by studying the global concentration of the methane recorded in ice cores, Blunier et al. (1998) inferred that Antarctic climate changes lead those of Greenland by 1-2.5 kyr over the period 47-23 kyr before present. More recently, a near-zero-phase anticorrelation between the Greenland temperature anomaly and the rate of change of Antarctic temperature was observed (Barker et al., 2011). They also built up, by using the Antarctic record, an 800 kyr synthetic record of Greenland climate reproducing much of the variability for the last 100 kyr. We investigate this issue by studying the cross-correlation betweeen the EDML and NGRIP reconstructions obtained from the EMD as illustrated in Sect. 8.3. Generally, the cross-correlation coefficient $P_{xy}(\Delta)$ between two time samples $x(t_k)$ and $y(t_k)$ is defined as

$$P_{xy}(\Delta) = \frac{\sum_k [x(t_k+\Delta) - <x>][y(t_k) - <y>]}{\sqrt{\sum_k [x(t_k+\Delta) - <x>]^2 \sum_k [y(t_k+\Delta) - <y>]^2}} \tag{8.9}$$

where brackets denote time average and Δ the time lag. The two coefficients $P_{N_H S_H}(\Delta)$ and $P_{N_L S_L}(\Delta)$, for both the short timescale reconstructions (Eqs. (8.1) and (8.2)) and for the long timescale ones (Eqs. (8.3) and (8.4)), are shown in Figure 8.7.

$P_{N_H S_H}(\Delta)$ presents oscillations with many peaks of similar amplitude at both negative and positive lags, a typical behavior of oscillating signals having nearly the same frequency. This not allow to identify leading/following processes. Conversely, a single significant peak, with a maximum value of $\sim$0.73 and $\Delta = 3.05 \pm 0.19$ kyr, is found in $P_{N_L S_L}(\Delta)$. We also build up a procedure to estimate the uncertainty in the correlation peak position by means of the following procedure. We use the errors on the age scale available in the EDML and NGRIP data to built up a Monte Carlo algorithm, allowing us to estimate the time errors on $N_L(t)$ and $S_L(t)$. More specifically, a set of 10^3 realizations of the long timescale reconstructions, randomly varying within the age-scale error window of each data point, is obtained. Then, the corresponding 10^3 cross-correlations between the EDML and NGRIP long timescale reconstructions and the peak positions for each of them are evaluated. Following this procedure we obtained the above-mentioned estimate of 0.19 kyr for the error on the position of the long timescale cross-correlation peak. The result obtained through the cross-correlation analysis supports

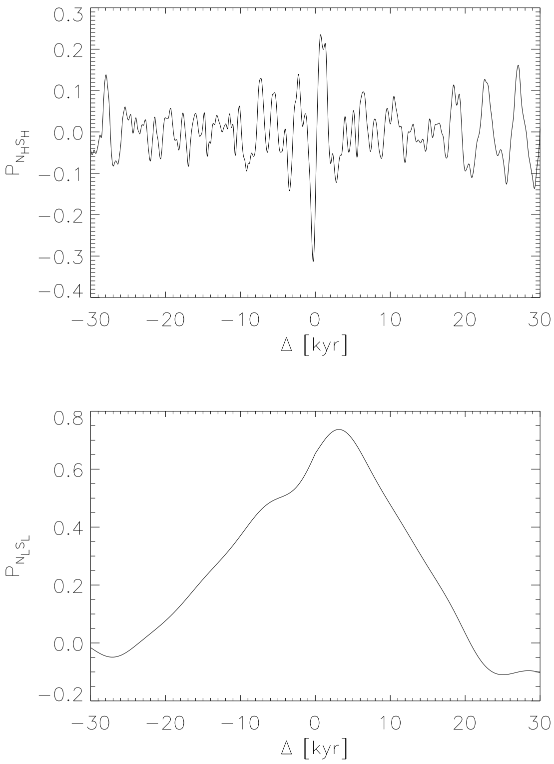

Figure 8.7: Cross-correlation coefficients between EDML and NGRIP short timescale ($P_{N_H S_H}(\Delta)$, top panel) and long timescale ($P_{N_L S_L}(\Delta)$, bottom panel) EMD reconstructions as functions of the time lag Δ.

the view according to which the Antarctic climate changes actually lead those of Greenland, but on longer timescale than previously reported.

8.6 Conclusions and discussion

In the present study, we investigate both the EDML and NGRIP data sets, their periodicities and the possible existence of synchronization of abrupt climate changes observed in the Northern and Southern hemispheres. Our results can be summarized as follows.

1. Proper EMD modes, significant with respect to a random null hypothesis, are present in both data sets, thus confirming that natural cycles of abrupt climate changes during the last glacial period exist and their occurrence cannot be due to random fluctuations in time.

2. Due to the non-stationarity of the process, the variability at the typical timescales of DO events is reproduced through signal reconstructions

obtained by summing more than one EMD mode, kore precisely $j = 6 - 10$ for NGRIP and $j = 5 - 8$ for EDML. On the other hand, the reconstructions obtained by summing the successive modes can be used to describe the climate evolution at longer timescales, characterized by intervals in which DO events happen and intervals when these are not observed.

3. By comparing the EMD signal reconstructions to the results of a simple model based on the one-dimensional Langevin equation, evidence is found that the occurrences of DO events can be described as excitations of the system within the same climate state, rather than transitions between different states. Conversely, the longer timescale dynamics appear to be due to transitions between different climate states.

4. On the basis of a cross-correlation analysis between the NGRIP and EDML EMD reconstructions, performed to investigate the north-south asynchrony, it is found that the clearest correlation occurs between the long-scale reconstructions at a lag $\Delta = 3.05 \pm 0.19$ kyr, which support the view according to which the Antarctic climate changes lead those of Greenland, but on a longer timescale than previously reported.

The methodological novelty of this work is represented by the fact that we use EMD reconstructions to investigate the climate dynamics at different timescales and to highlight, through a potential analysis fo the EMD reconstructions, some characteristics of the climate transitions. The main new results are:

1. the presence of two different climate transitions occurring at different timescales;

2. the finding of a significant correlation between long timescale Antarctic and Greenland signals, with the first leading the second, at a lag of $\sim$3 kyr, which was not found in past studies of paleoclimatic records.

The EMD filtering procedure applied on EDML and NGRIP data sets and the correlation analysis based on it are able to identify timescale-dependent dynamical features of the climate evolution which have not been underlined in previous works. How the interhemispheric coupling mechanisms, such as the THC, can be involved in the behavior highlighted by our study is a question which needs to be investigated in future works. We suggest that the results of our correlation analysis, and in particular the correlation found in association with the long timescale dynamics, could be explained in the framework of seesaw models. But, since the correlation lag ($\sim$3 kyr) obtained from our analysis is quite different from the characteristic thermal timescale (about 1-1.5 kyr) of previous bipolar seesaw models

(Stocker and Johnsen, 2003; Barker et al., 2011), it would be necessary to build up a thermal seesaw model starting from our EMD filtered long timescale series to properly deal with this problem.

Chapter 9

Spatial interactions in a modified Daisyworld model: heat diffusivity and greenhouse effects[1]

In this chapter we investigate a modified version of the Daisyworld model, originally introduced by Lovelock and Watson to describe in a simple way the interactions between an Earth-like planet, its biosphere and the incoming solar radiation. The main novelties refer to the inclusion of a spatial dependency on latitude, and both a variable heat diffusivity along latitudes and a simple greenhouse effect description are introduced in the model. We show that the spatial interactions between the variables of the system can locally stabilize the coexistence of the two vegetation types. The feedback of albedo is able to generate new equilibrium solutions which can efficiently self-regulate the planet climate, even for values of the solar luminosity relatively far from the current Earth conditions.

9.1 Introduction

The interaction mechanisms between the Earth, its biosphere and the solar radiation, drive local and global climate changes within the complex system of the Earth's climate. This complexity can be investigated by using advanced climate simulations, even though the existence of many forcings and parameters that are not easy to control represent a considerable difficulty. Although their simplicity, energy-balance models are able to capture the fundamental dynamical mechanisms of the system. One of the most famous examples is the so called Daisyworld model, originally developed by

---

[1] The work presented in this chapter is included in the paper Alberti et al. (2015).

Lovelock and Watson (Lovelock, 1972; Lovelock and Watson, 1982; Lovelock, 1992*a*,*b*; Watson and Lovelock, 1983; Wood et al., 2008). It is based on a hypothetical planet, like the Earth, populated by two kinds of identical plants differing in their colour: white and black daisies. They reflect or absorb the incoming stellar radiation, producing local micro-climate and self-regulating the surface temperature, allowing to maintain the conditions for life.

The first version of the Daisyworld is a zero dimensional model, without any explicit representation of space and negligible atmospheric greenhouse effect. Moreover, solar radiation can be assumed to be distributed evenly over the planet and the two daisy populations receive the same amount of radiation. Watson and Lovelock (1983) showed that the surface temperature of the Daisyworld remains almost constant for a broad range of solar incoming variations, modifying the fractions of daisies covering the planet as solar input changes.

Several papers have been revisited the original model (De Gregorio et al., 1992; Harding and Lovelock, 1996; Nevison et al., 1999; Weber, 2001; Lenton and Lovelock, 2000, 2001) but only few authors (see e.g. Wood et al. (2008)) investigated the spatial dependence of the model to study the evolution of climate patterns (Wood et al., 2008; von Bloh et al., 1997; Ackland et al., 2003; Adams et al., 2003; Adams and Carr, 2003). Indeed, when a latitudinal spatial dependence is included, a striped pattern, consisting of black and white daisies bands, related to a Turing-like process (De Gregorio et al., 1992; Harding and Lovelock, 1996; Nevison et al., 1999; Weber, 2001; Lenton and Lovelock, 2000, 2001), emerges as an unrealistic aspect (Adams et al., 2003; Adams and Carr, 2003), causing destabilization of the system.

This study concerns the development of a new version of the Daisyworld model which includes spatial dependency, variable heat diffusivity and a parametrization of the the greenhouse effect by means of a grayness function. Significant new features have been shown, including a destabilization effect due to heat diffusion, a global heating process driven by the greenhouse effect, and a remarkable dependence on the initial conditions of both daisy coverage and temperature profile.

9.2 The model

The Daisyworld model (Lovelock, 1972; Lovelock and Watson, 1982; Lovelock, 1992*a*,*b*; Watson and Lovelock, 1983) describes the evolution of white and black daisies as logistic equations

$$\frac{d\alpha_w}{dt} = \alpha_w(x\beta_w - \gamma) \tag{9.1}$$

$$\frac{d\alpha_b}{dt} = \alpha_b(x\beta_b - \gamma) \tag{9.2}$$

where α_w and α_b are the fractions of surface covered by white and black daisies respectively, $x = 1 - \alpha_w - \alpha_b$ is the fraction of surface of fertile ground not covered by daisies, β_w and β_b are the growth rates of white and black daisies, and γ is the death rate per unit of time. The parameter γ is fixed to 0.3 (Lovelock, 1972; Lovelock and Watson, 1982; Lovelock, 1992*a*,*b*; Watson and Lovelock, 1983; Adams and Carr, 2003), while the growth rate of the daisies is assumed to be

$$\beta_\ell(T) = \begin{cases} 1 - \delta(T_e - T_\ell(T))^2 & |T_e - T_\ell(T)| \leq \delta^{-\frac{1}{2}} \\ 0 & \text{otherwise} \end{cases} \tag{9.3}$$

where the subscript ℓ denotes the species (either w or b), $\delta = 0.003265$ corresponds to a growth interval $5\ ^\circ\mathrm{C} \leq T_\ell(T) \leq 40\ ^\circ\mathrm{C}$, T is the planetary surface temperature, and T_ℓ represents the local temperature of each daisy species (Lovelock, 1972; Lovelock and Watson, 1982; Lovelock, 1992*a*,*b*; Watson and Lovelock, 1983). The growth rate β_ℓ reaches the maximum value ($\beta = 1$) when the local temperature is equal to the effective temperature $T_e = 22.5$ °C. In a simple linear approximation (Lovelock, 1972; Lovelock and Watson, 1982; Lovelock, 1992*a*,*b*; Wood et al., 2008), the local temperature can be assumed as depending by the albedo of the Daisyworld surface A and by T as $T_\ell = q(A(\theta, t) - A_\ell) + T(\theta, t)$, with the parameter q measuring the local heat diffusion ($q = 20$ K according to the original model (Lovelock, 1972; Lovelock and Watson, 1982; Lovelock, 1992*a*,*b*; Watson and Lovelock, 1983)). The albedo A of the planet depends on the planetary surface coverage as

$$A = \alpha_w A_w + \alpha_b A_b \tag{9.4}$$

where A_w and A_b represent the albedos of the two species ($A_w = 0.75$ and $A_b = 0.25$ (Watson and Lovelock, 1983; Lovelock, 1972; Lovelock and Watson, 1982; Lovelock, 1992*a*,*b*)). The planet radiates at a temperature which is calculated from the equilibrium between absorbed and emitted radiation, $\sigma T^4 = SL(1 - A)$, where σ is the Stefan's constant, S is the solar constant, L is a dimensionless parameter that describes the luminosity of the Daisyworld's sun ($L = 1$ for the present Earth). Numerical simulations show that the system settles down towards an equilibrium solution for values of the luminosity $0.5 \leq L \leq 1.5$ (Lovelock, 1972; Lovelock and Watson, 1982; Lovelock, 1992*a*,*b*; Adams and Carr, 2003).

Though the development of a spatial Daisyworld model we are able to investigate the effects of inhomogeneous solar forcing in a spherical planet, with explicit differences between poles and equator, and the direct use of the heat diffusion equation, so that the thermal equilibrium equation can be written as

$$\rho c_p \frac{\partial T}{\partial t} = (1 - A)R(\theta) - \sigma T^4 + \nabla \cdot [\chi(\nabla T)] \tag{9.5}$$

in which c_p and χ are the heat capacity and the conductivity of the Earth, ρ is the mass density of the atmosphere and R describes the incident radiation. As a first approach, by using a “spherical” planet, we assume that the temperature $T(\theta, t)$ and the surface coverage depend only on time and on latitude θ ($-90° \leq \theta \leq 90°$). Moreover, to take into account solar irradiance distribution along latitudes we introduce a simple functional form for R

$$R(\theta) = \frac{4}{\pi} SL \cos(\theta) \tag{9.6}$$

where we set $S = 1366$ W/m^2 which is a typical value for the solar constant. In addition, one of the weak points of the classical Daisyworld model is the absence of the atmosphere, corresponding to a lack in the contribution of greenhouse gases which play an important role in an Earth-like planet. To this purpose, we introduce, as a further step, the greenhouse effect in the model, by using a grayness function $g(T)$ (Sellers, 1969; Ghil, 1985) in the Equation (9.5), through the term $g(T)\sigma T^4$. Finally, we also consider a latitude dependence of the Earth's conductivity, $\chi = \chi(\theta)$.

By adding these terms and using spherical coordinates, the modified Daisyworld model is described by the following set of equations

$$\begin{aligned}
\frac{\partial \alpha_w}{\partial t} &= \alpha_w \left[(1 - \alpha_w - \alpha_b)\beta_w(T) - \gamma\right] && (9.7)\\
\frac{\partial \alpha_b}{\partial t} &= \alpha_b \left[(1 - \alpha_w - \alpha_b)\beta_b(T) - \gamma\right] && (9.8)\\
\frac{\partial T}{\partial t} &= \frac{1}{\rho c_p} \left[1 - A(\theta, t)\right] R(\theta) - \frac{\sigma}{\rho c_p} g(T) T^4 + \\
&+ \frac{1}{r_E^2 \cos\theta} \frac{\partial}{\partial \theta} \left[\kappa(\theta) \cos\theta \frac{\partial T}{\partial \theta}\right] && (9.9)
\end{aligned}$$

where $\alpha_{w,b}$ are functions of both latitude and time, $\kappa(\theta) = \chi(\theta)/\rho c_P$, $r_E \simeq 6.37 \times 10^8$ cm is the Earth's radius. We use the expression of the Laplace operator in spherical coordinates, taking into account that, in our case, $-90° \leq \theta \leq 90°$.

9.3 Stability analysis

Firstly, we evaluate the role of the greenhouse effect into the energy budget between emitted and absorbed radiation in the Daisyworld by performing the stability analysis on the model described by Eqs. (9.7-9.9). By following the approach of Adams et al. (2003) and Adams and Carr (2003), these equations can be written in a compact form as

$$\frac{\partial u}{\partial t} = u\phi(u,v,T) \tag{9.10}$$

$$\frac{\partial v}{\partial t} = v\psi(u,v,T) \tag{9.11}$$

$$\frac{\partial T}{\partial t} = h(u,v,T) + \frac{1}{r_E^2 \cos\theta}\frac{\partial}{\partial\theta}\left[\kappa(\theta)\cos\theta\frac{\partial T}{\partial\theta}\right] \tag{9.12}$$

where $u \doteq \alpha_w$, $v \doteq \alpha_b$, and

$$\begin{aligned}
\phi(u,v,T) &= (1-\alpha_w-\alpha_b)\beta_w(T) - \gamma\ , \\
\psi(u,v,T) &= (1-\alpha_w-\alpha_b)\beta_b(T) - \gamma\ , \\
h(u,v,T) &= \frac{1}{\rho c_p}\{[1-A(\theta,t)]\,R(\theta) - \sigma g(T)T^4\}\ ,
\end{aligned}$$

and where the greenhouse term is included in $h(u,v,T)$.

For convenience, we discuss the stability of the system by considering three different cases: without greenhouse effect and diffusion; with greenhouse effect and no diffusion; with both greenhouse effect and diffusion.

9.3.1 No greenhouse effect ($g(T) = 1$) and no diffusion ($\kappa(\theta) = 0$)

This first case was previously studied by Adams et al. (2003) and Adams and Carr (2003) who found that, for a fixed T, four equilibrium points $P_i = (u,v)$, associated with four different physical situations, are obtained:

- $P_1 = (0,0) \Rightarrow$ No daisies. Unstable equilibrium point;
- $P_2 = (\bar{u},0) \Rightarrow$ White daisies only. This is a stable equilibrium point if $T \geq 292.13$ K;
- $P_3 = (0,\bar{v}) \Rightarrow$ Black daisies only. This is a stable equilibrium point if $T \leq 298.87$ K;
- $P_4 = (u_c,v_c) \Rightarrow$ Coexistence of white and black daisies. This is a stable equilibrium point if 292.13 K $< T <$ 298.87 K.

9.3.2 Greenhouse effect ($g(T) \neq 1$) and no diffusion ($\kappa(\theta) = 0$)

Let's now study the effects of the greenhouse by choosing a grayness function

$$g(T) = 1 - \frac{1}{2}\tanh\left(\frac{T}{T_0}\right)^6 . \tag{9.13}$$

This functional form of $g(T)$, with $T_0^{-6} = 1.9 \times 10^{-15}\ \mathrm{K}^{-6}$, was proposed by Sellers (1969) and allows to take into account a relaxation of the black-body radiation hypothesis (Ghil, 1985), since $g(T)$ is included into the term related to the emitted radiation.

We linearize Eqs. (9.10-9.12) to find and study the sign of the eigenvalues of the associated Jacobian matrix. We thus write down the variables as the sum of mean quantities (u_c, v_c, T_c) and small amplitude perturbations (u', v', T')

$$u = u_c + u' \tag{9.14}$$
$$v = v_c + v' \tag{9.15}$$
$$T = T_c + T' \tag{9.16}$$

with $(u', v', T') \ll (u_c, v_c, T_c)$ and $P_c = (u_c, v_c, T_c)$ which is the equilibrium point associated with the coexistence solution, the only stable solution found by Adams et al. (2003) and Adams and Carr (2003). After linearizing Eqs. (9.10-9.12), the Jacobian matrix (J) at the equilibrium point P_c is

$$J(P_c) = \begin{bmatrix} \phi(P_c) + u_c\phi_u(P_c) & u_c\phi_v(P_c) & u_c\phi_T(P_c) \\ v_c\psi_u(P_c) & \psi(P_c) + v_c\psi_v(P_c) & v_c\psi_T(P_c) \\ h_u(P_c) & h_v(P_c) & h_T(P_c) \end{bmatrix} \tag{9.17}$$

where we use the condition that $\phi(P_c) = \psi(P_c) = 0$, satisfied by the coexistence solution (Adams et al., 2003; Adams and Carr, 2003). The stability of the system is defined by the properties of the J eigenvalues obtained from the solutions of the equation $E(\lambda) = 0$, where $E(\lambda)$ is defined as

$$E(\lambda) = \begin{vmatrix} u_c\phi_u - \lambda & u_c\phi_v & u_c\phi_T \\ v_c\psi_u & v_c\psi_v - \lambda & v_c\psi_T \\ h_u & h_v & h_T - \lambda \end{vmatrix} \tag{9.18}$$

in which the dependence of ϕ, ψ, and h on P_c has been omitted.
The zeros of $E(\lambda)$ are obtained by expanding with respect to the third column:

$$\begin{aligned} E(\lambda) &= (h_T - \lambda) \begin{vmatrix} u_c\phi_u - \lambda & u_c\phi_v \\ v_c\psi_u & v_c\psi_v - \lambda \end{vmatrix} \\ &- v_c\psi_T \begin{vmatrix} u_c\phi_u - \lambda & u_c\phi_v \\ h_u & h_v \end{vmatrix} \\ &+ u_c\phi_T \begin{vmatrix} v_c\psi_u & v_c\psi_v - \lambda \\ h_u & h_v \end{vmatrix} \end{aligned} \tag{9.19}$$

Since the derivatives of the functions ϕ and ψ are of order δ and $\delta \ll 1$ (see Eq. (9.3)), the eigenvalues can be written as:

$$\lambda_1 = h_T + O(\delta) \tag{9.20}$$
$$\lambda_2 = -b + O(\delta) \tag{9.21}$$
$$\lambda_3 = c\delta + O(\delta^2) \tag{9.22}$$

where b and c are two constant with $b > 0$ and $c < 0$ (Adams and Carr, 2003). The system has two negative eigenvalues (λ_2 and λ_3), therefore the stability only depends on the sign of λ_1 which is related to the sign of h_T. A calculation shows that

$$h_T = \frac{1}{\rho c_p}\left\{-\sigma T^3\left[\frac{dg}{dT}T + 4g(T)\right] + \frac{R}{5}\right\} . \tag{9.23}$$

By defining $\tilde{h}_T = (\rho c_p h_T)/(\sigma {T_0}^3)$, $\zeta = R/(5\sigma {T_0}^3)$ and setting $x = (T/T_0)^3$, we obtain

$$\tilde{h}_T = -x\left[-3x^2\cosh^{-2}(x^2) + 4 - 2\tanh(x^2)\right] + \zeta \tag{9.24}$$

and, as a consequence,

$$\tilde{h}_T < 0 \quad \Rightarrow \quad x > x_0 = 0.149 . \tag{9.25}$$

This condition sets a critical value of temperature below which the coexistence solution becomes unstable. According to our choice $T_0 = 284.15$ K, the coexistence solution is stable if $T > 150.65$ K, but considering that the coexistence solution exists if $292.13 \text{ K} < T < 298.87$ K, the grayness function does not destabilize it.

9.3.3 Greenhouse effect ($g(T) \neq 1$) and constant diffusion ($\kappa(\theta) = constant$)

Which mechanism is able to destabilize the coexistence solution? The answer to this question can be found by analyzing the diffusion term, since is the only process able to set one of the three eigenvalues greater than zero. We evaluate the role of the diffusivity through the stability analysis on Eqs. (9.10-9.12) in which we consider a simplified diffusion term (Adams and Carr, 2003)

$$\frac{\partial u}{\partial t} = u\phi(u, v, T) \tag{9.26}$$
$$\frac{\partial v}{\partial t} = v\psi(u, v, T) \tag{9.27}$$
$$\frac{\partial T}{\partial t} = h(u, v, T) + D\frac{\partial^2 T}{\partial \theta^2} \tag{9.28}$$

by setting $\kappa(\theta)/r_E^2 = D = constant$ and neglecting the term of the Laplace operator which is proportional to the temperature gradient (Adams et al., 2003; Adams and Carr, 2003). By linearizing the system and by choosing a temperature perturbation in the form $\delta T \propto e^{ik_\theta \theta}$, the eigenvalues of the Jacobian matrix can be obtained as the zeros of the function $E(\lambda, Dk_\theta)$, whose functional form is the same of Eq. (9.18) with $h_T - \lambda$ replaced by $h_T - D{k_\theta}^2 - \lambda$. Then, the eigenvalues are evaluated:

$$\lambda_1 = h_T - D{k_\theta}^2 + O(\delta) \tag{9.29}$$

$$\lambda_2 = -b - k_\theta^2 + O(\delta) \tag{9.30}$$

$$\lambda_3 = c(Dk_\theta)\delta + O(\delta^2) \tag{9.31}$$

where $c(Dk_\theta)$ is a function of Dk_θ (Adams et al., 2003; Adams and Carr, 2003). It is possible to note that the eigenvalues λ_1 and λ_2 are negative, while the sign of the third eigenvalue λ_3 can change. Following Adams et al. (2003) and Adams and Carr (2003), we show that the sign of λ_3 depends on Dk_θ and that $\lambda_3 > 0$ is given by $Dk_\theta = 8$. This set a critical parameter, higher than the corresponding parameter evaluated by Adams et al. (2003) where no greenhouse term was included, which can be seen as a measure of the effect of the diffusion and the grayness function on the stability of the coexistence solution. In the Daisyworld model we developed, the destabilization process is modified by the concurrent effect of both the greenhouse effect, modelled through the grayness function, and the latitudinal diffusion process.

9.4 Numerical results

We numerically solved eqs. (9.7-9.9), with the condition (9.4), by using a second order Runge-Kutta scheme for time integration and spectral methods for integration on latitude θ. Since in the Laplace operator the poles are singular points, for ($\theta = \pm 90°$) we assume a free-flux boundary condition, corresponding to zero derivatives for all the variables. In this way the continuity of the laplacian in these points is ensured, with suitable parity boundary conditions imposed.

A first set of solutions was calculated by imposing a constant normalized grayness function $g(T) = 1$ and normalized heat conductivity $\kappa(\theta) = 1$ for each θ, as in the classical model. In this case, we set the initial condition for T as $T(\theta, 0) = -20 + 40L\cos^2(\theta)$, while we choose the initial coverages constant $\alpha_w(\theta, 0) = \alpha_b(\theta, 0) = 0.5$ over θ.

Figure 9.1 shows the equilibrium solutions for temperature and daisy coverage, as functions of the variable θ, for three different values of L, corresponding to the present conditions ($L = 1$) and to the so-called “snowball” ($L = 0.5$) and “fireball” ($L = 1.5$) Earth.

As expected, the equilibrium temperature profile is a bell shaped curve peaked at the equator ($\theta = 0°$). The increase/decrease of L corresponds

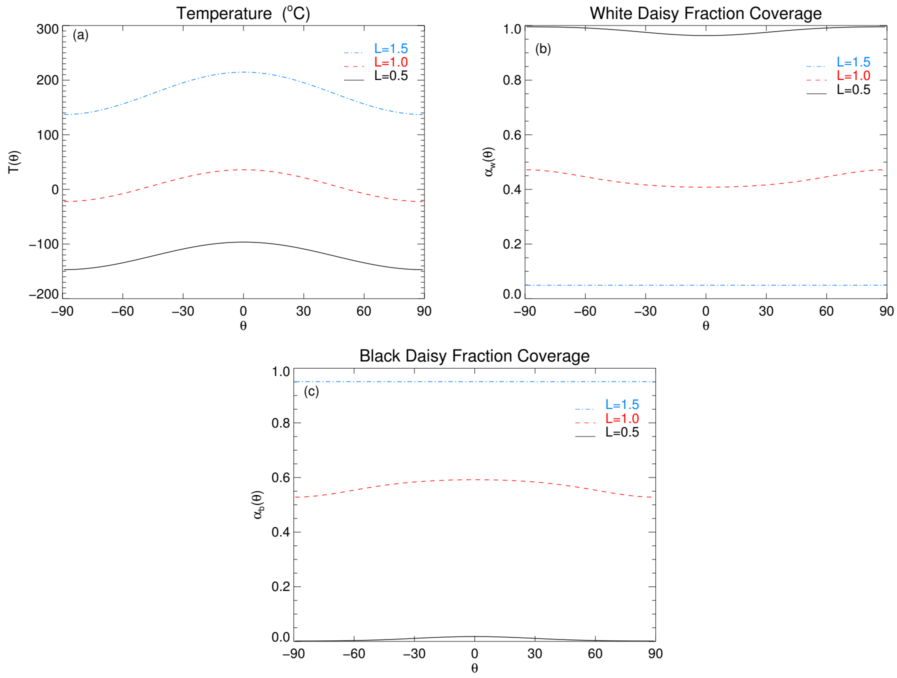

Figure 9.1: Stationary solutions for (a) temperature $T(\theta)$, (b) white daisy population $\alpha_w(\theta)$ and (c) black daisy population $\alpha_b(\theta)$, as a function of latitude, from the numerical solution of Eq. (9.9), using $\kappa(\theta) = 1$, $g(T) = 1$ and three different value of the parameter L.

to a global enhancement/decrease of temperature (Lovelock, 1972; Lovelock and Watson, 1982; Lovelock, 1992a,b; Adams and Carr, 2003). For the lowest value $L = 0.5$, corresponding to half the present solar luminosity, the planet becomes completely frozen, with the highest temperature being $T(\theta = 0^\circ) \simeq -120$ °C. Conversely, for the highest value of L, $L = 1.5$, the planet is extremely hot, with the lowest temperature being $T(\theta = \pm 90^\circ) \simeq$ 100 °C.

For daisies coverage we note that an increase of luminosity L produces an increase of the planetary surface covered by black daisies and a decrease of the area covered by white daisies. This suggests that black daisies withstand high temperatures, while the growth of white flowers is favoured by low temperatures. By changing L in a continuous way the contour plots of equilibrium temperature and daisy coverages as functions of latitude and luminosity L can be built (Figure 9.2). Numerical results show that, after some time steps, the system settles down to an equilibrium state where the various quantities do not change anymore in time. Moreover, Figure 9.2 shows that global temperature increases with luminosity and the planet is almost completely frozen for $L \lesssim 1$. Conversely, enhancements of black daisies are obtained for high values of luminosity ($L \gtrsim 1$).

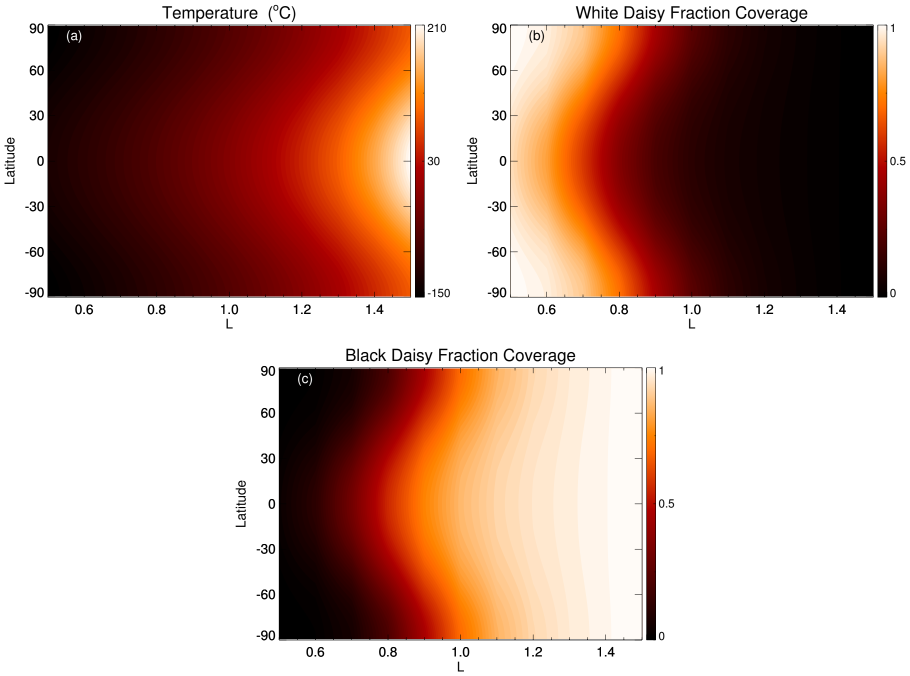

Figure 9.2: Contour plots of the stationary solutions for (a) $T(\theta)$, (b) white daisy population $\alpha_w(\theta)$ and (c) black daisy population $\alpha_b(\theta)$, in the plane (L, θ) using $\kappa(\theta) = 1$, $g(T) = 1$.

9.4.1 The effects of a non-uniform heat diffusion

It is well-known that surface temperature is affected by changes in redistribution of heat, which depend by local changes of the heat conductivity. To this purpose, we use a heat conductivity depending by latitude and assuming that it is peaked at the equator, decreasing toward the poles, where it vanishes. We modelled it by using a simple functional form as

$$\kappa(\theta) = \frac{1 + \cos(2\theta)}{2} , \tag{9.32}$$

which is symmetrical around $\theta = 0°$. Results obtained by using Eq. (9.32) in Eqs. (9.9) and with the same initial conditions as in previous case are shown in Figures 9.3 and 9.4.

We firstly note that the temperature variations with L are smaller with respect to the previous case in which the thermal diffusivity was not in-

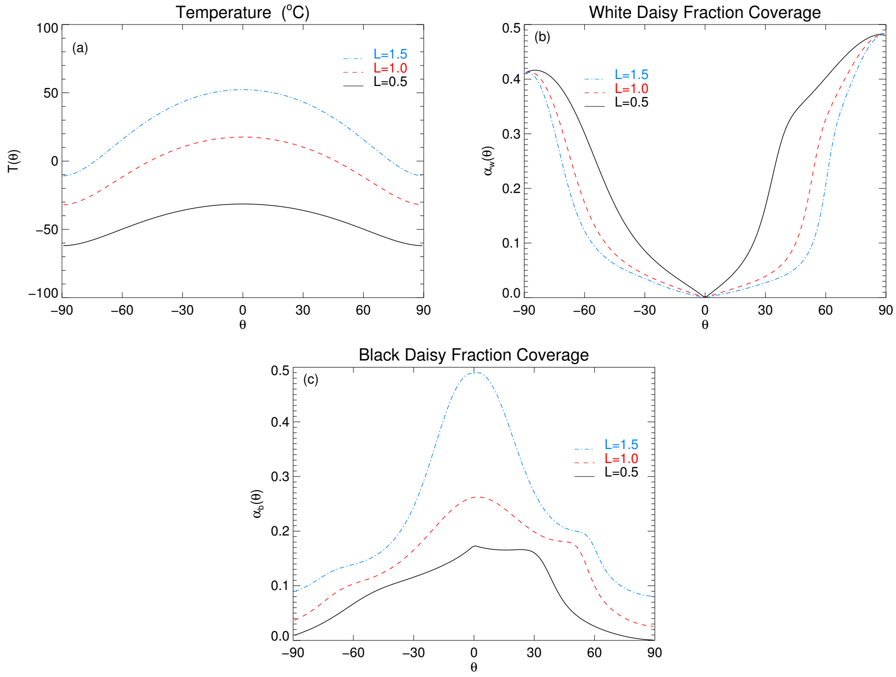

Figure 9.3: Stationary solutions for (a) temperature $T(\theta)$, (b) white daisy population $\alpha_w(\theta)$ and (c) black daisy population $\alpha_b(\theta)$, as a function of latitude, by numerical solution of Eq. (9.9), using the profile (9.32) for $\kappa(\theta)$ and $g(T) = 1$, and three different value of the parameter L.

cluded. This is related to the effects of the heat diffusion on the redistribution of the heat across latitudes. Moreover, heat diffusion produces, for extreme values of L, larger differences in daisy fraction between polar and equatorial regions (see Figure 9.4). Indeed, different from the previous case, the polar areas ($|\theta| \gtrsim 60°$) are mainly populated by white daisies (for all L values). Conversely, also for low L values, black daisy coverage persists in the region $0° < \theta \lesssim 40°$, higher than in the previous case. Interestingly, we also note a particular characteristic in the equilibrium solutions related to the presence of an asymmetry with respect to the equator, not observed in the previous case. This behaviour is due to the Laplace operator which consists in two different terms: the first one is symmetric, while the second one is not, since it is proportional to the derivative of $\kappa(\theta)$ with respect to θ.

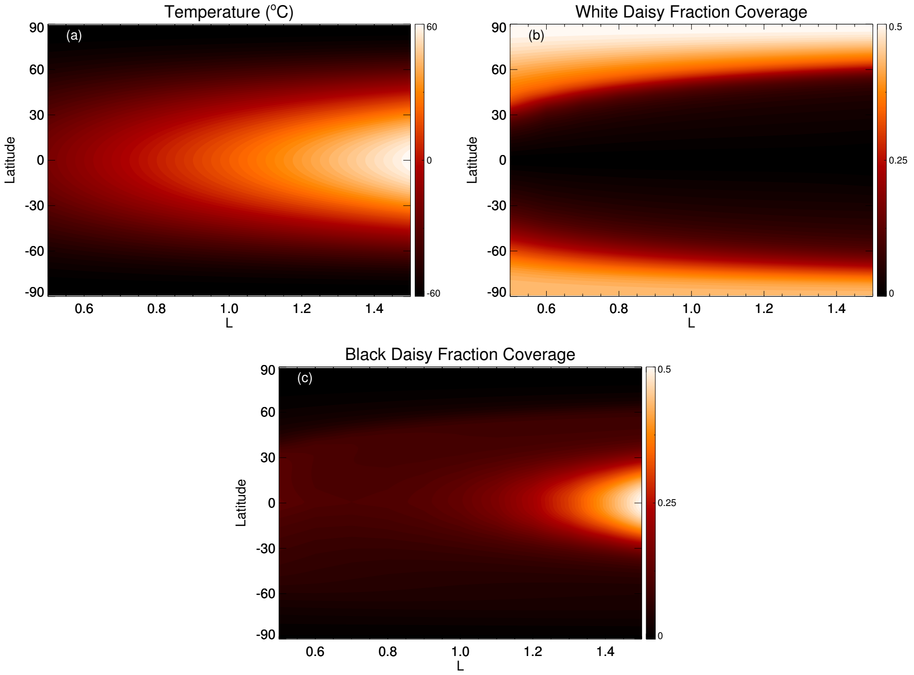

Figure 9.4: Contour plots of the stationary solutions for (a) $T(\theta)$, (b) white daisy population $\alpha_w(\theta)$ and (c) black daisy population $\alpha_b(\theta)$, in the plane (L, θ) using the profile (9.32) for $\kappa(\theta)$ and $g(T) = 1$.

9.4.2 The greenhouse effect

One of the main points in climate research, particularly in climate modeling, is the investigation of the effect of the atmospheric greenhouse gases on the planetary energy budget. We study this effect by using the grayness function given in Eq. (9.13) into the heat equation. Figures 9.5 and 9.6 show the results obtained with the greenhouse effect. When both greenhouse and diffusion terms are considered, the global equilibrium temperature is changed again. Since the greenhouse effect produces a global temperature increase, as expected we note a general increase of the temperature. Morevoer, the greenhouse effect acts as a self-regulating process for the planet climate, although when solar irradiance changes abruptly, because the temperature variations show a typical range between -30 °C (at the poles, for $L = 0.5$) and 110 °C (at the equator, for $L = 1.5$). Figure 9.6 show that there is an increase of black daisy coverage in the region $|\theta| \lesssim 40°$ for $L > 1$. Moreover, we note that by including the greenhouse effect we recovered the symmetry because, when the grayness function is considered, the diffusion and the Stefan-Boltzmann terms are of the same order of magnitude; the symmetry with respect to θ is thus restored because these two terms are opposite in sign.

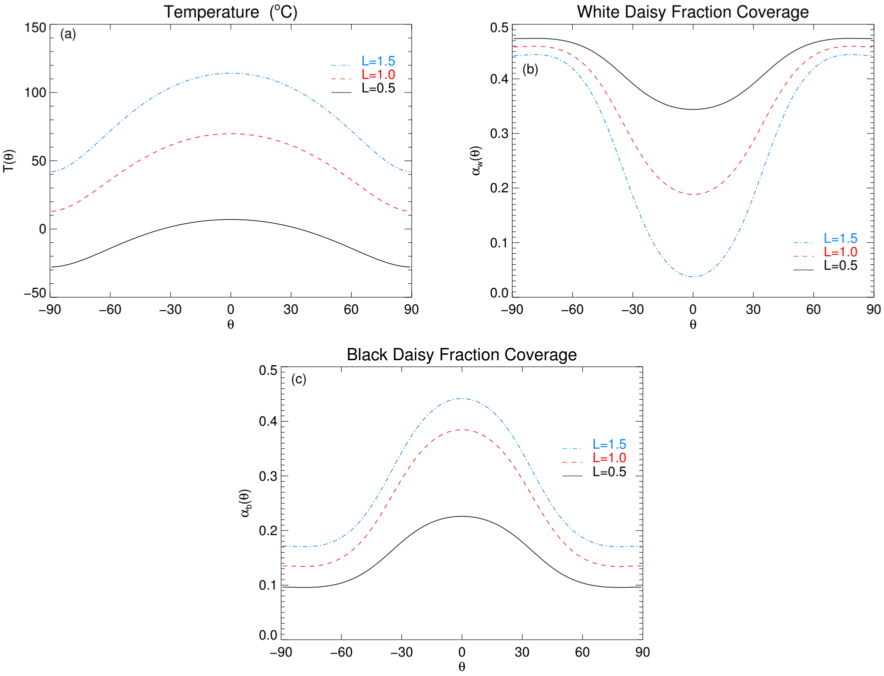

Figure 9.5: Stationary solutions for (a) $T(\theta)$, (b) white daisy population $\alpha_w(\theta)$ and (c) black daisy population $\alpha_b(\theta)$, as a function of latitude, by numerical solution of Eq. (9.9), using the profile (9.32) for $\kappa(\theta)$ and (9.13) for $g(T)$, and three different value of the parameter L.

9.4.3 Dependence on initial conditions

As shown by the stability analysis, several equilibrium points are obtained with different stability properties. This suggest that the equilibrium vegetation profiles depend also, to some extent, on the initial conditions of daisy coverage. To assess this idea we change the initial conditions as

$$\begin{aligned} \alpha_w(\theta,0) &= \begin{cases} \left|\frac{\theta}{\pi}\right| & \text{if } |\theta| < 85^\circ \\ 0.5 & \text{otherwise} \end{cases} \\ \alpha_b(\theta,0) &= 0.5 - \alpha_w(\theta,0) \quad . \end{aligned} \tag{9.33}$$

with the initial temperature profile unchanged and choosing a linear form for the initial daisy coverages. As shown in Figures 9.7 and 9.8, the temperature profile remains unchanged, while the surface coverage gives rise to different dynamics.

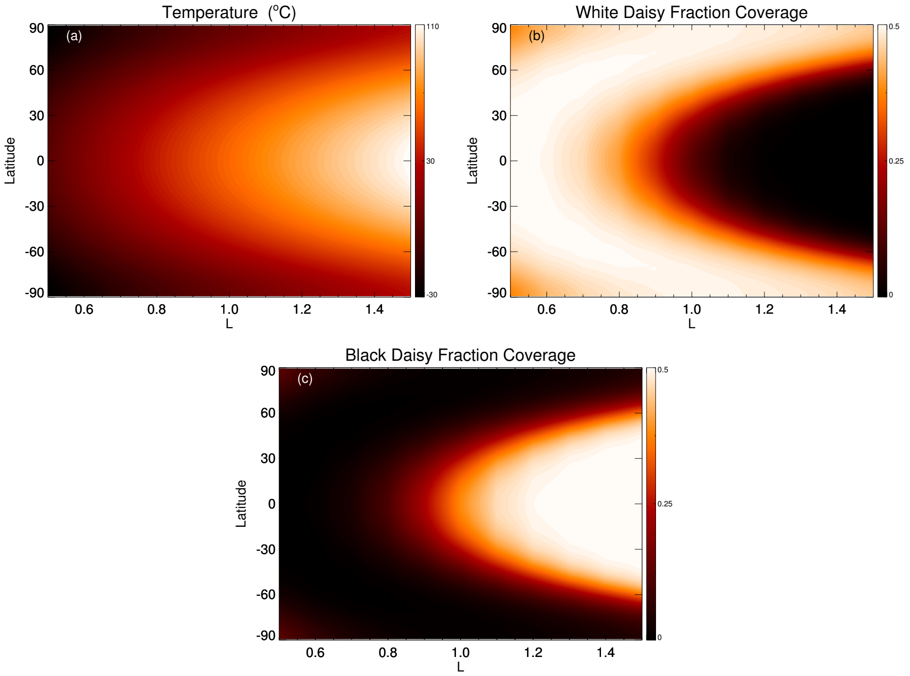

Figure 9.6: Contour plots of the stationary solutions for (a) $T(\theta)$, (b) white daisy population $\alpha_w(\theta)$ and (c) black daisy population $\alpha_b(\theta)$, in the plane (L, θ) using the profile (9.32) for $\kappa(\theta)$ and (9.13) for $g(T)$.

Due to symmetry in the initial conditions, the time evolution of the fraction coverage for both species is symmetric but with different shapes and values with respect to the previous case.

9.4.4 Multiple steady-states

Another issue which is worth to be investigated is the occurrence of multiple steady-states and the stability of the system with respect to the presence of perturbations in the initial temperature profile. To this aim, we numerically solved Eqs. (9.7-9.9) for a set of initial conditions such as

$$\begin{aligned} T(\theta,0) &= 295.5 + \cos(k_\theta \theta) && (9.34) \\ \alpha_w(\theta,0) &= \frac{T(\theta,0) - 292.13}{10} && (9.35) \\ \alpha_b(\theta,0) &= \frac{298.87 - T(\theta,0)}{10} && (9.36) \end{aligned}$$

where $0 < k_\theta < 25$. This peculiar initial conditions are chosen in a way that the initial coverages correspond to the equilibrium coexistence solution

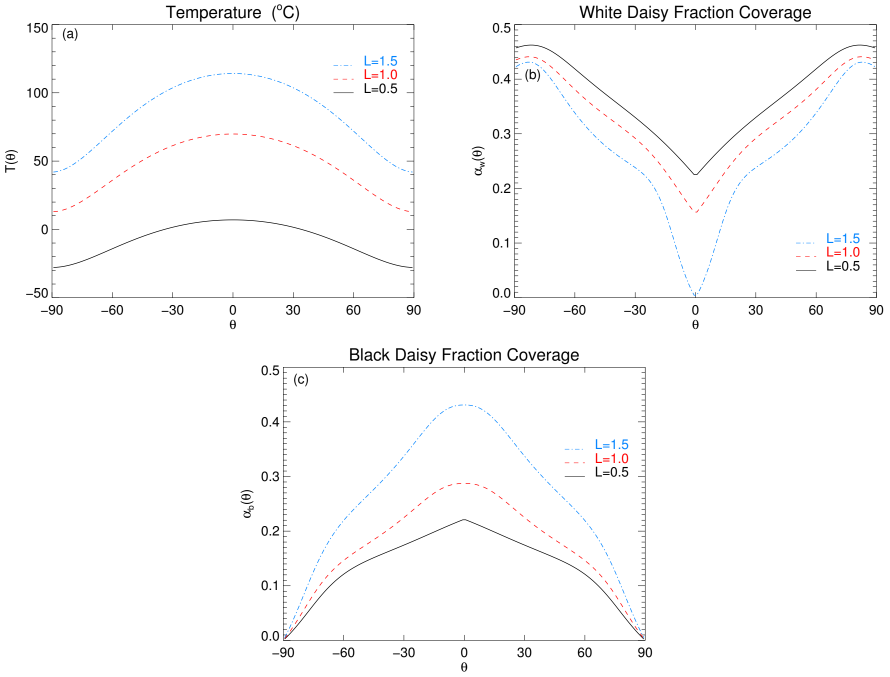

Figure 9.7: The same as Figure 9.5, but with different initial values for vegetal coverages.

and the temperature is kept in the range where the coexistence solution is stable. We introduce the function $\cos(k_\theta \theta)$ to study how initial temperature profile perturbations can affect the equilibrium solutions and allows to build up diagrams showing when multiple solutions take place.

Figures 9.9, 9.10 and 9.11 show the temperature and daisy coverages solutions as functions of latitude and k_θ for three different values of L ($L = 0.5$ Figure 9.9, $L = 1.0$ Figure 9.10, $L = 1.5$ Figure 9.11). We can note that the temperature profile shape is almost not affected by the initial perturbation, since it does not vary substantially with k_θ and only an increase of temperature with L is found, as expected, without changes in the profile shape. Conversely, the daisy coverages are clearly affected by temperature perturbations, significantly depending on k_θ. More specifically, for $L = 0.5$ (Figure 9.9), a striped pattern appears when $k_\theta \gtrsim 8$. This value of k_θ is in agreement with the value found through the stability analysis and it is simultaneously observed in both daisy coverages, with the two populations covering almost the same area even for this low luminosity value. This effect is probably related to the grayness function which regulates the temperature in a way that black daisies increase their growth rate. For $L = 1.0$, the same k_θ critical value is found and a large scale pattern is observed in addition to

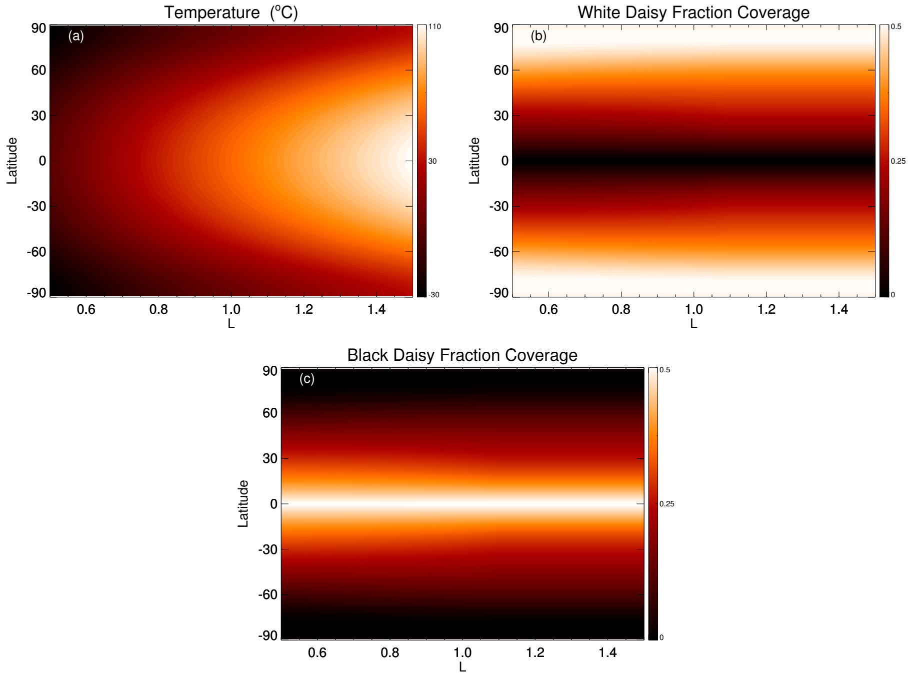

Figure 9.8: The same as Figure 9.6, but with different initial values for vegetal coverages.

the stripes. More precisely, a clear separation between polar and equatorial regions is evident, white daisy stripes being dominant in the polar regions and black stripes at $|\theta| \lesssim 40°$. For $L = 1.5$, the equilibrium solutions for the daisy coverages change again; only the large scale pattern survives, while no striped pattern occurs.

The different behaviors observed for different L values are mainly attributable to the grayness function, whose effects are more pronounced for higher values of the temperature. On the other hand, the diffusion process produces a striped or continuous pattern for both white and black daisies according to the different values of the L parameter and to the different initial condition when a small perturbation is introduced.

9.5 Conclusions

By investigating a modified Daisyworld model which includes latitudinal dependency (of both solar incoming and planetary outcoming energies), variable heat diffusivity and the greenhouse effect, we found that, at variance with previous results, the system is able to self-regulate even in presence of values of the incident luminosity which are far from the current Sun-Earth

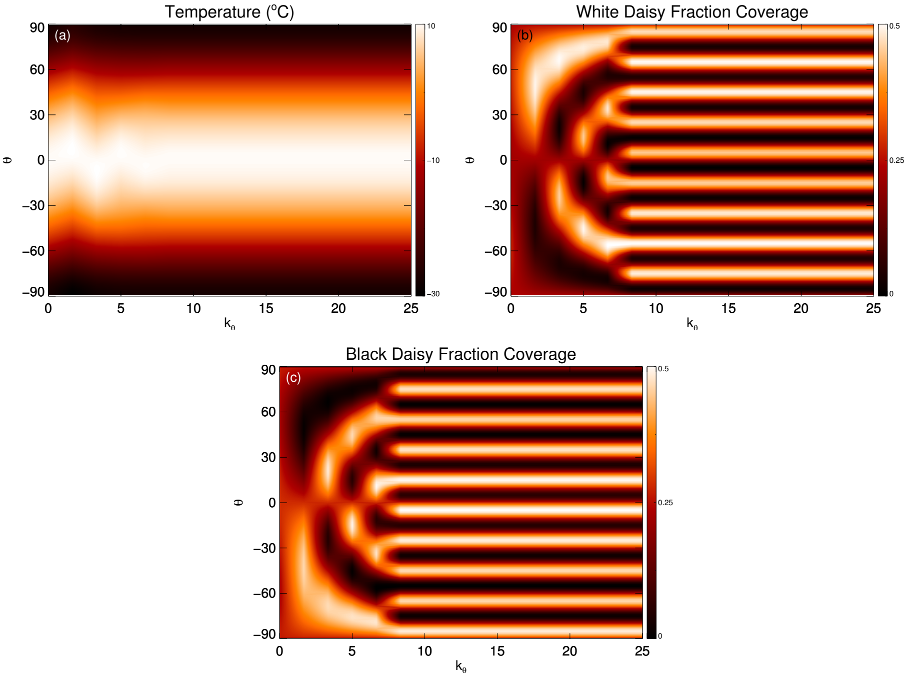

Figure 9.9: Contour plots of the stationary solutions for (a) $T(\theta)$, (b) white daisy population $\alpha_w(\theta)$ and (c) black daisy population $\alpha_b(\theta)$, in the plane (k_θ, θ) for different initial conditions according to the value of k_θ and fixing $L = 0.5$.

conditions. This is related to the grayness function which models the greenhouse effects because it affects the temperature evolution and contributes to self-regulating the planet climate, without any evidence of destabilization of the system, although it modifies its stability properties. Conversely, a non-constant diffusion term can destabilize both the system properties and symmetry with respect to the equator, producing striped patterns when a temperature perturbation affects the equilibrium solution. Moreover, this equilibrium solution is significantly dependent on the initial conditions. Indeed, by modifying initial conditions of daisy coverage we note a sensitive dependence in vegetation profiles, although they do not significantly modify the temperature behaviour. Finally, the observed striped pattern changes from low to high luminosity values: for low values, it occurs when the perturbation wave number exceeds a threshold value, while for higher values the greenhouse effect leads to the disappearing of the striped patterns.

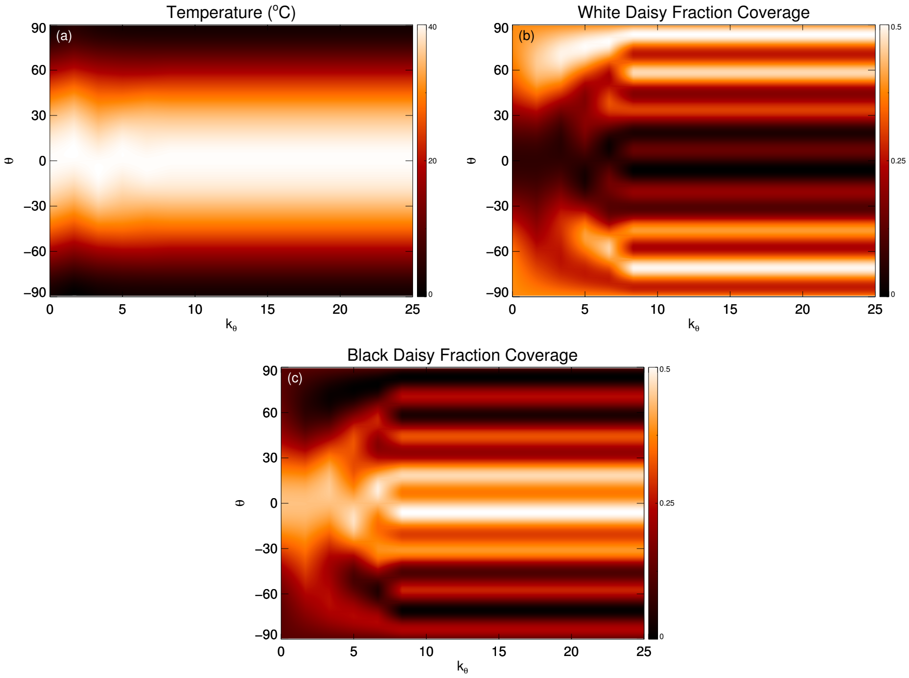

Figure 9.10: Contour plots of the stationary solutions for (a) $T(\theta)$, (b) white daisy population $\alpha_w(\theta)$ and (c) black daisy population $\alpha_b(\theta)$, in the plane (k_θ, θ) for different initial conditions according to the value of k_θ and fixing $L = 1.0$.

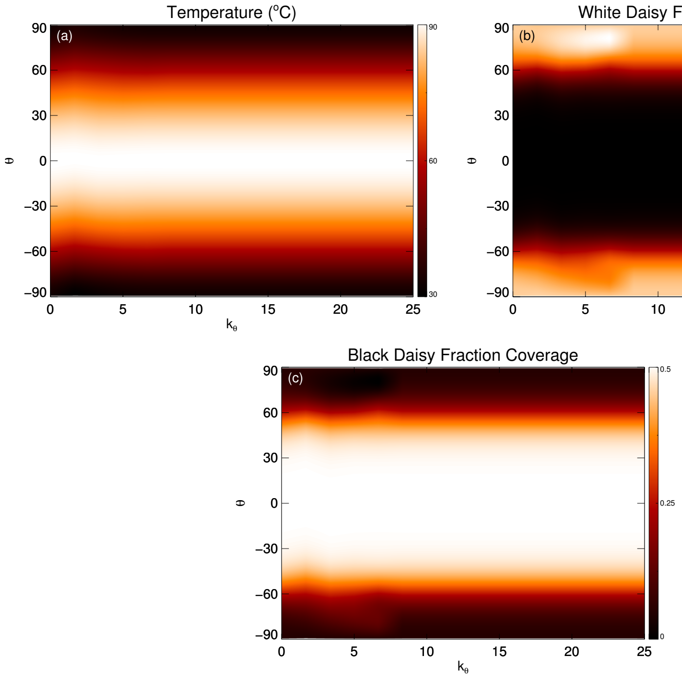

Figure 9.11: Contour plots of the stationary solutions for (a) $T(\theta)$, (b) white daisy population $\alpha_w(\theta)$ and (c) black daisy population $\alpha_b(\theta)$, in the plane (k_θ, θ) for different initial conditions according to the value of k_θ and fixing $L = 1.5$.

Chapter 10

On the stability of a climate model for an Earth–like planet with ground–water coverage[1]

The discovery of potentially habitable Earth-like exoplanets orbiting around hosting stars increases the interest in investigating their climate systems. In this perspective, we study the stability properties of a simple energy balance climate-vegetation model. It considers the interaction between the planetary surface, that should be partially covered by vegetation, a large ocean and a land surface, which can change in response to variations in the hosting star irradiance (e.g. due to mutual distance variations). The stability of the system changes according to variations into the control parameters, as for example the growth-death rate of vegetation γ and planet-star distance a. In particular, the model presents both stable and unstable fixed points, which can exhibit several kinds of stability properties, according to the distance of the planet from the hosting star.

10.1 Introduction

As described in Chapter 7, a complete description of the Earth's climate system in terms of atmospheric variables (temperature, humidity, pressure) is quite complex, due to their variability on several timescales (Tessier et al., 1993; Schmitt et al., 1995; Marsh and Ditlevsen, 1997; Lovejoy and Schertzer, 2013; Alberti et al., 2014; Shao and Ditlevsen, 2016). To investigate the main features of the climate system and describe the basic atmospheric

---

[1] The work presented in this chapter is included in the paper Alberti, Lepreti, Vecchio and Carbone (2017*c*).

mechanisms characterizing it some kinds of simple climate models, the so-called Energy Balance Models (EBMs) have been proposed (e.g., Budyko, 1969; Sellers, 1969; Watson and Lovelock, 1983). These models, based on the radiative equilibrium between the incoming solar radiation and the outgoing infrared radiation, are particularly simple since governed by a set of Ordinary Differential Equations (ODEs), which depend on parameters determining the dynamical properties of the system.

The recent discoveries of Earth-like exoplanet planets (Anglada-Escudé et al., 2016) increases the interest of the scientific community toward these astronomical objects, also fostered by the high probability that several of them will be identified in the near future. A very interesting point concerns the possible characterization of the Earth-like exoplanet climate conditions, a topic strongly related to their possible habitability. Since the exact chemical content of the exoplanet atmospheres is unknown, the classical approach, consisting in characterizing the climate by starting from the basic physical atmospherical processes, it is challenging (Spiegel et al., 2008). In this context, where the knowledge of physical mechanisms is limited, EBMs are suitable to gain new insight into the global properties of the exoplanet climate.

In the framework of the Budyko-Sellers climate models (Budyko, 1969; Sellers, 1969), a simple equation governs the time-evolution of the global surface planetary temperature T

$$C_T \frac{dT}{dt} = E_{in}(S, \alpha) - E_{out}(T) \tag{10.1}$$

where C_T is the heat capacity of the planet, E_{in} is the incoming solar radiation depending by the solar flux S reaching the planetary surface and on the albedo $\alpha(T)$, namely the reflected energy flux, and E_{out} is the infrared outgoing planetary radiation.

A different number of fixed points, and consequently climate states, can be found for different E_{out} and when different dependences of the albedo on the temperature is considered. Previous works (see e.g., Ghil, 1976) showed the existence of two stable fixed points, corresponding to a glacial and a desert state, respectively, and an unstable one, corresponding to the present climate state. Although its simplicity, this model can describe the main features of the climate states, even if it does not consider some components of the climate system which can affect its evolution such as the interaction with the biota (i.e., atmosphere-biosphere interaction), a changing solar irradiance and the greenhouse effect. As described in Chapter 9, the first attempt to include the climate–vegetation interaction is the well known Daisyworld model (Watson and Lovelock, 1983). It is governed by two ODEs, for the time–evolution of two types of vegetation (white and black daisies) coupled with Eq. (10.1) for the global surface temperature. This model allows to investigate how vegetation regulates the temperature via the albedo feedback when the incoming solar radiation changes (see Chapter 9 and references therein).

In the previous chapter, we show that, by including spatial dependence on the latitude, a non-constant heat diffusion term, and, for the first time, a parametrization of the greenhouse effect through a grayness function (Sellers, 1969), the system self-regulates even for solar incoming radiation values far from the present condition. In situations where the latitude dependence of average temperature or incoming radiation cannot be observationally verified, such as the case of Earth like exoplanets, the use of 0-D models is preferred. For example, a simple climate-vegetation model, based on the ice-albedo feedback characterizing a planet with a large ocean, has been recently investigated by Rombouts and Ghil (2015). The model is governed by two nonlinear and coupled ODEs for both temperature and vegetation coverage. Some stability states, from bistability between a desert and a vegetated state to an anharmonic oscillatory behavior which manifests through a Hopf bifurcation, were observed. Moreover, the stability properties can change according to variations in the death rate of vegetation by the occurrence of Hopf and a saddle-node bifurcations. In particular, this model presents three fixed points: two of these are stable, while the intermediate one is unstable and classified as a saddle point.

This study investigates the stability properties of a modified version of the climate–vegetation model by Rombouts and Ghil (2015) by introducing a varying solar incoming radiation. We present an analytical solution for the stability conditions in the simple case when the vegetation drop off, while a numerical investigation is performed for the vegetated state solution. We show that the unstable fixed point depends on changes in growth–death rate of vegetation, on the level of incoming radiation and that its stability properties change accordingly.

10.2 The model

The model describing the star–planet system we investigate, inspired by the Daysiworld model, is based on two equations for the global average temperature T and the fraction of land A covered by vegetation

$$C_T\frac{dT}{dt} = [1-\alpha(T,A)]\,S - R(T) \tag{10.2}$$

$$\frac{dA}{dt} = A\,[\beta(T)(1-A)-\gamma] \tag{10.3}$$

where $\alpha(T,A)$ is the planetary albedo, S is the mean incoming radiation, $R(T)$ is the energy outgoing from the planet $\beta(T)$ and γ are the growth and death rate for vegetation, respectively (see Watson and Lovelock (1983);

Rombouts and Ghil (2015); Alberti et al. (2015) for more details). To investigate the stability of the model as regards to an Earth–like exoplanet climate, the incoming radiation is assumed to be $S = Q_{\odot} a^{-2}$, where $Q_{\odot}$ is the mean solar radiation modulated by the parameter $a = d/d_{\odot}$, where d is the star–planet distance and $d_{\odot}$ is the Sun–Earth distance. The albedo of the planet depends on the fraction of covered land

$$\alpha(T, A) = (1 - p)\alpha_o(T) + p[\alpha_v A + \alpha_g (1 - A)] \tag{10.4}$$

where p is the fraction of land on the planet, while α_o, α_v and α_g represent the albedos for ocean, vegetation and bare ground, respectively, with $\alpha_v < \alpha_g$. The albedo of the ocean is not fixed, rather it is allowed to depend on the temperature, to account for the presence of a given fraction of ice. The dependence is given in terms of a ramp function that introduces a nonlinearity in Eq. (10.2) leading to multiple equilibria

$$\alpha_o(T) = \begin{cases} \alpha_{max} & \text{if} \quad T \leq T_{low} \\ \alpha_{max} + \xi (T - T_{low}) & \text{if} \quad T_{low} < T \leq T_{up} \\ \alpha_{min} & \text{if} \quad T_{up} < T \end{cases}$$

where

$$\xi = \frac{\alpha_{min} - \alpha_{max}}{T_{up} - T_{low}}. \tag{10.5}$$

Here α_{max} refers to an ocean completly covered by ice, while α_{min} refers to an ice–free ocean.

Generally, the outgoing energy from the planet is described by a black-body radiation process $R(T) = \sigma T^4$, σ being the Stefan–Boltzmann constant. However, a linear functional shape is widely used in literature as an alternative to the blak–body radiation, according to the Budyko–Sellers framework (Budyko, 1969; Sellers, 1969). Since we would like to investigate the linear stability of the model, we use the linear approximation

$$R(T) = B_0 + B_1 (T - T_{opt}) \tag{10.6}$$

where the phenomenological constants B_0 and B_1, which are tuned on the optimal temperature T_{opt}, implicitly represent the effects of the present gaseous components of the planetary atmosphere.

The growth–rate of vegetation is described by a logistic equation depending on the temperature, according to the Daisyworld model,

$$\beta(T) = max\left\{0; 1 - k(T - T_{opt})^2\right\} \tag{10.7}$$

that is, the growth is zero except in an interval of temperatures where the growth is parabolic, with a maximum at the optimal temperature T_{opt}. The death–rate γ is assumed to be constant. The parameters usually used in the model to describe the Earth–like climate are reported in Table 10.1.

C_T	500 W yr K^{-1} m^{-2}	$Q_\odot$	342.5 W m^{-2}
p	0.3	k	0.004 yr^{-1} K^{-2}
α_v	0.1	α_g	0.4
α_{max}	0.85	α_{min}	0.25
$T_{\alpha,l}$	263 K	$T_{\alpha,u}$	300 K
B_0	200 W m^{-2}	B_1	2.5 W K^{-1} m^{-2}
T_{opt}	283 K		

Table 10.1: Parameters used in the model.

10.3 Multiple steady–states

The fixed points $T_\star$ and $A_\star$ of the system described by Eqs. (10.2)-(10.3) satisfy the following equations

$$\begin{aligned} 0 &= [1 - \alpha(T_\star, A_\star)]\, S - R(T_\star) \qquad (10.8)\\ 0 &= A_\star\, [\beta(T_\star)(1 - A_\star) - \gamma]\,. \qquad (10.9) \end{aligned}$$

Since $\beta(T)$ is a quadratic function, we expect at most three fixed points representing three different climate state of the planet. Looking at the equation for A, we immediately realize that two main class of fixed points can be supported by the system, namely climate states in absence of vegetation and in presence of vegetation. In the following we distinguish between these different situations.

10.3.1 Steady–states in absence of vegetation

In absence of vegetation, namely when $A = 0$, a fixed point $T = T_\star$ can be obtained from the classical equation $R(T_\star) = (1 - \alpha_g)S$, which reduces to the linear equation

$$T_\star + \frac{S}{B_1}(1 - p)\alpha_o(T_\star) = T_{opt} + \frac{S - B_0}{B_1} - p\alpha_g \frac{S}{B_1}, \tag{10.10}$$

when we use the linear approximation (10.6). The equilibrium point then depends on the definition of $\alpha_o(T_\star)$ and on the value of the parameters a and p, by keeping fixed the other parameters B_0, B_1 and T_{opt}. Note that this is a very peculiar condition for EBM models. As an example, let us consider the case of a planet without ocean, say $p = 1$. In this case the equilibrium solution does not depends on the ocean albedo α_o, and simply results

$$T_\star = T_{opt} + \frac{S}{B_1}(1 - \alpha_g) - \frac{B_0}{B_1}. \tag{10.11}$$

The simple EBM requires that this equilibrium point is possible (i.e., $T_\star > 0$) for a "rocky" planet orbiting at a distance a from their hosting star given by

$$a^{-2} > \frac{Q_\odot^{-1}}{(1 - \alpha_g)}(B_0 - T_{opt}B_1) \tag{10.12}$$

a condition that can be verified only when $(B_0/B_1) > T_{opt}$. Since the values of B_0 and B_1 are phenomenological constants derived by Budyko (1969) to fit the departure from a black—body function for the Earth's infrared emission in space, this condition of course cannot be verified for Earth.

For an Earth–like planet where $0 \leq p < 1$, the equilibrium solution depends on α_o and can be easily calculated from Eq. (10.10) as

$$T_\star = \left(T_{opt} - \frac{B_0}{B_1}\right) + \frac{S}{B_1}\left[1 - \alpha_o - p(\alpha_g - \alpha_o)\right], \tag{10.13}$$

where $\alpha_o = \alpha_{max}$ in the caso of ice–covered ocean, say for $T_\star \leq T_{low}$, while $\alpha_o = \alpha_{min}$ in the opposite case of ice–free ocean, say $T_\star \geq T_{up}$. These solutions exists only for determined distances of the planet from the hosting star. The ice–free ocean planet exists only when the distance from the hosting star is small enough

$$a^{-2} \geq \frac{Q_\odot^{-1}\left[(T_{up} - T_{opt})B_1 + B_0\right]}{\left[1 - \alpha_{min} - p(\alpha_g - \alpha_{min})\right]}. \tag{10.14}$$

In the opposite case, an ice–covered planet can exist only when

$$a^2 \leq \frac{Q_\odot^{-1}\left[(T_{low} - T_{opt})B_1 + B_0\right]}{\left[1 - \alpha_{max} - p(\alpha_g - \alpha_{max})\right]}. \tag{10.15}$$

When only a fraction of ocean is covered by ice, say when $T_\star \in [T_{low}, T_{up}]$, the fixed point results

$$T_\star = \frac{(T_{opt}B_1 - B_0) + S[1 - p\alpha_g - (1-p)(\alpha_{max} - \xi T_{low})]}{B_1 + S(1-p)\xi} \tag{10.16}$$

which is satisfied when

$$a^{-2} \in [f(T_{low}), f(T_{up})] , \tag{10.17}$$

where

$$f(x) = \frac{Q_\odot^{-1}}{\Pi}\left[B_1(x - T_{opt}) + B_0\right] \tag{10.18}$$

and

$$\begin{aligned} \Pi &= [1 - p\alpha_g - (1-p)(\alpha_{max} - \xi T_{low})] - \\ &- (T_{low} + T_{up})(1-p)\xi. \end{aligned} \tag{10.19}$$

In Figure 10.1 we report the contours of the equilibrium temperature in the plane (p, a). Of course, an Earth without vegetation lies at the border of the minimum and intermediate albedos, while an Earth with ocean covered by ice can exist even without vegetation.

10.3.2 Steady–states in presence of vegetation

By solving Eqs. (10.8)-(10.9) for the vegetated system, the steady–states $(T_\star, A_\star)$ can be obtained from the pair of equations

$$\beta(T_\star) = \frac{\gamma}{1 - A_\star} \tag{10.20}$$

$$A_\star = \frac{\mu}{p}\left\{\left[1 - \frac{R(T_\star)}{Q_\odot a^{-2}} - (1-p)\alpha_o(T_\star)\right] - p\alpha_g\right\} , \tag{10.21}$$

where $\mu = 1/(\alpha_v - \alpha_g)$. First of all, it can be noted that, when $\beta(T_\star) = \gamma$, the only steady–state solution is the absence of vegetation $A_\star = 0$. On the contrary, a solution with $A_\star \in (0, 1]$ corresponds to $\beta(T_\star) > \gamma$ and $T_\star \in (\mathrm{T}_{low}, \mathrm{T}_{up}]$. In the following we investigate this situation.

The solutions of Eqs. (10.20)–(10.21) identify two curves in the phase plane (T, A), called null isoclines (Rombouts and Ghil, 2015), and their intersection defines the fixed points of the climate system. The equation for null isoclines are easily calculated as an equation for $T_\star$ obtained by substituting Eq. (10.21) into Eq. (10.20)

$$\begin{aligned}\beta(T_\star)\left[R(T_\star)\mu S^{-1} + \mu(1-p)\alpha_o(T_\star) + \right.\\ \left. +(p-\mu+p\alpha_g\mu)\right] = p\gamma\end{aligned} \tag{10.22}$$

which can be recast as a third–order polynomial

$$\begin{aligned}-k\Psi T_\star^3 &+ k\left(2T_{opt}\Psi-\Gamma\right)T_\star^2 + \\ &+ \left[2kT_{opt}\Gamma + (1-kT_{opt}^2)\Psi\right]T_\star + \\ &+ \left[(1-kT_{opt}^2)\Gamma - \gamma p\right] = 0,\end{aligned} \tag{10.23}$$

where

$$\begin{aligned}\Gamma &= \frac{\mu}{Q_\odot}a^2(B_0 - B_1T_{opt}) + (p-\mu+\mu p\alpha_g) + \\ &+ \mu(1-p)(\alpha_{max} - \xi T_{low}) \\ \Psi &= \mu\left[\frac{B_1}{Q_\odot}a^2 + (1-p)\xi\right].\end{aligned} \tag{10.24}$$

Using Earth–like conditions for the different parameters, it can be found that

$$2T_{opt} >> \frac{\Gamma}{\Psi} \tag{10.25}$$

so that Eq. (10.23) becomes a second–order polynomial

$$\begin{aligned}2kT_{opt}T_\star^2 &+ \left[2kT_{opt}\Gamma + (1-kT_{opt}^2)\Psi\right]T_\star + \\ &+ \left[(1-kT_{opt}^2)\Gamma - \gamma p\right] = 0\end{aligned} \tag{10.26}$$

The solutions of Eq. (10.26) define up to two equilibrium temperatures $T_\star$ characterizing the vegetated solution.

The two null isoclines are reported in Figure 10.2 in the phase space (T, A), for different values of the parameters γ and a and two values of p. The steady states correspond to the intersections of the two curves. It can be seen that, in general, low values of the vegetation death–rate γ correspond to two climate states, and one single climate state for distances $a > 1$ with a low equilibrium temperature. As γ increases, some steady states tend to disappear, the only two steady states that survive corresponds to a close to the Earth's orbit $a \simeq 1$. Higher values of γ correspond to absence of vegetation and steady states tend to disappear. The same behavior can be observed for different values of p, what is changing is just the range of equilibrium temperatures and albedos.

10.4 Stability analysis of climate states

According to the usual dynamical system theory, the nature and stability of a fixed point can be investigated by studying the eigenvalues λ_k (in our case $k = 2$) of the Jacobian matrix $\mathbf{J}(T, A)$,

$$\mathbf{J} = -\frac{1}{C_T}\begin{bmatrix} S\frac{\partial \alpha}{\partial T} + \frac{\partial R}{\partial T} & S\frac{\partial \alpha}{\partial A} \\ \frac{\partial \beta(T)}{\partial T}A(1-A) & \beta(T)(1-2A)-\gamma \end{bmatrix} \tag{10.27}$$

its determinant $Det(\mathbf{J})$ and the discriminant $\Delta(\mathbf{J}) = Tr(\mathbf{J})^2 - 4Det(\mathbf{J})$. Let us briefly recall that, for real eigenvalues, we can have either a node (stable or unstable depending by the sign of $Tr(\mathbf{J})$) or a saddle (if $Det(\mathbf{J}) < 0$). On the contrary, for complex conjugate eigenvalues (i.e., $\Delta(\mathbf{J}) < 0$) we can have a stable (unstable) focus, according to the sign of $Tr(\mathbf{J})$, or a center ($Tr(\mathbf{J}) = 0$), corresponding to a marginal stability state.

10.4.1 Stability of the climatic states in absence of vegetation

In absence of vegetation $A_\star = 0$, the stability of the climate system of our planet can be analytically investigated. In fact, in this case, the eigenvalues of the Jacobian matrix are

$$\begin{aligned} \lambda_1 &= -\frac{1}{C_T}\left[S(1-p)\left(\frac{\partial \alpha_o}{\partial T}\right)_{T=T_\star} + B_1\right], \\ \lambda_2 &= \beta(T_\star) - \gamma. \end{aligned} \tag{10.28}$$

For both the extreme cases when the ocean is ice–free or ice covered, the ocean albedo does not depend on temperature, as well as $\beta(T_\star) = 0$ because either $T_\star > T_{up}$ or $T_\star < T_{low}$. In this case the two eigenvalues $\lambda_{1,2}$ of the matrix are $\lambda_1 = -B_1/C_T$ and $\lambda_2 = -\gamma$, which correspond to a stable node, whose stability is independent on the various parameters of the model.

In the case when the ocean is partially covered by ice, the albedo depends on temperature and the situation changes. In fact, in this case the node is stable only when

$$\begin{aligned} S(1-p)\xi + B_1 &> 0 \\ \beta(T_\star) - \gamma &< 0 \end{aligned} \tag{10.29}$$

which corresponds to a planet not too close to their hosting star

$$a^2 > (1-p)\left(\frac{Q_\odot}{B_1}\right)\left(\frac{\alpha_{max} - \alpha_{min}}{T_{up} - T_{low}}\right) \tag{10.30}$$

with an equilibrium temperature not so far from T_{opt}, namely

$$(T_\star - T_{opt})^2 > \left(\frac{1-\gamma}{k}\right) \tag{10.31}$$

which corresponds to

$$\begin{aligned} T_{low} &< T_\star < T_{opt} - \sqrt{\frac{1-\gamma}{k}} \\ T_{opt} + \sqrt{\frac{1-\gamma}{k}} &< T_\star \leq T_{up}. \end{aligned} \tag{10.32}$$

In the case of Earth–like parameters, the above conditions results in $a > 1.97$ and $T_\star \in \{[263, 268] \cup [298, 300]\}$, which means that the climate of a Earth–like planet with soil and ocean cannot be stable in absence of vegetation. When the above conditions are not satisfied, the fixed point can become an unstable node, when both signs of Eq. (10.29) are reversed, or a saddle when only one is reversed.

10.4.2 Stability of the vegetated steady–state solution

The stability of the vegetated steady–state solution cannot be analytically investigated and a numerical solution of Eq. (10.27) is required. Figure 10.3 shows the sign of $\Delta(\mathbf{J})$ in the plane (γ, a) for three different values of p (i.e., $p = 0.3$, $p = 0.5$ and $p = 0.8$), with two white lines referred to the contour lines at which $Det(\mathbf{J}) = 0$ (solid line) and $Tr(\mathbf{J}) = 0$ (dashed line).

As pointed out in Section 10.4, several steady states can be identified, according to the different nature of the eigenvalues. From Figure 10.3 (upper panel), representing the Earth-like case with $p = 0.3$, we can highlight the following results.

- For $\gamma \in [0., 0.06]$ and $a \in [1.01, 1.04]$ an unstable saddle point is found, indicating that a temperature perturbation increase and the system will leave its steady state.

- Regions II and III are both characterized by stable fixed points, classified as node (region II) and focus (region III). For region II we have that a temperature perturbation will decrease with respect to time and the system will come back to its steady state, with an exponential approach. Conversely, for region III, where eigenvalues are complex ($\Delta(\mathbf{J}) < 0$), their imaginary parts are responsible of oscillations around the steady state (stable focus).

- On the contrary, regions IV and V are both characterized by unstable fixed points. For region IV, an unstable node is found, with both positive eigenvalues (and, as a consequence $Tr(\mathbf{J}) > 0$), suggesting that a temperature perturbation will increase with respect to time and the system will leave its steady state. Similarly, in region V a perturbation will increase with amplified oscillations, leaving its steady state (unstable focus).

Similar results are found when p increases (i.e., middle and lower panels in Figure 10.3), with similar steady-state points obtained with different combinations of γ and a parameters.

An interesting situation can be investigated by looking at fixed points where $\Delta(\mathbf{J}) = 0$, indicating that a Hopf bifurcation occurs. It is a critical point where a system's stability switches and a periodic solution arises, corresponding to a fixed point which loses its stability, with a pair of complex conjugate eigenvalues that cross the complex plane imaginary axis. As shown in Rombouts and Ghil (2015), by setting $\gamma = 0.02$, a Hopf bifurcation occurs for which the system exhibits an anharmonic oscillatory behavior. Moreover, they showed that the corresponding unstable fixed point (i.e. (T^*,A^*)=(280.8,0.898)) is a saddle because the growth rate is an increasing function (e.g. $\beta'(T^*) > 0$). This implies that (Rombouts and Ghil, 2015, Fig. 5)

1. for T(t=0) < T^* the equilibrium solution will move towards the stable steady-state with no vegetation (A=0),
2. for T(t=0) > T^* the stationary solution will lead to the fixed point with higher temperature.

In our case, since the solar irradiance is not constant but depends on a control parameter a, we can have a Hopf bifurcation for different combinations of γ and a parameters. Figure 10.4 shows the evolution of the amplitude of the temperature oscillations ΔT and the characteristic period of oscillation as C_T changes (since C_T is responsible of the system characteristic time).

We note that, moving towards higher values of γ and a, both the amplitude and the period of oscillations tend to increase. Interestingly, for the present conditions of solar irradiance ($a = 1$) a Hopf bifurcation will occur if $\gamma \sim 0.4$. In this case, a $\Delta T \sim 3$ K with oscillations on 800-yr timescale is found. This behavior is well in agrement with that observed by Rombouts and Ghil (2015, Figure 7) who found temperature oscillations with an amplitude of 2-3 K and larger amplitude oscillations for the vegetation (until 70% of no vegetation). These results were also pointed out in several works (De Gregorio et al., 1992; Nevison et al., 1999; Rombouts and Ghil, 2015, and references therein) where the Daisyworld system exhibits self-sustained oscillations in a range of C_T and γ. Also Alberti et al. (2015) showed that, when small temperature perturbations are introduces in the initial condition, a striped pattern occurs in the range of low-to-intermediate luminosity values; conversely, for high luminosities (in this case $a < 1$), the greenhouse effect leads to the disappearance of the striped patterns. The main difference is that the albedo feedback of Daisyworld model is due to two types of daisies, black and white, respectively. This bimodality behavior of the albedo can be seen as similar to the role of sea ice in the model developed by Rombouts and Ghil (2015).

The observed oscillatory behavior needs to be investigated with more accuracy because it can reproduce several quasi-periodic behaviors observed in climatic time series (Alberti et al., 2014; Denton and Karlèn, 1973; Ditlevsen et al., 1973, 2007; Shao and Ditlevsen, 2016; Rahmstorf, 1994, 2003; Schulz, 2002, and references therein). Indeed, the climate system exhibits periodic or quasi-periodic oscillations, observed by different climatic proxies (e.g., $\delta^{18}O$, carbon dioxide), on different timescales (from years to millennia). These oscillations are related to several physical mechanisms of both internal and external origin (Shao and Ditlevsen, 2016) and present both sawtooth-like and smoothed behaviors, characterizing changes in the ice sheets volume. This behavior can be seen as a nonlinear response of the climate system to orbital forcing (see e.g., Ganopolski and Calov, 2011) or to internal "see-saw" mechanisms (Stocker, 1998). Also Rombouts and Ghil (2015) showed that, since the shape of the temperature and vegetations curves are similar but time-shifted, this could resemble the behavior of land ice volume during glacial-interglacial cycles. For these reasons, as also pointed out by Rombouts and Ghil (2015), the vegetation dynamics needs to be included in ice-oscillatory models to describe the observed nonlinear oscillations.

10.5 Conclusions

In this chapter we investigated the stability properties of a simple energy balance climate–vegetation model, consisting of a planetary surface partially covered by vegetation, a large ocean and a land surface, which can change in response to variation in stellar irradiance as, for example, related to its variable distance with respect to the hosting star. We showed that the nature of the fixed points and their stability change according to variations into the control parameters, as for example the growth–death rate of vegetation γ and the solar irradiance a. We note that the climate of an Earth–like planet with soil and ocean cannot be stable in absence of vegetation, showing unstable fixed points identified as unstable nodes or saddle. Conversely, in presence of vegetation the Earth-like case ($p = 0.3$) shows an unstable saddle point for $\gamma \in [0., 0.06]$ and $a \in [1.01, 1.04]$ and unstable nodes and focus (see Figure 10.3, upper panel). Stable fixed points are found in regions II and III in Figure 10.3. They are classified as node and focus, indicating that a temperature perturbation will decrease with respect to time and the system will come back to its steady state, with an exponential approach, or will present oscillations around the steady state (stable focus).

We also show that, since the solar irradiance is not constant but depends on a control parameter a, we can have a Hopf bifurcation for different combinations of γ and a parameters, evidencing that, moving towards higher values of γ and a, both the amplitude and the period of oscillations tend to increase. Interestingly, for the present conditions of solar irradiance ($a = 1$) a Hopf bifurcation will occur if $\gamma \sim 0.4$ and a $\Delta T \sim 3$ K with oscillations on 800-yr timescale is found, well in agrement with that observed by Rombouts and Ghil (2015, Figure 7). The observed oscillatory behavior needs to be investigated with more accuracy because it can reproduce several quasi-periodic behaviors observed in climatic time series.

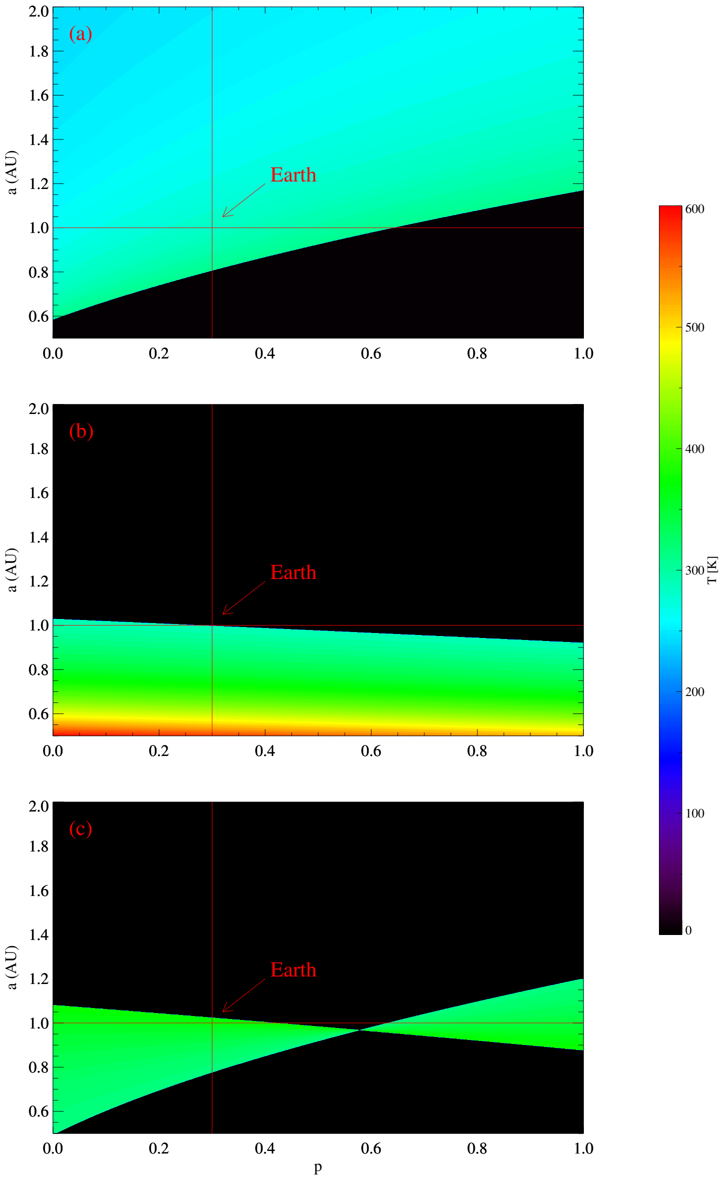

Figure 10.1: Contours of the equilibrium solutions $T_\star$ in the plane (p, a), when the vegetation is set to zero $A_\star = 0$. Panel (a) refers to the maximal albedo for ocean covered by ice $\alpha_o = \alpha_{max}$, panel (b) refers to the minimum albedo $\alpha_o = \alpha_{min}$ for ice–free ocean, and panel (c) refers to the intermediate case when only a fraction of ocean is covered by ice.

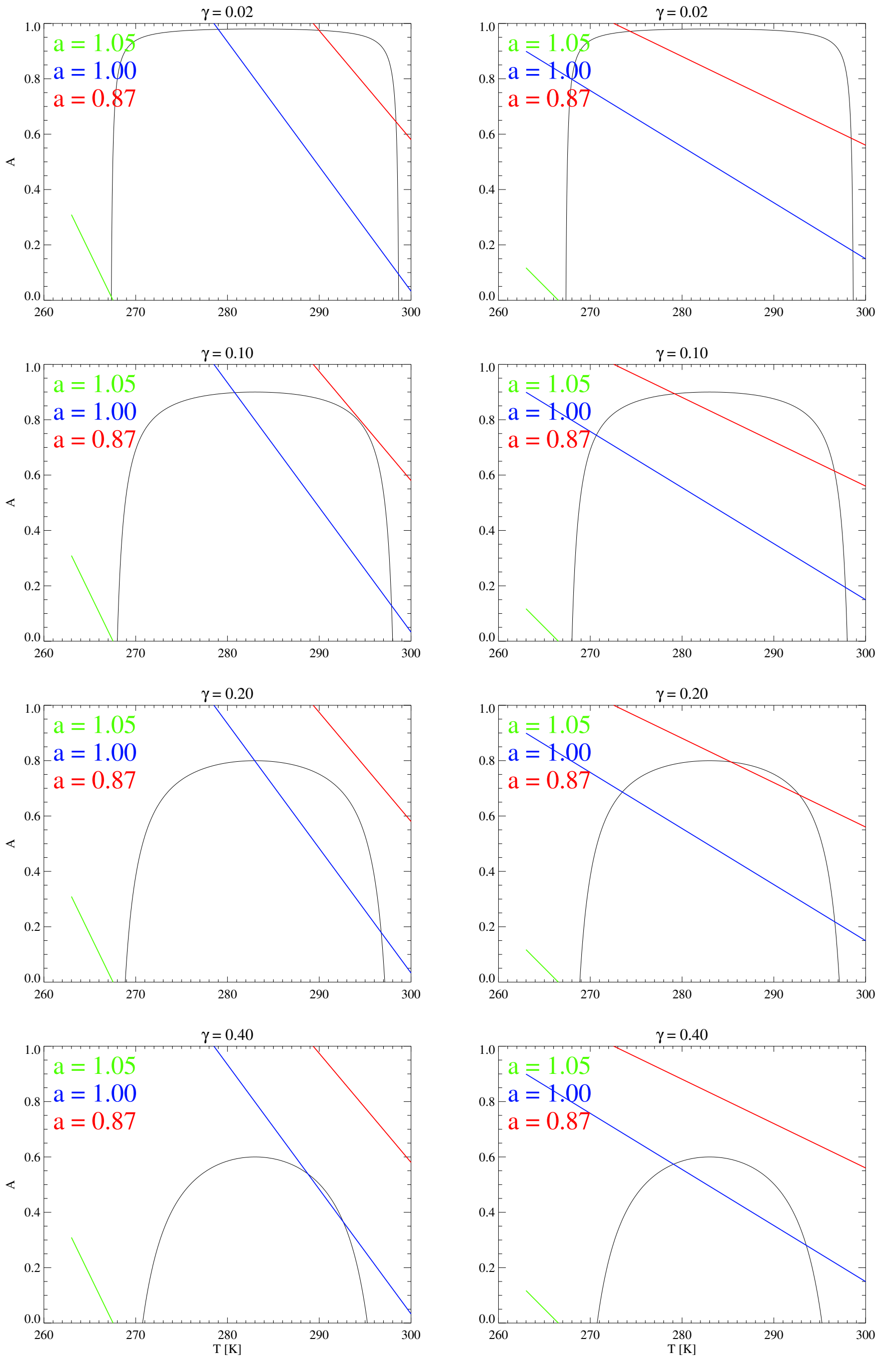

Figure 10.2: The (T,A) phase plane with the two nullclines obtained from Eq. (10.20) (black curve) and Eq. (10.21) (colored lines), respectively. The fixed points are the intersections of these two curves. The colored lines refer to three different values of the parameter a. Left and right panels are obtained by fixing $p = 0.3$ and $p = 0.8$, respectively, and four different values of γ ($\gamma = 0.02, 0.1, 0.2, 0.4$).

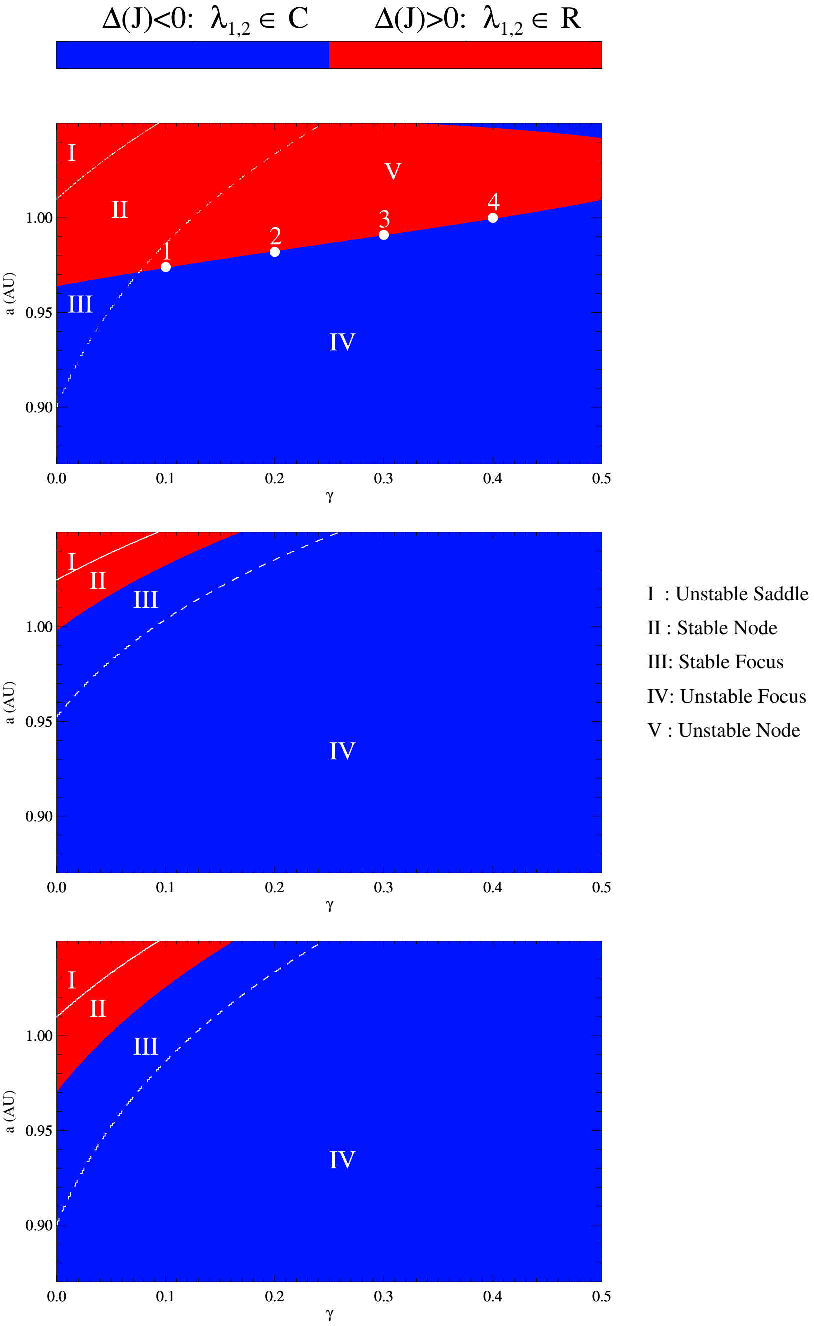

Figure 10.3: Contour plots of $\Delta(\mathbf{J})$ in the γ-a plane for $p = 0.3$ (upper panel), $p = 0.5$ (middle panel) and $p = 0.8$ (lower panel). White lines represent the contour lines at which $Det(\mathbf{J}) = 0$ (solid line) and $Tr(\mathbf{J}) = 0$ (dashed line) allowing us to identify several regimes (reported in Roman numbers).

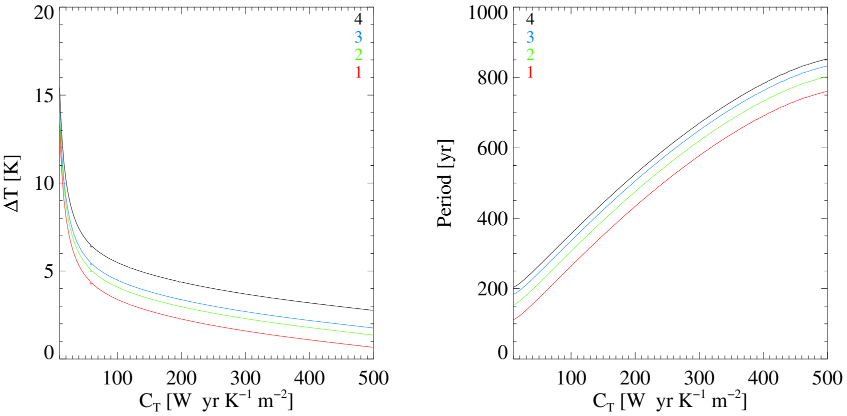

Figure 10.4: Numerical solutions of the model when a Hopf bifurcation occurs for a fixed $p = 0.3$. Right panel: evolution of the amplitude of temperature variations as a function of C_T. Left panel: dependence on C_T of the characteristic period of oscillations. The numbers refer to four cases obtained when $\Delta(\mathbf{J}) = 0$, as shown in Figure 10.3 (upper panel).

Chapter 11

Summary & Conclusions

The work in this thesis has been undertaken to investigate the effects of the solar variability on the Earth's environment, by using both observations and numerical models.

Concerning the short-term dynamical variability of the solar activity the results can be summarized as follows.

- The study of the geospace conditions during two major geomagnetic storms of solar cycle 24, i.e., the St. Patrick's Day storms in 2013 and 2015, reveals that solar wind changes, in terms of interplanetary magnetic field and transfer energy rate, lead changes in the magnetospheric configurations, by producing local changes on both ring current and auroral electrojets activities, on large timescales (typically $>$200 min). These processes are related to the so-called "directly driven" processes characterizing solar wind-magnetosphere coupling. On the other hand, on shorter timescales ($<$ 200 min) magnetospheric dynamics is only triggered by solar wind fast changes, related to the occurrence of "in situ" processes. This suggests that the short-timescale dynamics of the Earth's magnetosphere is governed by internal processes, well-known as "loading-unloading" mechanisms, related to the internal coupling between magnetospheric current systems (i.e., tail-ring coupling).

- By using both ground-based and geostationary observations of the geomagnetic field we provide a useful method to easily discriminate between a time-dependent large-timescale magnetic field and its time variations in both magnetospheric and ground observations. The analysis of magnetospheric observations shows that the large-timescale variations can be associated to the magnetic field observed by the spacecraft during its diurnal orbit (Rufenach et al., 1992), while the short-timescale variations could be related to the magnetospheric field fluctuations associated to the symmetric and partial ring current dynamics (De Michelis et al., 1999). Ground-based measurements show the existence of geomagnetic field variability governed by three different contributions: the short-timescale, related to the variations of the geomagnetic field driven by the magnetospheric current system dynamics, the intermediate-timescale variations, associated to the ionospheric origin contribution (i.e., solar quiet and disturbed current systems), as confirmed by the lack in magnetospheric reconstructions, and the large-timescale variations, related to the local average of the geomagnetic field.

- The implementation of a database of 276 SXR flares and 23 > 10 MeV SEP events that met the SWPC ≥ 10 pfu flux threshold criterion, covering the period 2006-2014, i.e., the declining phase of the 23rd solar cycle and the beginning part of the 24th solar cycle, was used to test the performance of ESPERTA, a SEP forecasting model developed by Laurenza et al. (2009). First, we compared the number of $\geq$ M2 1-8 $\mathring{A}$ SXR bursts for corresponding years, i.e., the first six years of solar cycles 23 (15 Sep 1996 - 15 Sep 2002, period A) and 24 (15 Dec 2008 - 15 Dec 2014, period B), corresponding to the ascending phases of the two cycles, respectively, and found that 40% [1-(257/430)] fewer of such bursts occurred during the rise phase of cycle 23. This could be related to several factors, such as the weak interplanetary magnetic field, decreasing the efficiency of particle acceleration mechanisms, the lower large-scale magnetic activity (i.e., active regions and sunspot areas), the reduction in the total heliospheric pressure, producing an anomalous expansion of CMEs, or to the paucity of CMEs producing the seed particles (Gopalswamy, Mäkelä, Akiyama, Yashiro and Thakur, 2015; Gopalswamy, Mäkelä, Yashiro, Xie, Akiyama and Thakur, 2015). From a comparison of the probability distribution functions of the 1-8 $\mathring{A}$ and ~ 1 MHz fluences of all $\geq$ M2 SXR bursts during the larger intervals C (1995-2005) and D (2006-2014), we found that the percentage of all the events exceeding the SXR fluence threshold of 0.1 J/m^2 is higher in period C than in period D (33% and 19%, respectively), as well as the percentage of all the events exceeding the radio fluence threshold of 6×10^5 sfu min (36% and 21%, respectively). Then, we test the reliability of the ESPERTA model (Laurenza et al., 2009) by evaluating the probability of detection (POD) and the False Alarm Rate (FAR) of this method on a new (2006-2014) database. We found that the POD and FAR levels (59% and 30%, respectively) were comparable to those (63%, 42%) obtained for the original 1995-2005 dataset, an indication of model robustness. Finally, the ESPERTA median (average) warning time (delta between the time the forecast is issued and the time event threshold is crossed) for the 66 SEP events with peak fluxes ≥ 10 pfu that were correctly called ("hits") from 1995-2014, was 4.8 h (~ 9 h), in the range 0.4-52.8 h, exceeding those obtained by other methods (e.g., Núñez (2011) average warning time of ~ 5 hours).

On the other hand, the long-term variability of solar activity produces different effects on the Earth's climate.

- Paleoclimate records of δ^{18}O related to the last glacial period show that proper EMD modes, significant with respect to a random null hypothesis, are present in both data sets of Northern and Southern hemispheres, thus confirming that natural cycles of abrupt climate changes during the last glacial period exist and their occurrence cannot be due to random fluctuations in time. Moreover, we showed that paleoclimate changes are the result of two distinct mechanisms, operating at different timescales: the first one is related to the occurrence of the so-called DO events, while the other one is useful to describe the climate evolution at longer timescales, characterized by intervals in which DO events happen and intervals when these are not observed. It was also found that the occurrences of DO events can be described as excitations of the system within the same climate state, while the longer timescale dynamics appear to be due to transitions between different climate states. Finally, through the cross-correlation analysis we show that Antarctic climate changes lead those of Greenland, with a characteristic time delay of $\sim$3 kyr, longer than previously reported.
- The study of a modified Daisyworld model, where spatial dependency, variable heat diffusivity and greenhouse effect are explicitly taken into account, evidenced that the system is able to self-regulate even in presence of values of the incident luminosity which are far from the current Sun-Earth conditions, at variance with previous results. We found that the diffusion process can destabilize the system, playing an important role in setting the symmetry with respect to the equator. Conversely, the greenhouse effect, modelled through a grayness function, affects the temperature evolution and contributes to self-regulating the planet climate, without any destabilization of the system, although it modifies its stability properties. Finally, we showed that when small perturbations are present in the initial conditions of both temperature and daisy coverages, these give rise to striped patterns for low-to-intermediate luminosity values when the perturbation wave number exceeds a threshold value. For high luminosities, the greenhouse effect leads to the disappearing of the striped patterns.
- By investigating the stability properties of a simple energy balance climate-vegetation model, consisting of a planetary surface partially covered by vegetation, a large ocean and a land surface, which can change in response to variation in stellar irradiance as, for example,

related to its variable distance with respect to the hosting star, we showed that the nature of the fixed points, and their stability, changes according to variations into the control parameters. We noted that the climate of an Earth-like planet with soil and ocean cannot be stable in absence of vegetation, showing unstable fixed points referring to unstable nodes or saddle. Conversely, in presence of vegetation the Earth-like case ($p = 0.3$) shows stable fixed points, classified as node and focus, or present oscillations around the steady state (stable focus). This observed oscillatory behavior needs to be investigated with more accuracy because it can reproduce several quasi-periodic behaviors observed in climatic time series.

These studies can be useful in the framework of solar-terrestrial relations to investigate both dynamical and energetic/radiative coupling mechanisms. Specifically, the short-term solar energetic particle events prediction model can be used as a tool, in near–real-time (if there will be real-time radio observations), to predict the occurrence of enhancements in proton flux, allowing us to turn off satellite instrumentation and prevent astonauts health problems due to high-energy particles. At the same time, the results obtained by the analysis of the St. Patrick's Day storms, allowing us to detect a timescale separation in solar wind-magnetosphere coupling, could be very useful to build up numerical prediction models of Sym-H or AE behavior, particularly helpful to forecast the occurrence of geomagnetic storms and substorms. Moreover, the EMD reconstructions obtained for both geostationary and ground-based observations could be used to efficiently calibrate the IGRF model, useful for ring current activity modeling, or to evaluate the local intensity of a geomagnetic storm on the ground, without any calculation and subtraction of average value for its evaluation (including the Sq field), allowing, for any ground observatory, the calculation of a local geomagnetic disturbance index. The methodological novelty, related to the use of EMD reconstructions to investigate the climate dynamics at different timescales, presented in Chapter 8, allows to highlight some characteristics of the climate transitions, useful to build up paleoclimate models to reconstruct climate variability and investigate inter-hemispheric connections. Finally, both climate models presented in Chapters 9 and 10 could be useful to explore the evolution of the Earth's climate, as for example when greenhouse effect changes, as well as exoplanets climate and habitability, since information about the atmospheres, and therefore greenhouse effect, of these planets are not available with accuracy.

Appendix A

Abbreviations

ACE	Advanced Composition Explorer
AU	Astronomical Unit
CIR	Corotating Interaction Region
CME	Coronal Mass Ejection
EMD	Empirical Mode Decomposition
GOES	Geostationary Operational Environmental Satellites
GSE	Geocentric Solar Ecliptic
GSM	Geocentric Solar Magnetospheric
HSS	High-speed stream
ICME	Interplanetary Coronal Mass Ejection
IMF	Interplanetary Magnetic Field
IMF	Intrinsic Mode Function
MHD	Magnetohydrodynamics
NASA	National Aeronautics and Space Administration
NOAA	National Oceanic and Atmospheric Administration
PFN	Phase Front Normal

Appendix B

Physical Constants

Astronomical Unit	1 AU = 1.49598×10^{11} m
Boltzmann Constant	$k_B = 1.38065 \times 10^{23}$ J K^{-1}
Electron Volt	1 eV = 1.60218×10^{-19} J
Earth radius	$R_E = 6.371 \times 10^{6}$ m
Solar mass	$M_\odot = 1.98855 \times 10^{30}$ kg
Solar radius	$R_\odot = 6.995 \times 10^{8}$ m
Speed of Light	$c = 2.99792 \times 10^{8}$ m s^{-1}

Appendix C

Kernel Density Estimator

The empirical pdf $p_{emp}(z)$ can be estimated through the kernel density estimator technique (Silvermann, 1998; Hall, 1992). Given a set of data points $z_i(i = 1, ..., n)$, the kernel density estimator of the pdf is defined as

$$\hat{f}(z) = \frac{1}{nh} \sum_{i=1}^{n} K\left(\frac{z - z_i}{h}\right) \tag{C.1}$$

where K is the kernel, a symmetric function that integrates to one, and $h > 0$ is a smoothing parameter denoted as bandwidth. The corresponding variance is

$$\hat{\sigma}(z) = \frac{1}{nh}\left[\frac{1}{nh} \sum_{i=1}^{n} K\left(\frac{z - z_i}{h}\right)^2 - h\hat{f}(z)^2\right] \tag{C.2}$$

Several kernel functions have been proposed (Gaussian, Epanechnikov, Triangular and so on) but a good choice is the Epanechnikov kernel, which is optimal in a minimum variance sense, choosing $h = 0.9s/n^{0.2}$, where s is the standard deviation of the data set. The confidence interval of $\hat{f}(z)$ has been evaluated through a bootstrap. Being

$$\hat{f}^*(z) = \frac{1}{nh^*} \sum_{i=1}^{n} K\left(\frac{z - z_i^*}{h}\right) \tag{C.3}$$

the bootstrap estimator of $\hat{f}(z)$,

$$\hat{\sigma^*}(z) = \frac{1}{nh^*}\left[\frac{1}{nh^*} \sum_{i=1}^{n} K\left(\frac{z - z_i^*}{h}\right)^2 - h^*\hat{f}^*(z)^2\right] \tag{C.4}$$

the variance of $\hat{f}^*(z)$ and

$$\hat{t}^*(z) = \frac{\hat{f}^*(z) - \hat{f}(z)}{\widehat{\sigma^*}(z)} \tag{C.5}$$

the bootstrap t statistic (Hall, 1992), the symmetric confidence interval with coverage probability $1 - \alpha$ is

$$[\hat{f}(z) - \hat{\sigma}(z)u^*_{1-\alpha/2}, \hat{f}(z) - \hat{\sigma}(z)u^*_{\alpha/2}] \tag{C.6}$$

where $u^*_{\alpha/2}$ is the bootstrap estimate of the quantile defined by $P(\hat{t}^*(z) \leq u^*_{\alpha/2} = \alpha/2$ and $u^*_{1-\alpha/2}$ is the bootstrap estimate of the quantile defined by $P(\hat{t}^*(z) \leq u^*_{1-\alpha/2} = 1 - \alpha/2$ (Hall, 1992). In order to remove asymptotic biases which are not correctly taken into account by the bootstrap procedure, we perform an under-smoothing by choosing a smaller bandwidth $h^* = 0.9s/n^{0.25} < h$ (Hall, 1992).

Bibliography

Ackland, G. J., Clark, M. A. and Lenton, T. M. (2003), 'Catastrophic desert formation in Daisyworld', *J. Theor. Biol.*, **223**, 239.

Adams, B. and Carr, J. (2003), 'Spatial pattern formation in a model of vegetation–climate feedback', *Nonlinearity*, **16**, 1339.

Adams, B., Carr, J., Lenton, T. M. and White, A. (2003), 'One–dimensional daisyworld: spatial interactions and pattern formation', *J. Theor. Biol.*, **223**, 505.

Ahn, B. H., Akasofu, S.-I. and Kamide, Y. (1983), 'The Joule heat–production rate and the particle energy injection rate as a function of the geomagnetic indices AE and AL', *J. Geophys. Res.*, **88**, 6275.

Akasofu, S.-I. and Chapman, S. (1961), 'The ring current, geomagnetic disturbance, and the Van Allen radiation belts', *J. Geophys. Res.*, **66**(5), 1321–1350. doi: 10.1029/JZ066i005p01321.

Alberti, T., Consolini, G., Lepreti, F., Laurenza, M., Vecchio, A. and Carbone, V. (2017*a*), 'Timescale separation in the solar wind–magnetosphere coupling during St. Patrick's Day storms in 2013 and 2015', *J. Geophys. Res.*, **112**. doi: 10.1002/2016JA023175.

Alberti, T., Laurenza, M., Cliver, E. W., Storini, M., Consolini, G. and Lepreti, F. (2017*b*), 'Solar activity from 2006–2014 and short–term forecasts of solar proton events using the ESPERTA model', *The Astrophys. J.*, **838**, 59. doi: https://doi.org/10.3847/1538-4357/aa5cb8.

Alberti, T., Lepreti, F., Vecchio, A., Bevacqua, E., Capparelli, V. and Carbone, V. (2014), 'Natural periodicities and Northern Hemisphere–Southern Hemisphere connection of fast temperature changes during the last glacial period: EPICA and NGRIP revisited', *Climate of the past*, **10**, 1751–1762. doi: 10.5194/cp–10–1751–2014.

Alberti, T., Lepreti, F., Vecchio, A. and Carbone, V. (2017*c*), 'On the stability of a climate model for an Earth–like planet with ground–water coverage', *Phys. Rev. E*, **submitted**.

Alberti, T., Piersanti, M., Vecchio, A., De Michelis, P., Lepreti, F., Carbone, V. and Primavera, L. (2016), ‘Identification of the different magnetic field contributions during a geomagnetic storm in magnetospheric and ground observations’, *Ann. Geophys.*, **34**, 1069–1084. doi: 10.5194/angeo–34–1069–2016.

Alberti, T., Primavera, L., Vecchio, A., Lepreti, F. and Carbone, V. (2015), ‘Spatial interactions in a modified Daisyworld model: heat diffusivity and greenhouse effects’, *Phys. Rev. E*, **92**, 052717. doi: http://dx.doi.org/10.1103/PhysRevE.92.052717.

Alley, R. B., Anandakrishnan, S. and Jung, P. (2001), ‘Stochastic resonance in the North Atlantic’, *Paleoceanography*, **16**, 190–198.

Anglada-Escudé, G., Amado, P. J., Barnes, J., Berdiñas, Z. M., Butler, R. P., Coleman, G. A. L., de la Cueva, I., Dreizler, S., Endl, M., Giesers, B., Jeffers, S. V., Jenkins, J. S., Jones, H. R. A., Kiraga, M., Kürster, M., Lòpez-Gonzàlez, M. J., Marvin, C. J., Morales, N., Morin, J., Nelson, R. P., Ortiz, J. L., Ofir, A., Paardekooper, S.-J., Reiners, A., Rodriguez, E., Rodriguez-Lòpez, C., Sarmiento, L. F., Strachan, J. P., Tsapras, Y., Tuomi, M. and Zechmeister, M. (2016), ‘A terrestrial planet candidate in a temperate orbit around Proxima Centauri’, *Nature*, **536**, 437–440.

Balasis, G., Daglis, I. A., Mann, I. R., Papadimitriou, C., Georgiou, M., Zesta, E. and Haagmans, R. (2015), ‘Multi–satellite study of the excitation of Pc3 and Pc4–5 ULF waves and their penetration across the plasmapause during the 2003 Halloween superstorm’, *Ann. Geophys.*, **33**, 1237–1252. doi: 10.5194/angeo–33–1237–2015.

Balasis, G., Daglis, I. A., Zesta, E., Papadimitriou, C., Georgiou, M., Haagmans, R. and Tsinganos, K. (2012), ‘ULF wave activity during the 2003 Halloween superstorm: multi–point observations from CHAMP, Cluster and Geotail missions’, *Ann. Geophys.*, **30**, 1751–1768. doi: 10.5194/angeo–30–1751–2012.

Balasis, G. and Egbert, G. D. (2006), ‘Empirical orthogonal function analysis of magnetic observatory data: Further evidence for non–axisymmetric magnetospheric sources for satellite induction studies’, *Geophys. Res. Lett.*, **33**, L11311. doi: 10.1029/2006GL025721.

Balch, C. C. (1999), ‘SEC proton prediction model: Verification and analysis’, *Radiat. Meas.*, **30**, 231–250.

Balch, C. C. (2008), ‘Updated verification of the Space Weather Prediction Center’s solar energetic particle prediction model’, *Space Weather*, **6**, S01001. doi: 10.1029/2007SW000337.

Barker, S., Knorr, G., Edwards, R. L., Parrenin, F., Putnam, A. E., Skinner, L. C., Wolff, E. and Ziegler, M. (2011), '800 000 Years of Abrupt Climate Variability', *Science*, **334**, 347–351. doi: 10.1126/science.1203580.

Bazilevskaya, G. A., Logachev, Y. I., Vashenyuk, E. V., Daibog, E. I., Ishkov, V. N., Lazutin, L. L., Miroshnichenko, L. I., Nazarova, M. N., Petrenko, I. E., Surova, G. M. and Yakovchouk, O. S. (2015), 'Solar Proton Events in Solar Activity Cycles 21–24', *Bulletin of the Russian Academy of Science*, **79**, 573–576.

Bazin, L., Landais, A., Lemieux-Dudon, B., Toyè Mahamadou Kele, H., Veres, D., Parrenin, F., Martinerie, P., Ritz, C., Capron, E., Lipenkov, V. Y., Loutre, M.-F., Raynaud, D., Vinther, B. M., Svensson, A., Rasmussen, S. O., Severi, M., Blunier, T., Leuenberger, M., Fischer, H., Masson-Delmotte, V., Chappellaz, J. A. and Wolff, E. W. (2013), 'An optimized multi–proxy, multi–site Antarctic ice and gas orbital chronology (AICC2012): 120–800 ka', *Clim. Past*, **9**, 1715–1731.

Belov, A., Garcia, H., Kurt, V., Mavromichalaki, H. and Gerontidou, M. (2005), 'Proton enhancements and their relation to the X–ray flares during the three last solar cycles', *Sol. Phys.*, **229**, 135–159.

Bender, M., Sowers, T., Dickson, M.-L., Orchardo, J., Grootes, P., Mayewski, P. A. and Meese, D. A. (1994), 'Climate correlations between Greenland and Antarctica during the past 100,000 years', *Nature*, **372**, 663–666.

Blunier, T., Chappellaz, J., Schwander, J., Dällenbach, A., Stauffer, B., Stocker, T. F., Raynaud, D., Jouzer, J., Clausen, H. B., Hammer, C. U. and Johnsen, S. J. (1998), 'Asyncrony of Antarctic and Greenland climate change during the last glacial period', *Nature*, **394**, 739–743.

Bond, G. C., Showers, W., Cheseby, M., Lotti, R., Almasi, P., de Menocal, P., Priore, P., Cullen, H., Hajdas, I. and Bonani, G. (1997), 'A pervasive millennial–scale cycle in North Atlantic Holocene and glacial climates', *Science*, **278**, 1257–1266.

Bond, G. C., Showers, W., Elliot, M., Evans, M., Lotti, R., Hajdas, I., Bonani, G. and Johnson, S. (1999), 'The North Atlantic's 1–2 kyr climate Rhythm: Relation to Heinrich Events, Dansgaard/Oeschger cycles and the Little Ice Age, Mechanisms of Global Climate Change at Millennial Time Scales', *Geophys. Monogr.*, **112**, 35–38. doi: 10.1029/GM112p0035.

Bond, G., Heinrich, H., Broecker, W., Labeyrie, L., McManus, J., Andrews, J., Huon, S., Jantschik, R., Clasen, S., Simet, C., Tedesco, K., Klas, M., Bonani, G. and Ivy, S. (1992), 'Evidence for massive discharges of icebergs into the North Atlantic ocean during the last glacial', *Nature*, **360**, 245–249.

Bond, G., Kromer, B., Beer, J., Muscheler, R., Evans, M. N., Showers, W., Hoffmann, S., Lotti-Bond, R., Hajdas, I. and Bonani, G. (2001), 'Persistent solar influence on North Atlantic climate during the Holocene', *Science*, **294**, 2130–2136.

Bougeret, J. L., Kaiser, M. L., Kellog, P. J., Manning, R., Goetz, K., Monson, S. J., Monge, N., Friel, L., Meetre, C. A., Perche, C., Sitruk, L. and Hoang, S. (1995), 'Waves: the radio and plasma wave investigation on the WIND spacecraft', *Space Sci. Rev.*, **71**, 231–263.

Broecker, W. S. (1994), 'Massive iceberg discharges as triggers for global climate change', *Nature*, **372**, 421–424.

Broecker, W. S. (1998), 'Paleocean circulation during the last deglaciation: A bipolar seesaw?', *Paleoceanography*, **13**, 119–121.

Broecker, W. S., Bond, G., Klas, M., Bonani, G. and Wolfi, W. (1990), 'A salt oscillator in the glacial North Atlantic? 1. The concept', *Paleoceanography*, **5**, 469–477.

Bruno, R. and Carbone, V. (2016), *Turbulence in the Solar Wind*, Springer International Publishing, 267 pp., Switzerland.

Budyko, M. I. (1969), 'The effect of solar radiation variations on the climate of the Earth', *Tellus*, **21**, 611–619.

Cade, W. B. and Christina, C.-P. (2015), 'The Origin of "Space Weather"', *Space Weather*, **13**(2), 99–103. doi: 10.1002/2014SW001141.

Cane, H. V. and Lario, D. (2006), 'An Introduction to CMEs and Energetic Particles', *Space Sci. Rev.*, **123**, 45–56. doi: 10.1007/s11214-006-9011-3.

Carrington, R. C. (1860), 'Description of a Singular Appearance seen in the Sun on September 1, 1859', *Monthly Notices Royal Astron. Soc.*, **20**, 13.

Chandra, R., Gopalswamy, N., Mäkelä, P., Xie, H., Yashiro, Y., Akiyama, S., Uddin, W., Srivastava, A. K., Joshi, N. C., Jain, R., Awasthi, A. K., Manoharan, P. K., Mahalakshmi, K., Dwivedi, V. C., Choudhary, D. P. and Nitta, N. V. (2013), 'Solar Energetic Particle Events during the Rise Phases of Solar Cycles 23 and 24', *Adv. Space Res.*, **52**, 2102.

Chandra, S., Vats, H. O. and Iyer, K. N. (2009), 'Differential coronal rotation using radio images at 17 GHz', *Mon. Not. Roy. Astron. Soc.*, **400**, L34–L37.

Chapman, S. (1929), 'On the theory of the solar diurnal variation of the Earth's magnetism', *Proc. R. Soc. Lond. Ser. A*, **129**, 369–386.

Cid, C., Palacios, J., Saiz, E., Guerrero, A. and Cerrato, Y. (2013), 'On extreme geomagnetic storms', *J. Space Weather Space Clim.*, **4**, A28. doi: 10.1051/swsc/2014026.

Clauer, C. R. and McPherron, R. L. (1980), 'The Relative Importance of the Interplanetary Electric Field and Magnetospheric Substorms on Partial Ring Current Development', *J. Geophys. Res.*, **85**, 6747–6759.

Clauer, C. R., McPherron, R. L. and Searles, C. (1983), 'Solar wind control of the low latitude asymmetric magnetic disturbance field', *J. Geophys. Res.*, **88**, 2123–2130.

Cliver, E. W., Boriakoff, V. and Bounar, K. H. (1998), 'Geomagnetic activity and solar wind during the Maunder Minimum', *Geophys. Res. Lett.*, **25**, 897–900.

Cliver, E. W. and Svalgaard, L. (2004), 'The 1859 solar–terrestrial disturbance and the current limits of extreme space weather activity', *Sol. Phys.*, **224**, 407–422.

Consolini, G. (1998), *Sandpile cellular automata and the magnetospheric dynamics*, Società Italiana di Fisica, 123 pp., Bologna (Italy).

Consolini, G. (2002), 'Self–organized criticality: a new paradigm for the magnetotail dynamics', *Fractals*, **10**, 275.

Consolini, G. and De Michelis, P. (2005), 'Local intermittency measure analysis of AE index: The directly driven and unloading component', *Geophys. Res. Lett.*, **32**, L05101. doi: 10.1029/2004GL022063.

Consolini, G. and De Michelis, P. (2011), 'Rank ordering multifractal analysis of the auroral electroject index', *Nonlin. Proc. Geophys.*, **18**, 277–285.

Consolini, G., Marcucci, M. F. and Candidi, M. (1996), 'Multifractal structure of auroral electroject index data', *Phys. Rev. Lett.*, **76**, 4082.

Crooker, N. C. (1972), 'High–Time Resolution of the Low–Latitude Asymmetric Disturbance in the Geomagnetic Field', *J. Geophys. Res.*, **77**, 773–775.

Crooker, N. C. and Siscoe, G. L. (1971), 'A study of geomagnetic disturbance field asymmetry', *Radio Sci.*, **6**, 495–501.

Crucifix, M., Loutre, M. F. and Berger, A. (2006), 'The climate response to the astronomical forcing', *Space Sci. Rev.*, **125**, 213.

Cummings, D. A. T., Irizarry, R. A., Huang, N. E., Endy, T. P., Nisalak, A., Ungchusak, K. and Burke, D. S. (2004), 'Travelling waves in the occurrence of dengue haemorrhagic fever in Thailand', *Nature*, **427**, 344–347. doi: 10.1038/nature02225.

Daglis, I. A., Livi, S., Sarris, E. T. and Wilken, B. (1994), 'Energy density of ionospheric and solar wind origin ions in the near–Earth magnetotail during substorms', *J. Geophys. Res.*, **99**, 5691–5703.

Dansgaard, W., Johnsen, S. J., Clausen, H. B., Dahl-Jensen, D., Gundestrup, N. S., Hammer, C. U., Hvidberg, C. S., Steffensen, J. P., Sveinbjornsdottir, A. E., Jouzel, J. and Bond, G. (1993), 'Evidence for general instability of past climate from a 250–kyr ice–core record', *Nature*, **364**, 218–220.

Davis, T. N. and Sugiura, M. (1966), 'Auroral electroject activity index AE and its universal time variations', *J. Geophys. Res.*, **71**, 785.

De Gregorio, S., Pielke, A. and Dalu, G. A. (1992), 'A delayed biophysical system for the Earth's climate', *J. Nonlinear Sci.*, **2**, 263.

De Michelis, P. and Consolini, G. (2015), 'On the local Hurst exponent of geomagnetic field fluctuations: Spatial distribution for different geomagnetic activity levels', *J. Geophys. Res.*, **120**, 2691–2701. doi: 10.1002/2014JA020685.

De Michelis, P., Consolini, G., Materassi, M. and Tozzi, R. (2011), 'An information theory approach to the storm–substorm relationship', *J. Geophys. Res.*, **116**, A08225. doi: 10.1029/2011JA016535.

De Michelis, P., Consolini, G. and Tozzi, R. (2012), 'On the multi–scale nature of large geomagnetic storms: An empirical mode decomposition analysis', *Nonlin. Proc. Geophys.*, **19**, 667–673. doi: 10.5194/npg-19-667-2012.

De Michelis, P., Consolini, G. and Tozzi, R. (2015), 'Latitudinal dependence of short timescale fluctations during intense geomagnetic storms: A permutation entropy approach', *J. Geophys. Res.*, **120**, 5633–5644. doi: 10.1002/2015JA021279.

De Michelis, P., Daglis, I. A. and Consolini, G. (1999), 'An average image of proton plasma pressure and of current systems in the equatorial plane derived from AMPTE/CCE–CHEM measurements', *J. Geophys. Res.*, **104**, 28615–28624. doi: 10.1029/1999JA900310.

De Michelis, P., Tozzi, R. and Consolini, G. (2010), 'Principal component's features of mid–latitude geomagnetic daily variation', *Ann. Geophys.*, **28**, 2213–2226. doi: 10.5194/angeo–28–2213–2010.

Denton, G. H. and Karlèn, W. (1973), 'Holocene climatic changes: Their pattern and possible cause', *Quaternary Res.*, **3**, 155–174. doi: 10.1016/0033–5894(73)90040–9.

Dessler, A. J. and Parker, E. N. (1959), 'Hydromagnetic theory of magnetic storms', *J. Geophys. Res.*, **64**, 2239–2259.

Diego, P., Storini, M. and Laurenza, M. (2010), 'Persistence in recurrent geomagnetic activity and its connection with Space Climate', *J. Geophys. Res.*, **115**, A06103. doi: 10.1029/2009JA014716.

Dierckxsens, M., Tziotziou, K., Dalla, S., Patsou, I., Marsh, M. S., Crosby, N. B., Malandraki, I. and Tsiropoula, G. (2015), 'Relationship between Solar Energetic Particles and Properties of Flares and CMEs: Statistical Analysis of Solar Cycle 23 Events', *Sol. Phys.*, **290**, 841–874.

Ditlevsen, P. D., Andersen, K. K. and Svensson, A. (2007), 'The DO–climate events are probably noise induced: statistical investigation of the claimed 1470 years cycle', *Clim. Past*, **3**, 129–134. doi: 10.5194/cp–3–129–2007.

Ditlevsen, P. D., Kristensen, M. S. and Andersen, K. K. (1973), 'The Recurrence Time of Dansgaard–Oeschger Events and Limits on the Possible Periodic Component', *J. Climate*, **18**, 2594–2603.

Duffin, R. T., White, S. M., Ray, P. S. and Kaiser, M. L. (2015), 'Type III–L Solar Radio Bursts and Solar Energetic Particle Events', *Journal of Physics: Conference Series*, **642**, 012006.

Dungey, J. W. (1961), 'Interplanetary magnetic field and the auroral zones', *Phys. Rev. Lett.*, **6**, 47–48.

Eddy, J. A. (1976), 'The Maunder Minimum', *Science*, **192**, 1189–1202. doi: 10.1126/science.192.4245.1189.

Eddy, J. A. (1983), 'The Maunder Minimum: A reappraisal', *Sol. Phys.*, **89**, 195–207. doi: 10.1007/BF00211962.

Emery, B. A., Richardson, I. G., Evans, D. S. and Rich, F. J. (2009), 'Solar wind structure sources and periodicities of auroral electron power over three solar cycles', *J. Atmos. Sol. Terr. Phys.*, **71**, 1157–1175.

Emery, B. A., Richardson, I. G., Evans, D. S., Rich, F. J. and Wilson, G. R. (2011), 'Solar Rotational Periodicities and the Semiannual Variation in the Solar Wind, Radiation Belt, and Aurora', *Sol. Phys.*, **274**, 399–425. doi: 10.1007/s11207–011–9758–x.

EPICA (2004), 'Eight glacial cycles from Antarctic ice core', *Nature*, **429**, 623–628.

EPICA (2006), ‘One–to–one coupling of glacial climate variability in Greenland and Antarctica’, *Nature*, **444**, 195–198.

Flandrin, P., Gonçalvès, P. and Rilling, G. (2004), *Detrending and denoising with empirical mode decompositions*, Proceedings of Eusipco, Wien (Austria).

Fröhlich, C. and Lean, J. (2004), ‘Solar radiative output and its variability: evindence and mechanisms’, *Astron. Astrophys. Rev.*, **12**, 273–320.

Fytterer, T., Arras, C. and Jacobi, C. (2013), ‘Terdiurnal signatures in sporadic E layers at mid–latitudes’, *Adv. Radio Sci.*, **11**, 1–7. doi: 10.5194/ars–11–1–2013.

Ganopolski, A. and Calov, R. (2011), ‘The role of orbital forcing, carbon dioxide and regolith in 100 kyr glacial cycles’, *Clim. Past*, **7**, 1415–1425. doi: 10.5194/cp–7–1415–2011.

Garcia, H. A. (1994), ‘Temperature and hard X–ray signatures for energetic proton events’, *Astrophys. J.*, **420**, 422–432. doi: 10.1086/173572.

Ghil, M. (1976), ‘Climate Stability for a Sellers–Type Model’, *J. Atmos. Sci.*, **33**, 3–20.

Ghil, M. (1985), *Turbulence and Predictability in Geophysical Fluid Dynamics and Climate Dynamics*, Theoretical Climate Dynamics: An Introduction, pp. 347–402, Procedings of the Internation School of Physics,.

Gleissberg, W. (1939), ‘A long–periodic fluctuation of the sun-spot numbers’, *Observatory*, **62**, 158–159.

Gleissberg, W. (1948), ‘A preliminary forecast of solar activity’, *Popular Astron.*, **56**, 399.

Gleissberg, W. (1952), ‘Die Häufigkeit der Sonnenflecken’, *Akademie–Verlag*, **2**.

Gleissberg, W. (1971), ‘The Probable Behaviour of Sunspot Cycle 21’, *Sol. Phys.*, **21**, 240–245. doi: 10.1007/BF00155794.

Gonzalez, W. D., Joselyn, J. A., Kamide, Y., Kroehl, H. W., Rostoker, G., Tsurutani, B. T. and Vasyliunas, V. M. (1994), ‘What is a geomagnetic storm?’, *Journal of Geophysical Research: Space Physics*, **99**(A4), 5771–5792. doi: 10.1029/93JA02867.
URL: *http://dx.doi.org/10.1029/93JA02867*

Gopalswamy, N. (2012), ‘Space Weather: the Space Radiation Environment’, *AIP Conference Proceedings*, **1500**, 14–19.

Gopalswamy, N., Akiyama, S., Yashiro, S., Michalek, G. and Lepping, R. P. (2008), ‘Solar Sources and Geospace Consequences of Interplanetary Magnetic Clouds Observed During Solar Cycle 23’, *J. Atmos. Sol. Terr. Phys.*, **70**, 245.

Gopalswamy, N., Mäkelä, P., Akiyama, S., Yashiro, S. and Thakur, N. (2015), ‘CMEs during the Two Activity Peaks in Cycle 24 and their Space Weather Consequences’, *Sun Geosph.*, **10**, 111.

Gopalswamy, N., Mäkelä, P., Yashiro, S., Xie, H., Akiyama, S. and Thakur, N. (2015), ‘High–energy solar particle events in cycle 24’, *J. Physics: Conference Series*, **642**, 012012.

Gopalswamy, N., Xie, H., Akiyama, S., Mäkelä, P. and Yashiro, S. (2014), ‘Major solar eruptions and high–energy particle events during solar cycle 24’, *Earth, Planets & Space*, **60**, 104. doi: 10.1186/1880–5981–66–104.

Hale, G. E., Ellerman, F., Nicholson, S. B. and Joy, A. H. (1919), ‘The Magnetic Polarity of Sun–Spots’, *Astrophys. J.*, **49**, 153–178. doi: 10.1086/142452.

Hall, P. (1992), ‘Effect of bias estimation on coverage accuracy of bootstrap confidence intervals for a probability density’, *Ann. Stat.*, **20**, 675–694.

Hansen, J. (2005), ‘A slippery slope: How much global warming constitutes “dangerous anthropogenic interference”?’, *Climatic Change*, **68**, 269–279.

Harding, S. P. and Lovelock, J. E. (1996), ‘Exploiter mediated coexistence and frequency–dependent selection in a geophysiological model’, *J. Theor. Biol.*, **182**, 109.

Harvey, K. L. and White, O. R. (1999), ‘What is solar cycle minimum?’, *J. Geophys. Res.*, **104**, 19759–19764. doi: 10.1029/1999JA900211.

Hathaway, D. H. (2010), ‘The Solar Cycle’, *Living Rev. Solar Phys.*, **7**, 1.
URL: *http://www.livingreviews.org/lrsp-2010-1*

Hawary, R. E., Yumoto, K., Yamazaki, Y., Mahrous, A., Ghamry, E., Meloni, A., Badi, K., Kianji, G., Uiso, C. B. S., Mwiinga, N., Joao, L., Affluo, T., Sutcliffe, P. R., Mengistu, G., Baki, P., Abe, S., Ikeda, A., Fujimoto, A. and Tokunaga, T. (2012), ‘Annual and semi–annual Sq variations at 96° MM MAGDAS I and II stations in Africa’, *Earth, Planets & Space*, **64**, 425–432. doi: 10.5047/eps.2011.10.013.

Heinrich, H. (1988), ‘Origin and consequences of cyclic ice rafting in the Northeast Atlantic Ocean during the past 130 000 years’, *Quat. Res.*, **29**, 142–152.

Hodgson, R. (1860), ‘On a curious Appearance seen in the Sun’, *Monthly Notices Royal Astron. Soc.*, **20**, 15.

Huang, N. E., Shen, Z., Long, S. R., Wu, M. C., Shih, H. H., Zheng, Q., Yen, N.-C., T. C. C. and Liu, H. H. (1998), ‘The empirical mode decomposition and the Hilbert spectrum for nonlinear and non–stationary time series analysis’, *Royal Soc. Lond. Proc. Ser. A*, **454**, 903–995. doi: 10.1098/rspa.1998.0193.

Huang, N. E. and Wu, Z. (2008), ‘A review on Hilbert–Huang transform: Method and its applications to geophysical studies’, *Rev. Geophys.*, **46**, RG2006. doi: 10.1029/2007RG000228.

Huang, X., Wang, H.-N. and Li, L.-P. (2012), ‘Ensemble prediction model of solar proton events associated with solar flares and coronal mass ejections’, *Res. in Astron. Astrophys.*, **12**, 313–321.

Ineson, S., Maycock, A. C., Gray, L. J., Scaife, A. A., Dunstone, N. J., Harder, J. W., Knight, J. R., Lockwood, M., Manners, J. C. and Wood, R. A. (2015), ‘Regional climate impacts of a possible future grand solar minimum’, *Nat. Comm.*, **6**, 7535.

IPCC (2014), *Climate Change 2014: Synthesis Report*, Core Writing Team, R.K. Pachauri and L.A. Meyer (eds.), 151 pp., Geneva, Switzerland.

Kahler, S. W., Cliver, E. W. and Ling, A. G. (2007), ‘Validating the proton prediction system (PPS)’, *J. Atmos. Sol. Terr. Phys.*, **69**, 43–49.

Kahler, S. W. and Ling, A. G. (2015), ‘Forecasting SEP events with same active region prior flares’, *Space Weather*, **13**, 665–675. doi: 10.1002/2015SW001222.

Kamide, Y. (1992), ‘Is substorm occurrence a necessary condition for a magnetic storm?’, *J. Geomagn. Geoelectr.*, **44**, 109–117.

Kamide, Y. (2001), ‘Interplanetary and magnetospheric electric fields during geomagnetic storms: what is more important, steady–state fields or fluctuating fields?’, *J. Atmos. Sol. Terr. Phys.*, **63**, 413–420.

Kamide, Y. and Kokubun, S. (1996), ‘Two–component auroral electrojet: Importance for substorm studies’, *J. Geophys. Res.*, **101**, 089.

Kawasaki, K. and Akasofu, S.-I. (1971), ‘Low latitude DS component of geomagnetic storm field’, *J. Geophys. Res.*, **76**, 2396–2405.

Klimas, A. J., Vassiliadis, D., Baker, N. and Roberts, D. A. (1996), ‘The organized nonlinear dynamics of the magnetosphere’, *J. Geophys. Res.*, **101**, 13089.

Kontogiannis, I., Belehaki, A., Tsiropoula, G., Tsagouri, I., Anastasiadis, A. and Papaioannou, A. (2016), 'Building a new space weather facility at the National Observatory of Athens', *Adv. Space Res.*, **57**, 418–430.

Kovacs, P., Carbone, V. and Voros, Z. (2001), 'Wavelet–based filtering of intermittent events from geomagnetic time–series', *Planetary and Space Science*, **49**, 1219–1231.

Laurenza, M., Cliver, E. W., Hewitt, J., Storini, M., Ling, A., Balch, C. C. and Kaiser, M. L. (2009), 'A technique for short–term warnings of solar energetic particle events based on flare location, flare size and evidence of particle escape', *Space Weather*, **7**, S04008. doi: 10.1029/2007SW000379.

Le Treut, H. (2012), 'Greenhouse gases, aerosols and reducing future climate uncertainties', *Surv. Geophys.*, **33**, 723–731.

Lenton, T. M. and Lovelock, J. E. (2000), 'Daisyworld is Darwinian: constraints on adaptation are important for planetary self–regulation', *J. Theor. Biol.*, **206**, 109.

Lenton, T. M. and Lovelock, J. E. (2001), 'Daisyworld revisited: quantifying biological effects on planetary self–regulation', *Tellus B*, **53**, 288.

Livina, V. N., Kwasniok, F. and Lenton, T. M. (2010), 'Potential analysis reveals changing number of climate states during the last 60 kyr', *Clim. Past*, **6**, 77–82.

Lockwood, M., Harrison, R. G., Woollings, T. and Solanki, S. K. (2010), 'Are cold winters in Europe associated with low solar activity?', *Environmental Research Letters*, **5**(2), 024001. doi: http://dx.doi.org/10.1088/1748–9326/5/2/024001.

Love, J. J. (2011), 'Secular trends in storm–level geomagnetic activity', *Ann. Geophys.*, **29**, 251–262. doi: 10.5194/angeo–29–251–2011.

Lovejoy, S. and Schertzer, D. (2013), *The Weather and Climate*, Cambridge Univ. Press.

Lovelock, J. E. (1972), 'Gaia as seen through the atmosphere', *Atm. Env.*, **6**, 579–580.

Lovelock, J. E. (1992*b*), *The Ages of Gaia: A Biography of Our Living Earth*, W.W. Norton & Co Eds.

Lovelock, J. E. (1992*a*), 'A numerical model for biodiversity', *Philos. Trans. R. Soc. Ser. B*, **338**, 383–391.

Lovelock, J. E. and Watson, A. J. (1982), 'The regulation of carbon dioxide and climate: Gaia or geochemistry', *Planet. Space Sci.*, **30**, 795–802.

Lyons, L. R., Blanchard, G. T., Samson, J. C., Lepping, R. P., Yamamoto, T. and Moretto, T. (1997), 'Coordinated observations demonstrating external substorm triggering', *J. Geophys. Res.*, **102**, 27039–27051.

Mann, I. R., O'Brien, T. P. and Milling, D. K. (2004), 'Correlations between ULF wave power, solar wind speed, and relativistic electron flux in the magnetosphere: solar cycle dependence', *J. Atm. Sol. Terr. Phys.*, **66**, 187–198.

Mannucci, A. J., Crowley, G., Tsurutani, B. T., Verkhoglyadova, O. P., Komjathy, A. and Stephens, P. (2014), 'Interplanetary magnetic field By control of prompt total electron content increases during superstorms', *J. Atm. Sol. Terr. Phys.*, **115**, 7–16. doi: 10.1016/j.jastp.2014.01.001.

Marsh, N. D. and Ditlevsen, P. D. (1997), 'Observation of atmospheric and climate dynamics from a high resolution ice core record of a passive tracer over the last glaciation', *J. Geophys. Res.*, **102**, 11219–11224.

Matsushita, S. and Maeda, H. (1965), 'On the geomagnetic quiet daily variation field during the IGY', *J. Geophys. Res.*, **70**, 2535–2558.

Maunder, E. W. (1890), 'Professor Spoerer's researches on sun–spots', *Monthly Notices of the Royal Astronomical Society*, **50**, 251–252.

Maunder, E. W. (1894), 'A prolonged sunspot minimum', *Knowledge*, **17**, 173–176.

McCullagh, P. and Nelder, J. A. (1983), *Generalized Linear Models*, chap. 4, pp. 98–155, Chapman and Hall, London (England).

McDonald, A. J., Baumgaertner, A. J. G., Fraser, G. J., George, S. E. and Marsh, S. (2007), 'Empirical Mode Decomposition of the atmospheric wave field', *Ann. Geophys.*, **25**, 375–384.

McPherron, R. L., Baker, D. N. and Bargatze, L. F. (1986), *Linear filters as a method of real time prediction of geomagnetic activity*, Solar Wind Magnetosphere Coupling, edited by Y. Kamide and J.A. Slavin, pp. 85–92.

Miller, G. H., Geirsdóttir, A., Zhong, Y., Larsen, D. J., Otto-Bliesner, B. L., Holland, M. M., Bailey, D. A., Refsnider, K. A., Lehman, S. J., Southon, J. R., Anderson, C., Björnsson, H. and Thordarson, T. (2012), 'Abrupt onset of the Little Ice Age triggered by volcanism and sustained by sea-ice/ocean feedbacks', *Geophysical Research Letters*, **39**(2), L02708. doi: 10.1029/2011GL050168.
URL: *http://dx.doi.org/10.1029/2011GL050168*

Morgan, V., Delmotte, M., van Ommen, T., Jouzel, J., Chappellaz, J., Woon, S., Masson-Delmotte, V. and Raynaud, D. (2002), 'Relative timing of deglacial climate events in Antarctica and Greenland', *Science*, **297**, 1862–1864.

Mursula, K., Usoskin, I. G. and Kovaltsov, G. A. (2001), 'Persistent 22–year cycle in sunspot activity: Evidence for a relic solar magnetic field', *Sol. Phys.*, **198**, 51–56.

Mursula, K. and Zieger, B. (1996), 'The 13.5–day periodicity in the sun, solar wind, and geomagnetic activity: The last three solar cycles', *J. Geophys. Res.*, **101**, 27077–27090.

N*úñ*ez, M. (2011), 'Predicting solar energetic proton events (E> 10 MeV)', *Space Weather*, **9**, S07003.

NASA (2006), *Heliophysics. The New Science of the Sun–Solar-System Connection: Recommended Roadmap for Science and Technology 2005-2035*, National Aeronautics and Space Administration, 181 pp., Washington, D.C.

Nevison, C., Gupta, C. and Klinger, L. (1999), 'Self–sustained temperature oscillations on Daisyworld', *Tellus B*, **51**, 806.

Newell, P. T., Sotirelis, T., Liou, K., Meng, C.-I. and Rich, F. J. (2007), 'A nearly universal solar wind–magnetosphere coupling function inferred from 10 magnetospheric state variables', *J. Geophys. Res.*, **112**, A01206. doi: 10.1029/2006JA012015.

NGRIP (2004), 'High–resolution records of Northern Hemisphere climate extending into the last interglacial period', *Nature*, **431**, 147–151.

Nymmik, R. A. (1999), 'Probabilistic model for fluences and peak fluxes of solar energetic particles', *Rad. Meas.*, **30**, 287–296.

O'Brien, S. R., Mayewski, P. A., Meeker, L. D., Meese, D. A., Twickler, M. S. and Whitlow, S. I. (1995), 'Complexity of Holocene Climate as Reconstructed from a Greenland Ice Core', *Science*, **270**, 1962–1964.

Ogurtsov, M. G., Nagovitsyn, Y. A., Kocharov, G. E. and Jungner, H. (2002), 'Long–period cycles of the Sun's activity recorded in direct solar data and proxies', *Sol. Phys.*, **211**, 371–394. doi: 10.1023/A:1022411209257.

Otkidychev, P. A. and Skorbezh, N. N. (2014), 'Activity indices in solar cycle 24 and their correlation with general regularities of cycle 19–23 according to mountain astronomical station data', *Geomagnetism and Aeronomy*, **54**, 1014.

Paillard, D. (2001), 'Glacial cycles: toward a new paradigm', *Rev. Geophys.*, **39**, 325–346.

Pallocchia, G., Amata, E., Consolini, G., Marcucci, M. F. and Bertello, I. (2007), 'AE index forecast at different time scales through an ANN algorithm based on L1 IMF and plasma measurements', *J. Atmos. Sol. Terr. Phys.*, **70**, 663–668.

Papaioannou, A., Anastasiadis, A., Sandberg, I., Georgoulis, M. K., Tsiropoula, G., Tziotziou, K., Jiggens, P. and Hilgers, A. (2015), 'A Novel Forecasting System for Solar Particle Events and Flares (FORSPEF)', *J. Physics: Conference Series*, **632**, 012075.

Papaioannou, A., Sandberg, I., Anastasiadis, A., Kouloumvakos, A., Georgoulis, M. K., Tziotziou, K., Tsiropoula, G., Jiggens, P. and Hilgers, A. (2016), 'Solar flares, coronal mass ejections and solar energetic particle event characteristics', *J. Space Weath. Space Clim.*, **632**, A42.

Park, J., Moon, Y.-J. and Gopalswamy, N. (2012), 'Dependence of solar proton events on their associated activities: Coronal mass ejection parameters', *J. Geophys. Res.*, **117**, A08108. doi: 10.1029/2011JA017477.

Parker, E. N. (1958), 'Dynamics of the interplanetary gas and magnetic fields', *Astrophys. J.*, **128**, 664.

Parker, E. N. (1965), 'The passage of energetic charged particles through interplanetary space', *Planet. Space Sci.*, **13**, 9–49. doi: 10.1016/0032–0633(65)90131–5.

Peavoy, D. and Franzke, C. (2010), 'Bayesian analysis of rapid climate change during the last glacial using Greenland δ^{18}O data', *Clim. Past*, **6**, 787–794. doi: 10.5194/cp–6–787–2010.

Perreault, P. and Akasofu, S.-I. (1978), 'A study of geomagnetic storms', *Geophys. J. R. Astr. Soc.*, **54**, 547–573.

Piersanti, M., Villante, U., Waters, C. L. and Coco, I. (2012), 'The 8 June 2000 ULF wave activity: A case study', *J. Geophys. Res.*, **117**, A02204. doi: 10.1029/2011JA016857.

Posner, A. (2007), 'Up to 1–hour forecasting of radiation hazards from solar energetic ion events with relativistic electrons', *Space Weather*, **5**, S05001. doi: 10.1029/2006SW000268.

Prasanna Subramanian, S. and Shanmugaraju, A. (2016), 'Study of intensive solar flares in the rise phase of solar cycle 23 and 24 and other activities', *Astrophys. Space Sci.*, **361**, 78.

Pulkkinen, T. (2007), 'Space Weather: Terrestrial Perspective', *Living Rev. Solar Phys.*, **4**, 1. doi: 10.12942/lrsp–2007–1.

Rahmstorf, S. (1994), 'Rapid climate transitions in a coupled ocean–atmosphere model', *Nature*, **372**, 82–85.

Rahmstorf, S. (2002), 'Ocean circulation and climate during the past 120,000 years', *Nature*, **419**, 207–214.

Rahmstorf, S. (2003), 'Timing of abrupt climate change: A precise clock', *Geophys. Res. Lett.*, **30**, 1510–1514.

Reames, D. V. (1999), 'Particle acceleration at the Sun and in the heliosphere', *Space Sci. Rev.*, **90**, 413–491.

Richardson, I. G. (2013), 'Geomagnetic activity during the rising phase of solar cycle 24', *J. Space Weather Space Clim.*, **3**, A08.

Richardson, I. G. (2014), 'Identification of Interplanetary Coronal Mass Ejections at Ulysses Using Multiple Solar Wind Signatures', *Sol. Phys.*, **289**, 3843. doi: 10.1007/s11207–014–0540–8.

Richmond, A. D., Matsushita, S. and Tarpley, J. D. (1976), 'On the production mechanism of electric currents and fields in the ionosphere', *J. Geophys. Res.*, **81**, 547–555. doi: 10.1029/JA081i004p00547.

Rombouts, J. and Ghil, M. (2015), 'Oscillations in a simple climate–vegetation model', *Nonlin. Proc. Geophys.*, **22**, 275–288. doi: 10.5194/npg–22–275–2015.

Rostoker, G. (1997), *Physics of magnetic storms*, Vol. 98, Geophys. Monogr., AGU, Washington, D.C.

Rostoker, G., Vallance, J. A., Gattinger, R. L., Anger, C. D. and Murphree, J. S. (1987), 'The development of the substorm expansive phase: the "eye" of the substorm', *Geophys. Res. Lett.*, **14**, 339–405.

Rufenach, C. L., McPherron, R. L. and Schaper, J. (1992), 'The quiet geomagnetic field at geosynchronous orbit and its dependence on solar wind dynamic pressure', *J. Geophys. Res.*, **97**, 25–42. doi: 10.1029/91JA02135.

Schmitt, F., Lovejoy, S. and Schertzer, D. (1995), 'Multifractal analysis of the Greenland Ice–Core Project climate data', *Geophys. Res. Lett.*, **22**, 13.

Schulz, M. (2002), 'On the 1470–year pacing of Dansgaard–Oeschger warm events', *Paleoceanography*, **17**, 4. doi: 10.1029/2000PA000571.

Schwabe, S. H. (1843), 'Sonnenbeobachtungen im Jahre 1843 (Observations of the sun in the year 1843)', *Astronomische Nachrichten*, **21**, 223–236.

Schwenn, R. (2006), 'Space Weather: The solar perspective', *Living Rev. Solar Phys.*, **3**, 2. doi: 10.12942/lrsp–2006–2.

Sciffer, M. D., Waters, C. L. and Menk, F. W. (2005), 'Propagation of ULF waves through the ionosphere: Inductive effect for oblique magnetic fields', *Ann. Geophys.*, **22**, 1155–1169.

Sckopke, N. (1966), 'A general relation between the energy of trapped particles and the disturbance field near the Earth', *J. Geophys. Res.*, **71**, 3125–3130.

Seleznyov, A. D., Solanki, S. K. and Krivova, N. A. (2011), 'Modeling solar irradiance variability on time scales from minutes to months', *Astron. Astrophys.*, **532**, A108.

Sellers, W. D. (1969), 'A Global Climatic Model Based on the Energy Balance of the Earth–Atmosphere System', *J. Appl. Meteor.*, **8**, 392.

Shannon, C. E. (1948), 'A mathematical theory of communication', *Bell Syst. Tech. J.*, **27**, 379–423.

Shao, Z. G. and Ditlevsen, P. D. (2016), 'Contrasting scaling properties of interglacial and glacial climates', *Nature Commun.*, **7**, 10951.

Sharma, A. S. (1995), 'Assessing the magnetosphere's nonlinear behavior: its dimensional is low, its predictability is high', *Rev. Geophys.*, **33**, 645.

Shaviv, N. J. (2002), 'Cosmic ray diffusion from the galactic spiral arms, iron meteorites, and a possible climatic connection', *Phys. Rev. Lett.*, **89**, 051102.

Shinbori, A., Koyama, Y., Nose, M., Hori, T., Otsuka, Y. and Yatagai, A. (2014), 'Long–term variation in the upper atmosphere as seen in the geomagnetic solar quiet daily variation', *Earth, Planets & Space*, **66**, 155–174. doi: 10.1186/s40623–014–0155–1.

Signoretti, F., Laurenza, M., Marcucci, M. F. and Storini, M. (2011), 'The Solar–Terrestrial Events during February 2011', *Proceedings of the 32nd International Cosmic Ray Conference*, **10**, 267–270.

Silvermann, B. W. (1998), *Density estimation for statistics and data analysis*, CRC Press, Boca Raton.

Singh, A. K. and Tonk, A. (2014), 'Solar activity during the first six years of solar cycle 24 and 23: a comparative study', *Astrophys. Space Sci.*, **353**, 367. doi: 10.1007/s10509–014–2067–8.

Sitnov, M. I., Sharma, S., Papdopoulos, K. and Vassiliadis, D. (2001), 'Modeling substorm dynamics of the magnetosphere: from self–organization and self–organized criticality to non equilibrium phase transitions', *Phys. Rev. E*, **65**, 16116.

Smart, D. F. and Shea, M. A. (1989), 'PPS-87–A new event oriented solar proton prediction model', *Adv. Space Res.*, **9**, 281–284.

Solanki, S. K., Krivova, N. A. and Haigh, J. D. (2013), 'Solar Irradiance Variability and Climate', *Ann. Rev. Astron. Astrophys.*, **51**, 311–351.

Solanki, S. K., Usoskin, I. G., Kromer, B., Schüssler, M. and Beer, J. (2004), 'Unusual activity of the Sun during recent decades compared to the previous 11,000 years', *Nature*, **431**, 1084–1089. doi: 10.1038/nature02995.

Solé, J., Turiel, A. and Llebot, J. E. (2007*a*), 'Classification of Dansgaard–Oeschger climatic cycles by the application of similitude signal processing', *Phys. Lett. A*, **366**, 184–189.

Solé, J., Turiel, A. and Llebot, J. E. (2007*b*), 'Using empirical mode decomposition to correlate paleoclimatic time-series', *Nat. Hazards Earth Syst. Sci.*, **7**, 299–307. doi: 10.5194/nhess–7–299–2007.

Solomon, S., Qin, D., Manning, M., Chen, Z., Marquis, M., Averyt, K. B., Tignor, M. and Miller, H. L. (2007), *Climate Change 2007: The Physical Science Basis. Contribution of Working Group I to the Fourth Assessment Report of the Intergovernmental Panel on Climate Change*, Cambridge Univ. Press, 996 pp., Cambridge, UK/New York.

Spiegel, D. S., Menou, K. and A., S. C. (2008), 'Habitable climates: the influence of obliquity', *Astrophys. J.*, **681**, 1069–1623.

Spörer, G. (1887), 'über die Periodicität der Sonnenflecken seit dem Jahre 1618, vornehmlich in Bezug auf die heliographische Breite derselben, und Hinweis auf eine erhebliche Störung dieser Periodicität während eines langen Zeitraumes" (on the periodicity of sunspots since the year 1618, especially with respect to the heliographic latitude of the same, and reference to a significant disturbance of this periodicity during a long period)', *Vierteljahrsschrift der Astronomischen Gesellschaft (Leipzig)*, **22**, 323–329.

Spörer, G. (1889), 'Sur les différences que présentent l'hémisphère nord et l'hémisphère sud du Soleil" (on the differences that the northern hemisphere and southern hemisphere of the sun present)', *Bulletin Astronomique*, **6**, 60–63.

Steinhilber, F., Abreu, J. A., Beer, J., Brunner, I., Christl, M., Fischer, H., Heikkilä, U., Kubik, P. W., Mann, M., McCracken, K. G., Miller, H., Miyahara, H., Oerter, H. and Wilhelms, F. (2012), '9,400 years of cosmic radiation and solar activity from ice cores and tree rings', *Proc. Nat. Acad. Sci. USA*, **109**, 5967–5971. doi: 10.1073/pnas.1118965109.

Stocker, T. F. (1998), 'The seesaw effect', *Science*, **282**, 61–62.

Stocker, T. F. and Johnsen, S. J. (2003), 'A minimum thermodynamic model for the bipolar seesaw', *Paleoceanography*, **18**, 1087. doi: 10.1029/2003PA000920.

Storini, M., Cliver, E. W., Laurenza, M. and Grimani, C. (2008), *Developing the scientific basis for monitoring, modelling and predicting Space Weather*, OPOCE publisher, pp. 63–69, COST 724 action.

Suess, H. E. (1980), 'The radiocarbon record in tree rings of the last 8000 years', *Radiocarbon*, **22**, 200–209.

Sugiura, M. and Poros, D. J. (1971), *Hourly values of equatorial Dst for years 1957 to 1970*, Goddard Space Flight Center, Greenbelt, Maryland.

Svalgaard, L. and Wilcox, J. W. (1975), 'Long term evolution of solar sector structure', *Sol. Phys.*, **41**, 461–475.

Svensmark, H. (2012), 'Evidence of nearby supernovae affecting life on Earth', *Monthly Not. Royal Astron. Soc.*, **423**, 1234–1253.

Terradas, J., Oliver, R. and Ballester, J. L. (2004), 'Application of Statistical Techniques to the Analysis of Solar Coronal Oscillations', *Astrophys. J.*, **614**, 435–447. doi: 10.1086/423332.

Tessier, Y., Lovejoy, S. and Schertzer, D. (1993), 'Universal multifractals: theory and observations for rain and clouds', *J. Appl. Meteorology*, **32**, 223–250.

Thayer, J. P., Lei, J., Forber, J. M., Sutton, E. K. and Nerem, R. S. (2008), 'Thermospheric density oscillations due to periodic solar wind high speed streams', *J. Geophys. Res.*, **113**, A06307.

Thebault, E., Finlay, C. C. and Toh, H. (2015), 'International Geomagnetic Reference Field–the twelfth generation', *Earth, Planets & Space*, **67**, 158. doi: 10.1186/s40623–015–0313–0.

Tsurutani, B. T., Hajra, R., Echer, E. and Gjerloev, J. W. (2015), 'Extremely intense (SML $\leq$ –2500 nT) substorms: isolated events that are externally triggered?', *Ann. Geophys.*, **33**, 519–524. doi: 10.5194/angeo–33–519–2015.

Tsurutani, B. T., Sugiura, M., Iyemori, T., Goldstein, B. E., Gonzalez, W. D., Akasofu, S.-I. and Smith, E. J. (1990), 'The nonlinear response of AE to the IMF B_S driver: A spectral break at 5 hours', *Geophys. Res. Lett.*, **17**, 279–282. doi: 10.1029/GL017i003p00279.

Uritsky, V. M., Klimas, A. J., Vassiliadis, D., Chua, D. and Parks, G. (2002), 'Scale–free statistics of spatiotemporal auroral emissions as depicted by POLAR UVI images: The dynamics magnetosphere is an avalanching system', *J. Geophys. Res.*, **107**, 1426.

Uritsky, V. M. and Pudovkin, M. I. (1998), 'Low frequency $1/f$–like fluctuations of the AE–index as a possible manifestation of self–organized criticality in the magnetosphere', *Ann. Geophys.*, **15**, 1580.

Usoskin, I. G. (2013), 'A History of Solar Activity over Millennia', *Living Rev. Sol. Phys.*, **10**, 1. doi: 10.12942/lrsp–2013–1.

Usoskin, I. G., Gallet, Y., Lopes, F., Kovaltsov, G. A. and Hulot, G. (2016), 'Solar activity during the Holocene: the Hallstatt cycle and its consequence for grand minima and maxima', *Astron. Astrophys.*, **587**, A150. doi: 10.1051/0004–6361/201527295.

Usoskin, I. G. and Mursula, K. (2003), 'Long–Term Solar Cycle Evolution: Review of Recent Developments', *Sol. Phys.*, **218**, 319–343. doi: 10.1023/B:SOLA.0000013049.27106.07.

Usoskin, I. G., Mursula, K. and Kovaltsov, G. A. (2001), 'Heliospheric modulation of cosmic rays and solar activity during the Maunder minimum', *J. Geophys. Res.*, **106**, 16039–16046.

Usoskin, I. G., Mursula, K., Solanki, S. K., Schüssler, M. and Alanko, K. (2004), 'Reconstruction of solar activity for the last millennium using ^{10}Be data', *Astron. Astrophys.*, **413**, 745–751. doi: 10.1051/0004–6361:20031533.

Usoskin, I. G., Solanki, S. K. and Kovaltsov, G. A. (2007), 'Grand minima and maxima of solar activity: new observational constraints', *Astron. Astrophys.*, **471**, 301–309. doi: 10.1051/0004-6361:20077704.

Vassiliadis, D. (2006), 'System theory for geospace plasma dynamics', *Rev. Geophys.*, **44**, RG2002. doi: 10.1029/2004RG000161.

Vecchio, A., Laurenza, M., Carbone, V. and Storini, M. (2010), 'Quasi–biennial Modulation of Solar Neutrino Flux and Solar and Galactic Cosmic Rays by Solar Cyclic Activity', *Astrophys. J. Lett.*, **709**, L1–L5. doi: 10.1088/2041–8205/709/1/L1.

Vecchio, A., Lepreti, F., Laurenza, M., Alberti, T. and Carbone, V. (2017), 'Connection between solar activity cycles and grand minima generation', *Astron. Astrophys.*, **in press**. doi: http://dx.doi.org/10.1051/0004–6361–201629758.

Veres, D., Bazin, L., Landais, A., Toyè Mahamadou Kele, H., Lemieux-Dudon, B., Parrenin, F., Martinerie, P., Blayo, E., Blunier, T., Capron, E., Chappellaz, J., Rasmussen, S. O., Severi, M., Svensson, A., Vinther, B. and Wolff, E. W. (2013), 'The Antarctic ice core chronology (AICC2012): an optimized multi–parameter and multi–site dating approach for the last 120 thousand years', *Clim. Past*, **9**, 1733–1748. doi: 10.5194/cp–9–1733–2013.

Vitinsky, Y. I., Kopecky, M. and Kuklin, G. V. (1986), *Statistics of Sunspot Activity (in Russian)*, Nauka, Moscow.

von Bloh, W., Block, A. and Schellnhuber, H. J. (1997), 'Self stabilization of the biosphere under global change: a tutorial geophysiological approach', *Tellus B*, **49**, 249.

Wang, Y.-M. and Colaninno, R. (2014), 'Is solar cycle 24 producing more coronal mass ejections than cycle 23?', *Astrophys. J. Lett.*, **784**, L27.

Wanliss, J. A. (2005), 'Fractal properties of Sym–H during quiet and active times', *J. Geophys. Res.*, **110**, A03202. doi: 10.1029/2004JA010544.

Wanliss, J. A. and Uritsky, V. M. (2010), 'Understanding bursty behavior in midlatitude geomagnetic activity', *J. Geophys. Res.*, **115**, L04107. doi: 10.1029/2009JA014642.

Waters, C. L., Lysak, R. L. and Sciffer, M. D. (2013), 'On the coupling of fast and shear Alfvén wave modes by the ionospheric Hall conductance', *Earth, Planets & Space*, **65**, 2. doi: 10.5047/eps.2012.08.002.

Watson, A. J. and Lovelock, J. E. (1983), 'Biological homeostasis of the global environment: the parable of Daisyworld', *Tellus B*, **35**, 284–289.

Weber, S. L. (2001), 'On Homeostasis in Daisyworld', *Climate Change*, **48**, 465.

White, W. B., Lean, J., Cayan, D. R. and Dettinger, M. D. (1997), 'Response of global upper ocean temperature to changing solar irradiance', *J. Geophys. Res.*, **102**, 3255–3266.

Willson, R. C. and Mordvinov, A. V. (1999), 'Time–frequency analysis of total solar irradiance variations', *Geophys. Res. Lett.*, **25**, 3613–3616.

Winter, L. M. and Ledbetter, K. (2015), 'Type II and Type III radio bursts and their correlation with solar energetic proton events', *Astrophys. J.*, **809**, 105.

Wood, A. J., Ackland, G. J., Dyke, J. G., Williams, H. T. P. and Lenton, T. M. (2008), 'Daisyworld: A review', *Rev. Geophys.*, **46**, 1.

Wu, Z. and Huang, N. E. (2004), 'A study of the characteristics of white noise using the Empirical mode decomposition method', *P. Roy. Soc. Lon. A*, **460**, 1597–1611. doi: 10.5047/eps.2012.08.002.

Wu, Z. and Huang, N. E. (2009), 'Ensemble Empirical Mode Decomposition: a Noise–Assisted Data Analysis Method', *Adv. Adapt. Data Anal.*, **1**, 1–41.

Wu, Z. and Huang, N. E. (2011), 'On the filtering properties of the empirical mode decomposition', *Adv. in Adap. Data Analysis*, **2**, 397–414.

Yang, G., Sun, X.-B., Zhang, M., Li, X. and Liu, X. (2014), 'Study on Ways to Restrain End Effect of Hilbert–Huang Transform', *Journal of Computers*, **25**, 22–31.